# A Millifluidic Bulge Test for Multiscale Properties of Engineered Biofilms

Thesis by

Priya K. Chittur

In Partial Fulfillment of the Requirements for

the degree of Doctor of Philosophy


CALIFORNIA INSTITUTE OF TECHNOLOGY

Pasadena, California

2023

(Defended August 17, 2022)

© 2023

Priya K. Chittur

ORCID: 0000-0002-9409-4671

All rights reserved

*Dedicated to Radha patti*

# Acknowledgements

This thesis and the last few years would not have been possible without support, advice, and mentorship from many, many people.

First, thank you to my advisor, Prof. Kornfield, for accepting me into your lab. Thank you for the many lessons I learned in your lab and will continue to apply in other fields as well. Thank you for teaching me how to be a better scientist, how to focus on and develop an idea, to think about details, and to construct better figures and presentations. I also had a chance to be exposed to a variety of different fields of research I had no familiarity with before coming here, and am grateful to you for giving me exciting opportunities to work with new collaborators.

Next, thank you to my committee, Prof. Tirrell, Prof. Ravichandran, and Prof. Okumura, for helpful feedback on my research and proposals.

Prof. Ravichandran, thank you especially for your kindness and encouragement, for always sending helpful resources and suggesting possible directions of research, for your willingness to be on my committee across time zones, and for guiding me through much of the mechanics: thank you for reading through pages and powerpoint slides full of questions and taking the time to respond to each one in detail. I am sincerely grateful for your advice, mentorship, and kind feedback.

Thank you to Prof. Leadbetter for your mentorship on the CEMI project; it has been an exciting experience for me to learn more about iridescent bacteria.

My undergraduate research and classroom experiences were the reason I chose to go to graduate school. Thank you G Sir, for giving me the opportunity to learn from you (even though I broke an adapter on my first day), for sharing your excitement for research and amazing ideas: I chose to go to graduate school because of my experiences in your class and your lab. Thank you GK Sir for the opportunity to work in your lab, for taking the time to teach me about fluorescence in detail, and letting me work on an exciting project. Thank you also to Prof. Record for the time I spent in your lab as part of the Khorana Program.

Next, thank you to my family: Amma, Appa, Krishna, and Patti, thank you for your support, for talking to me and guiding me through tough times.

Thank you to all my collaborators on the ELM project from other labs whom I had a chance to collaborate with and learn from. Prof. Shapiro and Prof. Ismagilov, thank you for helpful comments. Thank you to Hanwei for collaborating and sharing biofilms for testing, Leah and Prof. Sim for collaborating and discussing data analysis.

Thank you to Dr. Collazo and Dr. Spigolon at the BIF for your advice and discussions on imaging, samples, and setups.

Thank you to everyone in the Kornfield group, past and present, whom I had a chance to interact with. Christine and Abigail, thank you for keeping the group running and functional. Paresh and Hojin, thank you for reading and editing my thesis, and for advice and coffee chats. Lealia and Tiziana, thank you for collaborations, advice, and support in ELM and otherwise. Rachel, Dan, Orland, Jinmo, Hyesoo, thank you for the friendly chats.

Andy, thank you for your insightful comments and questions during group meeting and in general. Red, Rob, Ben, Joey, Jeremy, and Prof. Tanner, thank you for helpful suggestions.

Thank you also to those I had a chance to interact with from other labs: Kimberley for explaining DIC to me, Suraj (now Prof. Ravindran!) for guiding me through AFM, Michelle for help with the initial selection of OCT parts and for letting us use your lab's OCT in the meantime, Bradley for discussions and bacterial strains, Saransh for letting me borrow the Gaussmeter, Mary for advice and helping me find a lab. Thank you also to Sasha and Johnny, my summer undergraduate students who gave me a chance to mentor and to learn about other interesting research ideas. Thank you Dr. Blümler (U Mainz) for sharing your Halbach array design. Unfortunately while the final setup didn't make it into this thesis, it was a great experience for me to put the instrument together.

Thank you to our Chemistry admin Ms. Ross for taking the time to advise me on labs, to Mr. Suresha Guptha for technical help, and to Leslie for morning chats. Finally, thank you to Caltech Center for Environmental Microbiology and DARPA for funding this work.

# Abstract

Biofilms – communities of bacterial cells associated with their extracellular polymeric matrices – are complex materials whose features span many length scales, ranging from bulk cohesive material properties, to mesoscale structural and compositional heterogeneity, down to the microscopic cellular morphology and cell-cell interaction chemistry.

Here, we demonstrate a tool to study the mechanical properties of biofilms across length scales from the mesoscale (0.2 mm) to the bulk (1 mm) using a simplified model system based on genetically engineered *E. coli*. Using a custom millifluidic device that suspends a 3 mm dia. biofilm across a support, we impose tunable hydrostatic pressure drops in the Pa-kPa range across the biofilm. The resulting deformation of the film through an aperture is visualized with optical coherence tomography and used to estimate bulk and mesoscale mechanical properties of the film. Our method requires only microliters of material, causes minimal disruption to the film structure, and allows for estimates of both average properties as well as local heterogeneity as a function of cell-cell interaction chemistry and biofilm damage and healing. In the final chapter we introduce other model biofilm systems for their unique optical and mechanical properties.

# Table of Contents

# List of Figures

# List of Tables

*Chapter 1*

# Introduction

## 1.1 Motivation

The ability to quantify bulk biofilm mechanical properties is a relevant challenge for multiple fields: in medical applications, insights into composition-mechanics relationships can guide better solutions to eradicating pathogenic microbes[1–4] (e.g. *Pseudomonas aeruginosa*), while recent work on engineered living materials has focused on targeted improvements to material properties (e.g. toughness, stiffness) via engineering aspects of cell or biofilm chemistry[5].

Common to these diverse applications is the open question: how does one characterize the bulk properties of a biofilm?

Biofilms are inherently challenging materials to test at a bulk scale: their properties are tied to their underlying structure, composition, and chemistry, demanding a multiscale approach, and many (even engineered) biofilms are too fragile to be used with tools common to other non-biological materials, for example, a dynamic mechanical analyzer.

Here, we face a second question: what are the desirable characteristics of a mechanical measurement technique?

We began by identifying certain characteristics we felt were important to an ideal characterization method:

i) An ideal method would respect the integrity of the biofilm and cause minimal disruption to its internal structure and composition during handling and loading.

ii) An ideal technique would also span multiple length scales and provide some degree of spatial resolution in addition to bulk measurements.

iii) It would also be convenient to have a well-characterized stress and strain.

iv) A fourth desirable characteristic would be the ability to image a range of properties from those at small strains to yielding and failure.

A review of literature shows that existing techniques for biofilm characterization capture various partial combinations of the above requirements, some of which are detailed below (see[6–10] for reviews).

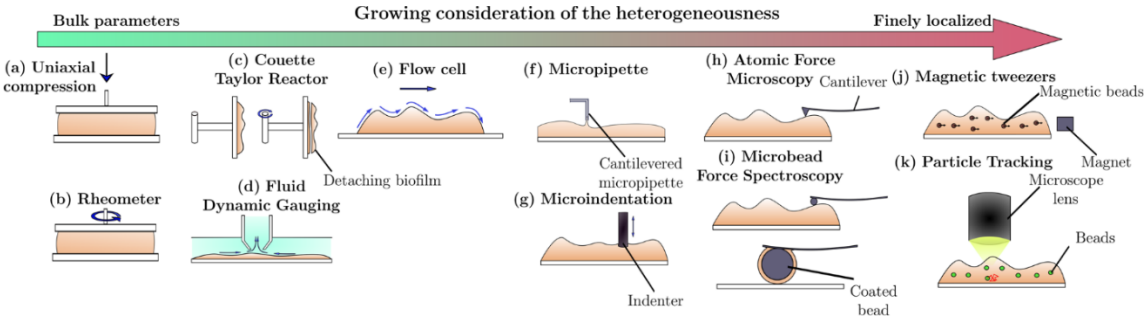


Figure 1.1. Biofilm mechanical characterization at various length scales (reproduced from [8] with permission, open access).

### 1.2 Existing methods to test bulk and mesoscale properties of biofilms

AFM indentation is one of the most common methods used to report biofilm properties, and can measure the elastic modulus of single cells or biofilm surfaces by indentation with various probe radii at different indentation depths.[3,11–19] It also causes minimal disruption to biofilm structure, thereby satisfying condition (i) above, but is limited to small indentation depths relative to the thickness of the biofilm (small strains) (Figure 1.1).

Other examples of techniques that preserve the integrity of the biofilm are microrheology and deformation under shear flow, where the former provides local information and the latter begins to approach the bulk scale (Figure 1.1). In microrheology, beads are added to the biofilm during growth to act as local tracers for observation with microscopy. Bead motion and paths driven by different external forces are observed and used to estimate the properties of the local microenvironment. In passive microrheology, bead motion is driven by thermal energy[20], while in active microrheology it is achieved using optical or magnetic tweezers for external manipulation. Microrheology has been used successfully to test the properties of both *E. coli*[21–23] and *P. aeruginosa*[24,25] biofilms, among others.

Using passive microrheology of 0.2 – 1 μm fluorescent tracer particles, Chew and coworkers discovered that both structural and compositional heterogeneity in *P. aeruginosa* biofilms contribute to local mechanical properties[24]. The overexpression of different exopolysaccharides (Psl, Pel, or alginate) determined the local morphology of the film and whether it developed into microcolonies, voids, or plains (Figure 1.2), and the internal properties (crosslinked and stiff vs. viscous). An advantage of this thermally driven method is the ability to characterize more viscous films–the creep compliance of films

tested was between $10^{-2}$ and $10^{-4}$ $Pa^{-1}$. A variation of passive microrheology was also performed by Rogers and coworkers[23], who used the cells themselves as tracers.

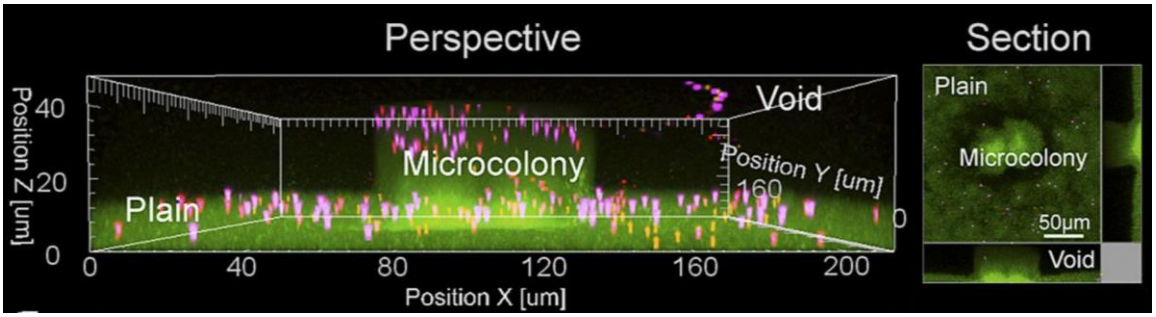


Figure 1.2. Passive microrheology with microsphere tracers embedded in biofilms (here, *P. aeruginosa*) can be used to study local mechanical properties as a result of composition and local structural features (microcolonies, plains, voids). Reproduced with permission from [24].

Magnetic microrheology can accommodate stiffer films as well and has been used successfully to observe heterogeneity in *E. coli* biofilms[21,26]; Galy and coworkers discovered that elastic instantaneous compliance $J_0$ exhibited a consistent pattern for F-pilus producing *E. coli* grown at low shear ($3 \times 10^{-3}$ $Pa^{-1}$, Re < 1), with three vertical zones ranging from the lowest zone with high rigidity (10 $\mu$m thickness, elastic modulus range 5-200 Pa), a second zone (20 $\mu$m thickness) with a broad distribution of compliance values (0.2-200 Pa), and a third upper layer of 15 $\mu$m thickness which had the highest average elasticity.[21]

Overall, while both AFM nanoindentation and microrheology can provide rich information at the local scale, have well-characterized stress and strain (iii), and respect biofilm structure and composition (i), they are limited in their abilities to access larger length scales or provide information about biofilm failure (i) and (iv).

Visualizing biofilm deformation under shear flow with optical coherence tomography (OCT)[27] is a method that provides information at the hundreds of microns to millimeter length scales (more "bulk" than AFM or microrheology). The biofilm is grown and tested in a flow cell with simultaneous OCT imaging, and hydrodynamic load is estimated by modeling the velocity profile of the fluid. Some of the advantages of this method include avoiding tracers or dyes in the film, the ability to accommodate softer biofilms, not having to consider tip-film or microsphere-film interactions, and not disrupting biofilm structure. However, the adhesion of the film to the substrate has to be considered in addition to its properties. Blauert and coworkers[28] performed image analysis of biofilm deformation to estimate shear moduli in the ~ 30 Pa range and estimated elastic moduli by visualizing the elongation of streamers in regions of the film (Figure 1.3). Although in this example the film was treated as homogeneous, digital image correlation to visualize potential regions of heterogeneity is also possible with this method using features present in the film[29]. Although this method addresses (i) and (ii) above, (iii) and (iv) are challenges associated with the setup.

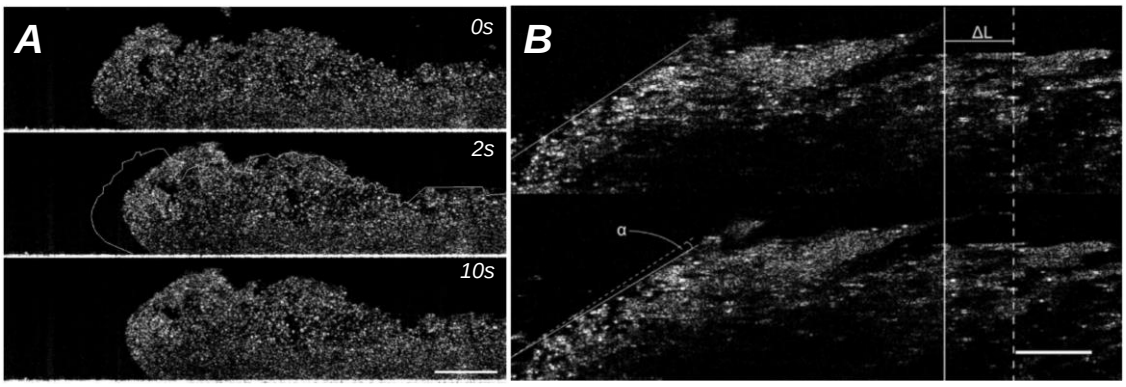


Figure 1.3. (A) OCT B-scan (vertical cross section) at shear stress = 0.8 Pa. Film deforms along the axis of flow (top: initial frame; middle: scan after 2s; bottom: scan after 10s). Scale 250 μm. (B) B-scans of biofilm showing both change in angle of the front of the film (α) as well as the elongation of a small streamer (ΔL) used to estimate Young's modulus. Top: initial frame at shear stress = 0.1 Pa. Bottom: shear stress = 1.64 Pa. Figures adapted with permission from [28].

Continuing with the bulk scale, the most commonly used instrument for bulk biofilm characterization is a rheometer, which has well-characterized stress and strain (iii), but requires large volumes (milliliters) of sample material and does not necessarily preserve the internal structure of the film (i) or apply a uniform deformation. Often it requires the scraping and pooling together of multiple samples, and presents additional challenges such as sample loading on to the tool geometry and evaporation. Even so, it has been used successfully in many cases to investigate biofilm properties[1,2,4,18,19,30–32]. Lielig and coworkers used frequency sweep and constant shear rate rheometer experiments to determine that *P. aeruginosa* biofilms were also able to recover their stiffness even after large deformations that induced yielding and failure[31]. This bulk technique was also sufficient to quantify decreases in stiffness of the film elasticity upon chemical perturbation by mono or divalent ions, polyelectrolytes, or changes to pH. Kovach and coworkers also

scraped and pooled samples of *P. aeruginosa* films to characterize the impact of different EPS components on film properties (Figure 1.4). Increased production of one of the exopolysaccharides, Psl, increased the plateau storage modulus by 80% compared to the wildtype strain while production of the alternate exopolysaccharide Pel increased yield strain by 60%.[33] Thus, while the conventional use of a rheometer with parallel plate geometry and pooled samples has disadvantages, it is able to characterize general properties such as stiffness, yielding, and toughness.

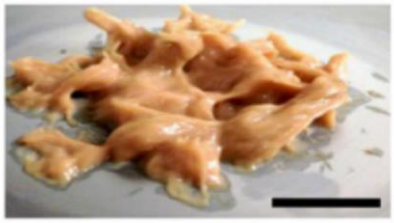

Figure 1.4. Psl overproducing *P. aeruginosa;* 10-15 plates of biofilm required (pooled) to perform rheology. Scale bar estimated 3 mm based on other publications by authors specifying tool geometry. Image adapted from [34], open access.

Efforts have been made to study biofilm mechanical properties at the bulk scale without perturbing the structure. One method has been to grow the films directly on the rheometer, with the fixture submerged in a continuous culture[1]. Another method is by using freely suspended films to avoid the issues of sample transfer, pooling, or clamping. In general this has been achieved by working with strains that grow into pellicles-robust sheets of material at the air-water interface. Hollenbeck and coworkers grew a *B. subtilis* pellicle on the order of 12 mm length and 350 μm thickness which naturally attached to two poly(ethylene terephthalate) plates as it grew. One was kept stationary and attached to a double cantilever spring used to measure force while the other was mobile and moved at a

constant strain rate (Figure 1.5A). Using this method, the authors were able to test the pellicle until failure and observe its properties at various strain rates[35]. The use of pellicle forming strains (e.g. curli-expressing *E. coli*[36] or pellicle-forming *V. cholerae*[37]) also facilitated the use of interfacial rheometry for biofilm characterization using a modified double-wall couette Teflon flow cell (Figure 1.5B). Hollenbeck and coworkers[37] and Wu and coworkers[36] used this tool geometry to grow the pellicle directly on the rheometer, avoid evaporation, and minimize sample handling prior to testing interfacial properties. Similar interfacial rheology measurements have been used for other films that grow at the air-water interface[38].

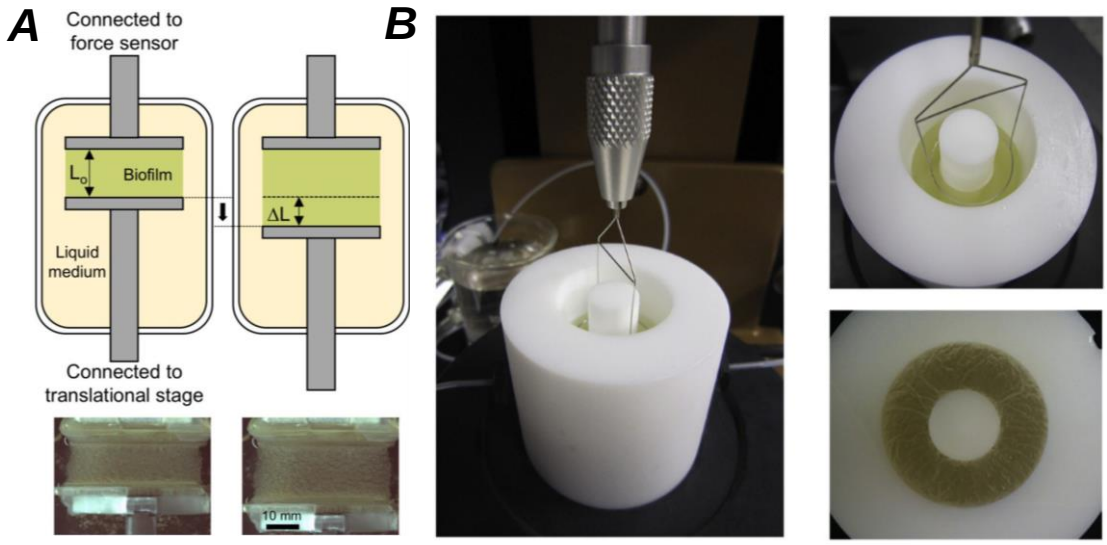


Figure 1.5. (A) Translational setup for *B. subtilis* pellicle, in situ. Adapted with permission from [35]. Copyright 2016 American Chemical Society. (B) Du Noüy ring positioned at air-water interface, and a double Couette teflon flow cell apparatus. Bottom right: pellicle formed in a double-couette teflon flow cell apparatus. Figures adapted with permission from [36].

Visible features on the pellicles have also enabled efforts to visualize heterogeneity in the same films, for example using visible features to perform particle image velocimetry (PIV)

to elucidate displacement field.[35] These above experiments have begun to address (i) through (iv) above, though so far they have been limited to pellicle expressing films which simplify the sample growth and handling process.

Apart from work with pellicles, studies on free biofilms have been limited. In one example by Grumbein and coworkers[39], *B. subtilis* biofilms were inoculated on pre-cut agar to form a central test region where the films were ideally freely suspended, and tested using a custom tensile instrument (Figure 1.6). This setup is aimed at determining rupture forces and tensile strength of films, since the setup targets 100-1000% strain and forces in the mN range. Other challenges in this approach are the use of a camera to monitor the process and estimate deformation field, and assumptions made regarding the thickness of the film since it cannot be directly monitored.

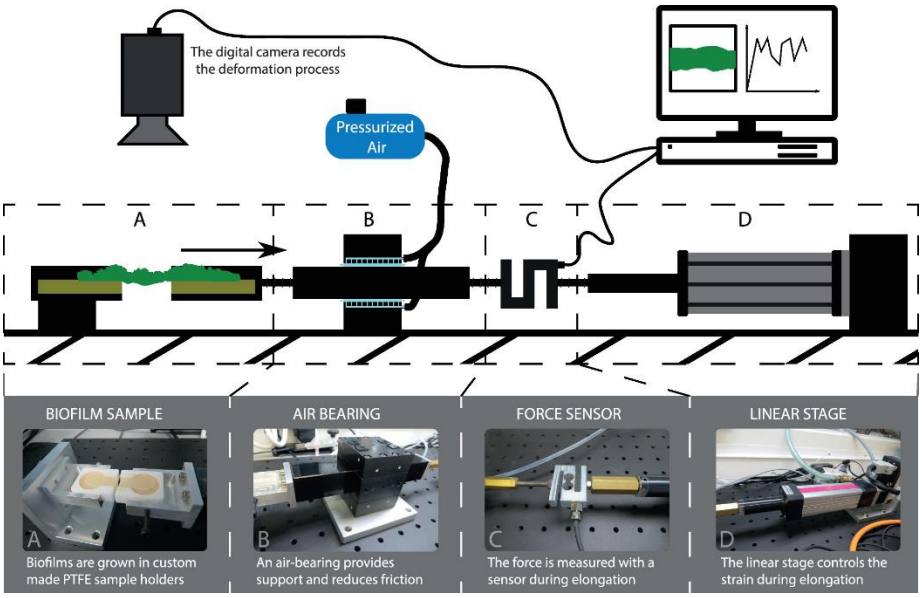


Figure 1.6. Freely suspended *B. subtilis* biofilms grown across cut agar supports tested at 100-1000% strain and mN forces. Reproduced from [39] with permission.

In the review of recent methods above, an aspect especially apparent at the bulk scale is the difficulty of developing techniques that are able to characterize both small and large strain behavior of a biofilm while minimizing sample pooling or damage of structure, finding methods to clamp and hold the sample in place, and being able to apply small forces and observe the deformation with an imaging modality that can access volumetric information, with techniques that can effectively characterize stress and strain state in the sample (i-iv in the previous section).

Is it possible to capture all of these aspects (i) through (iv)? In a limited way, we attempt to do so. In this thesis, we report a technique based on the bulge (inflation) test, a method that has been used for the characterization of sheet metals, polymers, and tissue[40–51], but has not yet been adapted for use with biofilms.

### 1.3 The bulge test, applied to biofilms

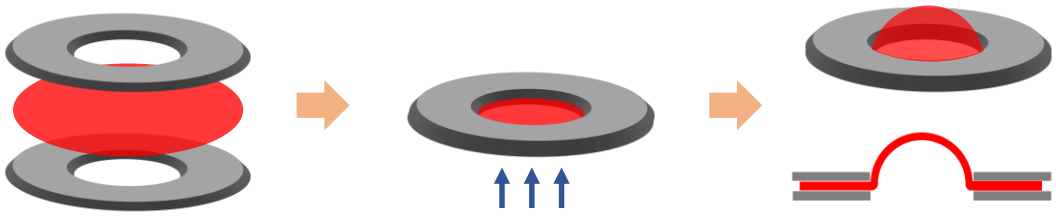

Figure 1.7. In the bulge test, a thin sheet of material is clamped such that the material can be inflated through an aperture of known dimensions with pressure applied to one side. The shape of the deformed material can be imaged.

The bulge test uses a thin film clamped in such a way that the application of pressure from one end causes the film to inflate through an aperture of desired size and aspect ratio (Figure 1.7).

In 1959, J.W. Beams first reported the use of the bulge test to measure properties of thin films of silver and gold cemented over the end of a copper tube[52]. Air pressure applied to the tube caused inflation of the films through the circular aperture created by the tube, monitored by microscopy or light interference methods. He also presented estimates of stress and strain by assuming the bulged shape was a spherical cap, with tension in the walls approximated by relations used for a spherical pressure vessel, and strain using a small deflection approximation.

Many studies followed after, using the bulge test to characterize thin metal films[40,43,53].

Work by W.D. Nix and Vlassak in 1992 expanded the framework, describing more accurate methods to extract properties from the bulge test and detailing relations for other aspect ratios and geometries of the aperture.[54–56] Since then the use of the bulge test as a characterization tool has been proposed for and expanded to a large variety of materials ranging from polymers[50,57,58] to soft biological tissue[41,59,60], and other biologically relevant systems[49,61].

Our choice of the bulge test as a tool was based on i) its broad applicability to various materials and extensive literature on data reduction and solutions for samples of specific dimensions[58,60,62–67] ii) the ability to test a biofilm in its freely suspended state iii) its ability to "map" the properties across a material, providing both local and bulk information, and iv) the small sample volumes required if the test were to be scaled down for biofilms.

In order to adapt the method for biofilms, which are inherently fragile, we constructed a custom millifluidic device to apply Pa-kPa pressure drops across a freely suspended

biofilm, and imaged the deformation of the film using optical coherence tomography. Optical coherence tomography (OCT) i) provides fast scanning on the order of milliseconds in 2D, ii) has a millimeter scale field of view (thus, “bulk”), iii) has a long working distance (millimeters), which allows us to image through devices, and iv) does not require staining, since signal is generated by scattering from the sample. OCT is used most extensively for corneal biomechanics, but has also been used for elastography of biological tissue[28,68]. There has been limited literature[28] on its use for characterizing the mechanical properties of biofilms, especially with large deformations.

Using our custom device and a model engineered biofilm system, we demonstrate here the bulge test-OCT method to estimate bulk and local mechanical properties of engineered biofilms for insights into chemistry-property relationships, failure, and healing of living materials.

### 1.4 Outline of this thesis

In Chapter 2 of this thesis, we discuss the apparatus and model engineered biofilms in more detail. Chapter 3 focuses on bulk biofilm characterization using the bulge test method and broad approximations, while Chapter 4 discusses analysis methods to localize properties to visualize heterogeneity and its physical implications in engineered films. Finally in Chapter 5, we move to a discussion of natural biofilms with interesting physical properties.

**References**


1. Pavlovsky, L., Younger, J. G., Solomon, M. J., Edu, J. & Edu, M. In situ rheology of Staphylococcus epidermidis bacterial biofilms. *Soft Matter* **9**, 122–131 (2013).

2. Pavlovsky, L., Sturtevant, R. A., Younger, J. G. & Solomon, M. J. Effects of temperature on the morphological, polymeric, and mechanical properties of Staphylococcus epidermidis bacterial biofilms. *Langmuir* **31**, 2036–2042 (2015).

3. Kundukad, B. *et al.* Mechanical properties of the superficial biofilm layer determine the architecture of biofilms. *Soft Matter* **12**, (2016).

4. Kovach, K. *et al.* Evolutionary adaptations of biofilms infecting cystic fibrosis lungs promote mechanical toughness by adjusting polysaccharide production. *npj Biofilms Microbiomes* **3**, (2017).

5. Nguyen, P. Q., Courchesne, N. M. D., Duraj-Thatte, A., Praveschotinunt, P. & Joshi, N. S. Engineered Living Materials: Prospects and Challenges for Using Biological Systems to Direct the Assembly of Smart Materials. *Advanced Materials* vol. 30 (2018).

6. Billings, N., Birjiniuk, A., Samad, T. S., Doyle, P. S. & Ribbeck, K. Material properties of biofilms—a review of methods for understanding permeability and mechanics. *Reports Prog. Phys.* **78**, 036601 (2015).

7. Böl, M., Ehret, A. E., Bolea Albero, A., Hellriegel, J. & Krull, R. Recent advances in mechanical characterisation of biofilm and their significance for material modelling. *Crit. Rev. Biotechnol.* **33**, 145–171 (2013).

8. Boudarel, H., Mathias, J. D., Blaysat, B. & Grédiac, M. Towards standardized mechanical characterization of microbial biofilms: analysis and critical review. *npj Biofilms and Microbiomes* vol. 4 1–15 (2018).

9. Tallawi, M., Opitz, M. & Lieleg, O. Modulation of the mechanical properties of bacterial biofilms in response to environmental challenges. *Biomaterials Science* vol. 5 887–900 (2017).

10. Peterson, B. W. *et al.* Viscoelasticity of biofilms and their recalcitrance to mechanical and chemical challenges. *FEMS Microbiology Reviews* vol. 39 234–245 (2015).

11. Zeng, G. *et al.* Functional bacterial amyloid increases Pseudomonas biofilm hydrophobicity and stiffness. *Front. Microbiol.* **6**, 1–14 (2015).

12. Díaz, C., Schilardi, P. L., Salvarezza, R. C. & Fernández Lorenzo de Mele, M. Have flagella a preferred orientation during early stages of biofilm formation?: AFM study using patterned substrates. *Colloids Surfaces B Biointerfaces* **82**, 536–542 (2010).

13. Li, C., Wagner, M., Lackner, S. & Horn, H. Assessing the influence of biofilm surface roughness on mass transfer by combining optical coherence tomography and two-dimensional modeling. *Biotechnol. Bioeng.* **113**, 989–1000 (2016).

14. McLean, R. J. C., McGowin, C. L., Barnes, M. B., Aron, G. M. & Bates, C. L. Methods of Studying Biofilms. *Microb. Biofilms* 379–413 (2004) doi:10.1128/9781555817718.ch20.

15. Billings, N., Birjiniuk, A., Samad, T. S., Doyle, P. S. & Ribbeck, K. Material properties of biofilms - A review of methods for understanding permeability and mechanics. *Reports Prog. Phys.* **78**, 036601 (2015).

16. Wang, H., Wilksch, J. J., Strugnell, R. A. & Gee, M. L. Role of Capsular Polysaccharides in Biofilm Formation: An AFM Nanomechanics Study. *ACS Appl. Mater. Interfaces* **7**, 13007–13013 (2015).

17. Dufrêne, Y. F. Sticky microbes: Forces in microbial cell adhesion. *Trends Microbiol.* **23**, 376–382 (2015).

18. Kovach, K., Davis-Fields, M., Rodesney, C. & Gordon, V. Measuring the mechanics of biofilms at multiple lengthscales. *SPIE Newsroom* 2–5 (2015) doi:10.1117/2.1201503.005754.

19. Safari, A., Tukovic, Z., Walter, M., Casey, E. & Ivankovic, A. Mechanical properties of a mature biofilm from a wastewater system: from microscale to macroscale level. *Biofouling* **31**, (2015).

20. Mason, T. G. & Weitz, D. A. Optical Measurements of Frequency-Dependent Linear Viscoelastic Moduli of Complex Fluids. *Phys. Rev. Lett.* **74**, 1250 (1995).

21. Galy, O. *et al.* Mapping of Bacterial Biofilm Local Mechanics by Magnetic Microparticle Actuation. *Biophysj* **103**, 1400–1408 (2012).

22. Birjiniuk, A. *et al.* Single particle tracking reveals spatial and dynamic organization of the E. coli biofilm matrix. *New J. Phys.* **16**, 085014 (2014).

23. Rogers, S. S., Van Der Walle, C. & Waigh, T. A. Microrheology of bacterial biofilms in Vitro: Staphylococcus aureus and Pseudomonas aeruginosa. *Langmuir* **24**, 13549–13555 (2008).

24. Chew, S. C. hue. *et al.* Dynamic remodeling of microbial biofilms by functionally distinct exopolysaccharides. *MBio* **5**, e01536–e01514 (2014).

25. Chew, S. C., Rice, S. A., Kjelleberg, S. & Yang, L. In Situ Mapping of the Mechanical Properties of Biofilms by Particle-tracking Microrheology. *J. Vis. Exp.* **2015**, (2015).

26. Zrelli K, Galy, O, Henry, N. Bacterial biofilm mechanical properties persist upon antibiotic treatment and survive cell death. *New J. Phys.* **15**, 2–16 (2013).

27. Wagner, M. & Horn, H. Optical coherence tomography in biofilm research: A comprehensive review. *Biotechnol. Bioeng.* (2017) doi:10.1002/bit.26283.

28. Blauert, F., Horn, H. & Wagner, M. Time-resolved biofilm deformation measurements using optical coherence tomography. *Biotechnol. Bioeng.* **112**, 1893–1905 (2015).

29. Mathias, J. D. & Stoodley, P. Applying the digital image correlation method to estimate the mechanical properties of bacterial biofilms subjected to a wall shear stress. *Biofouling* **25**, 695–703 (2009).

30. Huang, J. *et al.* Programmable and printable Bacillus subtilis biofilms as engineered living materials. *Nat. Chem. Biol.* **15**, 34–41 (2019).

31. Lieleg, O., Caldara, M., Baumgärtel, R. & Ribbeck, K. Mechanical robustness of Pseudomonas aeruginosa biofilms. *Soft Matter* **7**, 3307–3314 (2011).

32. Jones, W. L., Sutton, M. P., McKittrick, L. & Stewart, P. S. Chemical and antimicrobial treatments change the viscoelastic properties of bacterial biofilms. *Biofouling* **27**, 207–215 (2011).

33. Jennings, L. K. *et al.* Pel is a cationic exopolysaccharide that cross-links extracellular DNA in the Pseudomonas aeruginosa biofilm matrix. doi:10.1073/pnas.1503058112.

34. Kovach, K. *et al.* Evolutionary adaptations of biofilms infecting cystic fibrosis lungs promote mechanical toughness by adjusting polysaccharide production. *npj Biofilms Microbiomes* **3**, 1 (2017).

35. Hollenbeck, E. C. *et al.* Mechanical behavior of a Bacillus subtilis pellicle. *J. Phys. Chem. B* **120**, 6080–6088 (2016).

36. Wu, C., Lim, J. Y., Fuller, G. G. & Cegelski, L. Quantitative Analysis of Amyloid-Integrated Biofilms Formed by Uropathogenic Escherichia coli at the Air-Liquid Interface. *Biophys. J.* **103**, 464 (2012).

37. Hollenbeck, E. C. *et al.* Molecular Determinants of Mechanical Properties of V. cholerae Biofilms at the Air-Liquid Interface. *Biophys. J.* **107**, 2245 (2014).

38. Rühs, P. A., Böni, L., Fuller, G. G., Inglis, R. F. & Fischer, P. In-situ quantification of the interfacial rheological response of bacterial biofilms to environmental stimuli. *PLoS One* **8**, (2013).

39. Grumbein, S., Werb, M., Opitz, M. & Lieleg, O. Elongational rheology of bacterial biofilms in situ. *J. Rheol. (N. Y. N. Y).* **60**, 1085–1094 (2016).

40. Tsakalakos, T. & Hilliard, J. E. Elastic modulus in composition-modulated copper-nickel foils. *J. Appl. Phys.* **54**, 734–737 (1983).

41. Hsu, F. P. K., Liu, A. M. C., Downs, J., Rigamonti, D. & Humphrey, J. D. A Triplane Video-Based Experimental System for Studying Axisymmetrically Inflated Biomembranes. *IEEE Trans. Biomed. Eng.* **42**, 442–450 (1995).

42. Marra, S. P., Kennedy, F. E., Kinkaid, J. N. & Fillinger, M. F. Elastic and rupture properties of porcine aortic tissue measured using inflation testing. *Cardiovasc. Eng.* **6**, 123–131 (2006).

43. Tabata, O., Kawahata, K., Sugiyama, S. & Igarashi, I. Mechanical property measurements of thin films using load-deflection of composite rectangular membranes. *Sensors and Actuators* **20**, 135–141 (1989).

44. Mohan, D. & Melvin, J. W. Failure properties of passive human aortic tissue. II-Biaxial tension tests. *J. Biomech.* **16**, (1983).

45. Cavinato, C. *et al.* Biaxial loading of arterial tissues with 3D in situ observations of adventitia fibrous microstructure: A method coupling multi-photon confocal microscopy and bulge inflation test. *J. Mech. Behav. Biomed. Mater.* **74**, 488–498 (2017).

46. Midgett, D. E., Quigley, H. A. & Nguyen, T. D. In vivo characterization of the deformation of the human optic nerve head using optical coherence tomography and digital volume correlation. *Acta Biomater.* **96**, 385–399 (2019).

47. Tonge, T. K., Atlan, L. S., Voo, L. M. & Nguyen, T. D. Full-field bulge test for planar anisotropic tissues: Part I-Experimental methods applied to human skin tissue. *Acta Biomater.* **9**, 5913–5925 (2013).

48. Wang, L., Tian, L., Huang, Y., Huang, Y. & Zheng, Y. Assessment of Corneal Biomechanical Properties with Inflation Test Using Optical Coherence Tomography. *Ann. Biomed. Eng.* **46**, 247–256 (2018).

49. Zamprogno, P. *et al.* Mechanical properties of soft biological membranes for organ-on-a-chip assessed by bulge test and AFM. *ACS Biomater. Sci. Eng.* **7**, 2990–2997 (2021).

50. O'Connell, P. A. & McKenna, G. B. Novel nanobubble inflation method for determining the viscoelastic properties of ultrathin polymer films. *Rev. Sci. Instrum.* **78**, 14706 (2007).

51. Turner, J. A., Menary, G. H. & Martin, P. J. Biaxial characterization of poly(ether-ether-ketone) for thermoforming: A comparison between bulge and in-plane biaxial testing. *Polym. Eng. Sci.* **59**, 1853–1865 (2019).

52. Beams, J. W. Mechanical properties of thin films of gold and silver. *Struct. Prop. Thin Film.* 183–192 (1959).

53. Allen, M. G., Mehregany, M., Howe, R. T. & Senturia, S. D. Microfabricated structures for the in situ measurement of residual stress, Young's modulus, and ultimate strain of thin films. *Appl. Phys. Lett.* **51**, 241–243 (1987).

54. Vlassak, J. J. & Nix, W. D. A New Bulge Test Technique for the Determination of Young Modulus and Poisson Ratio of Thin-Films. *J. Mater. Res.* **7**, 3242–3249 (1992).

55. Small, M. K. & Nix, W. D. Analysis of the accuracy of the bulge test in determining the mechanical properties of thin films. *J. Mater. Res.* **7**, 1553–1563 (1992).

56. Small, M. K., Daniels, B. J., Clemens, B. M. & Nix, W. D. The elastic biaxial modulus of Ag–Pd multilayered thin films measured using the bulge test. *J. Mater. Res.* **9**, 25–30 (1994).

57. Feng, W. W. Viscoelastic Behavior of Elastomeric Membranes. *J. Appl. Mech.* **59**, S29–S34 (1992).

58. Selby, J. C. & Shannon, M. A. Inflation of a circular elastomeric membrane into a horizontally semi-infinite liquid reservoir of finite vertical depth: Quasi-static deformation model. *Int. J. Eng. Sci.* **47**, 700–717 (2009).

59. Wineman, A., Wilson, D. & Melvin, J. W. Material identification of soft tissue using membrane inflation. *J. Biomech.* **12**, 841–850 (1979).

60. Hsu, F. P. K., Schwab, C., Rigamonti, D. & Humphrey, J. D. Identification of response functions from axisymmetric membrane inflation tests: Implications for biomechanics. *Int. J. Solids Struct.* **31**, 3375–3386 (1994).

61. Selby, J. C. & Shannon, M. A. Apparatus for measuring the finite load-deformation behavior of a sheet of epithelial cells cultured on a mesoscopic freestanding elastomer membrane. *Rev. Sci. Instrum.* **78**, 094301 (2007).

62. Neggers, J., Hoefnagels, J. P. M., Hild, F., Roux, S. & Geers, M. G. D. Direct Stress-Strain Measurements from Bulged Membranes Using Topography Image Correlation. *Exp. Mech.* **54**, 717–727 (2014).

63. Hall, M. S., Long, R., Hui, C. Y. & Wu, M. Mapping three-dimensional stress and strain fields within a soft hydrogel using a fluorescence microscope. *Biophys. J.* **102**, 2241–2250 (2012).

64. Acosta Santamaría, V. A., Flechas García, M., Molimard, J. & Avril, S. Three-Dimensional Full-Field Strain Measurements across a Whole Porcine Aorta Subjected to Tensile Loading Using Optical Coherence Tomography–Digital Volume Correlation. *Front. Mech. Eng.* **4**, (2018).

65. Adkins, J.E.; Rivlin, R. S. IX. The deformation of thin shells. in *Large elastic deformations of isotropic materials* 66–70 (1952).

66. Elahi, S. A., Connesson, N., Chagnon, G. & Payan, Y. In-Vivo Soft Tissues Mechanical Characterization: Volume-Based Aspiration Method Validated on Silicones. *Exp. Mech.* **59**, 251–261 (2019).

67. Hart-Smith, L. J. & Crisp, J. D. C. Large elastic deformations of thin rubber membranes. *Int. J. Eng. Sci.* **5**, 1–24 (1967).

68. Valladares Linares, R. *et al.* Compaction and relaxation of biofilms. *Desalin. Water Treat.* **57**, (2016).

*Chapter 2*

# An apparatus to measure the extensional properties of freely suspended biofilms

## 2.1 Introduction

To apply the bulge test to biofilms it was necessary to develop an apparatus and testing protocol. This chapter describes the design requirements, the resulting apparatus and measurement method, and a model engineered biofilm system used to demonstrate their utility. Literature on the bulge test has typically focused on its application to metal sheets, polymer films, and biological skin tissue[1,2,11,12,3–10]. The delicate nature of biofilms, however, requires a device that applies much smaller pressure differences than described previously.

## 2.2 A millifluidic device to adapt the bulge test to biofilms

To adapt the bulge test to biofilms, our minimum requirements were i) a chamber that could hold a thin, flat disk of biofilm with ii) the ability to independently modulate the pressure difference across the two faces of the film, and iii) an imaging protocol to record the deformation. We determined from early trials that fluid (in our case, buffer - PBS) pressure was preferable to air pressure to avoid issues of drying, and fully submerged samples (rather than those at an air-water interface) would avoid undesired lensing while imaging.

With the choice of fluid pressure finalized, we next had to determine how we could construct a suitable sealed chamber that would enable us to independently modulate fluid

pressure applied to either face of the biofilm, and how to hold the film in place during this process. However, to a large extent the design was determined by the dimensions of free biofilm that could be lifted and manipulated freely.

Since we were interested in a range of properties in the mesoscale to bulk range, we aimed for biofilm sample diameters at the millimeter length scale. At this length scale, we found that “TEM grids” could be suitable sample supports. Designed to support samples during transmission electron microscopy (TEM), these were thin metal disks of a standard outer diameter (3.00 to 3.05 mm) and a consistent thickness (typically 25 μm) with precision openings of variable size and geometry. Thus we determined that if we could freely lift a 3 mm diameter sample of biofilm, we could sandwich it in between two TEM grids as sample supports and then construct a chamber to hold the system in place while applying a pressure difference to the two faces of the film. Ideally, the different TEM grid aperture geometries would provide a range of boundary conditions for the experiment.

The next challenge was determining the thickness of biofilm that could be used for our experiments. We attempted to minimize the thickness of the films used since the bulge test relies on membrane approximations, for which thinner films are more appropriate; however the minimum thickness for consistent properties and ease of handling (given the 3 mm diameter punch requirement above) was determined to be in the 65-90 μm range, corresponding to 7 days of growth for all strains tested. With this thickness range, we could then determine the aperture geometries and sizes that would be suitable for our experiments. For the membrane approximation, the aperture diameter should ideally be 20 times the thickness: for our 65-90 μm films, this would mean an aperture diameter of 1.3-

1.8 mm. This range of aperture size was among the geometries available in TEM grids that have a single slot or circular opening. We chose to work with circular openings and tested both 1.5 mm and 2 mm openings in the available materials (copper and stainless steel respectively). The latter failed due to its mechanical instability. On the other hand, a 1.5 mm diameter opening in a copper TEM grid was relatively easy to handle and provided enough space between the edge of the aperture and the outer diameter (3 mm) of the grid to accommodate a nitrile o-ring, which created a seal between the metal disk and the millifluidic device (below). The o-ring was also essential because the biofilm thicknesses were not perfectly fixed and spanned almost a 30 μm range–the o-ring compensated for this by fixing the assembly in place and preventing vertical displacement during testing.

The next aspects of design were the chamber itself and the mechanism by which we would impose a pressure difference, subject to the constraints of our choice of imaging modality. We considered both confocal microscopy and optical coherence tomography (OCT) and chose the latter for its superior penetration depth (on the order of 2 mm) despite the tradeoff in resolution (2-10μm vs ~1μm or less for confocal microscopy), since we were ultimately interested in mesoscale properties. The setup can be modified for confocal microscopy as well (briefly discussed in Chapter 3), but for our purposes of visualizing the entire process of biofilm deformation and failure and constructing a chamber that was sufficiently deep to accommodate this, we found that OCT was ideal. Our ultimate choice of OCT system had an imaging depth of 2.9/2.2/1.9 mm in air/water/glass, and this also narrowed down our choices for fabrication techniques and materials to use to construct the actual device.

Multiple prototypes were screened prior to the final design (combinations of devices made via photolithography and/or PDMS fabrication, 3D printing, and laser cut acrylic) and through those, some key considerations emerged that were taken into account in the final version:

1) The sample chamber had to be designed so that the air, transparent windows, biofilm, and fluid between the objective and the sample fit within the imaging depth constraint of the OCT, allowing for the thickness of adhesive layers and deformation of the biofilm. Furthermore, the geometry of the OCT head necessitated a device that was at least 10 cm in length to have sufficient access space for the reservoirs on the sides. Some degree of transparency was also necessary to monitor fluid within the channels.

2) The device was designed for ease of prototyping and fabrication and ease of loading and unloading, in addition to 3) having adequate rigidity to survive multiple uses, accommodating reversible water-tight seals, and being constructed with channel dimensions and materials that allowed fluid to flow freely.

Many of these aspects could be achieved with a multilayer design.[13]

Clear cast acrylic sheets (1/16" thickness, McMaster-Carr) were used as the base of the millifluidic device. Two sets of channels were etched or cut into the acrylic using a laser cutter (Industrial Laser ILS 9.75), and the individual pieces were assembled with epoxy adhesive to form the device in two parts that could be assembled reversibly (Figure 2.1A). One vertical cylindrical hole and horizontal channel allowed "Reservoir 1" to be connected the top face of the device and control the pressure on the top face of the sample ($p_1$ in

Figure 2.1B); another vertical cylindrical hole passed through the top part and connected to the horizontal channel in the lower part, allowing “Reservoir 2” to control the pressure below the sample ($p_2$ in Figure 2.1B). The channel above the sample was sealed with a glass cover slip to enable imaging. For the connections to the top face, thicker acrylic slabs with through holes threaded to accept quick-tube coupling fittings (51525K442, McMaster-Carr) were bonded to the top surface. The reservoirs themselves were syringes of known internal diameters.

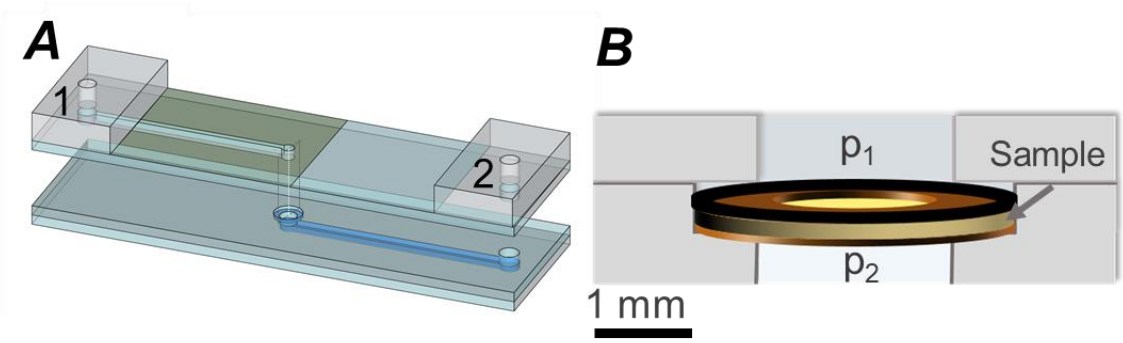


Figure 2.1 (A) Schematic of bulge test device, fabricated as two parts that are separated to load a sample in the central chamber at the center of the device; the top and bottom parts seal with vacuum grease. When loaded and sealed, port 1 connects to a reservoir of fluid that is used to control pressure on the top face of the sample (not shown); similarly, port 2 permits control of the pressure on the bottom face of the sample. Gray layers are acrylic; blue layer indicates etched channel; green thin layer is cover slip glass; layers are bonded using epoxy. Horizontal channels are longer than shown. (B) Schematic diagram of central chamber. Bacterial film sample is supported by two washer-shaped disks. A thin O-ring seals this “sandwich” to the top half of the device.

## 2.3 Engineered biofilms as model systems

Demonstrating our method required a suitable model living material system. Engineered bacterial films developed and grown by Hanwei Liu were used for this purpose. A short description of the materials is presented here; further details to be found in the thesis of H. Liu[14].

Model bacterial films were grown from *E. coli K-12* DH10B engineered to express a plasmid-encoded protein on their cell surface, enabling the cells to assemble into a cohesive bacterial film during growth[15]. The engineered proteins were based on elastin-like polypeptides (ELPs), sequences which contain variable number of repeats of a short amino acid stretch. These engineered proteins were tethered to the cell membrane, effectively creating "brick-and-cement" style materials that could self assemble (Figure 2.2A). Results are reported for different variations of this base strain.

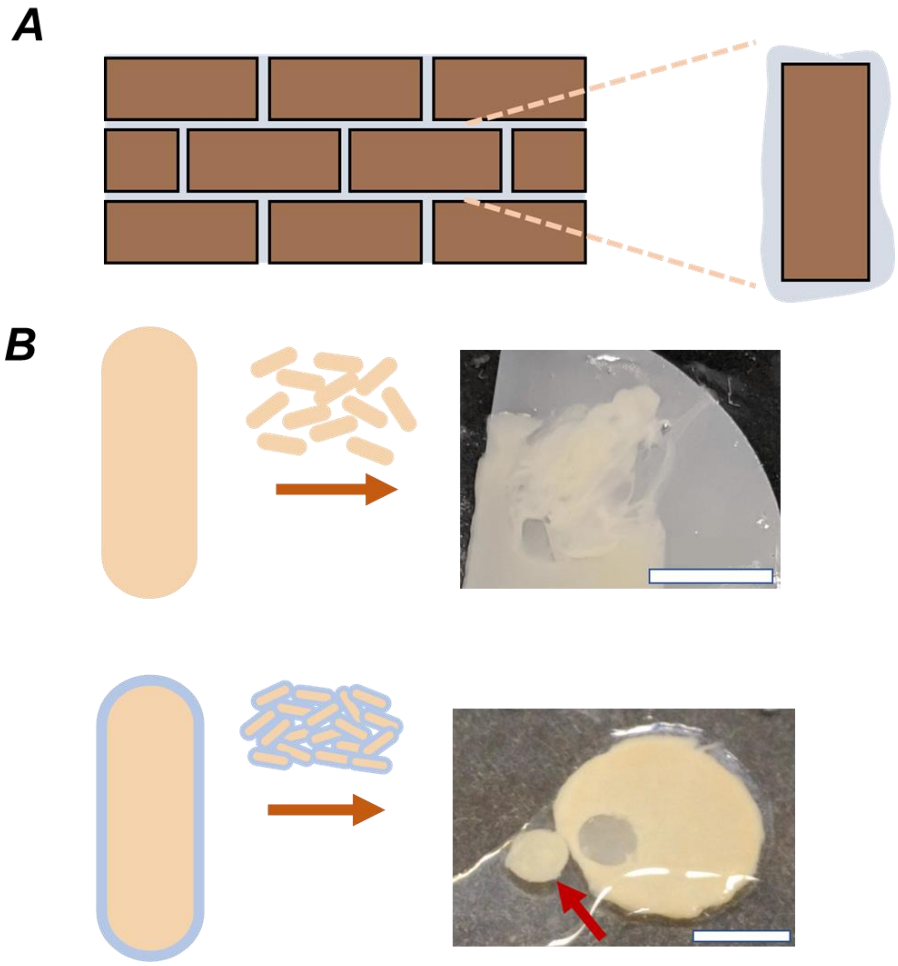


Figure 2.2. A) Brick-and-cement model bacterial film, schematic. B) Film without engineered proteins is not cohesive, while film expressing engineered proteins is cohesive and can be gently peeled from the support underneath (red arrow). Scale = 5 mm.

The control strain with no engineered protein expressed was not cohesive enough to be tested by our method–results are not reported for this strain, which was more akin to a viscous liquid than a solid (Figure 2.2B, top). In contrast, the engineered strains could be manipulated and tested by our method (Figure 2.2B, bottom). The naming scheme in further text follows that developed by H. Liu: “E6” denotes six repeats of the ELP, while “CE6” presented an additional cysteine residue near the N-terminus (farthest from the cell

membrane) capable of forming additional disulfide bonds (Figure 2.3A). Different numbers denote the number of repeats: E.g. “CE9” and “CE12” have 9 and 12 repeats of the base ELP, with the additional cysteine residue (Figure 2.3B).

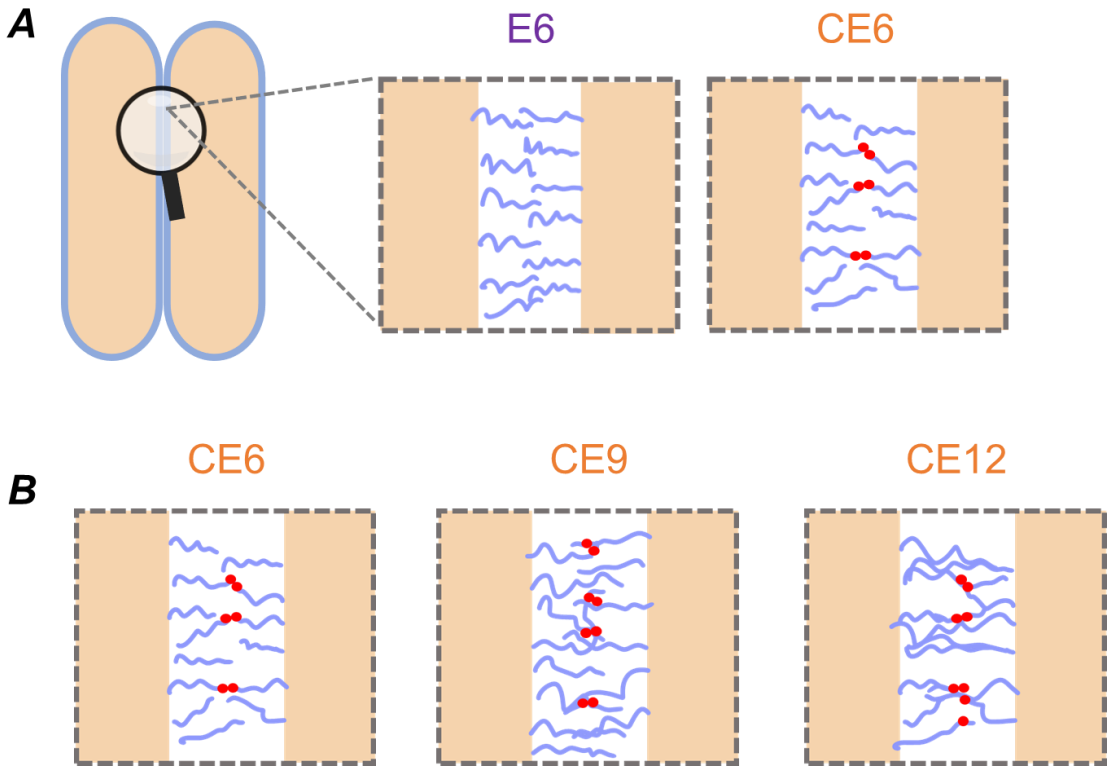


Figure. 2.3 A) Schematic of *E. coli K-12* DH10B (left, oblong, short axis ~500 nm) expressing associative protein (purple) tethered to the outer membrane, with cysteine residues denoted by red circles. ELP repeat sequence: $[-(VPGAG)_2\text{-}VPGEG\text{-}(VPGAG)_2\text{-}]_n$ not including linker residues. B) Linker length series CEn denotes films with varying number of ELP repeats.

### 2.3 Sample growth and loading protocol

Bacterial films were grown as follows: Individual colonies from Luria Bertani (LB) plates were grown to stationary phase in LB liquid medium supplemented with 100 mg/L ampicillin. The stationary phase culture was diluted to a fixed turbidity, optical density

$(OD)_{600}$ around 0.8. 200 µl of the diluted culture was suction coated onto a track etched polycarbonate filter (0.2 µm pore size, Whatman), pre-sterilized with a UV lamp in a biosafety cabinet for fifteen minutes, and the filters were placed onto LB agar plates and grown for 7 days at 37°C, changing the plate every 24 hours. The final bacterial films ranged in thickness from 60-90 µm as measured by optical coherence tomography assuming a refractive index of 1.4. In further text, "biological replicates" refers to biofilms grown from different parent colonies, while the phrase "technical replicates" refers to multiple biofilms grown from the same stationary phase culture (same parent colony).

The sample growth protocol was modified for measurements of heterogeneity. Modifications described in Chapter 4.

Prior to mechanical testing, the bacterial films had to be peeled from their polycarbonate substrates (Figure 2.2B, bottom right). To do this, a polycarbonate filter with bacterial film grown on top was placed into a petri dish containing sterile phosphate buffered saline (PBS, Corning, 1X). A 3 mm diameter biopsy punch (Integra Biosciences) was used to gently make a circular cut through the bacterial film but not the polycarbonate. The sample support disk (copper TEM disk, 1.5 mm diameter circular aperture, 3.05 mm outer diameter, thickness 25 µm, Ted Pella) was then slid in between the bacterial film and polycarbonate from the outer edge of the film and used to gently separate the film from the polycarbonate. Once the edge of the film was freed, the cut 3 mm bacterial film disk freely floated away from its polycarbonate support (Figure 2.2B), and it could be lifted out of the PBS using the support disk and placed into the bottom chamber of the device (pre-filled

with PBS). A second support disk was placed on top to sandwich the bacterial film, followed by an o-ring (Precision Associates, Inc).

Prior to sealing the two halves of the device together, a 5 ml syringe was filled with PBS and capped with a 30G needle connected to thin silicone tubing (0.31 mm ID, 0.64 mm OD, HelixMark). This strategy was devised to avoid air bubbles in the viewing window as the device was filled with PBS. The tubing was threaded through into the Luer socket on the top half of the device and placed along the top channel using forceps, such that the tube terminated in the viewing window of the chamber that would eventually be directly above the sample. Following this, the two chamber halves were sealed using a thin layer of vacuum grease. The two chambers were then filled simultaneously with PBS: the upper channel using the tubing connected to the PBS-filled syringe, and the lower channel by way of the associated Luer slip connector, drop by drop, until both connectors were filled, following which the tubing was gently extracted and two reservoirs were attached to the Luer slip connectors on either side. The reservoirs could be syringes of any known internal diameter (ID) with a Luer lock or Luer slip attachment.

Syringes used in the collected datasets were 60 ml syringes (BD Scientific) with ID = 26.72 mm. Where specified, certain samples were tested in HEPES buffer (20 mM HEPES, 115 mM NaCl, 1.2 mM $MgCl_2$, pH 7.0). The apparatus was rinsed with soap and DI water and allowed to dry between uses; separate reservoirs and syringes were used for different buffers.

## 2.4 Principle of operation

As indicated in Figure 2.2B and Figure 2.4, each face of the mounted bacterial film disk is in contact with a different reservoir whose applied hydrostatic pressure is controlled independently by varying the height of PBS in the reservoir. As a precaution against possible changes of the biofilm with time in PBS, experiments were completed within 30 minutes after mounting a specimen. For these experiments, the 60 ml syringes serve as reservoirs with cross-sectional area of 5.61 $cm^2$, such that adding 858 µl of PBS increases the reservoir level by 1.53 mm, which increases the hydrostatic pressure on the corresponding face of the sample by 15.0 Pa. (Figure 2.4)

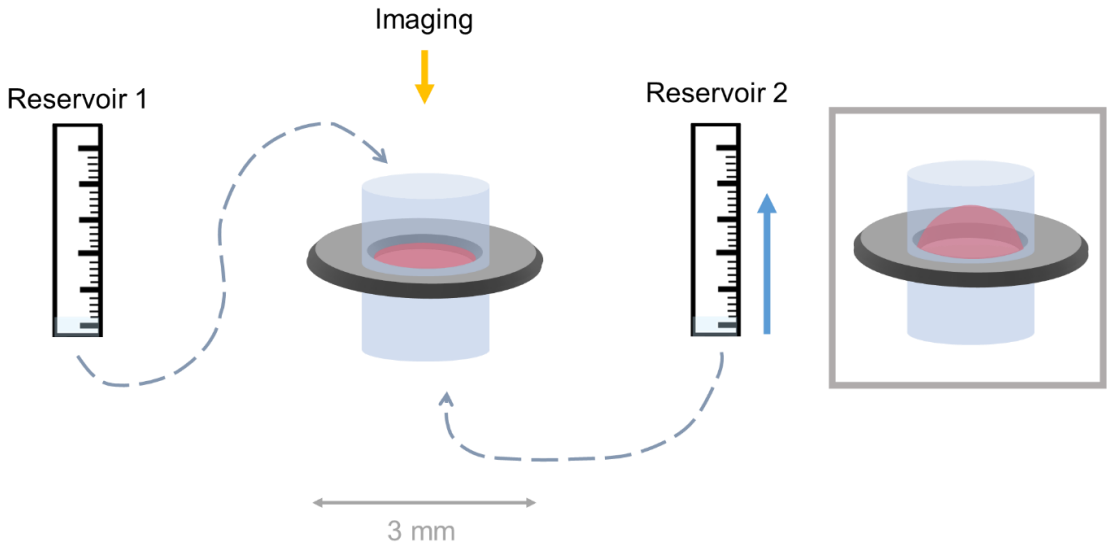


Figure 2.4. Schematic of bulge test process. As fluid height increases in the reservoir connected to the chamber underneath the film, the film "inflates" through central aperture (gray box).

A syringe pump was used to impose various pressure-time profiles. "Ramp" and "sawtooth" profiles involved PBS addition at a flow rate of 70 ml/min, with a final target

volume of 55 ml (ramp) and 2 ml (sawtooth) unless otherwise specified. The flow rate was chosen to be the maximum accommodated by the syringe pump in order to minimize perfusion through the biofilm for the duration of the experiment. Stepwise pressure profiles were also imposed by the syringe pump at the same flow rate. Total time between subsequent measurements was 6s for 3D stepwise experiments, confirmed using OCT image metadata.

Bacterial films are porous materials and some perfusion was visually observed as a rising fluid level in the second reservoir during some experiments. During 3D stepwise experiments, no perfusion was visually observed until pressure steps above 300 Pa. 1 ml was used as the threshold volume: the stepwise experiments were stopped once the 1 ml of total perfused volume was observed to collect in the second reservoir. Drop in pressure head due to perfusion was neglected in further calculations but is reported as a percentage of the final pressure head (< 5% of final pressure head for all biofilms studied). For ramp and sawtooth measurements, there was no observable perfusion.

### **2.**5 **Imaging**

All OCT imaging was performed with a Thorlabs OCT (GAN210 base unit: 930 nm central wavelength, 6/4.5 μm axial resolution in air/water, 2.9/2.2 mm imaging depth (air/water), OCTP-900 scan head, OCT-LK3-BB scan lens: 36 mm FL, 8 μm lateral resolution). A-Scan/Line Rate was 36 kHz for all measurements (acquisition time = 19 ms for 2D/ramp and 3.022 s for 3D/stepwise images). Biofilm thicknesses were calculated estimating a refractive index of 1.4. This value was based on both the manufacturer's recommendation as well as prior literature on *E. coli.*[16–18]

Both 2D cross sectional images and volumetric images (Figure 2.5) were used to extract information about biofilm properties. Chapter 3 describes data extraction from 2D images, while Chapter 4 covers volumetric images.

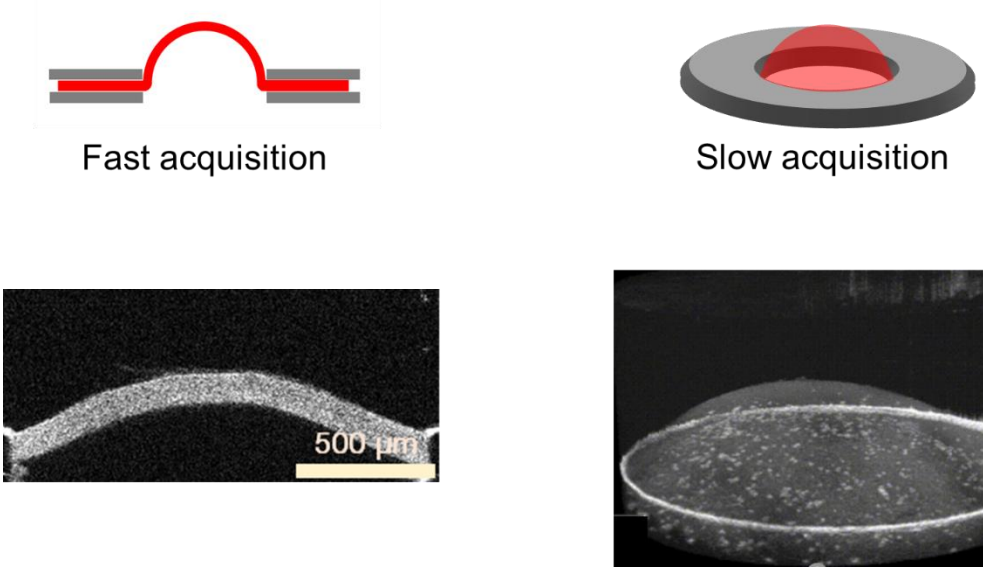


Figure 2.5. The deformed biofilm could be imaged either as a 2D cross section (left – top, schematic, bottom, OCT image) or as a volumetric image (right – top, schematic, bottom, OCT image). Images shown: CE6, 7 days growth, stepwise loading, $\Delta P = 450$ Pa.

## References


1. Tsakalakos, T. & Hilliard, J. E. Elastic modulus in composition-modulated copper-nickel foils. *J. Appl. Phys.* **54**, 734–737 (1983).

2. Hsu, F. P. K., Liu, A. M. C., Downs, J., Rigamonti, D. & Humphrey, J. D. A Triplane Video-Based Experimental System for Studying Axisymmetrically Inflated Biomembranes. *IEEE Trans. Biomed. Eng.* **42**, 442–450 (1995).

3. Mohan, D. & Melvin, J. W. Failure properties of passive human aortic tissue. II-Biaxial tension tests. *J. Biomech.* **16**, (1983).

4. Cavinato, C. *et al.* Biaxial loading of arterial tissues with 3D in situ observations of adventitia fibrous microstructure: A method coupling multi-photon confocal microscopy and bulge inflation test. *J. Mech. Behav. Biomed. Mater.* **74**, 488–498 (2017).

5. Midgett, D. E., Quigley, H. A. & Nguyen, T. D. In vivo characterization of the deformation of the human optic nerve head using optical coherence tomography and digital volume correlation. *Acta Biomater.* **96**, 385–399 (2019).

6. Tonge, T. K., Atlan, L. S., Voo, L. M. & Nguyen, T. D. Full-field bulge test for planar anisotropic tissues: Part I-Experimental methods applied to human skin tissue. *Acta Biomater.* **9**, 5913–5925 (2013).

7. Wang, L., Tian, L., Huang, Y., Huang, Y. & Zheng, Y. Assessment of Corneal Biomechanical Properties with Inflation Test Using Optical Coherence Tomography. *Ann. Biomed. Eng.* **46**, 247–256 (2018).

8. Zamprogno, P. *et al.* Mechanical properties of soft biological membranes for organ-on-a-chip assessed by bulge test and AFM. *ACS Biomater. Sci. Eng.* **7**, 2990–2997 (2021).

9. O'Connell, P. A. & McKenna, G. B. Novel nanobubble inflation method for determining the viscoelastic properties of ultrathin polymer films. *Rev. Sci. Instrum.* **78**, 14706 (2007).

10. Turner, J. A., Menary, G. H. & Martin, P. J. Biaxial characterization of poly(ether-ether-ketone) for thermoforming: A comparison between bulge and in-plane biaxial testing. *Polym. Eng. Sci.* **59**, 1853–1865 (2019).

11. Marra, S. P., Kennedy, F. E., Kinkaid, J. N. & Fillinger, M. F. Elastic and rupture properties of porcine aortic tissue measured using inflation testing. *Cardiovasc. Eng.* **6**, 123–131 (2006).

12. Tabata, O., Kawahata, K., Sugiyama, S. & Igarashi, I. Mechanical property measurements of thin films using load-deflection of composite rectangular membranes. *Sensors and Actuators* **20**, 135–141 (1989).

13. Martinez, A. W., Phillips, S. T. & Whitesides, G. M. Three-dimensional

microfluidic devices fabricated in layered paper and tape. *Proc. Natl. Acad. Sci. U. S. A.* **105**, 19606–19611 (2008).

14. Liu, H. Engineered living material based on protein mediated bacterial assembly. (2022).

15. Kozlowski, M. T., Silverman, B. R., Johnstone, C. P. & Tirrell, D. A. Genetically Programmable Microbial Assembly. *ACS Synth. Biol.* **10**, 1351–1359 (2021).

16. Hart, S. J., Terray, A. V, Kuhn, K. L., Arnold, J. & Leski, T. A. Optical chromatography for biological separations. in *Optical Trapping and Optical Micromanipulation* vol. 5514 35 (SPIE, 2004).

17. Liu, P. Y. *et al.* Real-time Measurement of Single Bacterium's Refractive Index Using Optofluidic Immersion Refractometry. *Procedia Eng.* **87**, 356–359 (2014).

18. Balaev, A. E., Dvoretski, K. N. & Doubrovski, V. A. Refractive index of Escherichia coli cells. in *Saratov Fall Meeting 2001: Optical Technologies in Biophysics and Medicine III* vol. 4707 253–260 (SPIE, 2002).

*C h a p t e r  3*

# Probing dynamics, elasticity, and healing of engineered biofilms with a 2D view

*Experiments in this chapter were performed in collaboration with Hanwei Liu (H.L.). H.L. grew and provided engineered biofilms for testing. Priya Chittur (P.K.C.) designed and performed the mechanical studies, developed analysis methods, and analyzed data.*

## 3.1 Introduction

Once we had established the testing device and a method to handle, deform, and image living materials, the next question became: what material properties could we obtain, and at what level of approximation?

Here, our journey bifurcates: in Chapter 3, we focus on a primitive but still powerful and readily accessible method that can estimate bulk properties using fast, 2D cross sectional images. In Chapter 4, we extract information about spatial heterogeneity.

We begin here with a description of the 2D method, followed by its practical use in understanding the effects of engineering on living material properties.

## 3.2 Experimental methods

Following the sample loading protocol described in Chapter 2, we proceeded to impose a series of hydrostatic pressures across the biofilm, image the film simultaneously, and use the images to estimate bulk stress and strain in the material.

Pressure profiles could be imposed as any of the following shown in Figure 3.1, using the protocol described in Chapter 2.

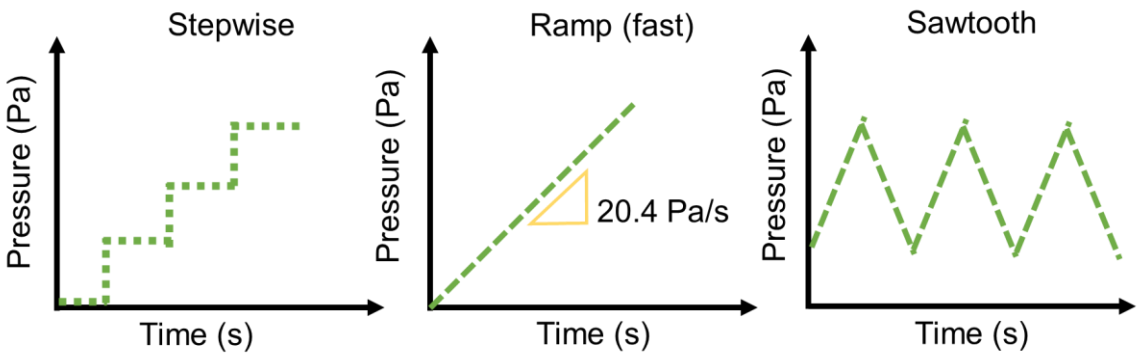


Figure 3.1. Schematic of pressure profiles imposed during bulge test. Stepwise used for 3D measurements (Chapter 4); ramp profile used at varying rates for 2D measurements (Chapter 3), sawtooth profile used to estimate viscoelasticity and fatigue.

The typical loading and imaging process generated over 2500 images showing the evolution of a biofilm cross section throughout the experiment (some snapshots, Figure 3.2, numbered images). The features that could be captured were limited only by i) perfusion, which in most cases was negligible, ii) maximum fluid held by the reservoir, which was 70 ml, and iii) the thickness of the samples tested. Thicker samples would experience less stress at a given hydrostatic pressure, which meant the failure of a particular sample could not always be captured. A typical analysis protocol resulted in the stress-strain curve shown in Figure 3.2 (bottom).

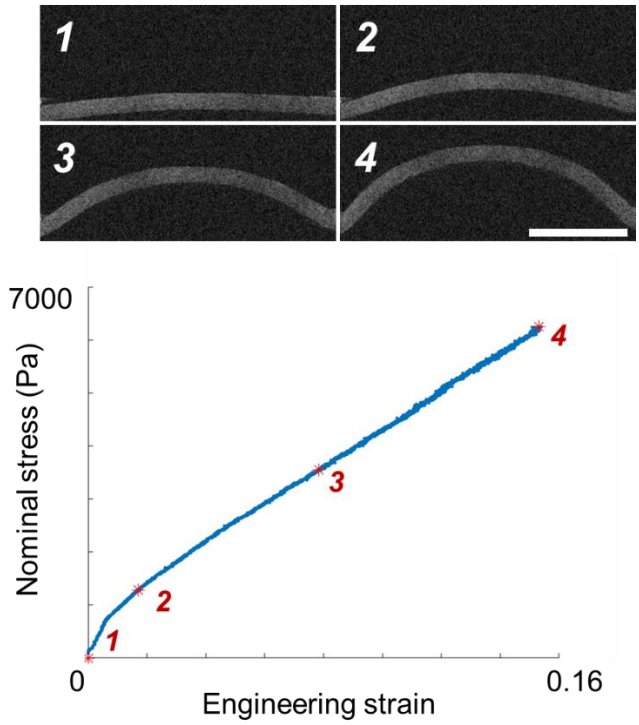


Figure 3.2. Cross sectional OCT images (top, numbered) acquired during the bulge test of a CE6 biofilm with subsequent 2D processing and stress-strain curve displayed below. Numbers with asterisks indicate data points corresponding to the images. Scale bar 500 μm. Biofilm did not fail during experiment. Films grown for 7 days; ramp loading protocol; $\Delta P \sim 0, 74, 488, 1009$ Pa for (1-4) respectively.

### *3.2.1 Analysis protocol*

The analysis protocol followed different assumptions for 2D (Chapter 3) vs. 3D (Chapter 4) analysis. We begin with a broad overview here before discussing the specifics of each type of analysis in the relevant chapters. First, common to both are the assumptions involved in membrane theory, that i) the thickness of the membrane is small in comparison to the in-plane dimensions (that it can be treated as a surface), ii) the bending stiffness is negligible (an ideal membrane would not experience bending moments or out-of-plane shear, and only accommodate all loads via in-plane stresses), and iii) due to (i) and (ii), in-

plane stresses are assumed to be constant throughout the thickness of the membrane. A few additional assumptions are present in Chapter 3: i) that there is an idealized equibiaxial deformation throughout the entire inflated membrane. In practice this is true only at the pole, and the deformation transitions to a constant width elongation at the clamped edge; also ii) that stress could be estimated using a spherical cap assumption, and strain could be estimated by changes in arc length of the deformed biofilm (Figure 3.3A).

Following the assumptions outlined above, the stress and strain states are as follows:

$$\sigma_{ij} = \begin{pmatrix} \sigma_1 & 0 & 0 \\ 0 & \sigma_2 & 0 \\ 0 & 0 & 0 \end{pmatrix}$$

$$\epsilon_{ij} = \begin{pmatrix} \epsilon_1 & 0 & 0 \\ 0 & \epsilon_2 & 0 \\ 0 & 0 & \epsilon_3 \end{pmatrix}$$

We assume here that $\sigma_1 = \sigma_2 = \sigma$ and $\epsilon_1 = \epsilon_2 = \epsilon$ across the entire membrane.

Applying Hooke's law, the relationship between $\sigma$ and $\epsilon$ is:

$$\sigma = \frac{E}{1-\nu}\epsilon$$

where $\frac{E}{1-\nu}$ is the biaxial modulus of the material, referred to as the "modulus" in further text, and evaluated from initial linear regions of each plot. We do not report the two quantities $E$ and $\nu$ independently since they cannot be deconvolved using only one measurement method. Additional measurements with the plane strain configuration of the bulge test (e.g. a rectangular aperture with aspect ratio > 4:1) would enable the calculation of each quantity independently; however, extending our measurements to the

plane strain configuration was challenging due to the dimensions of the biofilm that were required to be considered a membrane relative to the smaller dimension of the rectangular aperture in a TEM grid (~ 100 μm). We assume comparable Poisson's ratio across all samples.

In Chapter 4, we continue with membrane theory, but avoid the assumption that $\sigma_1 = \sigma_2$ and $\epsilon_1 = \epsilon_2$ across the membrane. Using microsphere markers in the film, we directly calculate and fit local displacement fields to obtain deformation gradient (and other derived quantities, e.g. Green-Lagrange strains). Similarly, using known force balance relations for the inflated membrane, we use the same tracers to estimate local curvature and stress resultants. A stress resultant is an in-plane force per unit in-plane length and is a two-dimensional quantity by definition, also referred to as a "membrane tension" or "membrane stress".

The (in-plane physical) components of the stress resultant tensor $\overline{\overline{\mathbf{T}}}$ are given by

$$T_{12} = \int_{-h/2}^{h/2} \sigma_{12}\, dx_3$$

where $h$ is the thickness of the deformed membrane and $\overline{\overline{\boldsymbol{\sigma}}}$ is the usual Cauchy stress tensor described above (force per oriented area in a deformed configuration). Further details and derivations can be found in the following.[1–4]

With these broad assumptions laid out, we now move to a detailed discussion of the 2D analysis method.

2D datasets were exported as tiff files and cropped using ImageJ. The resulting images were processed with in-house MATLAB scripts: the images were binarized; the top and bottom surfaces of the film were detected based on changes in pixel intensity and fit to fourth degree polynomials which were then used to estimate arc lengths of the top and bottom surfaces of the film (Figure 3.3B). Engineering strain $\epsilon$ was calculated as change in arc length divided by the original arc lengths of the top and bottom surfaces respectively.

Nominal stress was calculated with the equation for stress in a thin-walled spherical pressure vessel:

$$\sigma = \frac{PR}{2t}$$

where $\sigma$ is film stress, $P$ is the applied pressure, $R$ is bulge radius of curvature, and $t$ is film thickness. Further, $R = \sqrt{a^2 + h^2}$ where $a$ is radius of aperture of the support disk and $h$ is deflected height of the center of the film, directly measurable by OCT. For 2D datasets, the plotted data were averaged (top and bottom surfaces of the biofilm). True stress and strain were used for some films that yielded/were tested to failure, where indicated.

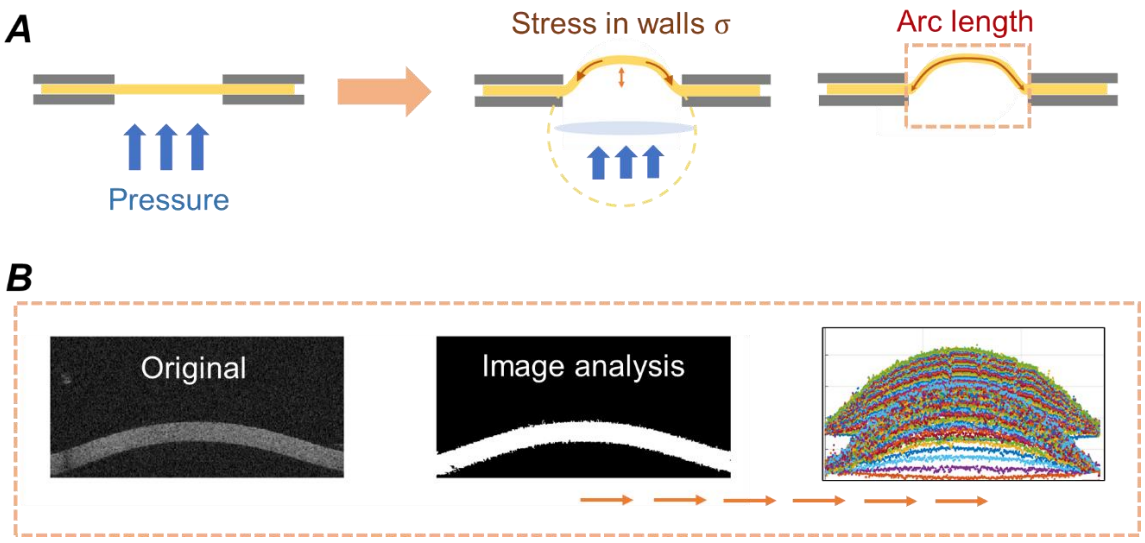


Figure 3.3. A) Spherical cap approximation for stress assumes that deformed biofilm is part of a larger spherical pressure vessel and the stress in the walls of the film balances the applied pressure. Strain is estimated as a difference in the arc length (red arrow) compared to the original (flat) length of the biofilm. B) Image processing scripts binarize and clean up OCT images and detect the top and bottom surfaces of the film over thousands of images (bottom right). Images shown: CE6 biofilm, 7 days growth, ramp loading protocol.

Based on the localized bending of the biofilm observed at the rim (Figure 3.4), we determined that flexural stiffness could be neglected and the membrane assumptions outlined above were valid. The spherical cap fit also assumed that the bulge radii of curvature were equal along the meridional and circumferential axes. Deviation between the polynomial fit and the ideal spherical cap was calculated as the minimum distance between the two curves at evenly spaced points along the length of the cap (Figure 3.4E) and reported as a percentage of the radius of the sphere. Typical deviation was <1% for the entirety of the experiment. The spherical cap model for stress estimation was determined to be suitable for our method based on the low deviation from the idealized shape and between the two models.

The ratio of aperture diameter $2a$ to film thickness $t$ ranged from 16.6 – 25. Although the ideal ratio for the membrane assumption would be > 20, variations of stresses and strains through the thickness were neglected in our calculations based on the fact that the top and bottom surfaces of the biofilm did not show a significant difference in their stress-strain data (Figure 3.5).

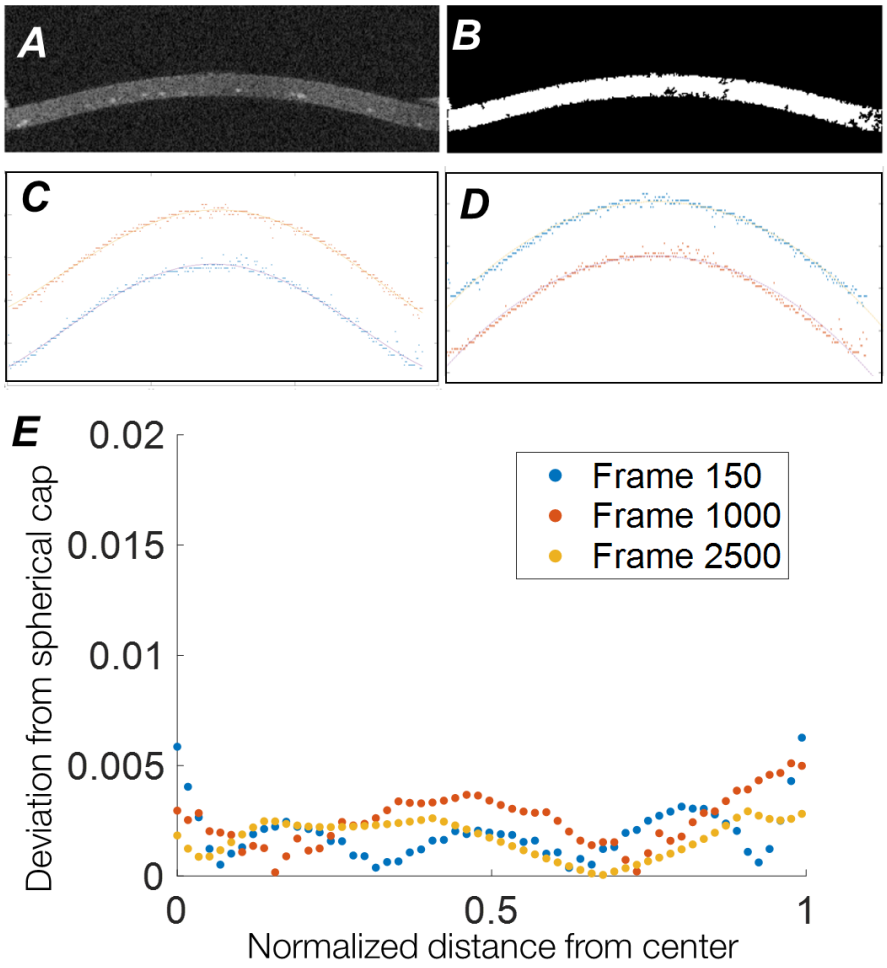


Figure 3.4. CE6 bulge test example. Frame 150 (A) as a binary image (B) after removing large noise (e.g. the TEM grid on the right edge). Fourth order polynomial fit to the top and bottom surfaces (C) indicated by smooth lines. D) Hemispherical fit to the same data points showing E) minimal deviation.

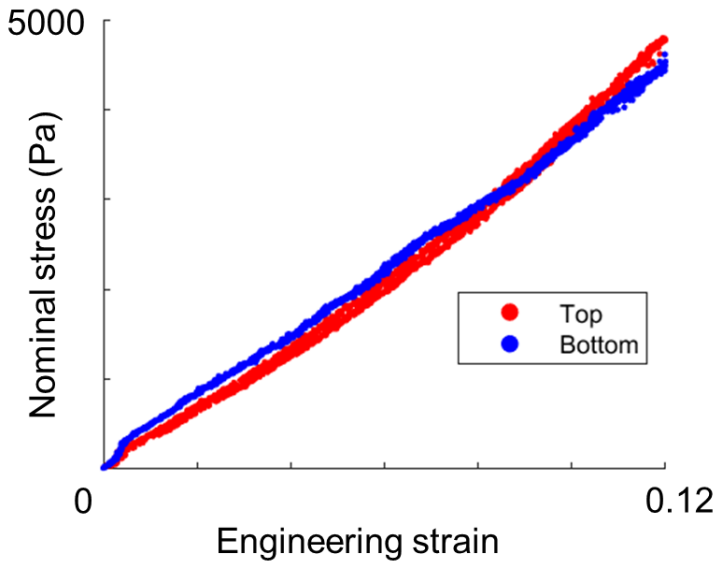


Figure 3.5. Minimal discrepancy between stress-strain curves from the top vs. bottom surfaces of the biofilm. Data shown from CE6 biofilm; 7 days growth; ramp loading.

## 3.3 Using 2D analysis to gain insight into the effects of engineering on biofilm bulk properties

### *3.3.1 E6 vs. CE6*

Now that the apparatus (Chapter 2) and a bulk analysis method (Chapter 3.1-2) were established, we could now ask the question: to what extent could we use it to characterize a model living material?

We initially compared E6 and CE6, a pair of biofilms (Liu and Tirrell[5]) grown from cells engineered to express similar polypeptides on their surface, but where CE6 could form additional disulfide bonds.

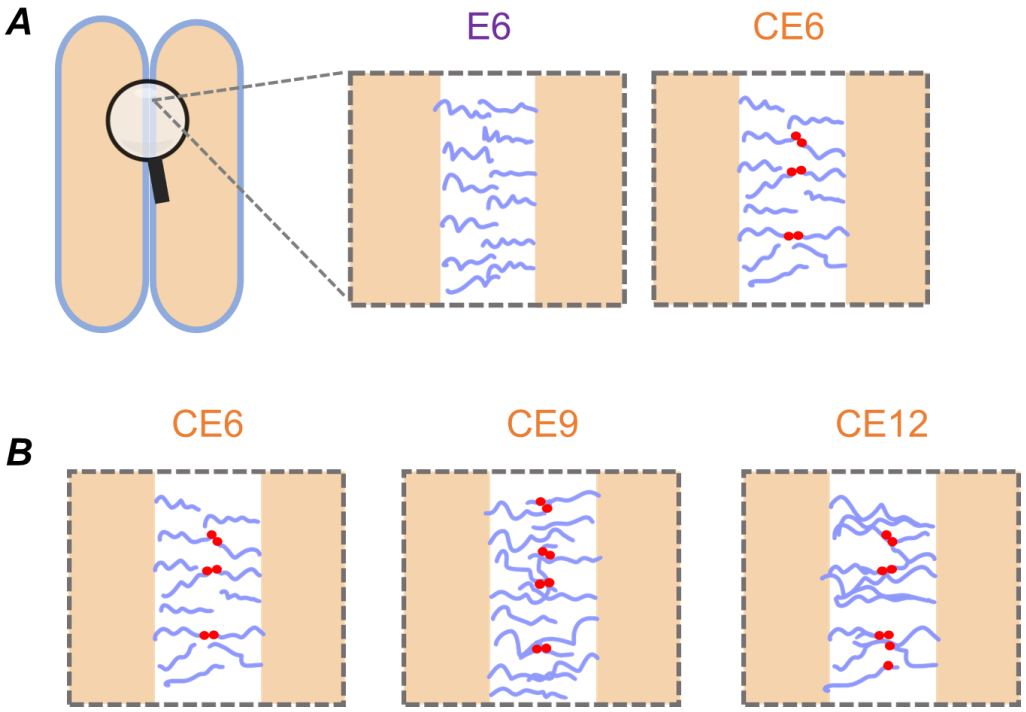


Figure. 3.6. Reproduced from Chapter 2. A) Schematic of *E. coli K-12* DH10B (left, oblong, short axis ~500 nm) expressing associative protein (purple) tethered to the outer membrane, with cysteine residues denoted by red circles. ELP repeat sequence: [-$(VPGAG)_2$-VPGEG-$(VPGAG)_2$-]$_n$ not including linker residues. B) Linker length series CEn denotes films with varying number of ELP repeats.

*CE6 is stiffer than E6*

2D analysis revealed that the addition of the cysteine residue resulted in biofilms that were nearly three times stiffer (Figure 3.7) and rarely failed during our test. E6 was also ductile, showing yielding prior to failure.

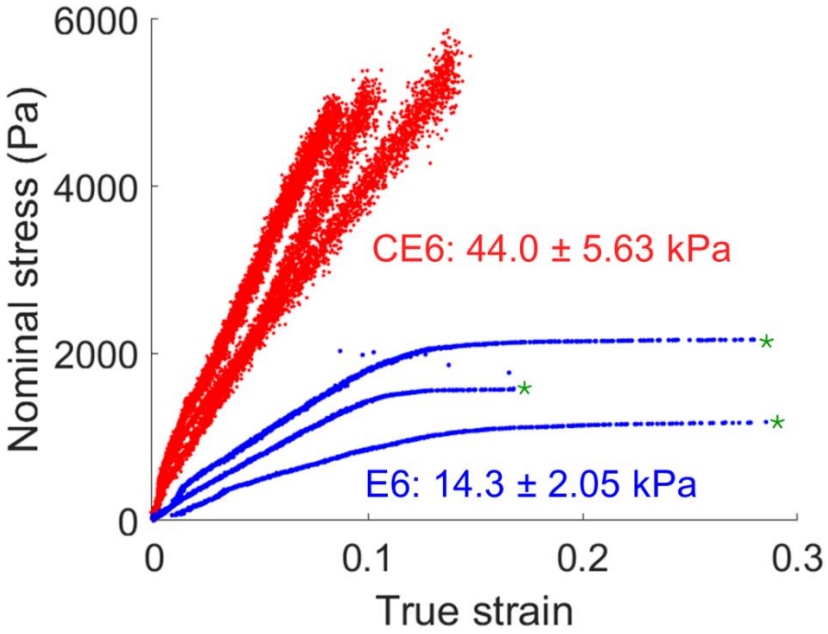


Figure 3.7. CE6 (red) is three times stiffer than E6 (blue). Three biological replicates tested; select data shown. CE6 data point size two points smaller than E6 for clarity. Modulus based on fit to the initial linear region of each curve. Green asterisks indicate failure. CE6 did not fail during the tests above. N = 18; six biological replicates tested for E6. N = 6; four biological replicates tested for E6. 7 days growth for all samples; ramp protocol.

*E6 is ductile, while CE6 is brittle*

Although CE6 was generally not prone to failure, both biovariability (for more information on biovariability, see section 3.6: *Additional information and supplementary information*) and deliberate weakening of the biofilm (e.g. via immersion in PBS for 3-4 hours) resulted in samples that failed within the pressure ranges of our test. In these scenarios, we discovered that our method could also be used to compare the modes of failure of different types of films.

While E6 had an obvious yield point and was ductile, often extending past the viewing window of the OCT, CE6 was brittle and failed with “clean edges” (Figure 3.8).

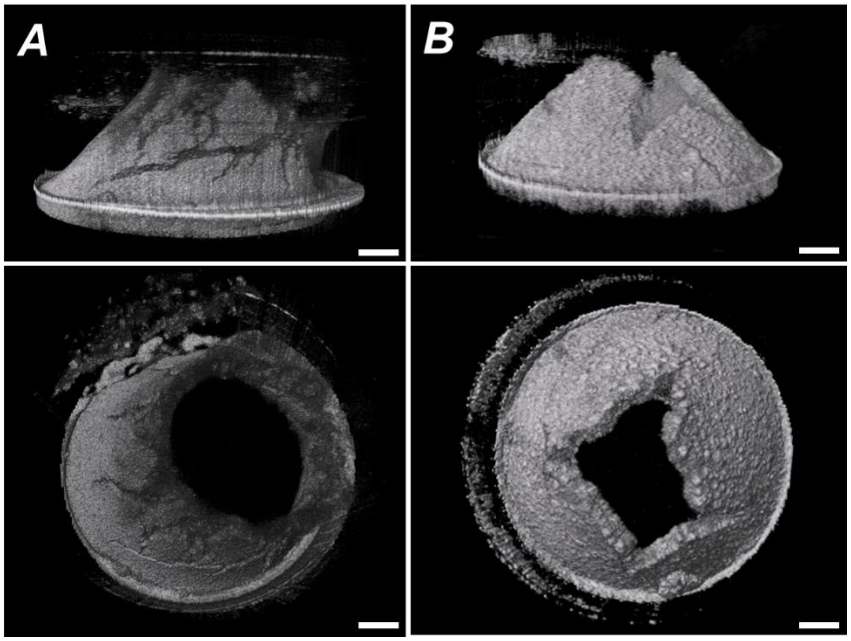


Figure 3.8 A) E6 elongates significantly, often past the viewing window of the OCT, prior to failure and "bursts", while CE6 (B) is brittle and fails with visible cracks and clean edges. Scale 200 μm. OCT images processed with Imaris to remove excess noise from edges of TEM grid; contrast enhanced using *Normal Shading* feature. Films grown for 7 days; stepwise loading protocol; ΔP = 380 Pa for E6 (A) and 720 Pa for CE6 (B).

A key advantage of our method is being able to visualize this process of failure, from the intact film to the propagating cracks, to the ultimate failed morphology.

Furthermore, we could directly correlate regions of the stress-strain curves to observable changes in the biofilms. Although CE6 failure occurred rapidly, due to the relatively fast acquisition times of our method, we were able to capture key features in the process (Figure 3.9). The shape initially transitioned to a more oblong, less spherical cap (77 frames, 1.4 seconds, orange rectangle in Figure 3.9A, B), followed by rapid failure within 133 ms (7 frames, 133 ms, green rectangles in Figure 3.9 A, B).

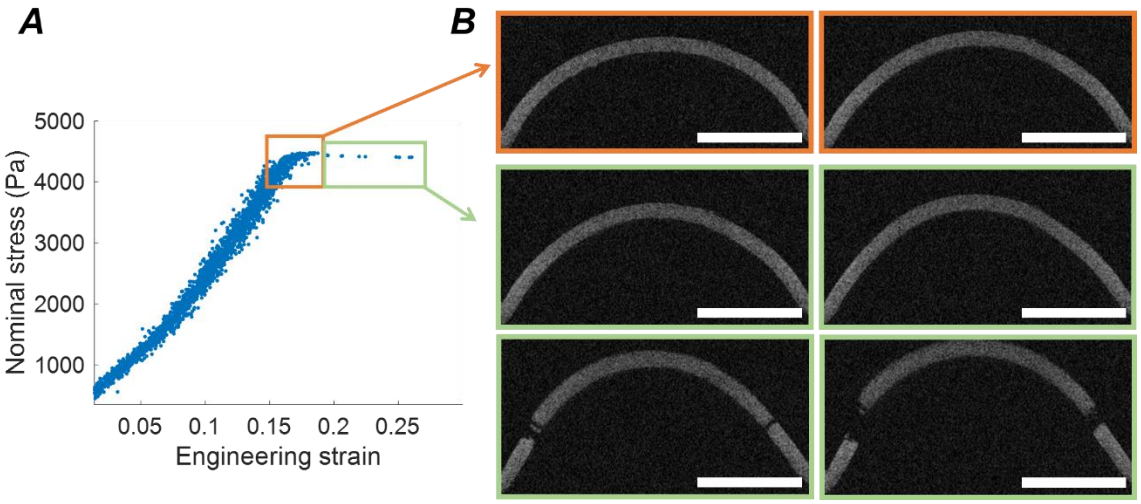


Figure 3.9. Regions of stress-strain curve correspond to physical features observable in the biofilm: short region of decreasing slope (A, orange) corresponds to shape transition from spherical cap to oblong (B, top), followed by failure within seven frames (A and B, bottom four images; last two images show continued acquisition). Scale 500 µm.

*CE6 initial response is elastic and transitions to viscoelastic behavior over multiple loading cycles*

Next, we investigated elasticity and changes in properties over multiple loading cycles. Since loading profiles were only limited by the syringe pump, we were able to apply a "sawtooth" loading pattern (Figure 3.1) and observe biofilm response simultaneously using OCT, processing the data in a similar manner.

Elasticity is the ability of a material to return to its original size and shape upon removal of applied loads.

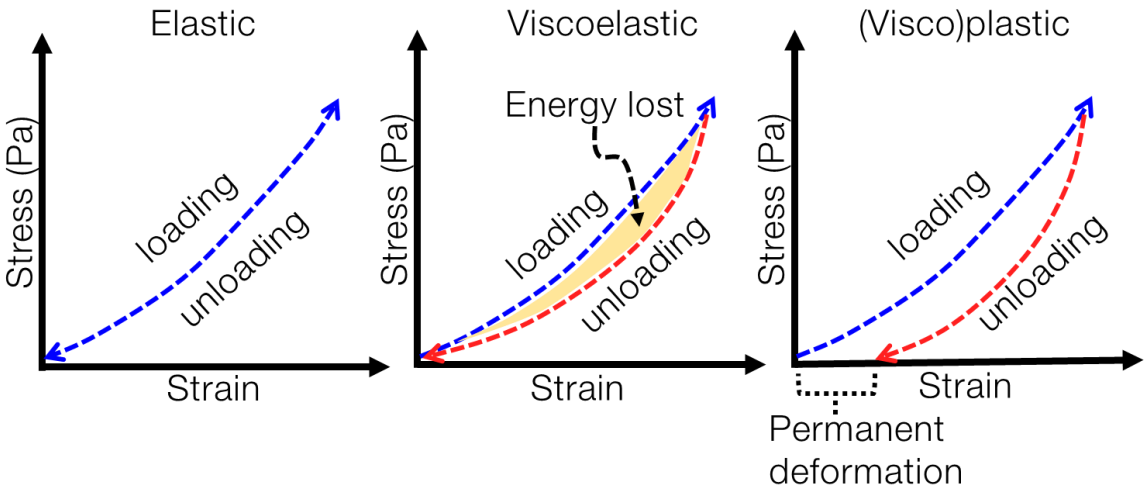


Figure 3.10. Elastic materials recover their original shape once the applied load is removed, and the loading and unloading responses are superimposable (left). In contrast, the responses are not superimposable in viscoelastic materials (center), with energy lost indicated by the area between the curves. Permanent deformation (right) is indicated by an increasing x-intercept.

A perfectly elastic material would return to its original size and shape, with either a linear or nonlinear stress-strain response (Figure 3.10, left) that is independent of loading rate with superimposable stress-strain curves during loading and unloading. In a cyclic loading experiment, there is no phase lag between the applied stress and measured response (Figure 3.11, left).

A viscoelastic material, on the other hand, has the characteristics of both a solid and a fluid: properties are dependent on loading rate, with steeper response curves at faster loading rates. For a particular loading rate, the stress-strain response does not follow the same path for loading and unloading (Figure 3.10, center), and the area between the curves signifies energy dissipated during the process. Within a certain region, viscoelastic materials can completely regain their properties, while in (visco)plastic deformation, there is permanent

deformation indicated by an increasing x-intercept (Figure 3.10, right). In a cyclic loading experiment, a perfectly viscous material would have a phase lag of 90°, while a viscoelastic material would have a phase lag between 0 and 90° (Figure 3.11).

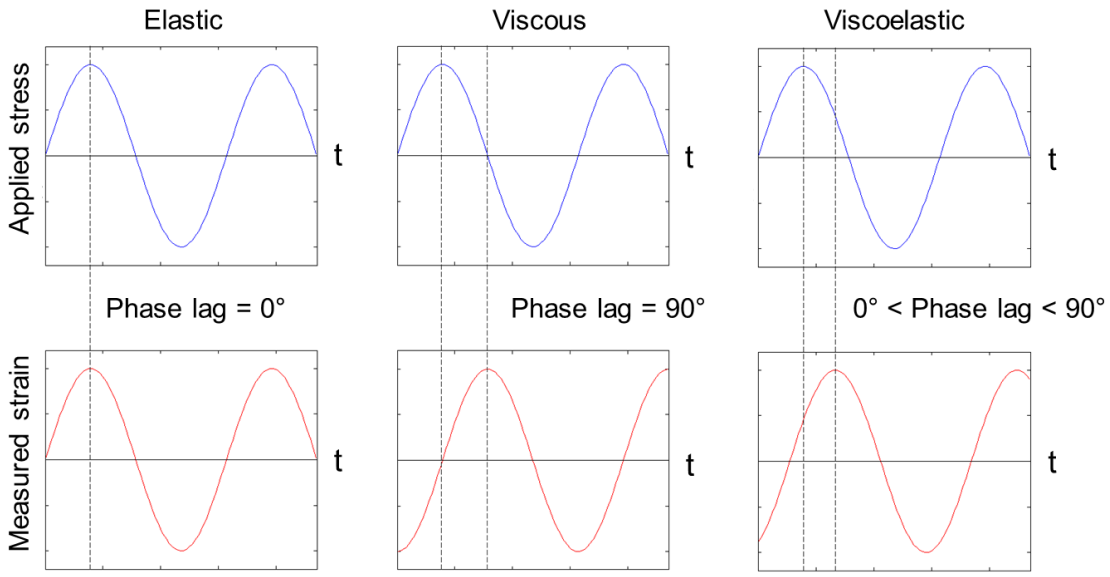


Figure 3.11. An elastic response involves no phase lag between an applied stress and the response (left); a perfectly viscous response would have a phase lag of 90° (center), and a viscoelastic material would have a phase lag in between the two (right). Image adapted from [6]

The bulge test was performed with a protocol similar to that of the "ramp" method, instead using a sawtooth profile (Figure 3.1, 3.12). The loading rate (slope) was 70 ml/min (maximum allowable by the syringe pump), to a maximum volume of 2 ml. The acquisition time was consistent at 19 ms. OCT images were processed with MATLAB with the same protocol described earlier. Inflection points were automatically detected in pressure vs. time (piecewise) plots and strain vs. time plots by identifying points with maximum change in mean and slope relative to surrounding data points, and then used to separate data points

and plot information for each loading cycle. Representative results are shown below (N = 8, three biological replicates tested).

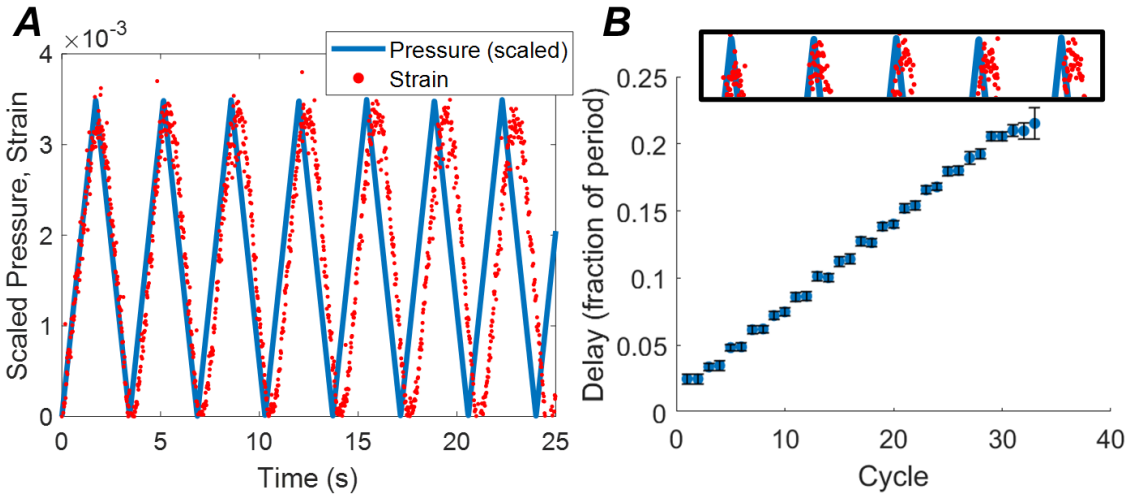


Figure 3.12. CE6 initially shows minimal lag between the applied load and response of the biofilm, increasing with number of cycles (A, pressure plotted as piecewise function in blue solid line scaled by $10^{-4}$ for ease of comparison; engineering strain as computed from OCT images as red data points; subset of cycles shown; additional inset in (B) magnified to highlight the increasing delay). Lag is consistent between biological replicates and increases almost linearly (B, 35 cycles shown; standard error). See text for details. 7 days growth for biofilm; sawtooth loading protocol.

CE6 showed minimal to no lag in the first loading cycle (Figure 3.12), with a correspondingly (nonlinear) elastic stress-strain trace (Figure 3.13, top left). The lag continued to increase over time with additional loading cycles, displaying viscoelastic behavior (Figures 3.12, 3.13).

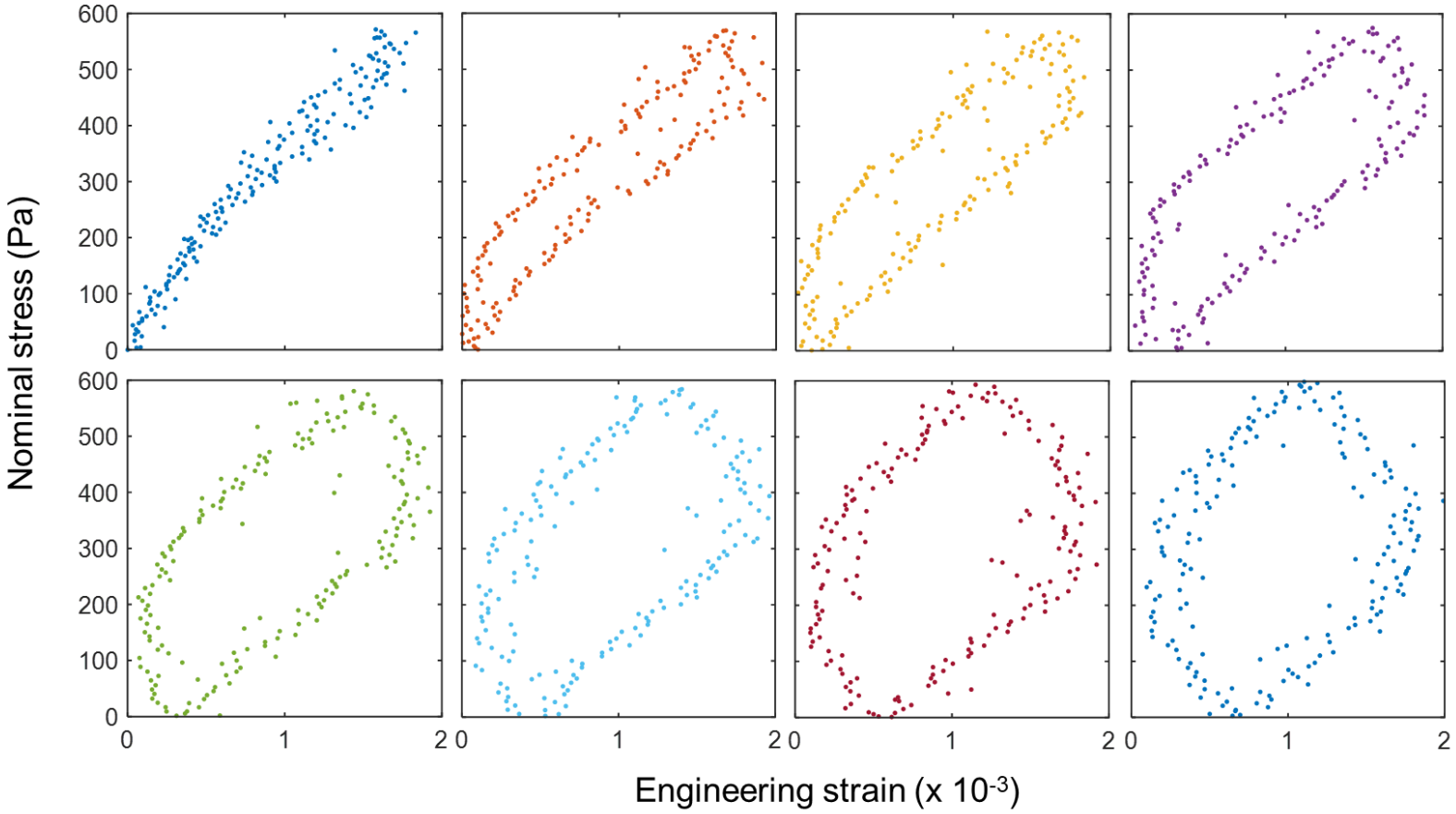


Figure 3.13. First eight loading cycles for CE6, ordered top left to bottom right. CE6 displays an initially elastic response (top left), transitioning to a more viscoelastic response indicated by the increasing area between the loading and unloading curves. Engineering strain axes are scaled by $10^3$ for clarity.

This elastic behavior also suggested that we could compare our 2D results to those from 3D analysis (Chapter 4) for a portion of the response, despite the differences in loading rate between the two methods.

E6 biofilms in contrast were challenging to test due to their variability; however representative results are included below. Phase lag was significant from the first cycle (Figure 3.14) with identical loading conditions (resulting in roughly half the stress used for CE6, and a strain response that was ten times that of CE6). The film exhibited viscoplastic deformation from the first cycle (Figure 3.15). Ideally, loading conditions could have been adjusted to find an elastic regime; however repeated experiments were limited due to film variability. This experiment does however, in general, highlight certain disadvantages of our method- the applied stress depends on both the pressure and the response of the biofilm (deflection *h*), making it difficult to predict *a priori* what the stress will be even with the pressure held constant. The need for image exporting and processing prior to visualizing the data also slows down the overall process since it is a prerequisite to being able to adjust experimental conditions as needed.

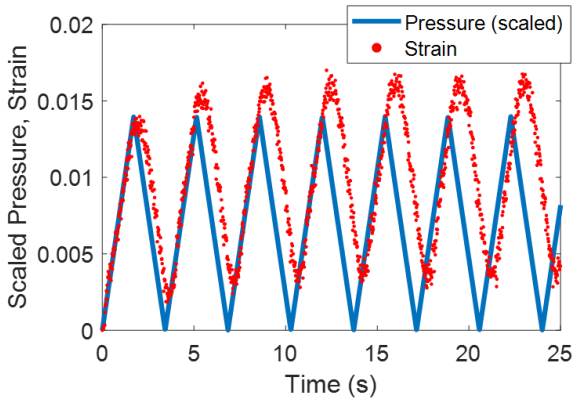


Figure 3.14. E6 at similar conditions was not within the elastic regime and underwent permanent deformation. 7 days sample growth; sawtooth loading protocol.

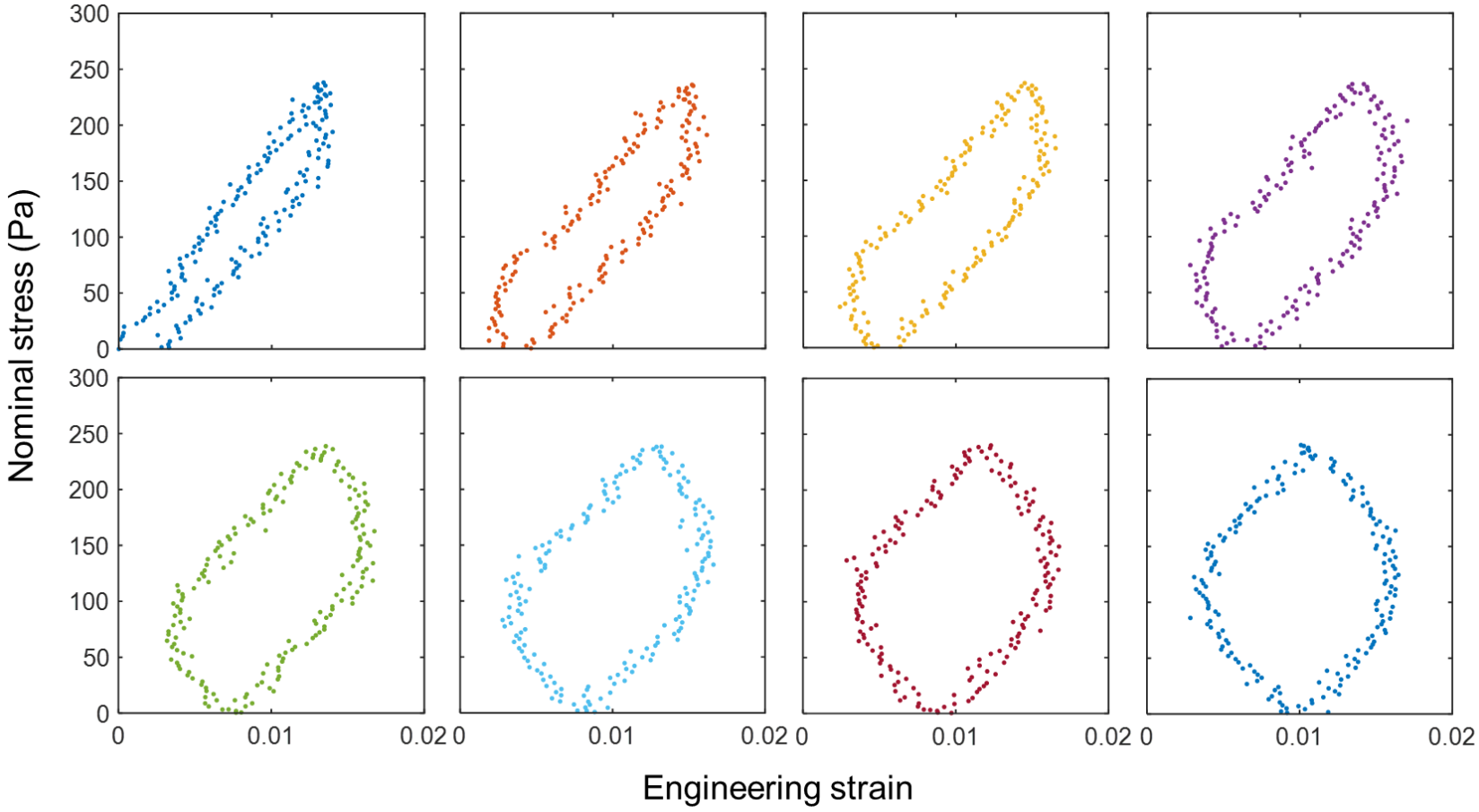


Figure 3.15. E6 displays a viscoplastic response at pressures comparable to those used for CE6. The permanent deformation is mostly in the first two cycles; after which the response is viscoelastic.

*3.3.2 Effect of linker length: CEn series*

So far, the discussion has focused on the use of the 2D method to quantify bulk biofilm properties, ranging from the modulus to visualizing failure, to probing the dynamics and viscoelasticity of a film, using a pair of model biofilms as examples.

Here, we explore a different set of model biofilms to highlight another potential advantage of our method. This study was motivated by a result from a set of biofilms: the "*CEn* series" (Figure 3.6, see Chapter 2 for details). Bulge tests on the *CEn* series did not reveal any clear trend in properties with varying linker length (Figure 3.16), especially not one that was consistent over time (see section 3.6 for further information). For the samples tested in 2022, the elastic moduli from the initial linear regime of each plot were: CE3 (51.9 ± 5.49 kPa), CE6 (59.7 ± 7.68 kPa), CE9 (41.0 ± 5.36 kPa), CE12 (33.1 ± 3.80 kPa). The CE6 value in particular was observed to be significantly different from the value measured (44.0 ± 5.63 kPa, denoted "CE6*" in the text) during the experiments with E6 or from those measured during subsequent healing experiments (see section 3.4), without which there may have been a trend towards decreasing modulus with increasing linker length. Additionally however, experiments in 2019 and 2020 had yielded properties that were nearly identical across samples with varying linker length (section 3.6).

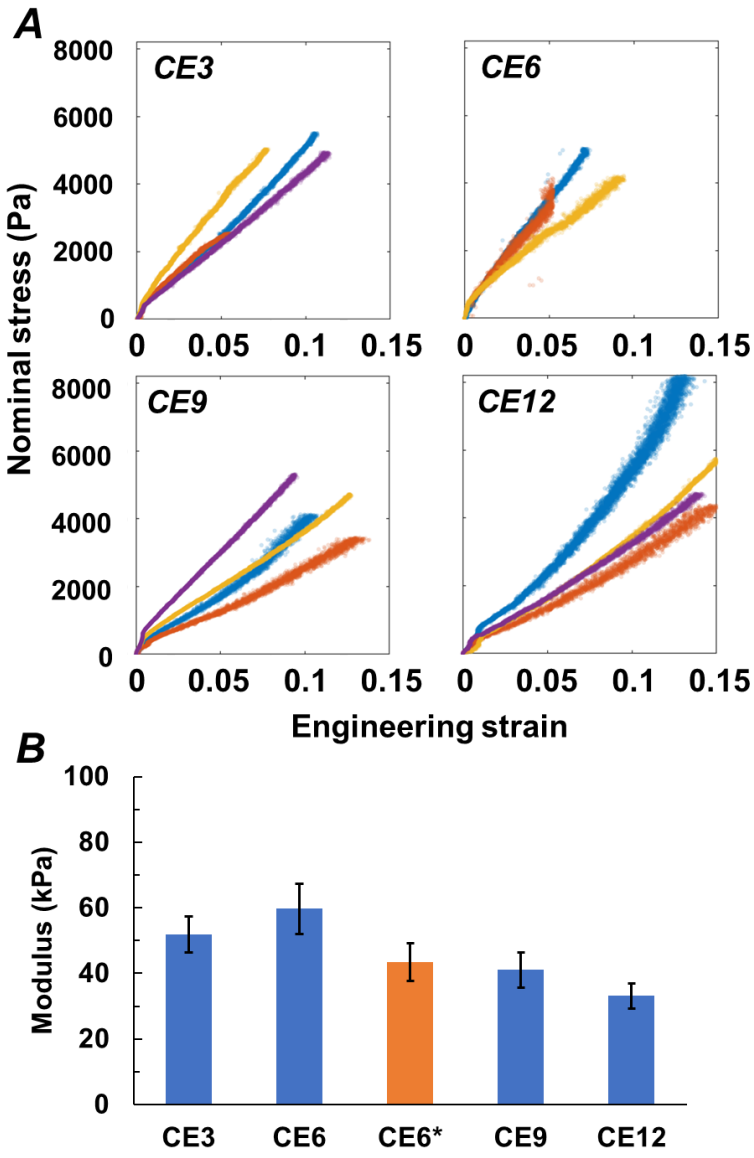


Figure 3.16. CEn series does not show a clear trend in mechanical properties with increasing linker length (see section 3.6 for more information). N = 4, 3, 5, 4 for CE3, 6, 9, and 12 respectively. Two biological replicates were tested for each sample. CE9 and CE12 were grown and tested on the same day, while CE3 and CE6 were tested separately due to CE3 variability. Initial batch of CE3 (grown with CE6) could not be tested; properties are reported for a second set of samples. CE6 properties in blue reported for samples grown within one week of the other CEn samples tested; observed modulus was higher for these samples than those tested in the E6 vs. CE6 study (the latter indicated by CE6*). Failure was not observed within the pressure regimes tested except for a single punch of CE3 (red trace). Modulus for the tested samples: CE3 (51.9 ± 5.49 kPa), CE6 (59.7 ± 7.68 kPa), CE6*(44.0 ± 5.63 kPa), CE9 (41.0 ± 5.36 kPa), CE12 (33.1 ± 3.80 kPa). Standard error reported. 7 days sample growth; ramp loading protocol.

Motivated by the initial result, we explored other properties that our setup could measure, e.g., perfusion, a quantity that is relevant to living materials for use as protective surface coatings. Since our "ramp" measurements were rapid, we were able to neglect the effects of perfusion through the films in our calculations; however using longer timeframes we could measure it. Other efforts to characterize permeability through biofilms include tracking of fluorescently labeled microspheres[7], dyes[8], or antibiotics[9], or using PSGE NMR[10].

Here we describe a simple version of an experiment to compare perfusion through CE9 and CE12. These films were chosen since at the time (see section 3.6) they had similar properties. With the same setup, we modified the testing protocol to characterize perfusion, with the purpose of demonstrating future opportunities to develop this technique further to include relationships among structure, perfusion, and deformation in biofilms.

Using the well-known integral form of the Darcy law, $Q = \frac{kA}{\mu L}\Delta P$ ,[11] where permeability $k$ is the unknown quantity of interest and $Q$ (flow rate in $m^3/s$), $A$ (cross sectional area of material in $m^2$), $L$ (thickness of material in m), and $\Delta P$ (pressure drop across the material in Pa) are measurable quantities ($\mu$ = assumed to be the dynamic viscosity of water, appx. $8.9 \times 10^{-4}$ Pa s at 25°C), we quantified the flow rate of PBS through the biofilms at various pressure drops in order to find $k$. N = 12 for CE9 and 13 for CE12; three biological replicates were tested for each biofilm. The existing bulge test apparatus was modified for this experiment: known pressure drops were applied using the same method described earlier, and OCT images were captured either continuously (if the experiment duration was less than two minutes, due to memory limitations) or at the beginning and end of each

experiment to measure change in thickness of the film. An additional syringe and tubing were used to withdraw the PBS as it perfused to the second reservoir and the mass of PBS that flowed through was measured at the end of each time point. Thickness $L$ used in calculations was treated as a constant due to the fact that the maximum reduction in thickness observed was less than 5 µm, below instrument resolution. A linear fit to plots of $Q$ vs. $\Delta P$ for both CE9 and CE12 (Figure 3.17) yielded slopes from which $k$ could be estimated ($5.4 \pm 3.0 \times 10^{-12}$ m$^2$ for CE9 and $1.6 \pm 0.69\ 10^{-11}$ m$^2$ for CE12; standard error reported).

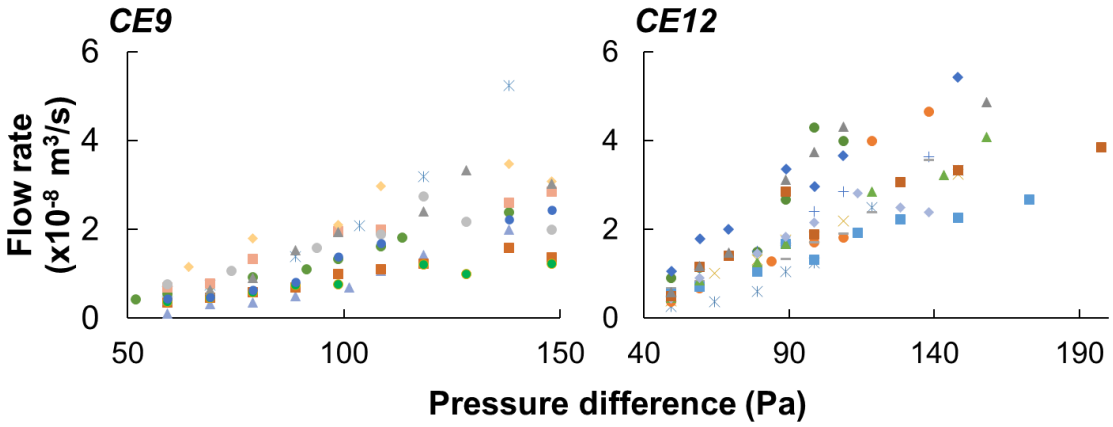


Figure 3.17. CE9 and CE12 flow rate through films as a function of pressure difference. Note different x axes in plots, adjusted for clarity. 7 days sample growth.

We were surprised to find that these simple measurements showed a statistically significant difference in permeability between CE9 and CE12 ($t(20) = 3.82$, $p = [0.001]$), suggesting that linker length could have an impact on permeability of engineered living materials. Further studies would have to explore this in more detail, e.g., Darcy's law is only valid for Re < 10, for which porosity of the biofilm would need to be measured.

Despite simplifying assumptions, our method offers certain advantages–the fast acquisition and penetration depth of OCT make this a useful system for studying combined mechanics and permeability of living materials. Simultaneous OCT imaging such as that demonstrated above can monitor the profile and thickness of biofilms and offers future opportunities–for example, studies of changes in permeability as a function of deformation, or Doppler OCT for spatially resolved (mesoscale) information about flow rate in different regions of a biofilm along with bulk measurements[12,13]. These measurements could be used in conjunction with those described earlier (e.g. fluorescent dyes) to connect properties across multiple length scales. One inherent challenge however, with our method, is that each data point involves a repeated measurement on the same biofilm, which may change its properties as a result of being tested multiple times.

### 3.4 Monitoring and quantifying healing

A unique, distinct aspect of living materials is the ability to grow or regenerate, leading to observable "healing". Current studies on living materials are limited in the physical characterization of the healing process: materials with sufficiently high modulus (e.g. in the GPa range) can be characterized by commercially available instruments[14], while soft, purely bacterial-cell based materials still rely on indirect methods of characterization (e.g. current transmission) that are not directly correlated to the recovery of mechanical properties[15].

We anticipated that our method could address this gap and directly provide evidence for healing by i) demonstrating the ability of the healed biofilm to hold pressure and ii)

assessing the extent of mechanical recovery directly by comparing the properties of the original and healed films (e.g., modulus and toughness).

*3.4.1 Methods*

CE6 biofilms additionally expressing mWasabi were used for healing experiments (referred to in further text as "CE6mW"; the mWasabi did not significantly impact the properties of the biofilms (Figure 3.18) but allowed for simultaneous measurements with fluorescence microscopy, reported elsewhere along with full sequence details[5].

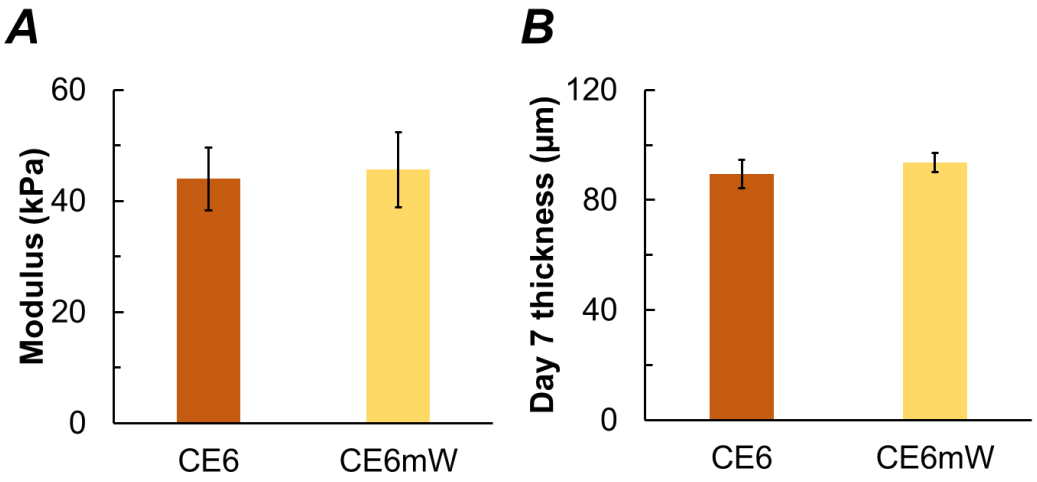


Figure 3.18. CE6mW exhibited modulus (A) and day 7 thickness (B) similar to those of CE6. Modulus: 44.0 ± 5.63 kPa (CE6), 45.6 ± 6.7 kPa (CE6mW). Thickness: 89.4 ± 5.07 µm (CE6), 93.6 ± 3.53 µm (CE6mW). Day 7 films did not fail within the pressure ranges imposed by our test.

For self-healing experiments, multiple 3 mm punches from biofilms were separated from the polycarbonate as described above and then placed onto a fresh agar plate for healing. 2YT plates were used for bulk healing experiments (Chapter 3), while LB plates were used for 3D experiments (Chapter 4).

A 25 µm thick TEM grid was used to make a cut through biofilms. Control films were placed onto fresh plates as well, without defect, for comparison.

Films were allowed to grow on the new plate at 37°C and monitored to assess the healing process. Details of the 3D bulge test experiments are described in Chapter 4. Here, we describe the experiments in 2D (Figure 3.19A).

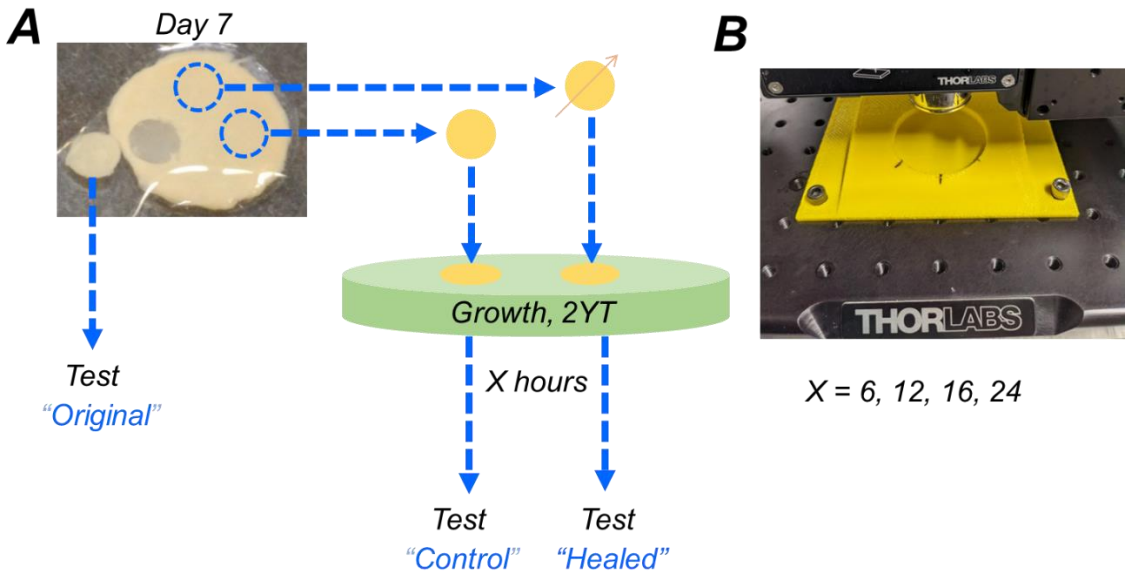


Figure 3.19. A) Schematic of biofilm healing experiment. B) 3D printed petri dish holder fixed to OCT base plate.

OCT imaging of the cut and control biofilms was performed at 3, 6, and 16 hours. In order to image comparable regions each time, we 3D printed a petri dish holder (Figure 3.19B) and secured it to the OCT base plate, with a cavity that provided a snug fit for a single 60 mm diameter petri dish. The holder was at roughly a 10° slant to avoid noise from reflections in the OCT image at the air-biofilm interface. Only one biofilm punch was placed at the center of each petri dish, and permanent marks on both the petri dish and

holder enabled the alignment of the petri dishes each time they were removed from the incubator for imaging. Although the vertical focus of the OCT could necessarily not be kept constant, we reproduced the scan settings in XY using the ThorImage OCT software to ensure that the scanned region was consistent for a given punch. Alignment was further confirmed using the camera images from the ThorImage OCT software, which provided an overall view of the sample itself as well as the specific scan box (Figures 3.20, 3.21, camera image insets with red rectangular boundaries).

*3.4.2. Results: Quantifying the recovery of mechanical properties in healed biofilms*

The OCT images of healing (Figures 3.20, 3.21) provided a baseline for our bulge test time points. From the OCT images, the region with a defect showed clear healing in as soon as 3 hours; however the timescale of recovery of mechanical properties could only be assessed by the bulge test. Images were exported either as 3D renders at the same viewing angle and contrast (Figures 3.20-3.21, top), or as 2D cross sections at the same XZ plane in each image (Figures 3.20-3.21, bottom).

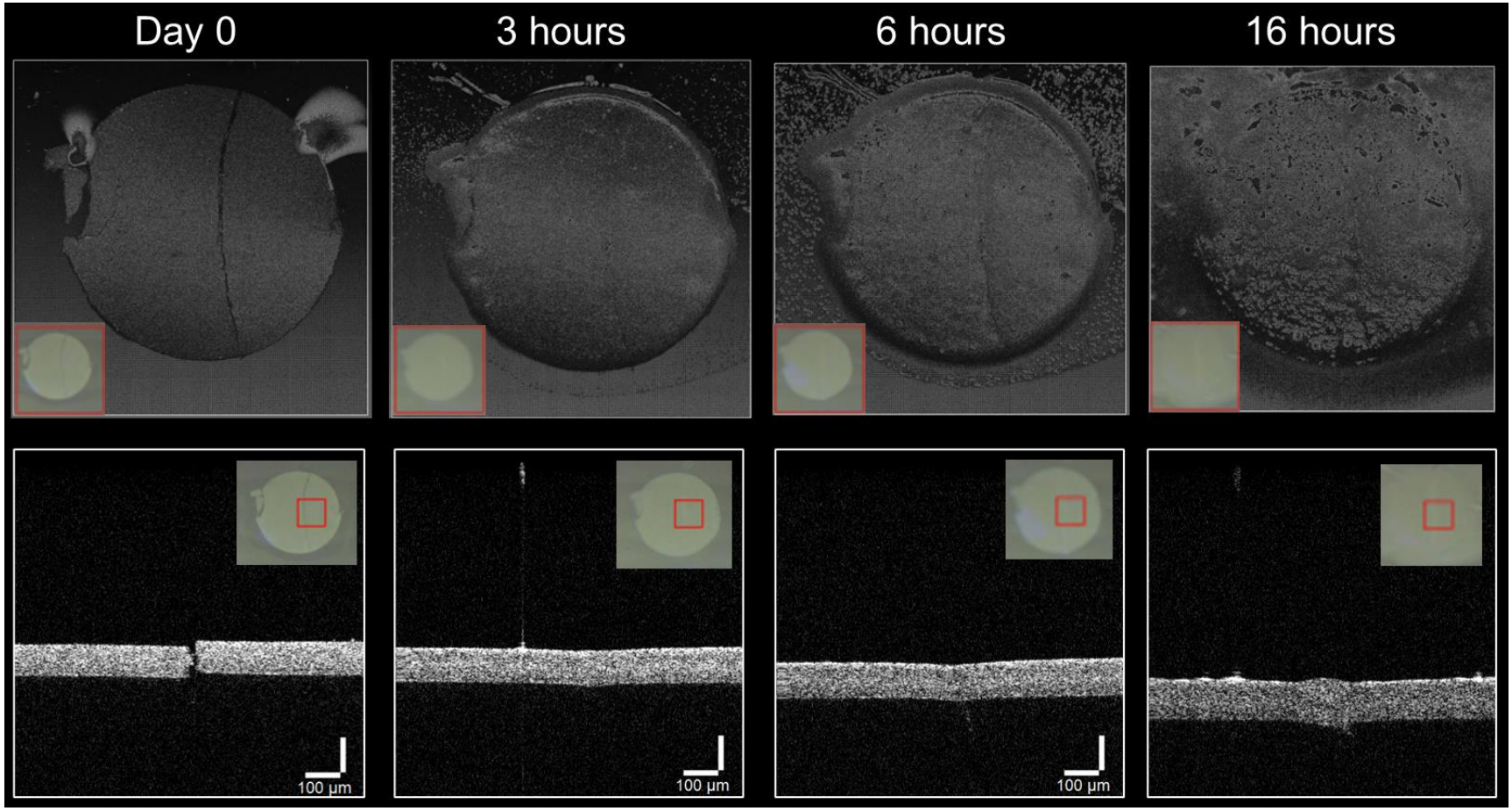


Figure 3.20. OCT scans of CE6mW healing on 2YT plate show rapid healing of biofilm with created defect. Top row exported as 3D renders. Scale: top, 4 x 4 mm scan box; bottom, 1 x 1 x 1 mm scan box. Insets are OCT camera images, manually cropped to region being scanned. Red rectangular outline represents scan box (automatic, from ThorImage OCT software).

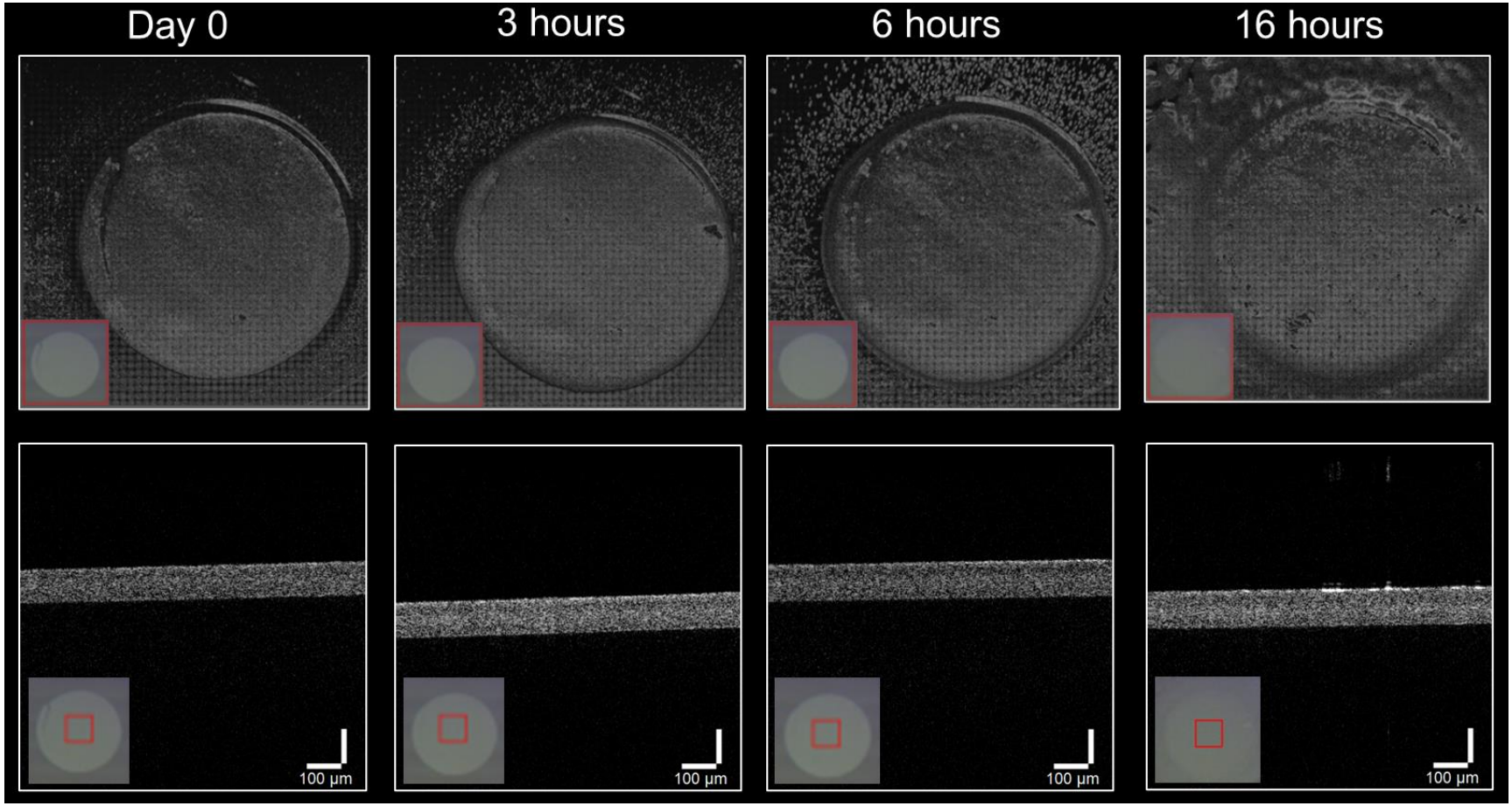


Figure 3.21. OCT scans of CE6mW control on 2YT plate. Top row – patterned artifact due to software, not biofilm. Scale: top, 4 x 4 mm scan box; bottom, 1 x 1 x 1 mm scan box. Insets are OCT camera images, manually cropped to region being scanned. Red rectangular outline represents scan box (automatic, from ThorImage OCT software).

We attempted to perform bulge tests at 6, 12, 16, and 24 hour time points. Statistics are reported in Table 3.1, describing number of samples tested at each time point along with major points of failure. We discovered that healed biofilms could easily be separated from the nutrient plate by gently flooding the plate with PBS. After approximately 1-2 minutes, the punches freely separated from the agar underneath. Despite the gentle nature of this step, a few samples failed when peeled from the agar, with the previous defect reopening (second column, Table 3.1). The next major point of failure was during the initial pressure equilibration step (third column, Table 3.1). The final column in Table 3.1 details whether films failed during the bulge test itself.

Table 3.1. Sample statistics for healed biofilms

| | Total number of samples | Successfully peeled from agar and loaded (% of total) | Survived initial filling/pressure equilibration (% of total) | Failed within imposed pressures during bulge test (% of **tested**) |
|---|---|---|---|---|
| Original (Day 0) | 4 | 4 (100) | 4 (100) | 0 (0) |
| Controls (16 hours) | 4 | 4 (100) | 4 (100) | 2 (50) |
| Healed (6 hours) | 4 | 3 (75) | 0 (0) | - |
| Healed (12 hours) | 6 | 5 (83) | 4 (66) | 4 (100) |
| Healed (16 hours) | 7 | 6 (86) | 3 (43) | 3 (100) |
| Healed (24 hours) | 10 | 8 (80) | 0 (0) | - |

Properties of the immediately cut biofilm are not reported, since the cut film did not have the ability to maintain a pressure difference (Figure 3.22B). Fluid simply flowed through

to the other side. This feature was also directly used in our experiments to determine the moment where the film failed, also visible under the OCT.

In comparing the various time points, we discovered that films healed for 6 hours healed to the extent that we could peel them from the agar and place them into our device; however the small differences in pressure resulting from the drop by drop filling of the device were sufficient to break the film once again.

Films healed for 12 and 16 hours could be readily tested. Surprisingly, 100% of films tested after 24 hours of healing could not withstand loading, suggesting that there is an optimal time frame for recovery of mechanical properties. Further studies could explore simultaneous staining with live-dead or metabolic dyes to assess the impact of other factors that act to degrade the biofilm over time.

Initial inspection suggested that films that broke a second time during loading or handling tore at a site similar to the location of the original defect. However, this (and other location-specific properties) could not be confirmed without some sort of tracking or marker, which partly motivated the development of the 3D method we describe in Chapter 4.

Next, we assessed the extent of recovery of mechanical properties using the 16 hour mark as our time point, comparing the original uncut film on day 0, the control (uncut film grown on the healing plate), and healed films (Figure 3.23). It is worth noting that due to the increased thickness of the control and healed films relative to the original film ($123 \pm 2.78$ and $120 \pm 15.0$ vs $103 \pm 11.1$ μm respectively, only considering films that were successfully tested), the range of stresses that could be imposed by our device (inversely

proportional to the thickness of the film) was not directly comparable. However, we did observe a few clear differences among the films tested: first, the original (uncut, day 7) films did not fail at the maximum pressure limits imposed by our device. The actual stress this corresponded to depended on the sample thickness and properties, but the highest observed stress tested on a CE6mW sample of 89 μm thickness was 7.21 kPa. While there was some variation in the range of applied stresses and observed strains during our test, we observed that CE6mW films on day 7 consistently tolerated stresses greater than 6.5 kPa (Figure 3.22A).

In contrast, two out of four of the control films (16 hours) failed during our experiment. One failed at a stress of 4.68 kPa, while the other film failed at a stress of 3.65 kPa. (Figure 3.22C)

100% of the healed films that could be loaded and tested failed within the range of stresses applied by our test (Figure 3.22D). Given this result, we hypothesized that perhaps toughness (energy absorbed by the material prior to failure) could be used as an additional metric to assess the extent of healing (elaborated on in later text).

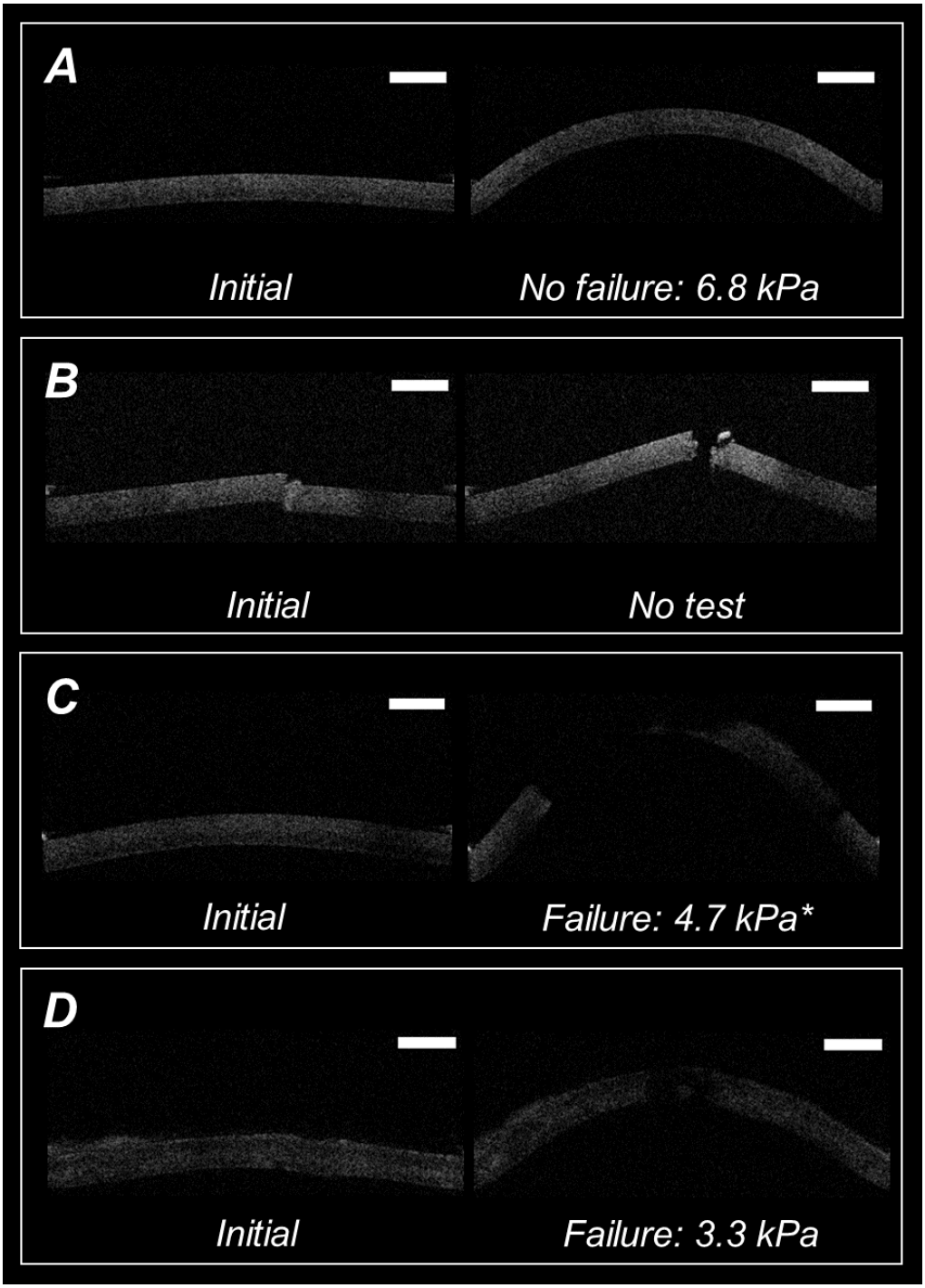


Figure 3.22. Original, day 7 CE6mW films (A) do not fail within the limits of our test. Pictured maximum stress tested: 6.68 kPa. Cut films (B) immediately after defect creation cannot be tested, as the fluid freely flows through the tear (right). *50% of control films failed; pictured film (C) showed failure at stress: 4.68 kPa. All healed films failed (D); pictured maximum stress tolerated 3.32 kPa. Scale 200 μm.

From the stress-strain plots (Figure 3.23B), we observed that the modulus was similar across all three sets of films! This was surprising to note, but in order to assess whether it was a reasonable metric to compare, we analyzed two time points of healing (12 vs 16 hours), to assess which aspects of the film changed as the film healed.

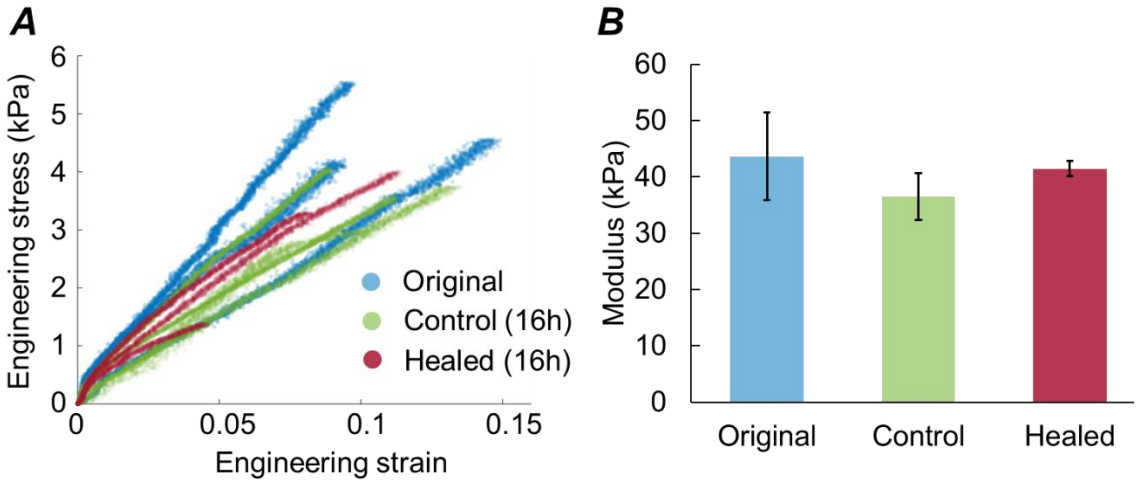


Figure 3.23. A) Living materials can recover their mechanical properties after healing (stress-strain plots). B) Moduli for original, control (16 hours) and healed (16 hour) films are comparable: Original: 45.6 ± 6.8 kPa, Control: 36.5 ± 8.24 kPa, Healed: 41.4 ± 2.31 kPa. N = 3 for original and healed; N = 4 for control. Standard error reported. Individual biofilm failure not marked on stress-strain curves for clarity; see text for details.

In comparing biofilms healed for 12 vs. 16 hours, we found that the elastic moduli did not show a clear variation (12 hour: 52.7 ± 11.4; 16 hour: 41.4 ± 2.31 kPa). However, based on previous observations that every healed biofilm punch that could be tested also failed before the end of the test, we hypothesized that the toughness could be a quantity that varied with healing time. We estimated toughness by calculating the area under the stress-strain plots (Figure 3.24A, dotted lines connecting points with shaded area representing the toughness), and discovered that the healing time did indeed influence toughness; despite a

large variability in the 16 hour samples, there was a clear increase in toughness of the healed films at the latter time point (Figure 3.24B).

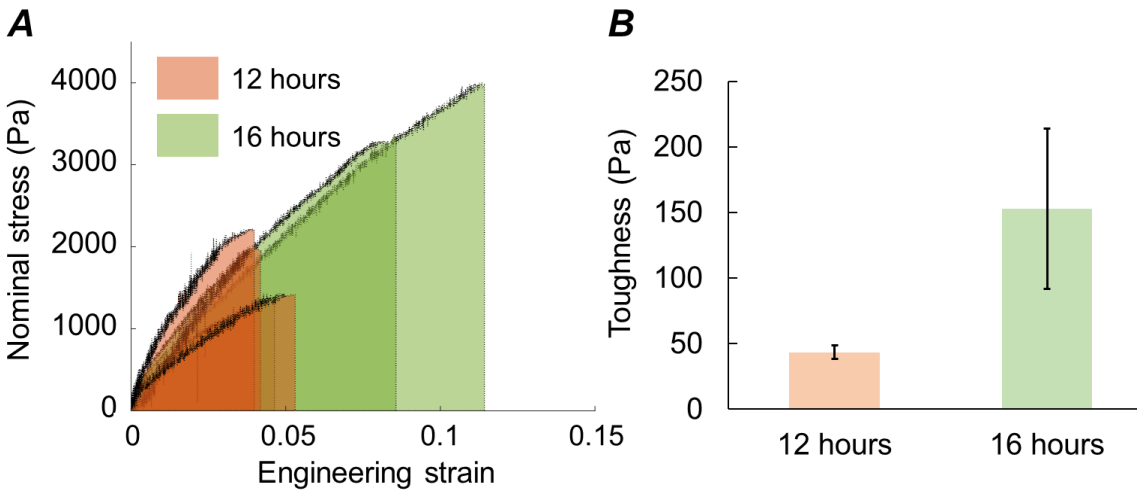


Figure 3.24. A) Area under stress-strain plots of biofilms healed for 12 (orange) vs. 16 (green) hours represents toughness (B), which increases with time. N = 3. Standard error reported.

### 3.5. Conclusion

In this chapter, we described a protocol for the application of the bulge test towards the characterization of living material dynamics and elasticity, with example applications using a model engineered biofilm system. We demonstrated how this fairly simple method could be used to quantify the effects of engineering on bulk film properties, image failure and correlate physical features to stress-strain curves, estimate perfusion, and visualize and measure the recovery of mechanical properties of healed living materials. The same method could be extended further to include other types of imaging as well–for example confocal microscopy or polarization-sensitive OCT for simultaneous studies of structure[16].

An inherent disadvantage is that this characterization is limited to bulk information and assumes homogeneous material properties. Living materials are not necessarily homogeneous, however, and living materials offer a unique system to study the presence or effects of possible heterogeneity.

For example, we demonstrated healing in CE6 films in Chapter 3, along with a recovery of bulk properties. This motivates the question: How does the newly healed region compare to the surrounding parent material?

In another example (Figure S3.11), we often observed variations among punches within a single E6 film, suggesting that these films may have inherent heterogeneities. This brings about new questions: What role does biofilm engineering (e.g. adding a single residue) play in introducing or eliminating biofilm heterogeneity? If this heterogeneity is real, can we localize it to certain regions of the film? Does it play a role in the properties of the film (e.g. failure)?

Answering any of these questions requires a more in-depth analysis that does not average properties across the entire sample as we have in Chapter 3. This aspect motivated us to consider alternative methods of analysis to capture “local” information, detailed in Chapter 4.

## 3.6 Additional figures and supplementary information

*Technical and biological replicates*

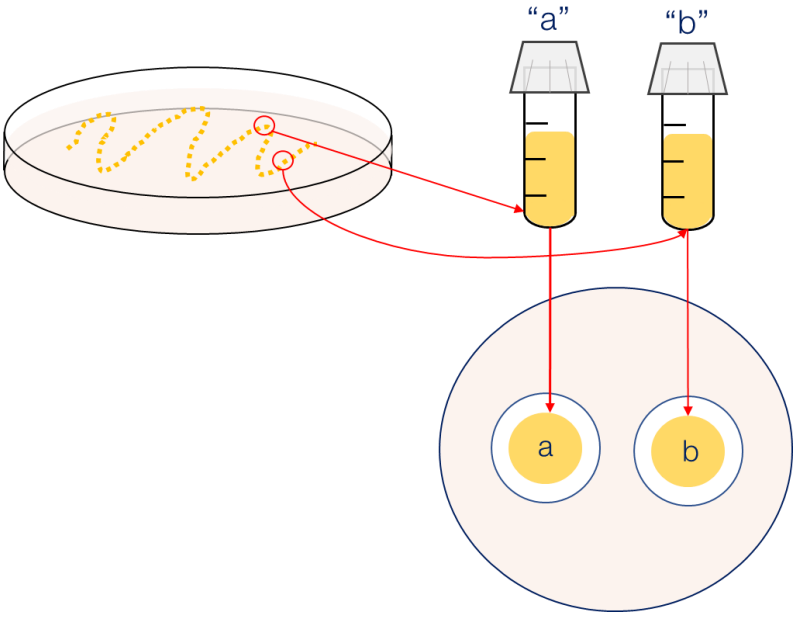


Figure S3.1. Biological replicates are grown from different colonies (e.g. "a" vs. "b"). Each liquid culture could be used for multiple biofilms, in which case the films would be technical replicates (denoted "a1" or "a2" in further text).

*E6 variability*

Due to (unclear sources of) biological variability, biofilm properties varied over time (Figure S3.2). Properties are reported for 7-day E6 where possible, but experiments transitioned to using 9-day E6mC where specified (e.g. healing) in cases where 7-day E6 was no longer possible to test, since these films were more consistent in their properties.

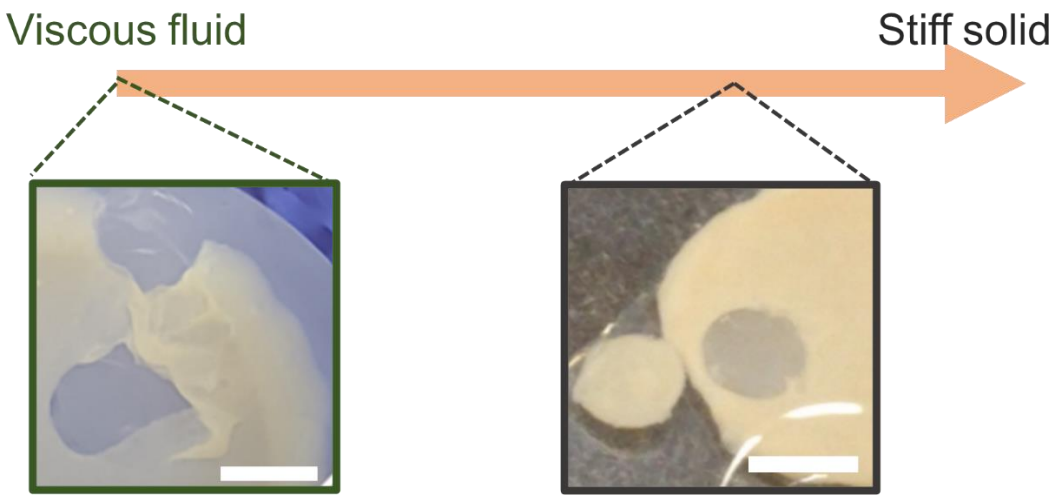


Figure S3.2. E6 biofilms varied in their properties over a spectrum from viscous liquid (could not be handled or tested) to more solid (could be tested). A further condition (not pictured) involved films that were cohesive but failed during loading and hence could not be tested. Scale 3 mm. 7 days sample growth.

All calculations in the bulge test used the thicknesses of tested, hydrated biofilms in the specified buffers. Initial thickness of the films on polycarbonate filters on agar was noted prior to the experiments and found to deviate from the thickness in buffer for E6-based films, but less so for CE6 films. Thickness is reported below for various films as “on agar” (initial condition), in PBS (immediate), in HEPES (immediate), and in HEPES (30 minutes).

*E6mC thickness*

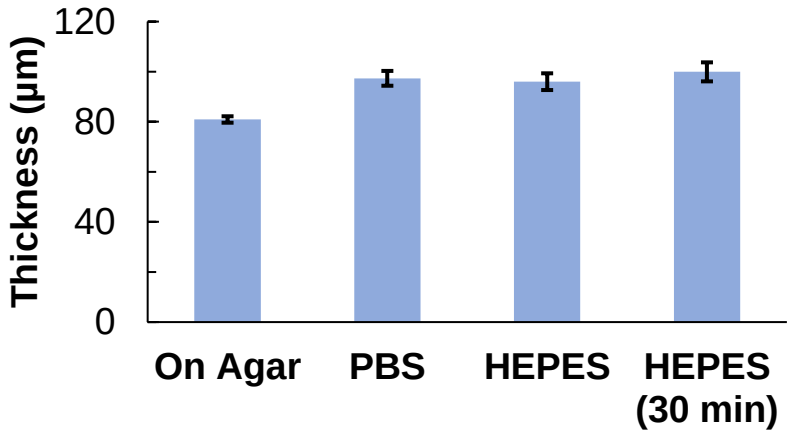


Figure S3.3. E6mC thickness in (9 days, values in µm): 80.9 ± 1.28 (agar), 97.3 ± 2.96 (PBS), 96.0 ± 3.34 (HEPES), 99.9 ± 3.80 (HEPES, 30 minutes). N = 10 (agar), 4 (PBS), 4 (HEPES), 7 (HEPES, 30 minutes). Biological replicates tested respectively: 10, 3, 4, 4.

A roughly 20% immediate increase in thickness was observed for E6mC when transferring from the original agar support to either PBS or HEPES; thickness did not vary significantly after 30 minutes of immersion.

*E6 thickness*

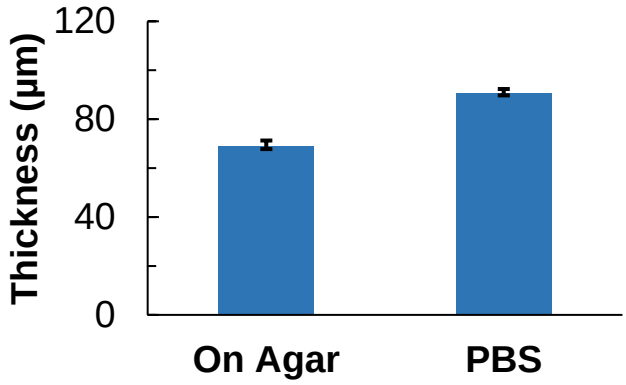


Figure S3.4. E6 showed a similar increase in thickness (7 days, values in µm): 68.8 ± 2.49 (agar), 90.7 ± 1.61 (PBS). N = 18 for both agar and PBS, all biological replicates.

E6 films exhibited a similar effect at 7 days, but the thickness increase was closer to 32% (Figure S3.4).

*E6mC healing*

Healing experiments similar to those of CE6 were attempted for E6mC (9 days old), but despite apparent healing from OCT images (Figure S3.4), the mechanical properties did not heal enough for the films to be tested.

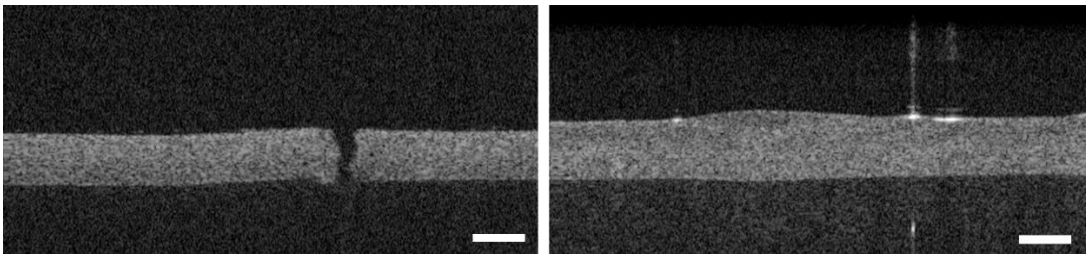

Figure S3.5. E6mC can also heal upon defect creation. OCT images taken immediately (left) and after 16 hours (right) show growth of biofilm in previously cut region. See main text for protocols. Scale 100 μm. 7 days sample growth for original biofilm.

At 16 hours, all healed films broke during loading. Only one out of the two control films could be tested (Figure S3.5), and it showed a reduction in modulus from 33 kPa to 26 kPa (Figure S3.6) and a failure stress of roughly 3.2 kPa compared to 4.5 kPa in the original film.

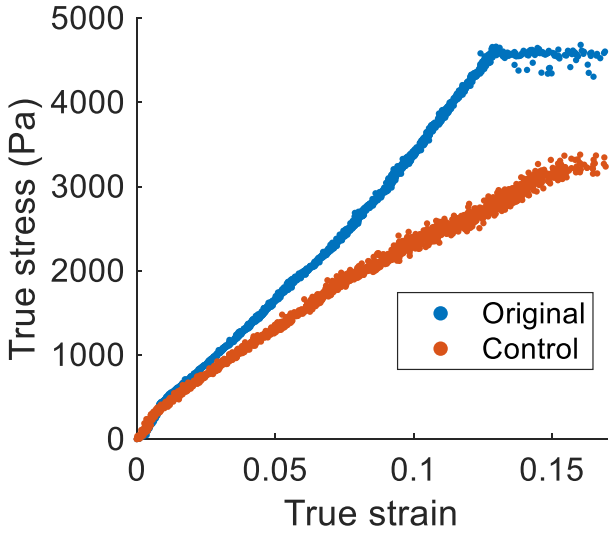


Figure S3.6. Representative E6mC data: films could not be tested after healing. Control film (orange, shallow trace) had a lower modulus than the original film (see text for details). 7 days sample growth; ramp loading protocol.

*CEn thickness*

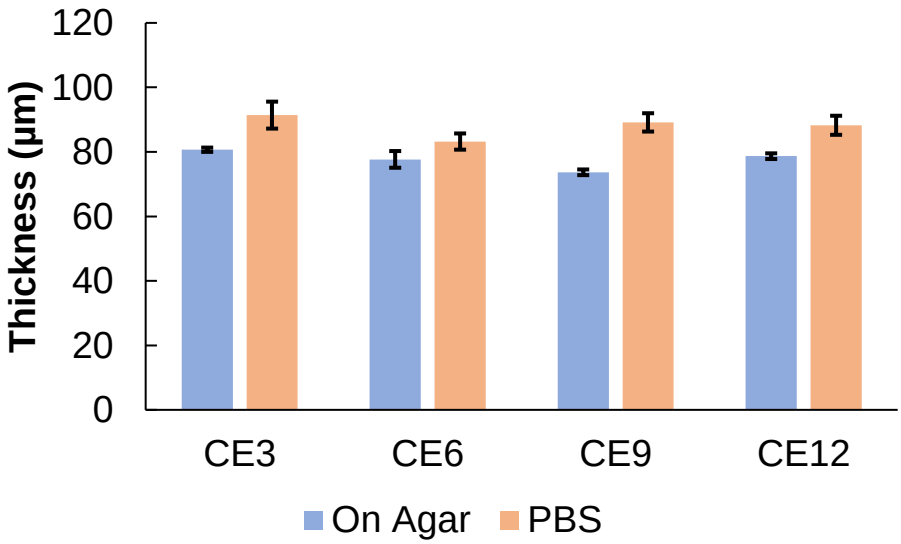


Figure S3.7. The *CEn* series also showed an increase in thickness when transferred from the agar to PBS. Increase in thickness did not exhibit a trend with linker length. Thickness (agar, ordered CE3-12): 80.7 ± 0.667, 77.7 ± 2.59, 73.7 ± 0.881, 78.7 ± 0.881. N = 3 for CE3, 9, 12, and N = 6 for CE6; PBS: 91.4 ± 4.17, 83.2 ± 2.52, 89.1 ± 2.84, 88.2 ± 2.95. N = 5 for CE3 and 6, N = 7 for CE9 and N = 4 for CE12. Only samples from 2022 were considered in this analysis. Standard error reported. 7 days sample growth.

*CEn biovariability and challenges in testing biofilm materials*

Data collection proceeded from 2019-2022; however properties and datasets reported in the main text only include data from 2022. Large variations in the properties of the engineered biofilms were observed in the three-year span and as a result it was important to test all samples within a few weeks of one another.

Some examples of this large variability are described below and can be attributed to a combination of factors such as changes in sample preparation methods by collaborators and natural unexplained biovariability, to name a few. The below datasets include those taken from 2019-2020. Note: the pressure profile applied (and acquisition) were "stepwise" in these experiments rather than the "ramp" profiles described above.

*CEn series*

In the main text, we report a consistent ability of CE6 (and the CEn series in general) to withstand the maximum pressures applied by our device.

However, earlier iterations (2019-2020) of CEn films were found to consistently and reliably fail around a pressure drop of ~1 kPa (Figure S3.8, S3.9, corresponding to a failure stress of roughly 5-6 kPa), with a modulus around 25 kPa (exact values in Figure S3.8 below).

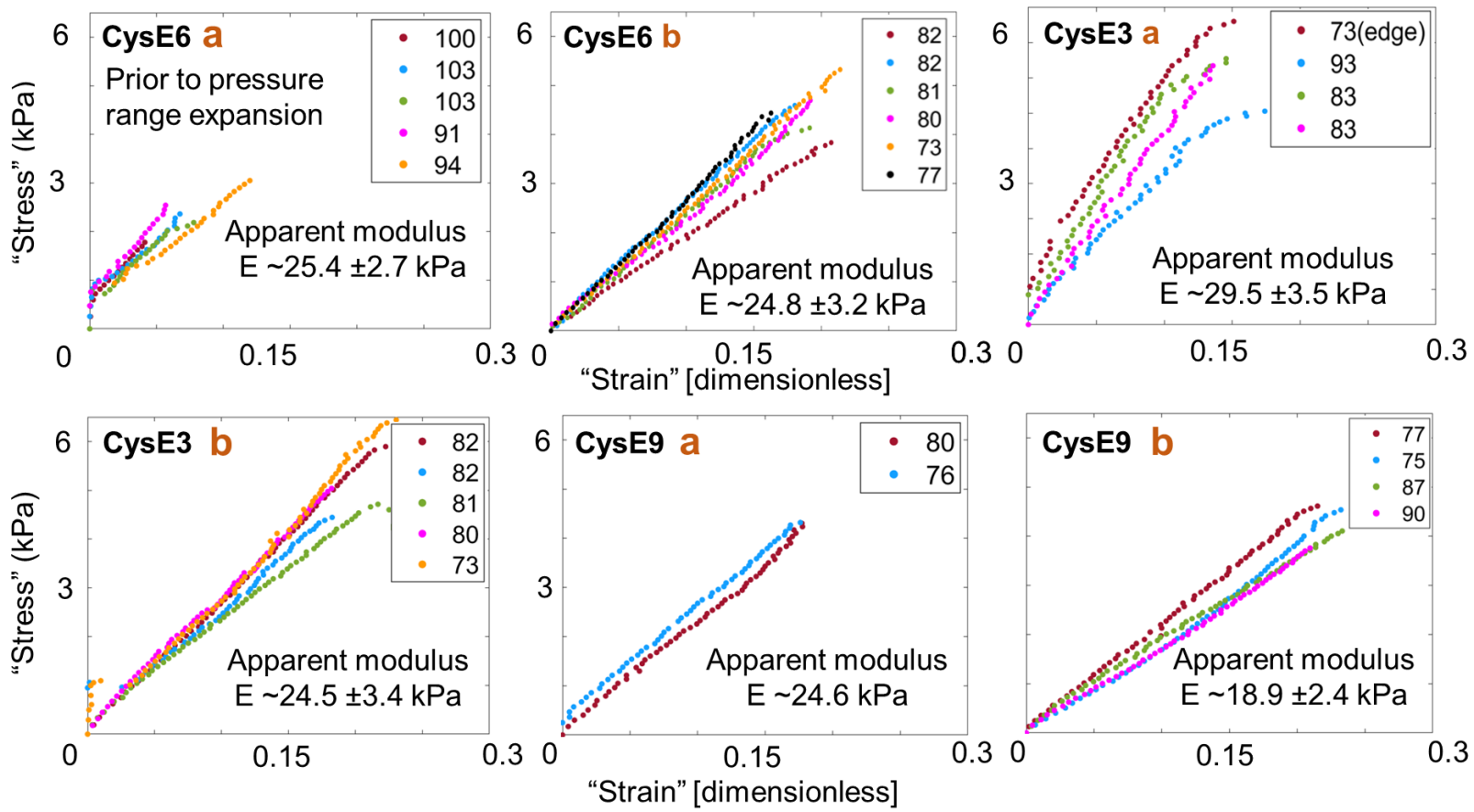


Figure S3.8. Early experiments on CE9 series yielded comparable properties. Labels: film name (top left of each plot), biological replicate denoted by "a" or "b", thickness denoted by colored markers and numbers on the right of each plot. "E" denotes modulus. Multiple traces on each plot correspond to punches from the same film. Top left CE6 film not tested to failure; all other films shown were tested to failure. Engineering stress and strain are reported. 7 days sample growth; stepwise loading protocol.

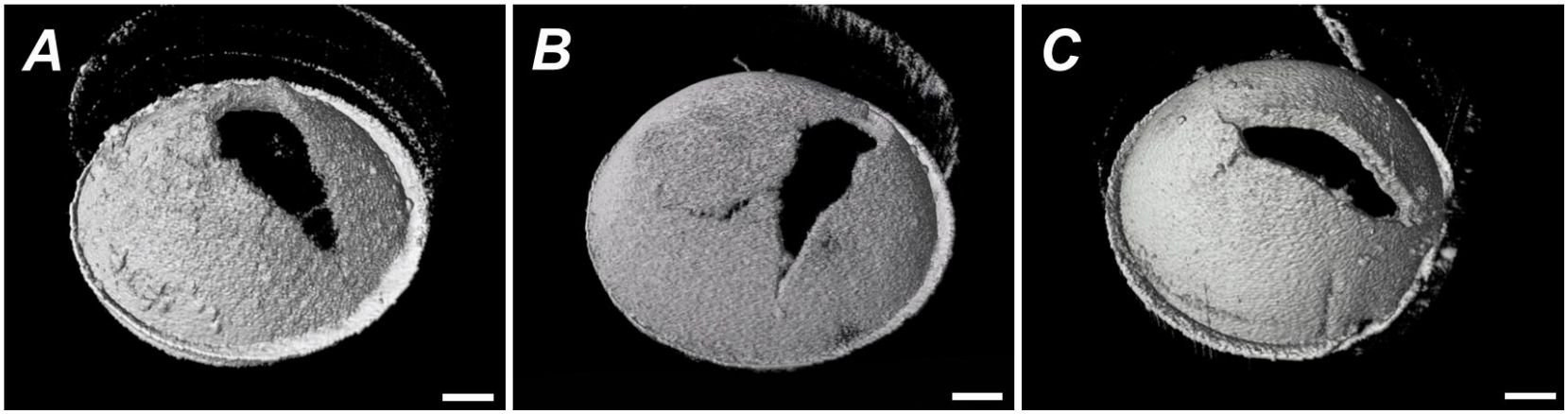


Figure S3.9. CE3 (A), CE6 (B), and CE9 (C) film failure accompanying Figure S3.8. All films showed brittle failure similar to that described in the main text for CE6. Scale 200 μm. 7 days sample growth; stepwise loading protocol; ΔP = 795 Pa (A), 760 Pa (B), 720 Pa (C).

The original pressure regimes in the device were chosen such that they could accommodate both the weaker films (e.g. En series) and the stiffer ones (CEn); however as the properties evolved over time, the new sets of CEn films were able to tolerate much larger stresses.

*En series*

In contrast to the CEn series, whose properties became stiffer with time, early iterations (2019) of E3 and E6 were sufficiently cohesive and could be characterized. The modulus could not be directly compared to that of E6mC films in the main text due to different loading rates.

Similar to CEn, no clear effect of linker length was observed on the properties; however, we observed that En (particularly E6) was less consistent in properties among punches within a single film. This motivated the development of methods described in Chapter 4, to probe whether this apparent heterogeneity was in fact real, and whether we could localize it to a specific region of biofilm.

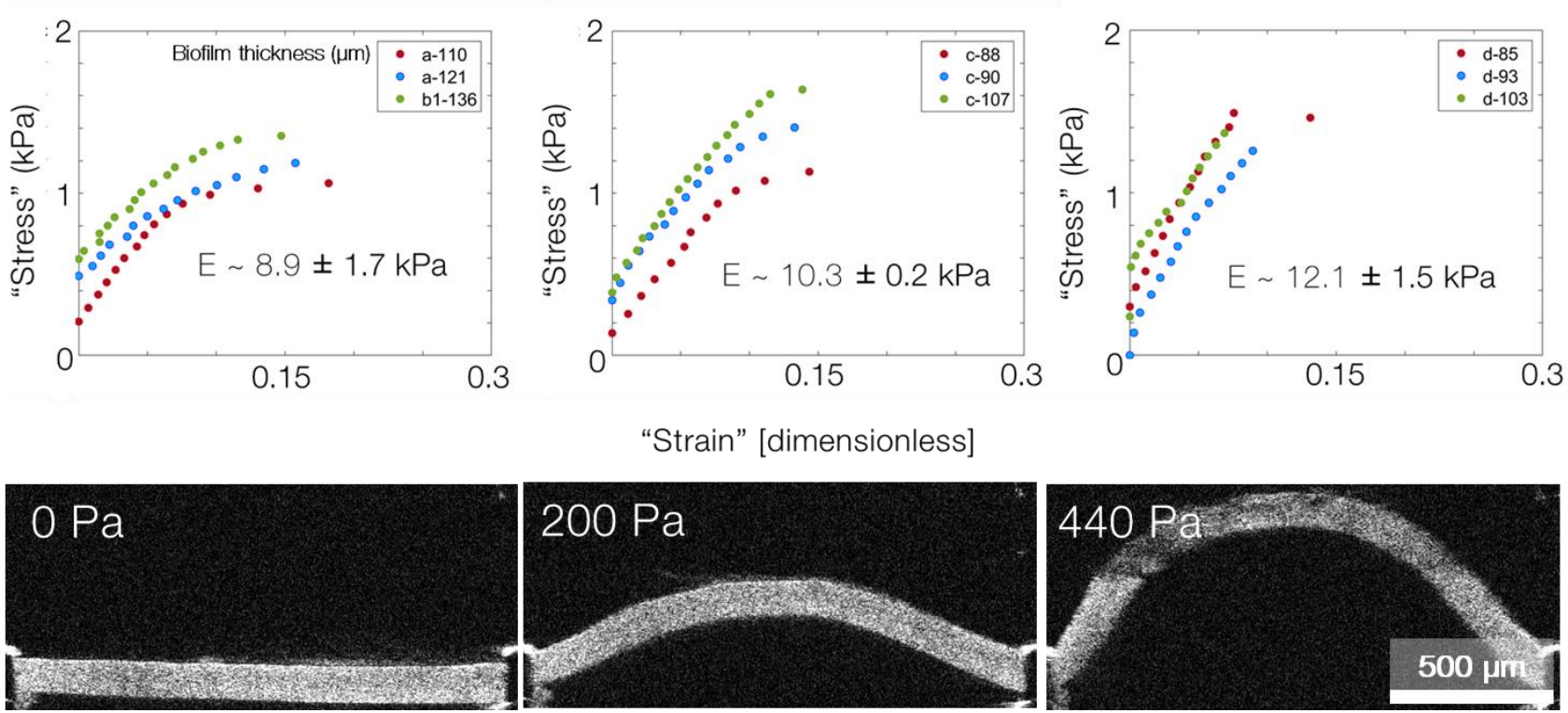


Figure S3.10. E3 properties, with legend: 'E' denotes modulus; letters on top right indicate biological or technical replicate; numbers indicate thickness in µm. Bottom: typical ductile failure of E3 film, here shown at 440 Pa pressure difference (roughly 1.2-1.6 kPa stress). Engineering stress and strain reported. 7 days sample growth; stepwise loading protocol.

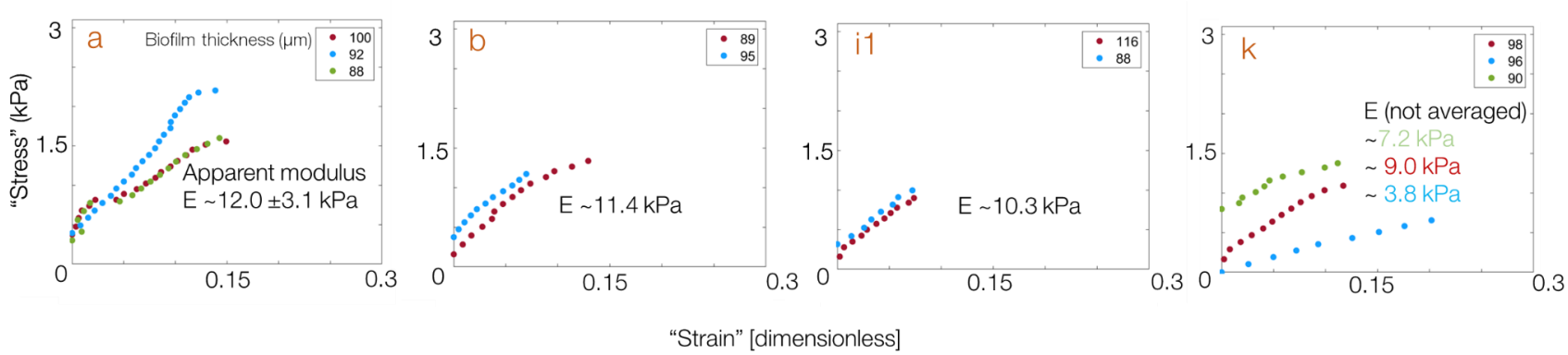


Figure S3.11. E6 films showed apparent heterogeneity among punches from the same film, but overall properties were comparable to those of E3 (see Figure S3.10). Legend: 'E' denotes modulus from initial linear region of each trace; numbers on top right indicate thickness in µm. Engineering stress and strain reported. All films tested to failure. 7 days sample growth; stepwise loading protocol.

*Creep and other applications*

In addition to the applications described in the main text, we also briefly explored other testing conditions and geometries. First, shorter working distances and fully transparent viewing windows could easily be accommodated, e.g. either using thinner acrylic or etching, rather than cutting, the channels using both sides of the same sheet (Figure S3.12), for use with confocal microscopy. Future studies for microstructure-property correlations or other types of microscopy (e.g. polarized light microscopy) would be possible using such modifications of our setup.

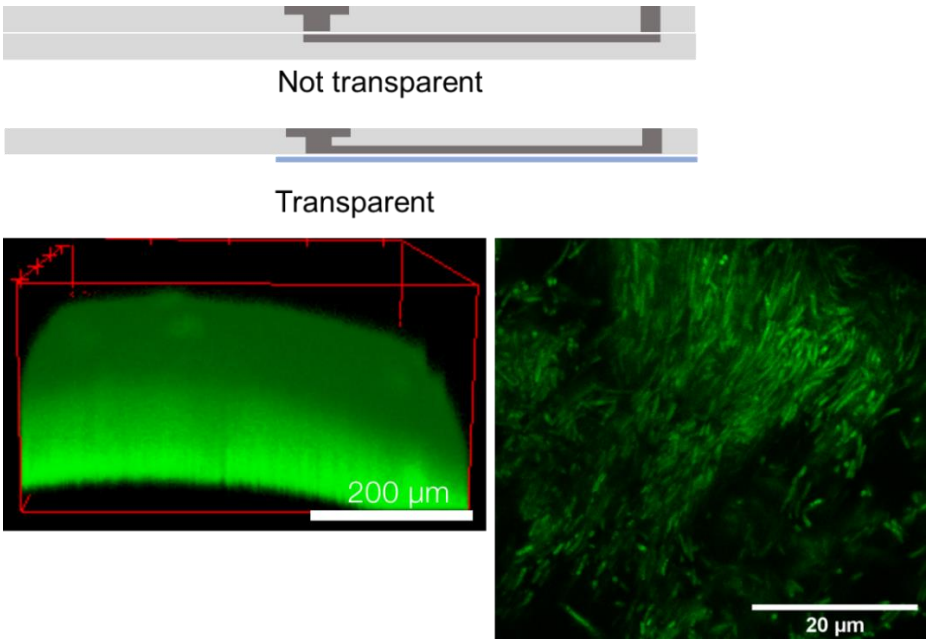


Figure S3.12. Top: channels made from single sheets of acrylic, etched on both sides and sealed with a glass cover slip reduce the total thickness of the device. Bottom: confocal microscopy of CE6mW films through the viewing window of devices with shorter working distances using NA = 0.6 (left) and 1 (right, with Airyscan) objectives using LSM 880.

Secondly, using our original setup, additional types of measurements are possible by varying pressure-time profiles, for example creep measurements (Figure S3.13). Here, similar limitations apply as described in the main text (e.g. perfusion over time).

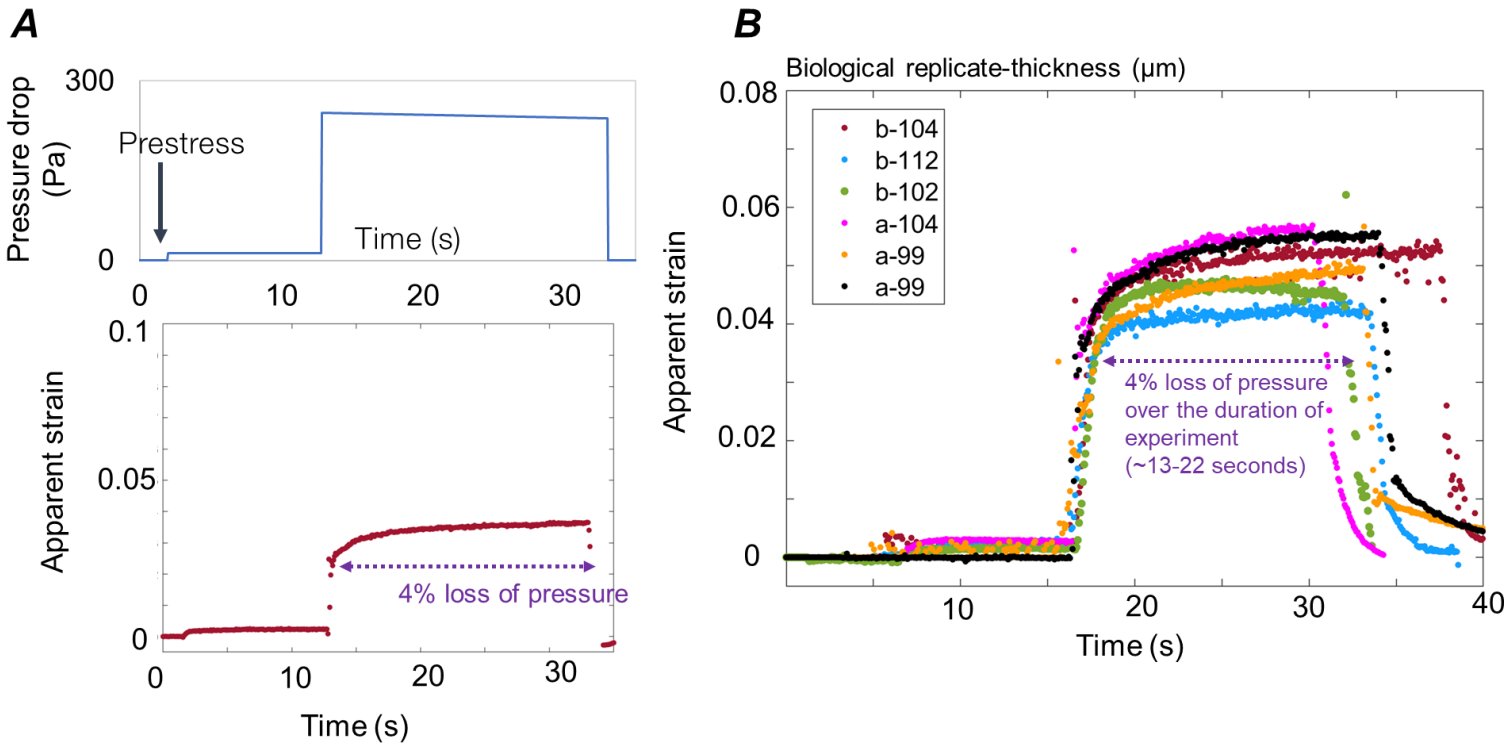


Figure S3.13. Creep protocol (A) with 5% prestress with representative data from 62 µm thick CE3 film. (B) Creep data from biological replicates (here CE6 shown, thickness 112 µm) is consistent. Biofilm was initially subjected to a pressure drop of 12.3 Pa, following which the pressure drop was increased to 247 Pa and held. Each point in the lower graph corresponds to strain calculated from a 2D image taken by OCT, 0.074 s/frame. Images were automatically processed to calculate engineering strain. Purple arrow indicates 4% pressure loss over the duration of the experiment.  7 days sample growth.

**References**


1. Hsu, F. P. K., Schwab, C., Rigamonti, D. & Humphrey, J. D. Identification of response functions from axisymmetric membrane inflation tests: Implications for biomechanics. *Int. J. Solids Struct.* **31**, 3375–3386 (1994).

2. Humphrey, J. D., Strumpf, R. K. & Yin, F. C. P. A Constitutive Theory for Biomembranes: Application to Epicardial Mechanics. *J. Biomech. Eng.* **114**, 461–466 (1992).

3. Humphrey, J. D. Computer Methods in Membrane Biomechanics. *Comput. Methods Biomech. Biomed. Engin.* **1**, 171–210 (1998).

4. Hsu, F. P. K., Liu, A. M. C., Downs, J., Rigamonti, D. & Humphrey, J. D. A Triplane Video-Based Experimental System for Studying Axisymmetrically Inflated Biomembranes. *IEEE Trans. Biomed. Eng.* **42**, 442–450 (1995).

5. Liu, H. Engineered living material based on protein mediated bacterial assembly. (2022).

6. Raja, Pavan MV; Barron, A. R. 2.10: Dynamic Mechanical Analysis - Chemistry LibreTexts. https://chem.libretexts.org/Bookshelves/Analytical_Chemistry/Book%3A_Physical_Methods_in_Chemistry_and_Nano_Science_(Barron)/02%3A_Physical_and_Thermal_Analysis/2.10%3A_Dynamic_Mechanical_Analysis.

7. de Beer, D., Stoodley, P. & Lewandowski, Z. Liquid flow in heterogeneous biofilms. *Biotechnol. Bioeng.* **44**, 636–641 (1994).

8. Rani, S. A., Pitts, B. & Stewart, P. S. Rapid diffusion of fluorescent tracers into Staphylococcus epidermidis biofilms visualized by time lapse microscopy. *Antimicrob. Agents Chemother.* **49**, 728–732 (2005).

9. Jefferson, K. K., Goldmann, D. A. & Pier, G. B. Use of confocal microscopy to analyze the rate of vancomycin penetration through Staphylococcus aureus biofilms. *Antimicrob. Agents Chemother.* **49**, 2467–2473 (2005).

10. Vogt, S. J., Sanderlin, A. B., Seymour, J. D. & Codd, S. L. Permeability of a growing biofilm in a porous media fluid flow analyzed by magnetic resonance displacement-relaxation correlations. *Biotechnol. Bioeng.* **110**, 1366–1375 (2013).

11. Carrel, M. *et al.* Pore-Scale Hydrodynamics in a Progressively Bioclogged Three-Dimensional Porous Medium: 3-D Particle Tracking Experiments and Stochastic Transport Modeling. *Water Resour. Res.* **54**, 2183–2198 (2018).

12. Leitgeb, R. A., Werkmeister, R. M., Blatter, C. & Schmetterer, L. Doppler Optical Coherence Tomography. *Progress in Retinal and Eye Research* vol. 41 26–43 (2014).

13. Li, Y., Chen, J. & Chen, Z. Advances in Doppler optical coherence tomography

and angiography. *Transl. Biophotonics* **1**, e201900005 (2019).

14. Caro-Astorga, J., Walker, K. T., Herrera, N., Lee, K. Y. & Ellis, T. Bacterial cellulose spheroids as building blocks for 3D and patterned living materials and for regeneration. *Nat. Commun.* **12**, 1–9 (2021).

15. Chen, B. *et al.* Programmable living assembly of materials by bacterial adhesion. *Nat. Chem. Biol.* **18**, 289–294 (2022).

16. de Boer, J. F., Hitzenberger, C. K. & Yasuno, Y. Polarization sensitive optical coherence tomography – a review. *Biomed. Opt. Express* **8**, 1838 (2017).

*C h a p t e r  4*

# Seeing heterogeneity in living materials requires 3D

*Experiments in this chapter were performed in collaboration with Hanwei Liu (H.L.). H.L. grew and provided biofilms and acquired CFU data. P.K.C. designed and performed the mechanical studies in this chapter, developed analysis methods, and analyzed the data.*

## 4.1 Introduction

In Chapter 3, we described a protocol to acquire and analyze 2D (cross-sectional) images tracking the deformation of an engineered living material as it evolved through the bulge test, to extract bulk properties averaged over the 3 mm diameter sample disk. This simplified analysis was sufficient to characterize many aspects of living materials: modulus, failure, dynamics, and healing.

However, it also came with certain drawbacks, most notably the inability to distinguish local properties or heterogeneity. Living materials (engineered or otherwise) are not necessarily homogeneous, and the ability to measure properties with some degree of spatial resolution would offer opportunities to study phenomena such as healing in greater detail, better understand the properties of mixed biofilms, or draw correlations between local structure/composition and mechanics. In this chapter, we describe an analysis method to extract local properties from volumetric images of the bulge test, and some examples of heterogeneity and its physical implications in living materials.

## 4.2 Methods

### *4.2.1 Sample growth, testing, and imaging*

In order to analyze "local" rather than bulk properties, we required contrast agents in the biofilm to act as tracers for further analysis. We analyzed a variety of microspheres (polystyrene, glass, polyethylene) for this purpose and found that silver coated hollow glass microspheres provided sufficient contrast under OCT for tracking.

For 3D measurements, a stock suspension (8 mg/700 µL, ~$1.5*10^7$ microspheres/ml) of silver coated hollow glass microspheres (5-15 µm dia., density 1.08 g/ml, Cospheric) in DI water with 2.5 mg/ml bovine serum albumin (BSA) to stabilize the dispersion (Figure S1) was prepared prior to experiments and sonicated for 10 minutes (40 kHz, ProSonik DSA50-SK2) to disperse the microspheres, and allowed to rest for at least 30 mins. The suspension was further vortexed before use. Bacterial film coating and growth proceeded in the same manner as for the particle-free films except that 5 µl of microsphere stock was additionally added to the 200 µl of coating suspension prior to coating, for a final particle concentration of roughly $10^4$ particles/µL of bacterial film (expected distance between particles ~ 46 µm, based on a final biofilm volume of ~10 µl). Biofilm viability and elastic moduli (measured using the 2D method) showed no measurable effect of adding the tracers (Figure 4.1).

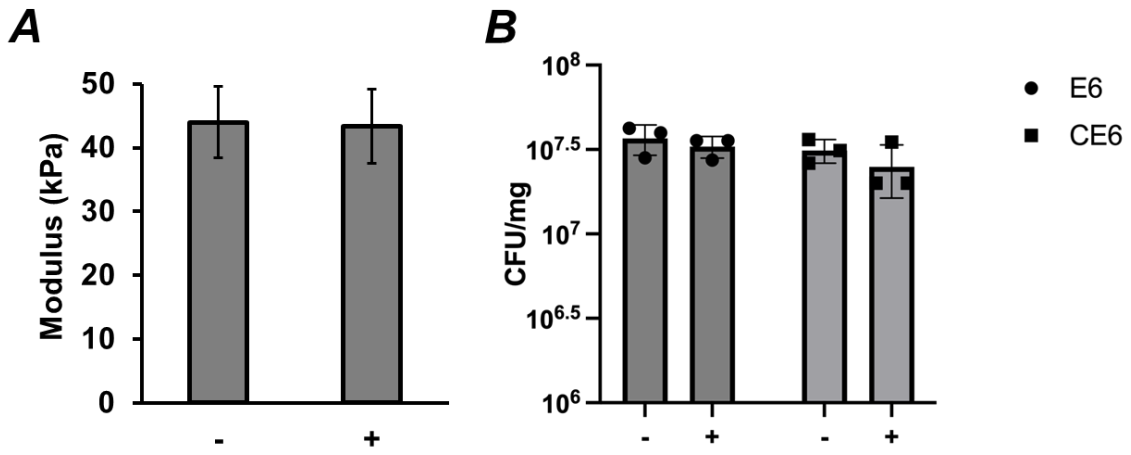


Figure 4.1 A) Mechanical properties of CE6 (modulus) as determined by the 2D bulge test were not significantly different between particle-containing and control films. "+" indicates particle-containing films, while "-" denotes control. Multiple punches from three biological replicates were tested. E6 could not be tested for this experiment. B) Viability of E6 and CE6 as measured by colony forming units (CFU) was not significantly impacted by the particles. Three biological replicates were used for the measurement. Measurement in (B) performed by H.L.

Volumetric OCT datasets were analyzed using Imaris (Oxford Instruments v. 9.5): TEM grid reflections were masked using the surface tool, then the reflective particles were tracked for their locations throughout the experiment, including the very edge of the TEM grid itself. To simplify downstream processing, particle traces that were not continuous throughout the experiment were removed. Data was exported as particle 3D coordinates for further processing with in-house scripts written in MATLAB.

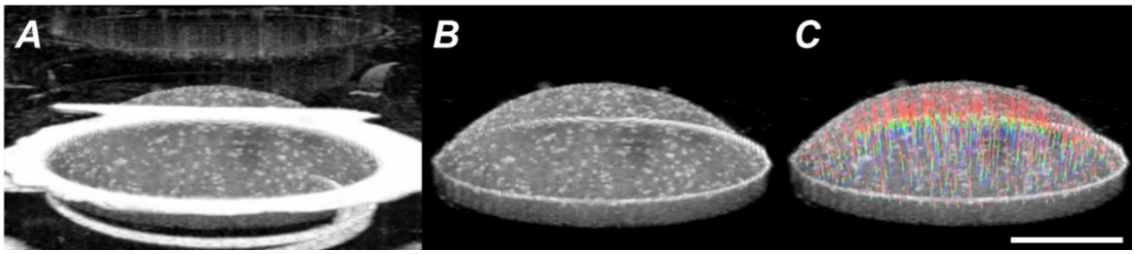


Figure 4.2 A) Original OCT image acquired during the bulge test (CE6) is noisy, with reflections from the TEM grids. B) OCT image after masking reflections from TEM grid. C) Particle tracking of embedded tracers; tracks shown as rainbow lines from the beginning of experiment ("flat" film, not shown) to final frame. TEM grid edge omitted from tracks for clarity. Scale 500 μm.

The TEM grid edge was fit to a 750 μm radius circle in MATLAB and used to correct for drift and center the particles in each pressure step. Following this, all particles (including the "particles" representing the TEM grid) with radial coordinate larger than 700 μm were deleted from the dataset and not used for further processing.

*4.2.2 Fitting displacement fields to obtain deformation gradient*

We next computed discrete displacement fields at each pressure step. Then, following previous approaches by Wu[1] and Geers[2], we used the discrete data to construct continuous, differentiable functions for the displacement field, suitable for the subsequent calculation of displacement gradients.

The following method was used:

The initial condition was sufficiently thin and flat that it provided a unique 2D position vector $\mathbf{X}_1$ for each tracer particle:

$$\mathbf{X}_1 = x\hat{\mathbf{i}} + y\hat{\mathbf{j}} \tag{1}$$

When pressure is imposed the specimen bulges out of plane and the resulting 3D displacement vector $\mathbf{u}$ for the particle originally at position $\mathbf{X}_1$in the initial condition is evaluated at a later pressure step $p$:

$$\mathbf{u}(\mathbf{X}_1) = u(\mathbf{X}_1)\hat{\mathbf{i}} + v(\mathbf{X}_1)\hat{\mathbf{j}} + w(\mathbf{X}_1)\hat{\mathbf{k}} \tag{2}$$

$$\mathbf{u}_{1,p} = \mathbf{X}_{1,p} - \mathbf{X}_{1,0}\ for\ p = 1, 2, 3 \ldots N_p \tag{3}$$

To obtain functional approximations for $u(\mathbf{X}), v(\mathbf{X}), w(\mathbf{X})$ for arbitrary initial position $\mathbf{X}$ at each pressure step $p$, we used moving least squares interpolation, a modified version of global least squares fitting with distance dependent weighting, described below.

The foundation for the analysis is the simpler case of global fitting. For data points given by $\mathbf{X}_i\ , i = 1 \ldots N\ particles$ the observed, scalar output value at each of these points is say, $u(\mathbf{X}_i) = u_i$ and we assume that the data can be approximated by some global polynomial function, $u^h(\mathbf{X})$, where $h$ indicates an approximation. For our data we use a quadratic basis of the form $u^h(\mathbf{X}) = c_0 + c_1x + c_2y + c_3xy + c_4x^2 + c_5y^2$ also written as $u^h(\mathbf{X}) = \mathbf{b}^T(\mathbf{X})\mathbf{c} = \sum_j^m b_j(\mathbf{X})c_j$, where $\mathbf{b}^T$ is a basis vector containing monomials up to the degree $m$ used (here, $m = 2$, $\mathbf{b}^T = [1 \quad x \quad y \quad xy \quad x^2 \quad y^2]^T$) and $\mathbf{c}^T = [c_0 \quad c_1 \quad c_2 \quad c_3 \quad c_4 \quad c_5]$ is the unknown vector of constant coefficients. The unknown coefficients are solved for by minimizing the least square error norm $R$ in Eqn (4) with respect to $\mathbf{c}$.

$$R = \sum_i^N (u^h(\mathbf{X}_i) - u_i)^2 = \sum_i^N \left( \sum_j^m b_j(\mathbf{X}_i)c_j - u_i \right)^2 \tag{4}$$

Moving least squares involves similar steps, except the objective function to be minimized is local, centered at an arbitrary point in the domain, $\widetilde{\mathbf{X}}$,

$$R|_{\widetilde{\mathbf{X}}} = \sum_{i}^{N} w(\mathbf{X}_i - \widetilde{\mathbf{X}})(u^h(\mathbf{X}_i) - u_i)^2 = \sum_{i}^{N} w(\mathbf{X}_i - \widetilde{\mathbf{X}}) \left( \sum_{j}^{m} b_j(\mathbf{X}_i) c_j - u_i \right)^2 \quad (5)$$

with a weighting function $w$ that varies with distance from the point of interest. Specifically, $w$ is ~1 for particle neighbors close to $\widetilde{\mathbf{X}}$ and decays to 0 farther away. We use the following exponentially decaying weight function[3] that successfully fit indentation strain fields in hydrogels[1].

$$w(\mathbf{X}_i - \widetilde{\mathbf{X}}) = \begin{cases} \dfrac{e^{\left(1 - \frac{d^2}{d_{cutoff}^2}\right)} - 1}{e - 1}, & d < d_{cutoff} \\ 0, & d \geq d_{cutoff} \end{cases} \quad (6)$$

where $d$ is the Euclidean distance between $\mathbf{X}_i$ and $\widetilde{\mathbf{X}}$ and $d_{cutoff}$ is a cutoff distance. Unless specified, $d_{cutoff}$ was set at 200 μm. Linear interpolation was used to generate additional data points as a mesh in 10 μm increments that stabilized the fitting. Final datasets shown below were only evaluated at particle locations, and all calculations were performed with a shifted basis centered at the point where the properties were being evaluated.

Once we performed the moving least squares interpolation, we now had functional approximations for $u^h(\mathbf{X})$, $v^h(\mathbf{X})$, and $w^h(\mathbf{X})$. Using the same protocol and weights, we also fit a local surface centered at each particle $z(\mathbf{X})$.

We then calculated the deformation gradient tensor

$$\bar{\bar{\mathbf{F}}}.\bar{\bar{\mathbf{F}}} = \mathbf{I} + \begin{bmatrix} \frac{\partial u^h}{\partial x} & \frac{\partial u^h}{\partial y} & 0 \\ \frac{\partial v^h}{\partial x} & \frac{\partial v^h}{\partial y} & 0 \\ \frac{\partial w^h}{\partial x} & \frac{\partial w^h}{\partial y} & 0 \end{bmatrix} \tag{7}$$

Right Cauchy-Green deformation tensor $\bar{\bar{\mathbf{C}}}$ whose eigenvalues are the principal stretches $\lambda_1, \lambda_2, \lambda_3$ (in the meridional, circumferential, and thickness direction in the ideal case):

$$\bar{\bar{\mathbf{C}}} = \bar{\bar{\mathbf{F}}}^T \bar{\bar{\mathbf{F}}} \tag{8}$$

Components of the in-plane 2D Green strain tensor $E_{11} = \frac{1}{2}(\lambda_1^2 - 1)$ and $E_{22} = \frac{1}{2}(\lambda_2^2 - 1)$ were also calculated.

The curvature tensor $\boldsymbol{\kappa}(\mathbf{X})$ is calculated as the spatial gradient of the normal vector field $\nabla\mathbf{n}(\mathbf{X})$ which in turn is calculated as the normalized gradient of the position field:

$$\mathbf{n}(\mathbf{X}) = \frac{\nabla z(\mathbf{X})}{\left|\left|\nabla z(\mathbf{X})\right|\right|} \tag{9}$$

The eigenvalues of the curvature tensor are the principal curvatures $\kappa_1$ and $\kappa_2$, where $\kappa_1$ is in the meridional direction and $\kappa_2$ in the circumferential orientation.

*4.2.3 Stress resultants*

We followed procedures from[4,5] to calculate the local principal stress resultants (in N/m, defined per unit undeformed length rather than unit area), as the following:

$$T_1 = \frac{P}{2\kappa_2} T_2 = \frac{P}{\kappa_2}\left(1 - \frac{\kappa_1}{2\kappa_2}\right) \quad (10)$$

where $T_1$ and $T_2$ correspond to stress resultants in the meridional and circumferential directions respectively, $P$ is applied pressure in the bulge test, and $\kappa_1$ and $\kappa_2$ are principal curvatures in the meridional and circumferential directions respectively, at each particle location, calculated from the geometry of the bulged sample at each pressure step (for more details, see:[2,4–7]). Prior to final plotting, a histogram of particle displacement magnitude was plotted between the first pressure step and a pressure value common to all biofilms and the top 5% of displacement magnitudes were manually inspected for outliers (Fig. S4-5); particles that traveled in a direction inconsistent with continuum mechanics were removed and neglected from further analysis.

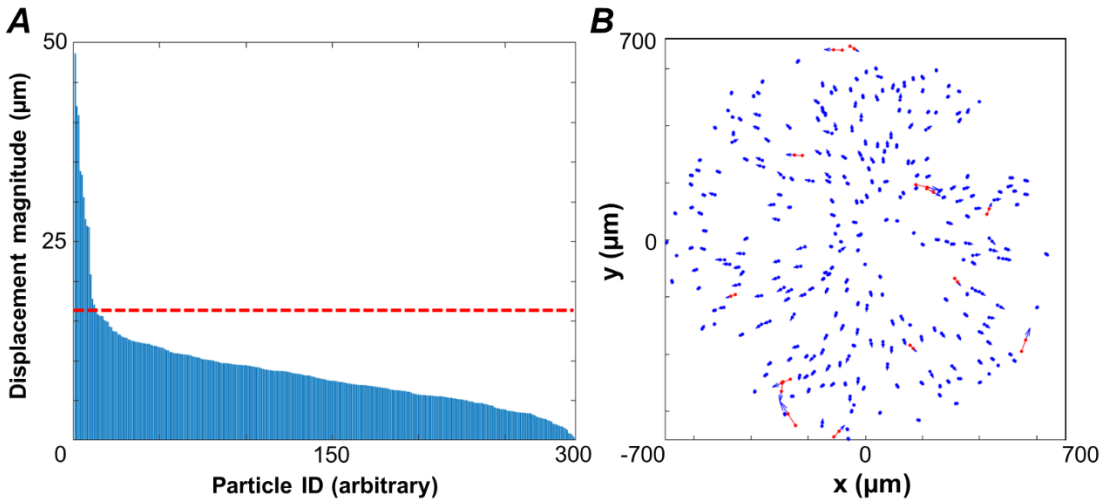


Figure 4.3. Representative protocol for inspection of outliers. A) Absolute value of displacement of all particles sorted and plotted as a bar chart (here, for CE6). Cutoff value based on top 5% is identified (here, 15.67 µm, red dashed line) for manual inspection. B) Outliers are removed from analysis if they do not adhere to continuum mechanics. Initial and final positions of particles (blue) with outliers highlighted (red); displacement vector between the two positions.

### 4.3 Results

A typical set of bulge test frames (volumetric images) is as below in Figure 4.4 for both E6 and CE6. Consistent with the 2D analysis, E6 failed within the pressure ranges imposed by the bulge test while CE6 did not. The following sections will discuss results from both E6 and CE6 in further detail.

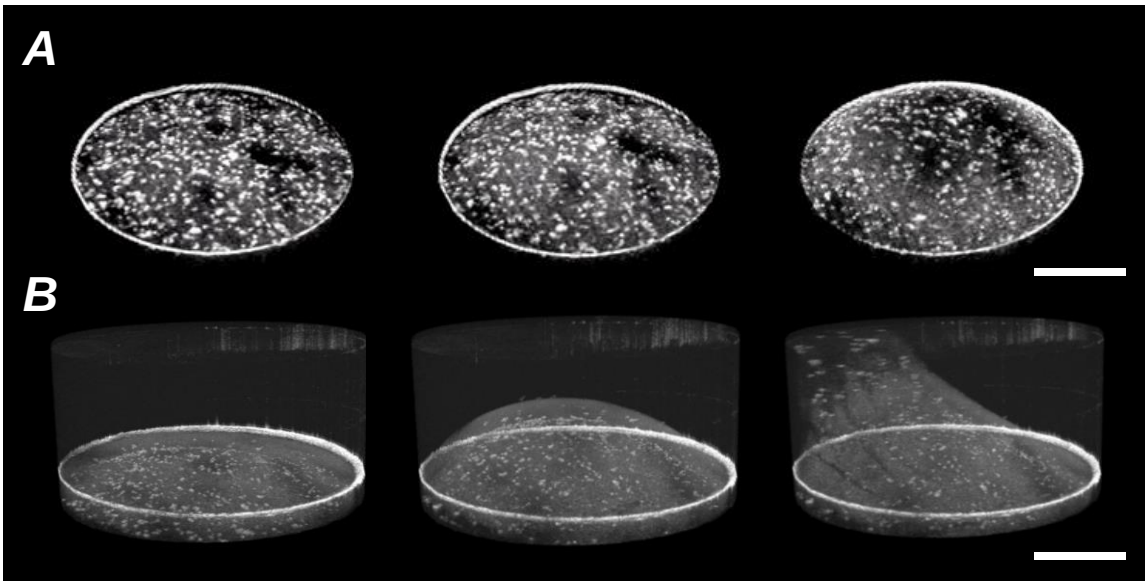


Figure 4.4. Typical 3D (Imaris-processed) OCT images (at various frames of the bulge test) used for particle tracking and downstream analysis. A) CE6 does not fail within the limits of the bulge test, similar to that observed in Chapter 3, while B) E6 does fail. Non-pole failure of E6 discussed in main text. Arbitrary frames chosen to highlight evolution of inflated shape as test proceeds. Contrast adjusted to highlight embedded microspheres. Scale 500 μm. 7 day sample growth; stepwise loading protocol; $\Delta P$ = top: 0, 135, 1048 Pa; bottom: 0, 135, 285 Pa.

*4.3.1 CE6 is homogeneous*

Our analysis first turns to CE6, a biofilm whose properties were detailed in Chapter 2: using 2D analysis, the film was found to have a modulus of 44.0 ± 5.63 kPa and consistently did not fail within the pressure regimes imposed by our test.

In this section, we instead use the 3D analysis described above, with the ultimate goal of i) comparing properties and the validity of the assumptions made with our 2D method and ii) assessing whether CE6 is homogeneous.

Initially, we calculated principal stretches and the eigenvectors corresponding to each orientation of stretch. These were ordered from maximum to minimum value of stretch indicated by a color in the corresponding orientations (Figures 4.5-4.10; final two frames are at a higher pressure–300 and 450 Pa higher pressure difference than the previous frame). The maximum stretch was consistently in the meridional orientation, followed by a stretch in the circumferential direction, with a reduction in thickness represented by $\lambda < 1$ (Figure 4.9-10). The top view images enable a comparison of stretch as a function of radial coordinate, while the oblique view images confirm the 3D orientation of each stretch.

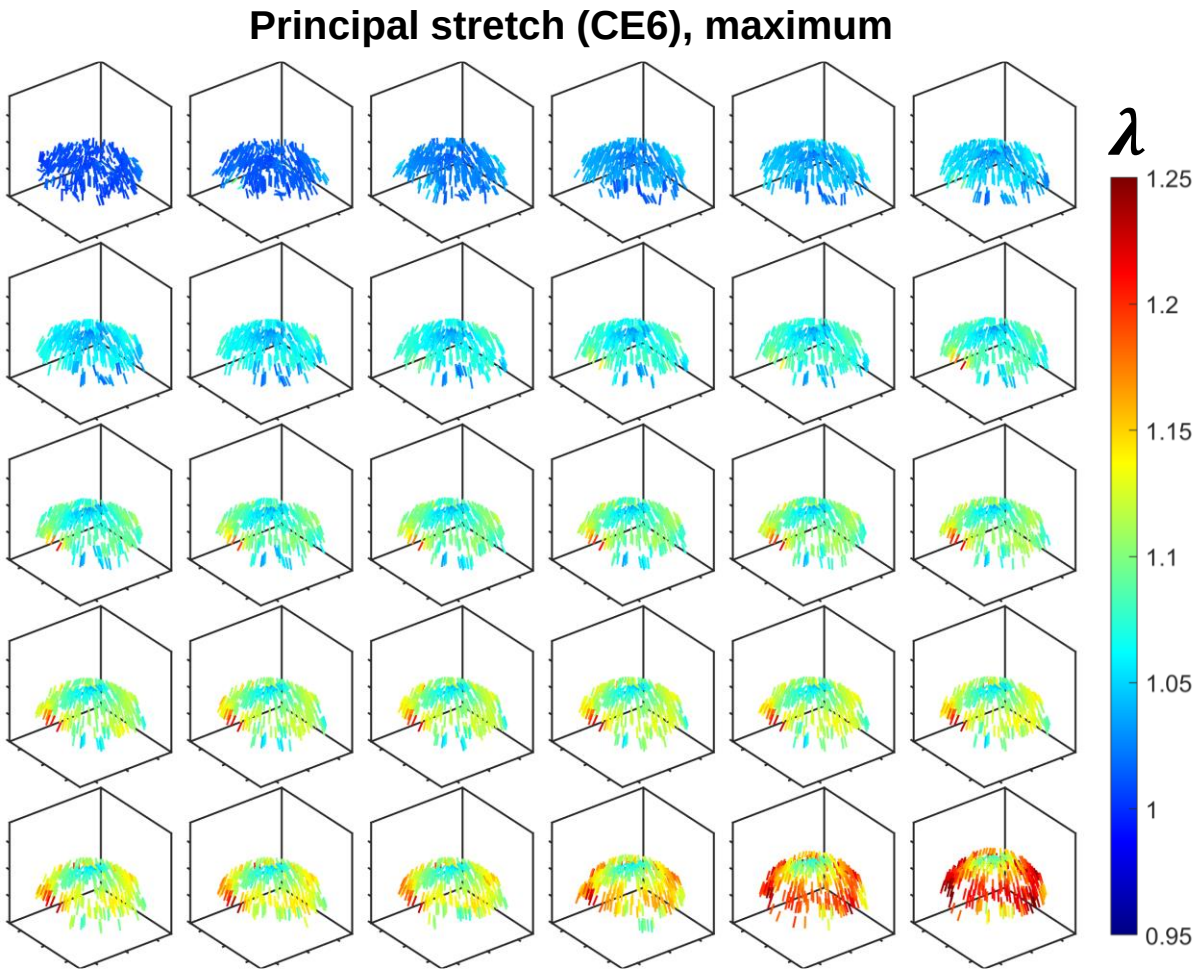


Figure 4.5. Maximum principal stretch, oblique view. Note: last two frames are at a higher pressure difference.

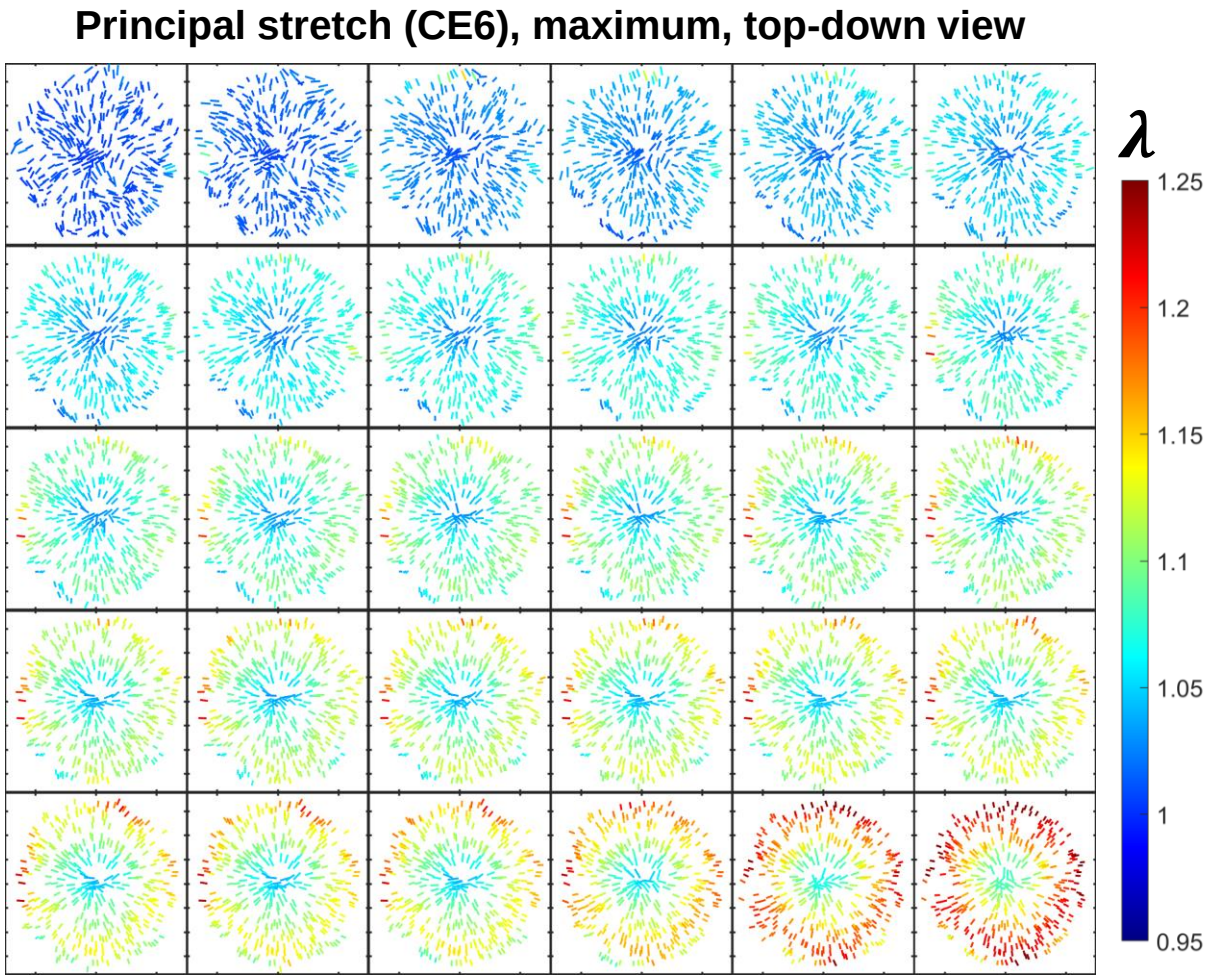


Figure 4.6. Maximum principal stretch, top-down view. Note: last two frames are at a higher pressure difference.

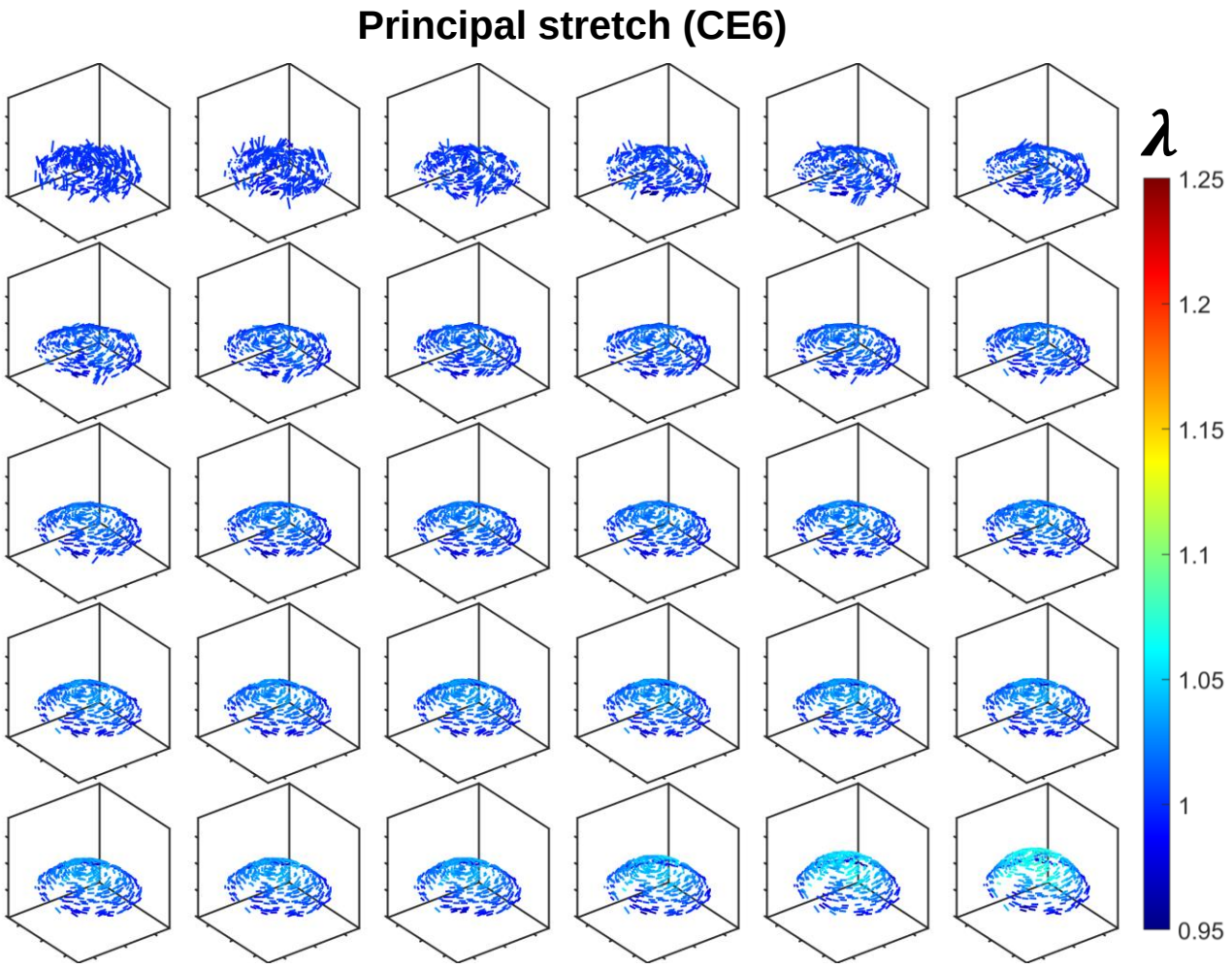


Figure 4.7. Medium principal stretch, oblique view. Note: last two frames are at a higher pressure difference.

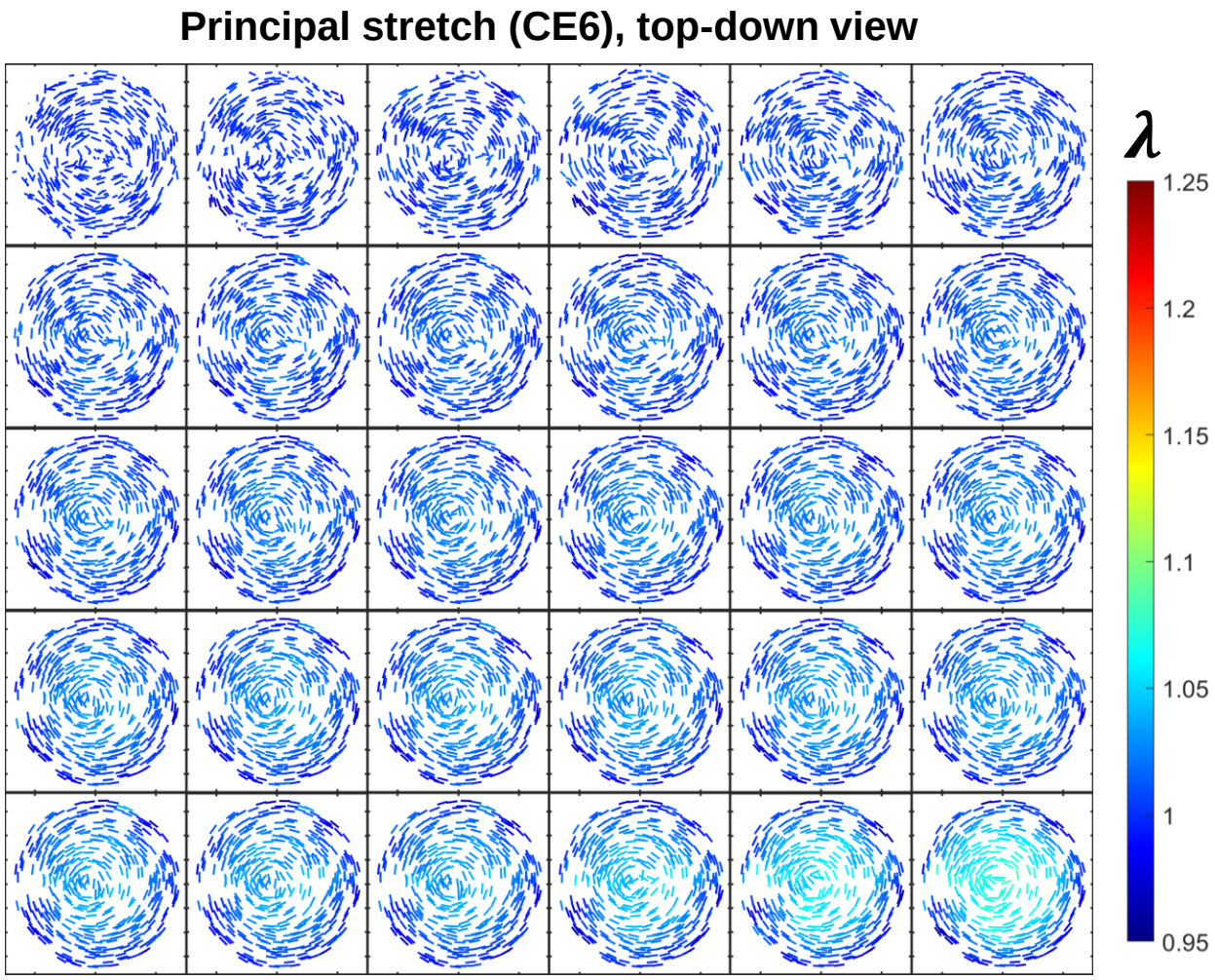


Figure 4.8. Medium principal stretch, top-down view. Note: last two frames are at a higher pressure difference.

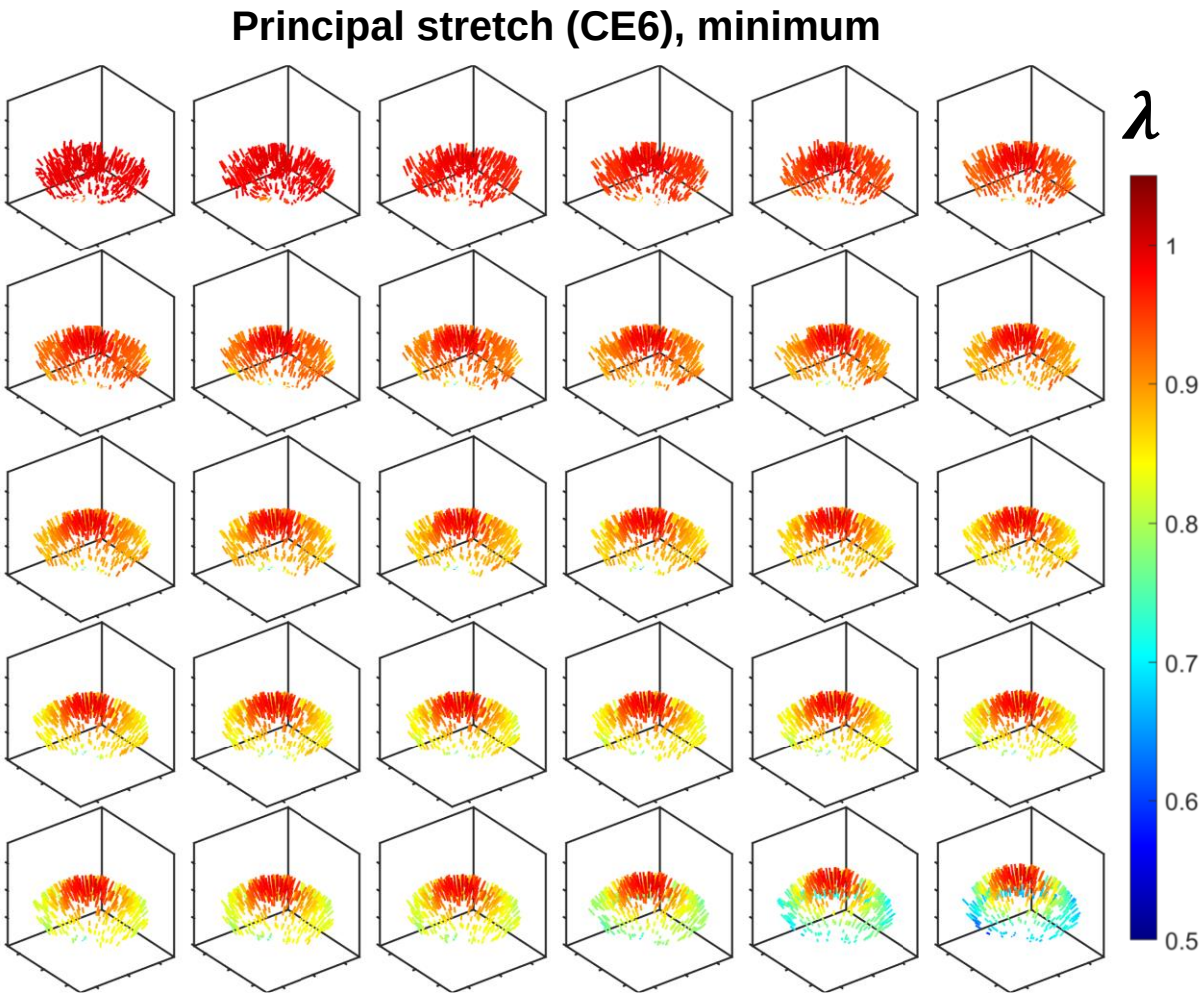


Figure 4.9. Minimum principal stretch, oblique view. Note: last two frames are at a higher pressure difference.

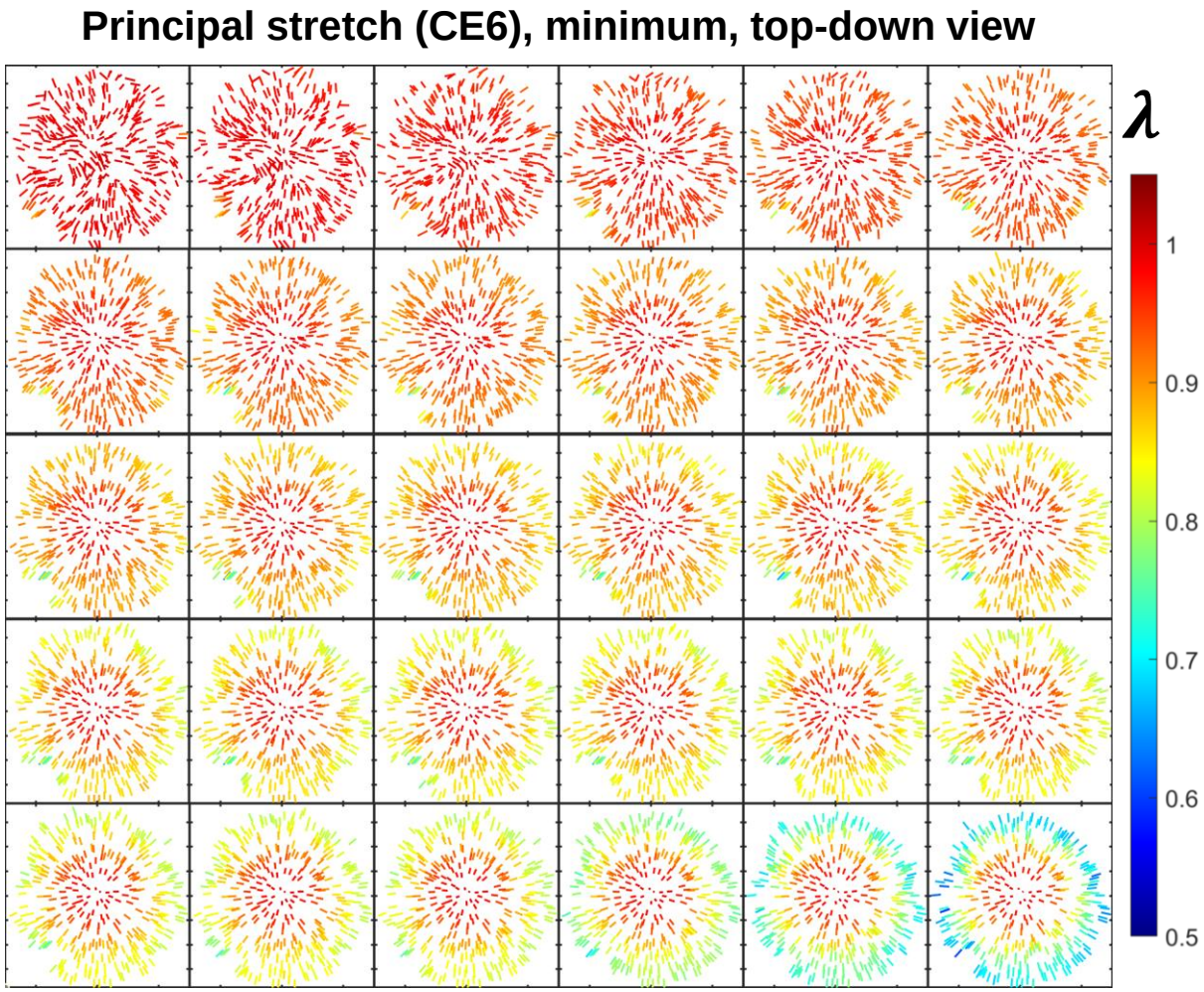


Figure 4.10. Minimum principal stretch, top-down view. Note: last two frames are at a higher pressure difference.

Similar plots for stress resultants $T_1$ and $T_2$ (Figures S2-S3) can be used to observe the variation of stress as a function of radial coordinate.

Below is another (graphical) way to broadly analyze the types of deformations occurring from center to edge; here we also consider E6.

At the pole: principal stretches $\lambda_1$ (meridional) and $\lambda_2$ (circumferential) were plotted for all microspheres within a 100 μm radius of the pole in the first, undeformed frame for E6 (Figure 4.11A) and CE6 (Figure 4.11B). While E6 shows close to equibiaxial deformation at the pole across all the frames (at frames 5, 10, and 25, the variation between principal stretches was as follows: 1.05-1.068, 1.085-1.11, 1.251-1.29), CE6 exhibits a similar or larger variation between the two principal stretches (at the same frames: 1.03-1.07 1.08-1.12, 1.13-1.17). This was expected as CE6 is stiffer than E6 and hence is likely to have a slight bending stiffness rather than purely in-plane stresses. Also, in the case of CE6, only one microsphere was within 50 μm of the center, biasing the results towards points farther away. Further plotting the properties at Frames 5 and 25 of the bulge test (arbitrarily chosen to represent early and late frames of the test) for E6 showed that as the test proceeded, the assumption of equibiaxial deformation became less valid and the discrepancy between the principal stretches increased rapidly (Figure 4.12 A-B). In the early frames of the bulge test the equibiaxial assumption is valid up to ~200 μm from the center, but this radius drops to < 100 μm by the end of the test.

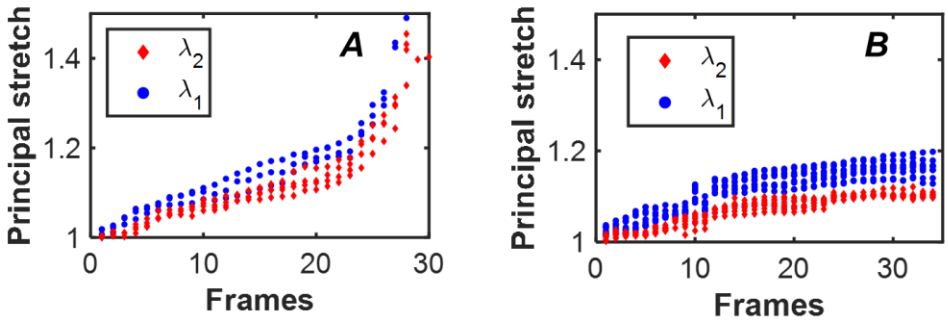


Figure 4.11. A) E6 shows equibiaxial deformation at the pole throughout the bulge test while B) CE6 shows a similar or larger variation between principal stretches.

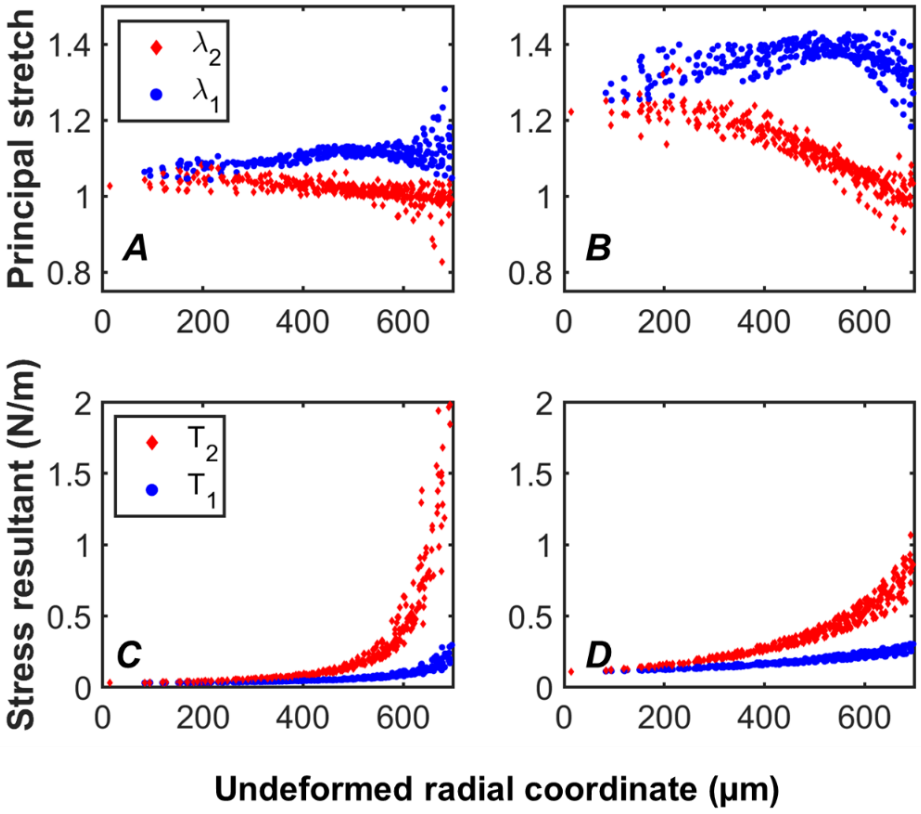


Figure 4.12. Principal stretches (A, B) and stress resultants (C, D) for E6 at Frames 5 (A, C) and 25 (B, D).

With this, four sets of $E$ vs $T$ plots were possible: $E_{11}$ vs. $T_1$ or $T_2$, and $E_{22}$ vs. $T_1$ or $T_2$, where the subscripts "1" and "2" indicate meridional and circumferential orientations respectively (Figure 4.13).

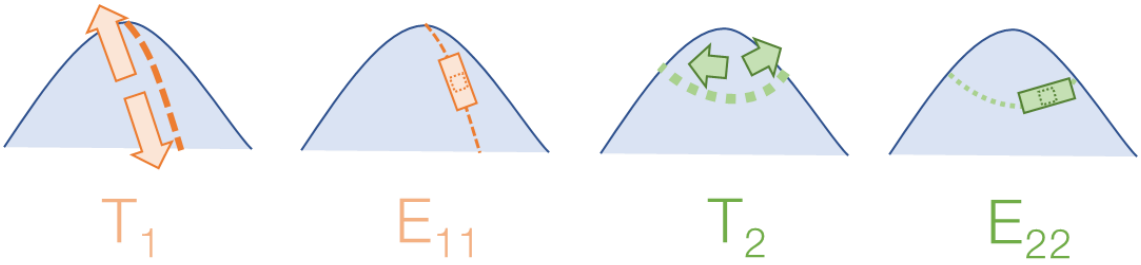


Figure 4.13. Cartoon of quantities plotted and their relative orientations. "1" in further text indicates the meridional orientation, while "2" indicates the circumferential orientation.

Due to the variation in deformation from center to edge, we organized the data according to radial coordinate in roughly 150 μm increments (Figures 4.14-4.17; "r" indicates radial coordinate from 0 at the center, increasing outwards). Fitting quality decreased near the clamped edge and as such data after 600 μm from the center is not shown below. These plots now give us a full picture of the properties of the films as they vary from center to edge–that is, "modulus mapping" across the film, and we can use this information to i) directly observe how the deformation changes from the center to the edge, ii) assess whether the biofilm is isotropic, and iii) evaluate the presence or absence of heterogeneities. Also, in addition to the limited discussion below, visual observation of the $E_{11}$ vs. $T_1$ or $T_2$ or $E_{22}$ vs. $T_1$ or $T_2$ relationships can inform the choice of a suitable strain energy density function that can be used to quantify the effects of engineering or changes due to heterogeneities.

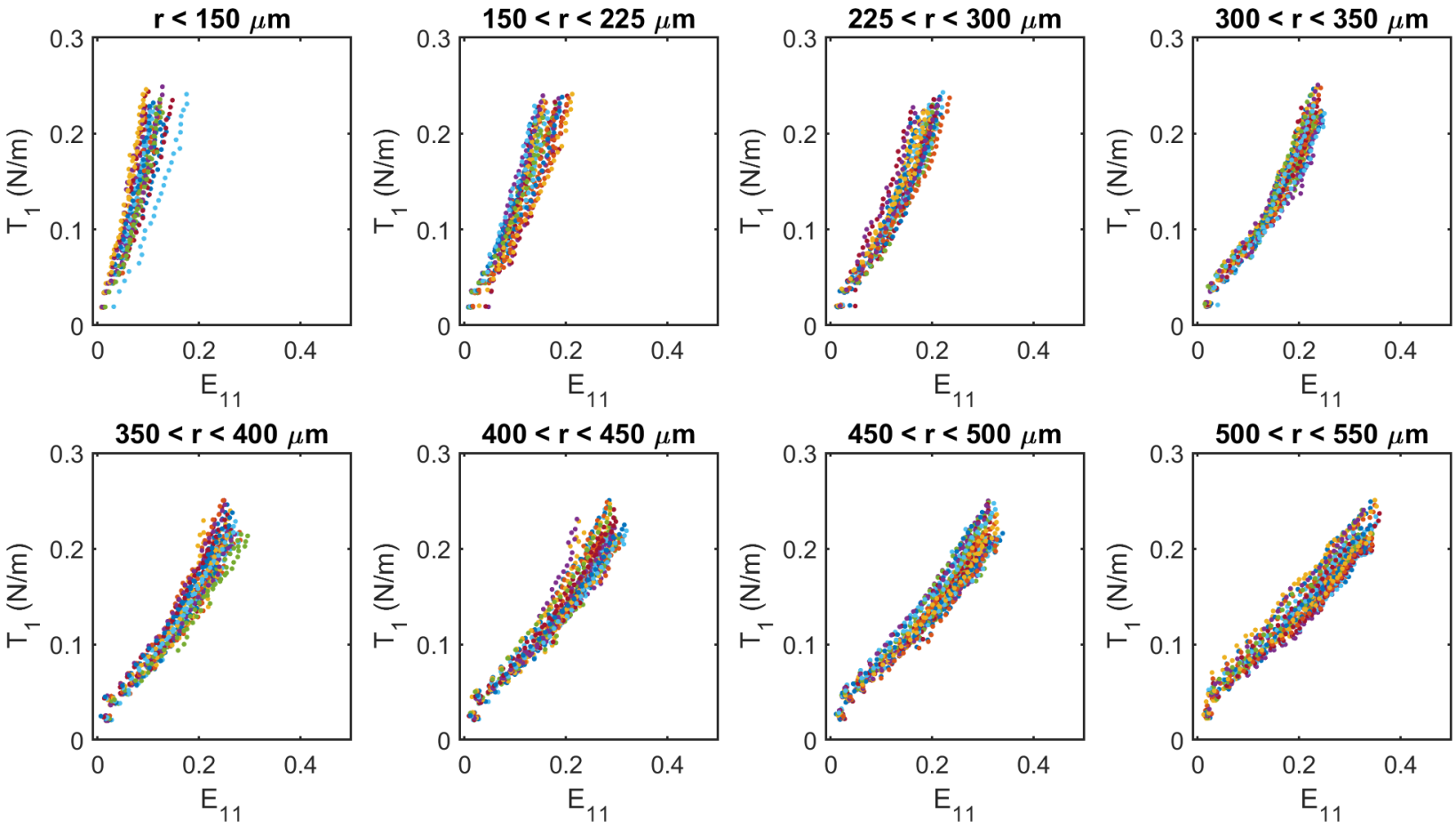


Figure 4.14. Meridional component of Green strain ($E_{11}$) vs. meridional stress resultant ($T_1$).

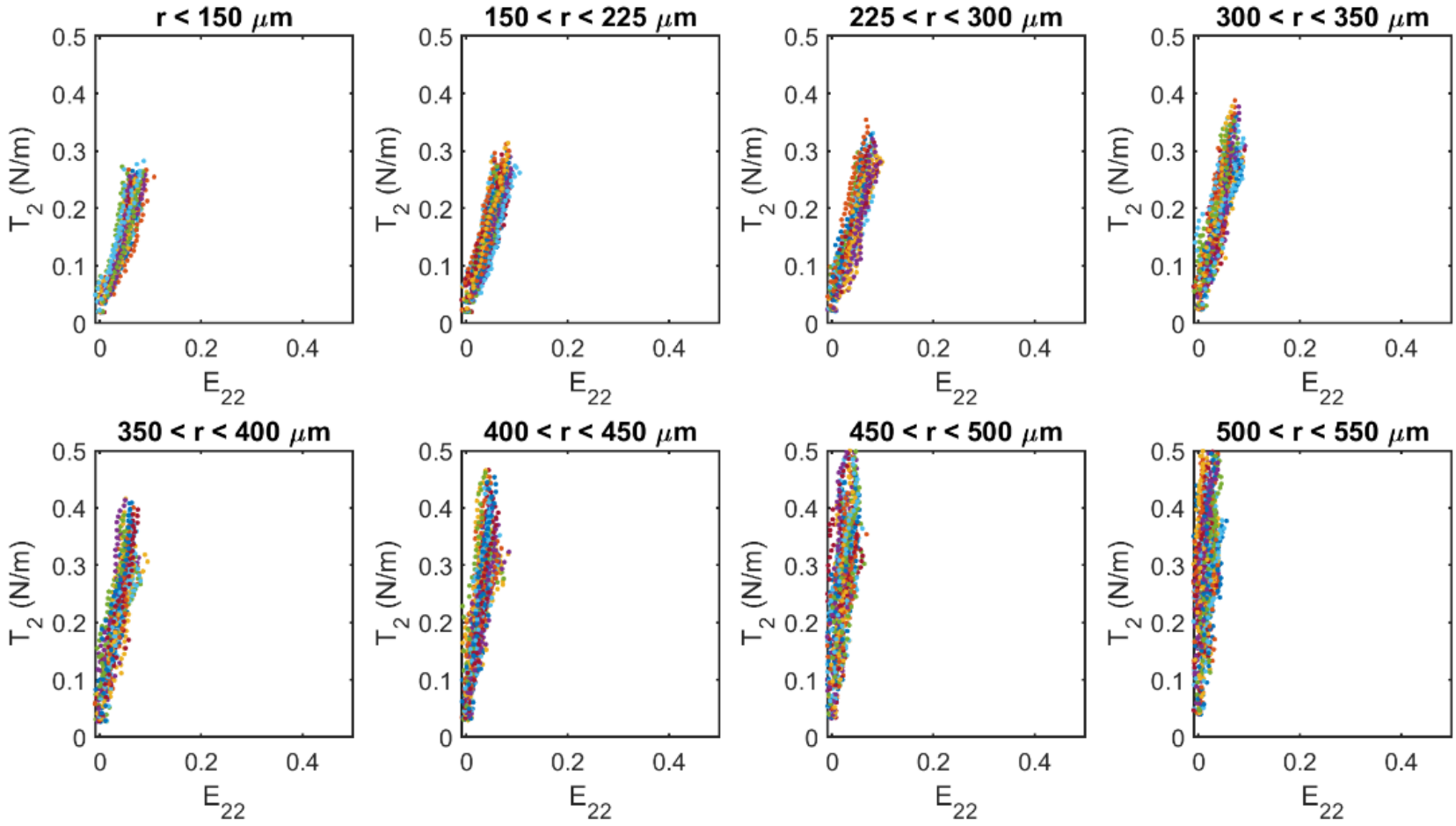


Figure 4.15. Circumferential component of Green strain ($E_{22}$) vs. circumferential stress resultant ($T_2$).

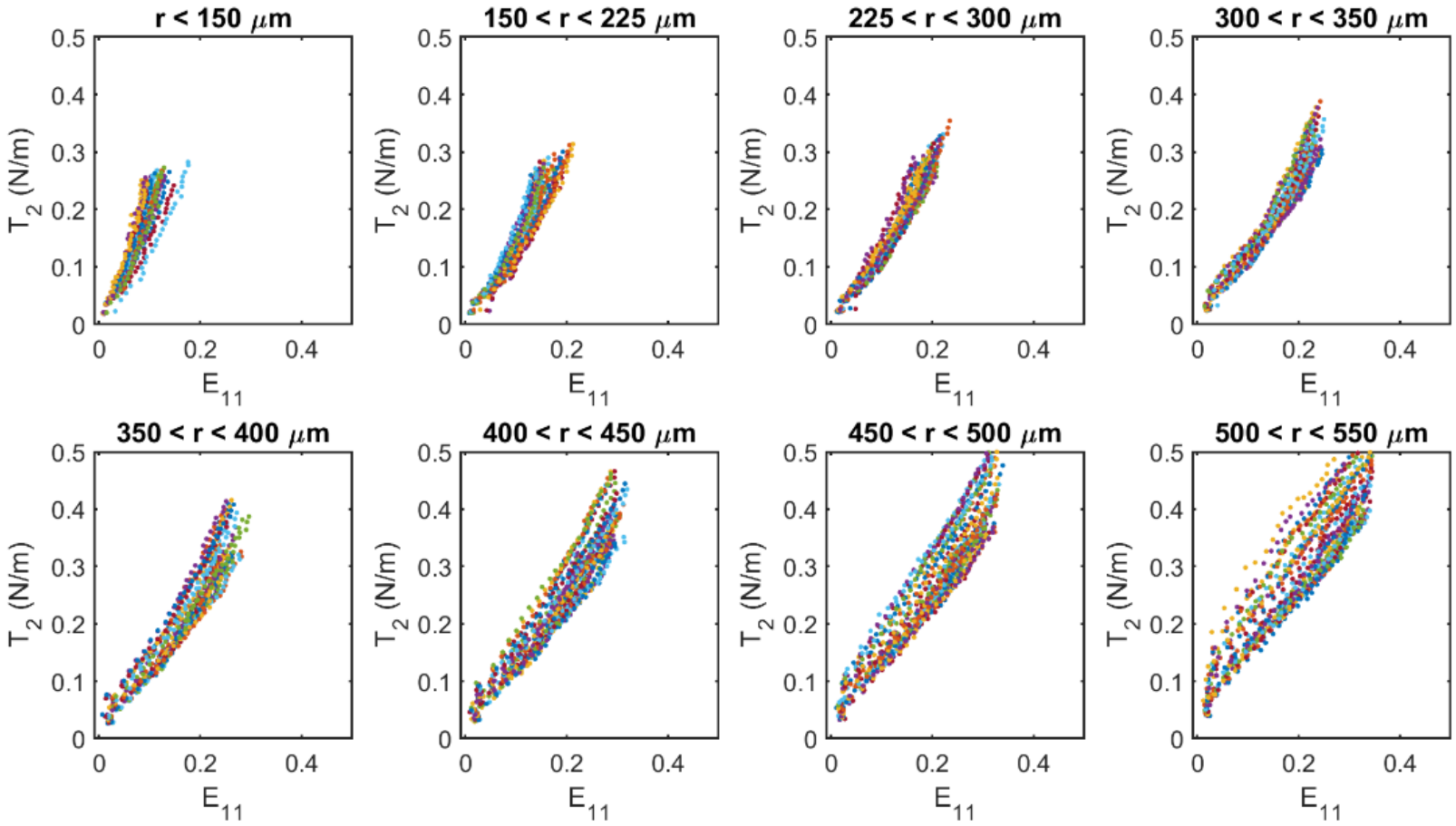


Figure 4.16. Meridional component of Green strain ($E_{11}$) vs. circumferential stress resultant ($T_2$).

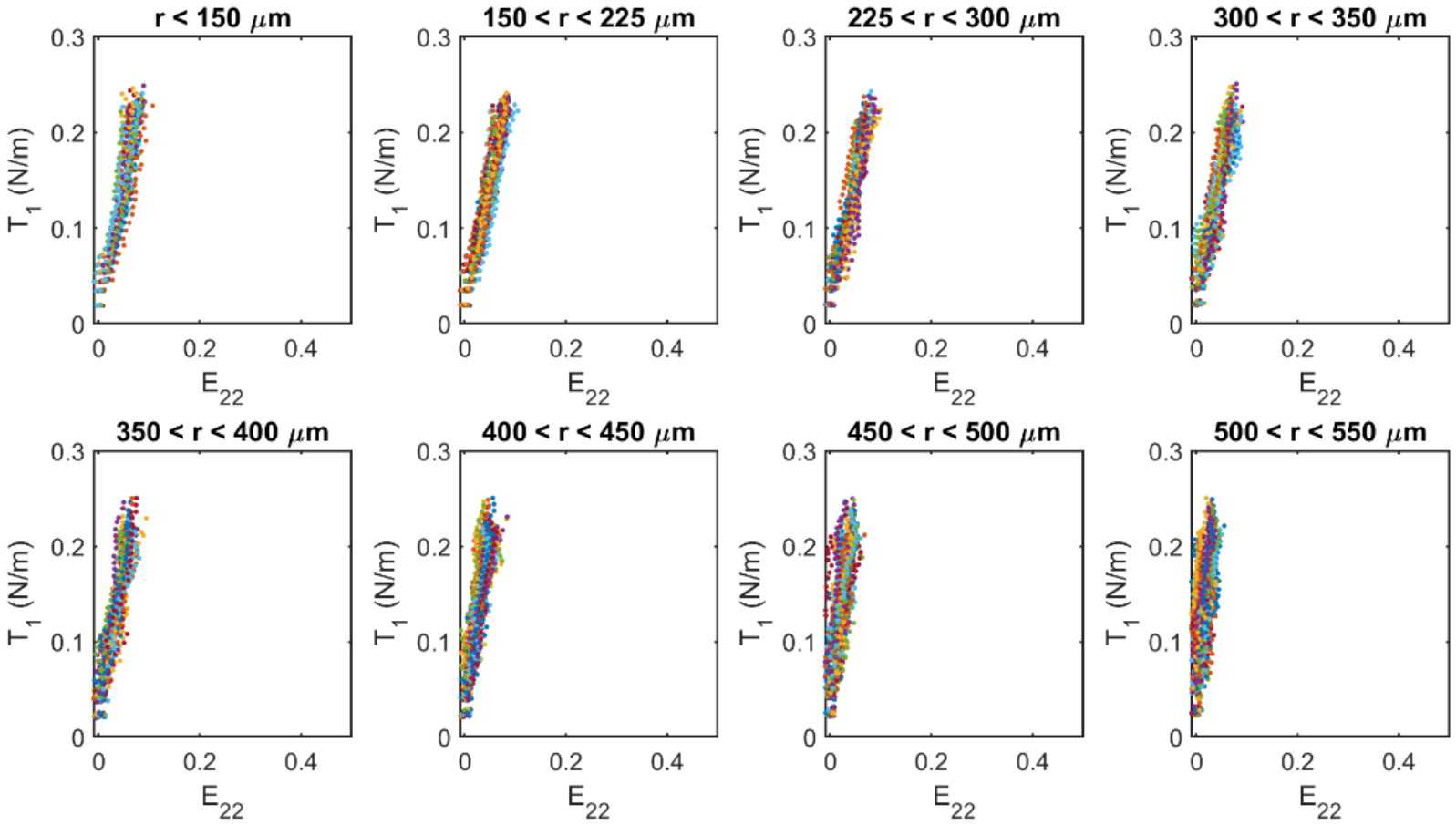


Figure 4.17. Circumferential component of Green strain ($E_{22}$) vs. meridional stress resultant ($T_1$).

Subsets of the plots from Figures 4.14-4.17 can be used to answer (i) and (ii) above. Near the center, $E_{11} \sim E_{22}$ (equibiaxial deformation at the center) and the variation of $T_1$ with $E_{11}$ and $E_{22}$ is similar to that of $T_2$ with $E_{11}$ and $E_{22}$, suggesting that the biofilm exhibits an isotropic response to equibiaxial deformation (Figure 4.18A). Closer to the clamped edge of the film, $E_{22}$ approaches 0, suggesting a transition to a constant width elongation (Figure 4.18B).

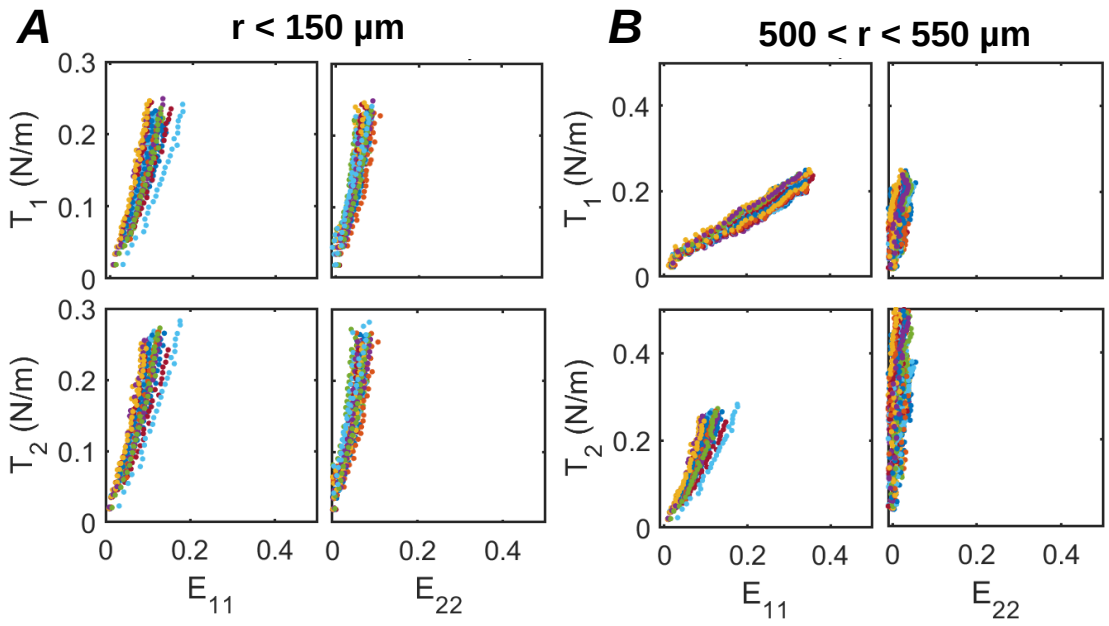


Figure 4.18 A) CE6 displays an isotropic response to equibiaxial stretching at the pole; B) circumferential strain approaches zero near the clamped edge.

From these plots (and others; N = 7 from three biological replicates), CE6 also appears to be fairly homogeneous based on the narrow distribution of traces within a given range of radial coordinates, an idea that is revisited in the later section comparing CE6 to E6. Finally, since we can now confirm that the pole undergoes an equibiaxial stretch, the properties at the pole can be compared with results from the 2D analysis ($T$ vs $(\lambda - 1)$ plots

not shown). In the above sample, the modulus ranges from 24.5 to 37.7 kPa, a fairly large range. Considering multiple samples, the range expands to 35.3 ± 2.54 kPa (highest) to 17.6 ± 1.98 kPa (lowest), although it is worth noting that the broadness is also due to all particles within 150 μm of the center being considered. The highest values are about 10 kPa lower than those predicted by our 2D method.

*4.3.2 Revisiting the effects of engineering: E6 vs. CE6*

In Chapter 3, we used E6 and CE6 as model biofilms to demonstrates insights that our method could yield into the effects of engineering on modulus and failure. We revisit this idea with the 3D analysis described above. As suggested by the off-pole failure in Figure 4.4B, we wondered whether E6 may be heterogeneous. E6 biofilms (N = 4, across three biological replicates) were analyzed using the same protocol as described for CE6. Results are reported below (Figure 4.19) for three examples, one from each biological replicate (Figure 4.19B-D), and compared to CE6 (Figure 4.19A). For clarity, only $E_{11}$ vs. $T_1$ plots are shown at a comparable radial coordinate ($225 < r < 300\ \mu m$) but a full dataset is included in Figure S4 (supplemental).

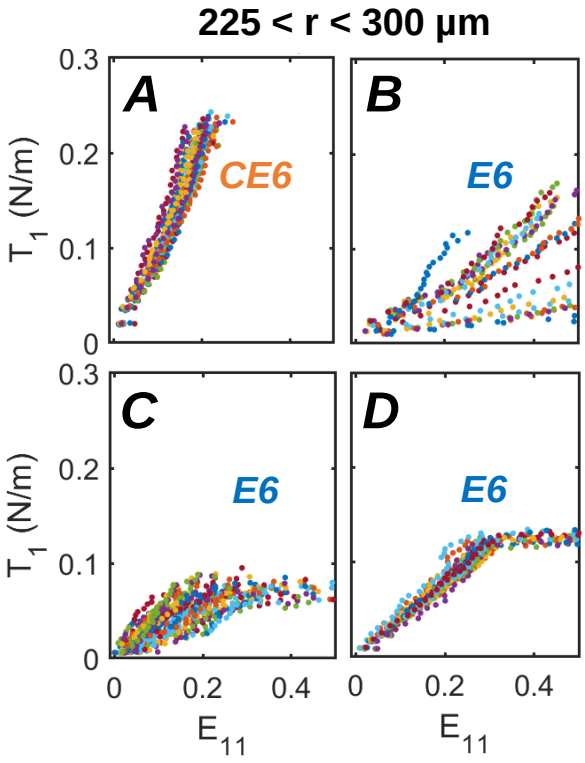


Figure 4.19. E6 films (B-D) are less stiff and more heterogeneous than CE6 films (A).

The first feature evident in Figure 4.19 is the variability of E6 relative to CE6, represented by the narrow distribution of traces for CE6 within a given radial section, in contrast to the broad "fan" of traces in E6, especially in Figure 4.19B-C. This suggests the presence of heterogeneities, where shallower traces (with a lower slope) should theoretically correspond to weaker regions of the biofilm. The second aspect is that of stiffness: in agreement with our 2D results, CE6 is stiffer than E6, represented by the steeper slope overall of all traces within a radial section. Finally, all E6 films in the above experiments failed between $E_{11}$ ~ 0.4 and 0.8, while CE6 did not fail within our imposed range of pressures.

Thus, using our 3D method, we can conclude that not only does the addition of the cysteine residue in engineering E6 to CE6 result in biofilms that are stiffer and stronger, but also ones that are more homogeneous!

*4.3.3 Physical implications of heterogeneity*

One aspect that stands in the above comparison of E6 vs. CE6 out is whether or not a biofilm fails at the pole. We investigate this question below, together with the closely related question: are these apparent heterogeneities real, and do they correspond to any physical features in the biofilm?

The properties plotted in Figure 4.19D have a narrow distribution similar to that of CE6. This film fails at the pole, which is the expected mode of failure for a homogeneous material undergoing the bulge test (Figure 4.20).

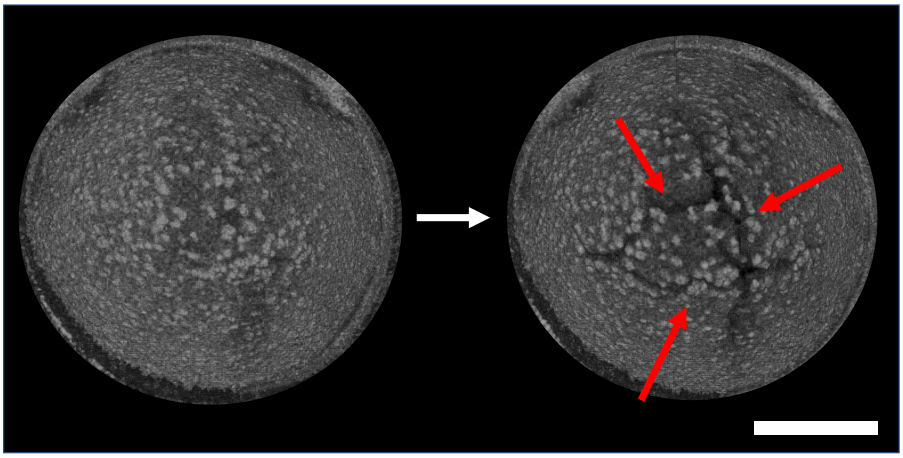

Figure 4.20. Homogeneous E6 (initial frame, left) fails at the pole (red arrows, right). Scale 500 µm. Top view OCT images. 7 day sample growth; stepwise loading; $\Delta P$ = 495 (left), 510 (right) Pa.

On the other hand, the data in Figure 4.19C exhibiting a broad spread corresponds to the film shown in Figure 4.4B (whose failure is clearly off-center, and in the central frame, develops an asymmetric dome shape).

Taken a step further, the shallow traces in highly heterogeneous datasets should correspond to weaker regions of the biofilm. We investigated this idea for the film in Figure 4.19B. Locating the particles responsible for the shallow traces across all radial positions revealed that they are clustered together in space (Figure 4.21, right, red) near the region of eventual crack formation in the biofilm.

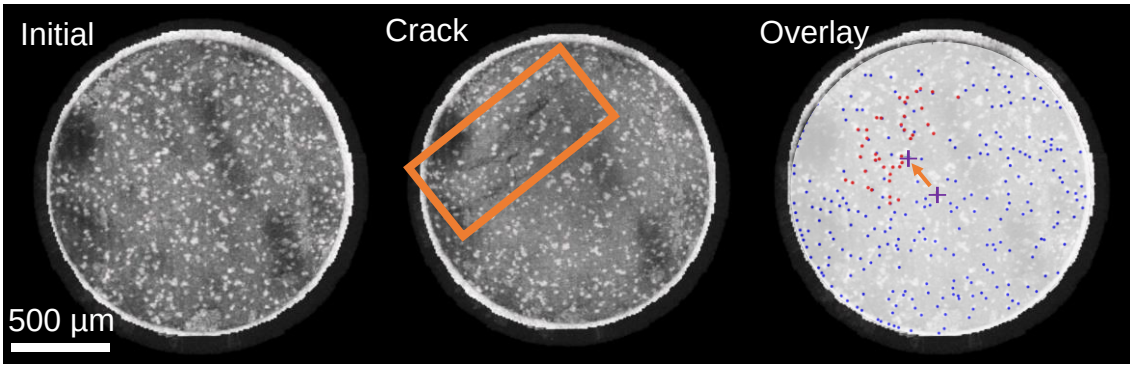


Figure 4.21. Heterogeneities do correspond to physical features. Top view OCT images of an E6 biofilm (from Figure 4.19B) as it evolves from the initial frame (left) to the first crack (center). Overlay of particle positions with shallow sloped heterogeneities highlighted in red (right) shows that failure off-pole occurs in weaker regions of the biofilm. Purple cross indicates movement of peak position through frames resulting in dome asymmetry. 7 day sample growth; stepwise loading; $\Delta P = 0$ (left), 315 (right) Pa.

### *4.3.4 The 3D bulge test for insights into biofilm healing*

Chapter 3 briefly covered the use of the (2D) bulge test to quantify healing in a living material, with the goal of characterizing the recovery of mechanical properties. Using the bulk analysis described, we were able to broadly comment on i) the ability of a healed film to hold a pressure difference and ii) the modulus and toughness. In the process, we also

discovered that healed films failed at lower stresses than control films; however, we could not characterize the failure in detail, since we lacked markers for different regions of the film. We also could not assess whether, as a result of the defect creation and healing process, the healed films developed regions of heterogeneity or differences in mechanical response.

Here, with the 3D method, we explore healing once again, this time in more detail.

The healing experiment was set up similarly to the setup described in Chapter 3 (Figure 4.22); LB was used as the nutrient medium for the tracer containing films. 2YT plates resulted in films that were insufficiently healed after 24 hours and excessively thick (and where the embedded microspheres could not be clearly distinguished under OCT) after 48 hours; LB plates resulted in films that healed in 48 hours with microspheres that were still visible enough for tracking and subsequent calculations. All healing experiments were performed with CE6 biofilms that were grown using the protocol described previously. Tested films are denoted Day 0 (“original”) and Day 2 (“control” and “healed”)–see Figure 4.23 (OCT images of healing and control).

OCT imaging was performed for all films immediately after they were placed on the LB plate (for films with defects, immediately following the cutting process) and then once again after 48 hours, using the 3D printed holder (Figure 4.22B) and OCT ThorImage software to align the scan locations. In addition to the scans shown in Figure 4.23, a 1.5 x 1.5 mm x 1 mm scan was taken for each film near the center at high resolution (oversampled) to visualize the microsphere positions and enable alignment between the bulge test images and OCT scans of the films on the agar prior to their testing. These scans

were preferable to the lower resolution (Figure 4.23, top row) images where microspheres could not be visualized clearly. In later text describing the manual alignment of the two types of images, “bulge test images” and “OCT images (agar)” refer to the images described above.

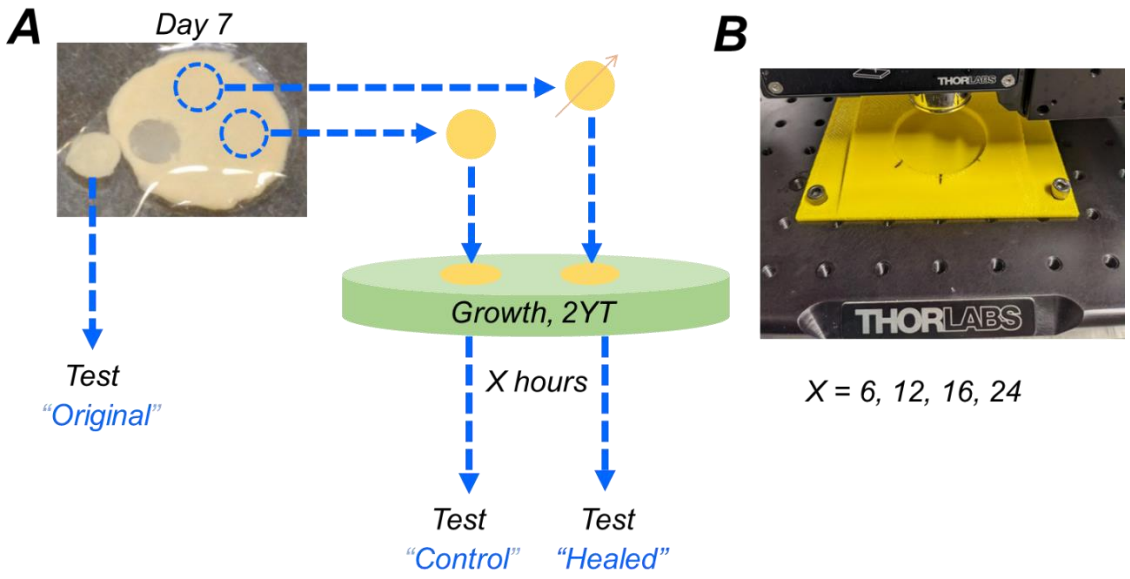


Figure 4.22. A) Schematic of biofilm healing experiment. B) 3D printed petri dish holder fixed to OCT base plate.

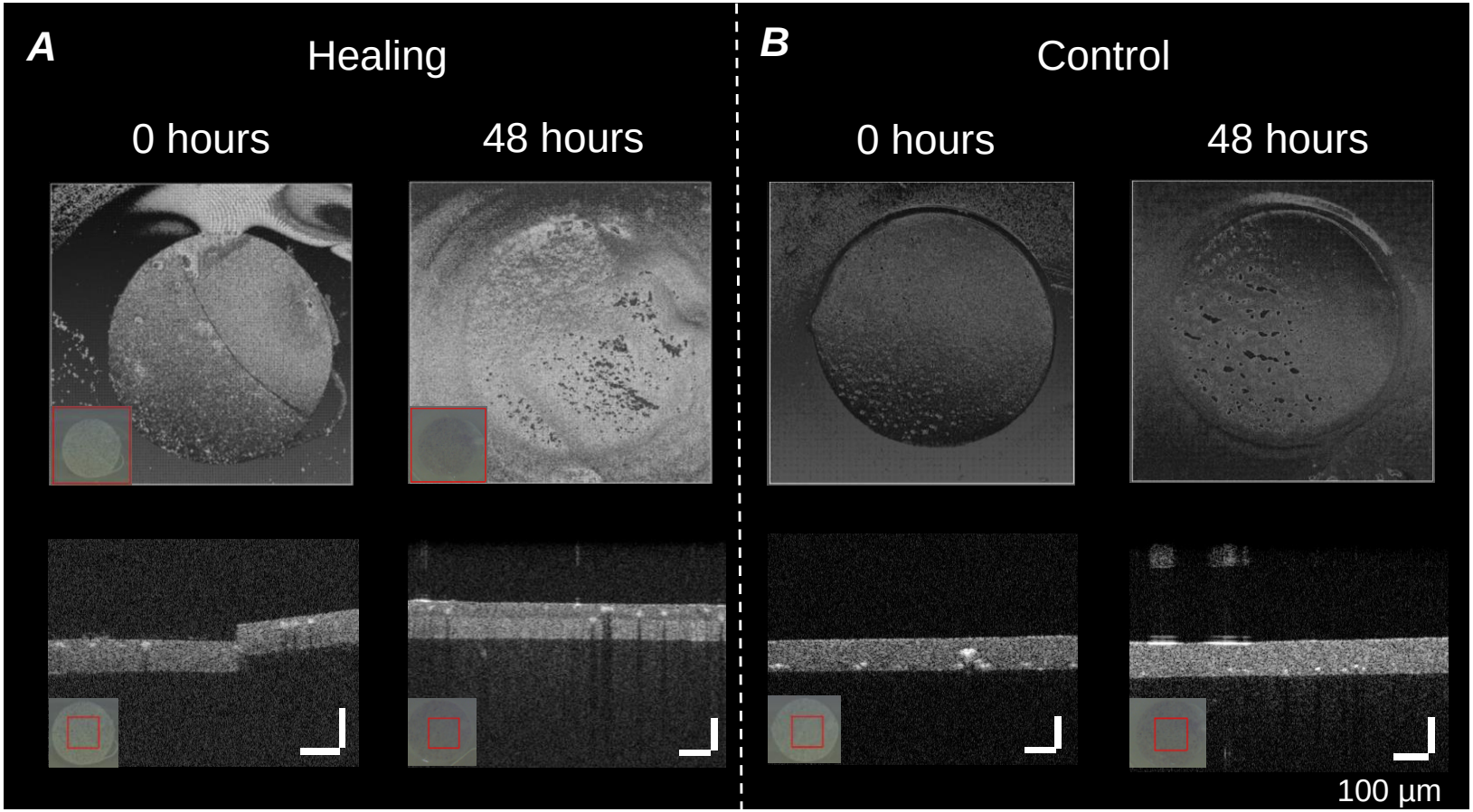


Figure 4.23. OCT scans of cut and healed (A) biofilm immediately after defect creation (A, left), after 48 hours (A, right). B) Control biofilm initially (B, left) and after 48 hours on LB nutrient agar plate (B, right). Top row: top view 3D OCT scans with camera inset (bottom left, red outline). Bottom row: 2D cross sectional image showing healing of defect.

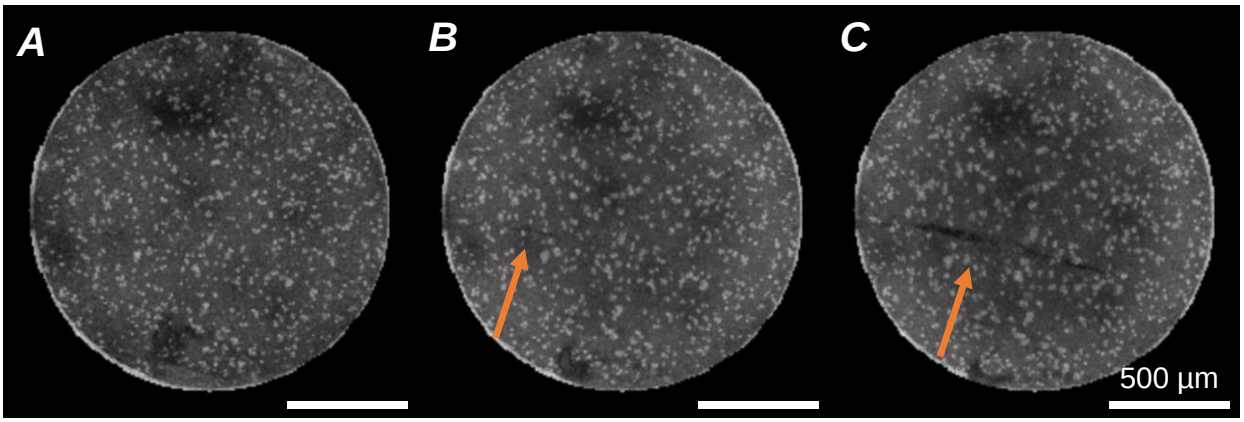


Figure 4.24. Top view OCT images of a bulge test for a healed CE6 biofilm, at initial frame (A), Frame 36 (B, initial moment of failure), and C) 61 (extra frames collected to observe propagation of tear). Microsphere tracking and properties only processed up to Frame 35. Scale 500 µm. Arrows indicate tear location (visible as dark lines forming against the gray background of the biofilm). 7 day sample growth; stepwise loading; ΔP = 0 (A), 540 (B) Pa.

Results are described for a healed CE6 film. The film was tested in 15 Pa increments of pressure and found to fail on the 36$^{th}$ frame (Figure 4.24: Frame 1 with no damage to the film, Frame 36 with appearance of a tear, Frame 61 with propagating tear). Particle tracking was only performed (and properties calculated) up to Frame 35; additional frames were collected to visualize crack propagation along the film. Contrast in Figure 4.24 was adjusted to highlight microsphere locations; crack is visible as a dark line forming on the gray background of the biofilm.

*Where does a healed biofilm fail?*

The first question we could ask was: where does the healed biofilm fail? Is it in a new location, or does it follow the path of the original cut?

To answer this question, we aligned multiple sets of images manually (Figure 4.25). Frame 36 was used to visualize the original defect location (Figure 4.25A, left) and contrast adjusted to display the microspheres clearly (Figure 4.25A, center). Microsphere positions (at Frame 35, the last frame tracked) as tracked by and exported from Imaris were plotted and overlaid manually with the bulge test image (Figure 4.25A, right, overlay; blue markers are tracked coordinates exported from Imaris).

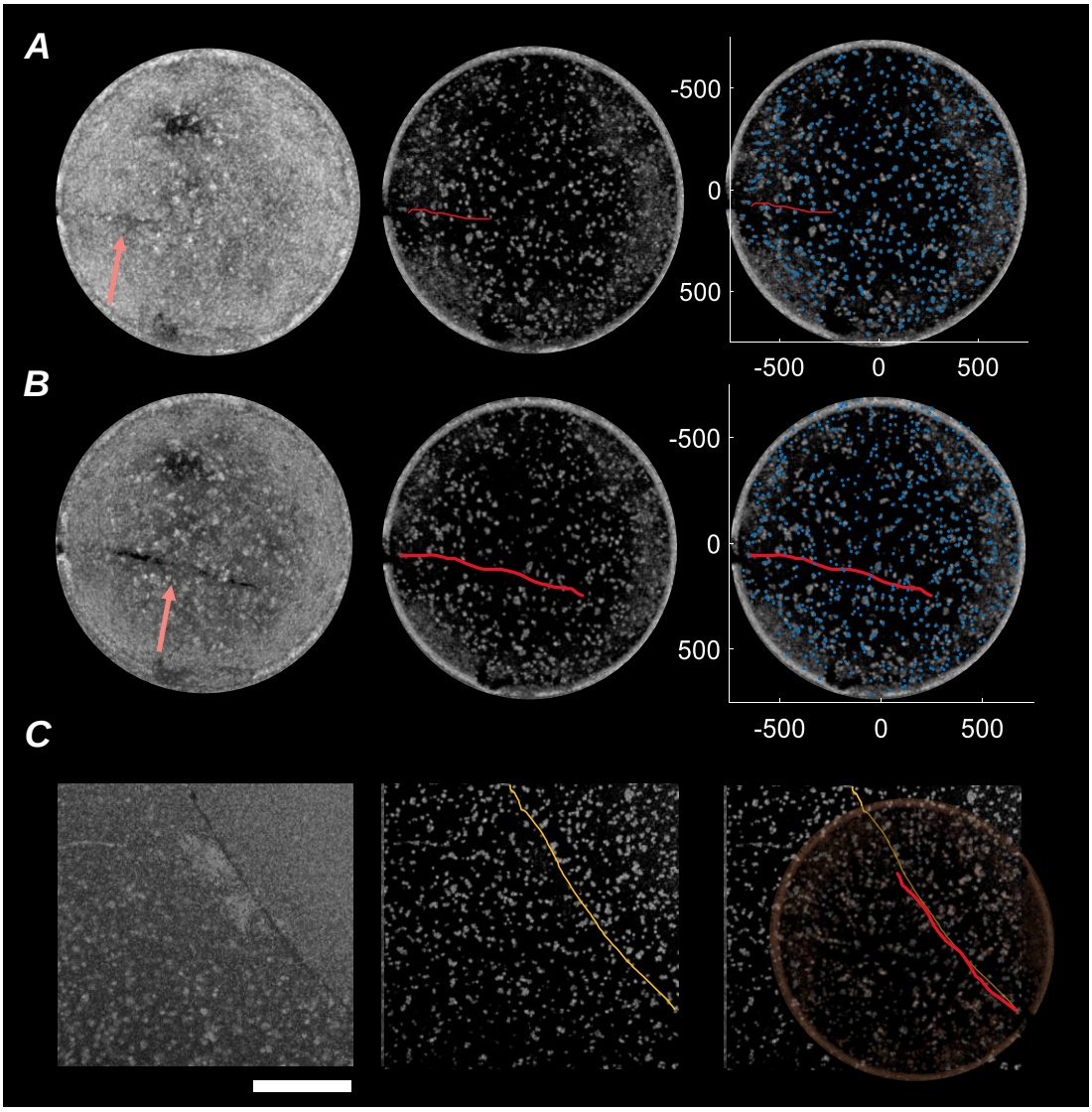


Figure 4.25. Bulge test images of healed CE6 highlighting tear formation (A, left and B, left) with adjusted contrast to display microspheres (A and B, center), overlaid with tracked microsphere coordinates in μm (A and B, right; blue scatter icons correspond to tracked coordinates). Arrows in (A) and (B) indicate location of original tear, traced onto the other images as red lines. C) Top view of OCT scan of tear (scale: 500 μm) immediately after defect creation, of biofilm placed on LB nutrient plate (left; center: contrast adjusted to highlight microsphere locations with tear traced as yellow line). (C, right): Bulge test frame from (B, center) overlaid onto (C, center) to highlight the overlap between locations of the two tears. Overlay shows that the healed film tears once again in the location of the original defect. Note that alignment in C is not ideal: the bulge tested film is deformed into a dome, while the scans in (C) are of a flat film on agar. The initial flat frame from the bulge test would provide better alignment but be less accurate as to the location of the tear.

Using this overlay and the known position of the tear (from Figure 4.25A, left) we marked the location of the tear (red line, Figure 4.25A, right). Next, we followed the same protocol for the path taken by the propagating tear (Figure 4.25B: note that alignment is less accurate here since Frame 35 used for microsphere coordinates significantly deviated from Frame 61). Finally, we used the OCT image of the biofilm (on LB agar, taken on day 0 with the defect clearly visible) to mark the location of the original cut (Figure 4.25C, left is original OCT scan, center is the scan adjusted to highlight microsphere locations with cut traced in yellow). An overlay of the bulge test frame onto the OCT image of the film on agar (with propagating tear marked in red; bulge test image colored in orange for clarity, Figure 4.25C, right) confirmed that the failure of the healed biofilm followed the same path as the original healed tear!

*Is a healed biofilm heterogeneous?*

Our next question was whether or not the newly healed biofilm developed heterogeneities as a result of the healing process and if so, their location(s) and effect(s). Plots of (outward) radial displacement of the microspheres across the frames of the bulge test were not sufficient to visualize this (Figure 4.26) and did not reveal any obvious heterogeneity; however the principal stretches revealed a region of apparent heterogeneity in the film in the lower left quadrant (Figures 4.27, 4.28, 4.29). Note the different scale in Figure 4.29 for clarity.

In this region of the film, the orientations (eigenvectors) for maximum stretch were along the circumferential rather than meridional orientation (Figure 4.27), in direct contrast to the remainder of the film and other films tested (Figures 4.5-4.10). The stretch orientation

along the boundaries of the heterogeneous region could not be clearly categorized into either meridional or circumferential directions and were at an angle to both, suggesting the presence of shear. For the purpose of plotting, they were included in the dataset closest to the relevant orientation but future work could characterize this complex response in greater detail.

In contrast to these observations in the healed film, the control film showed the expected axisymmetric response (Figures 4.30, 4.31, 4.32). Here we limit the discussion of properties to the healed film; full plots for the control can be found in Figure S5 (supplemental).

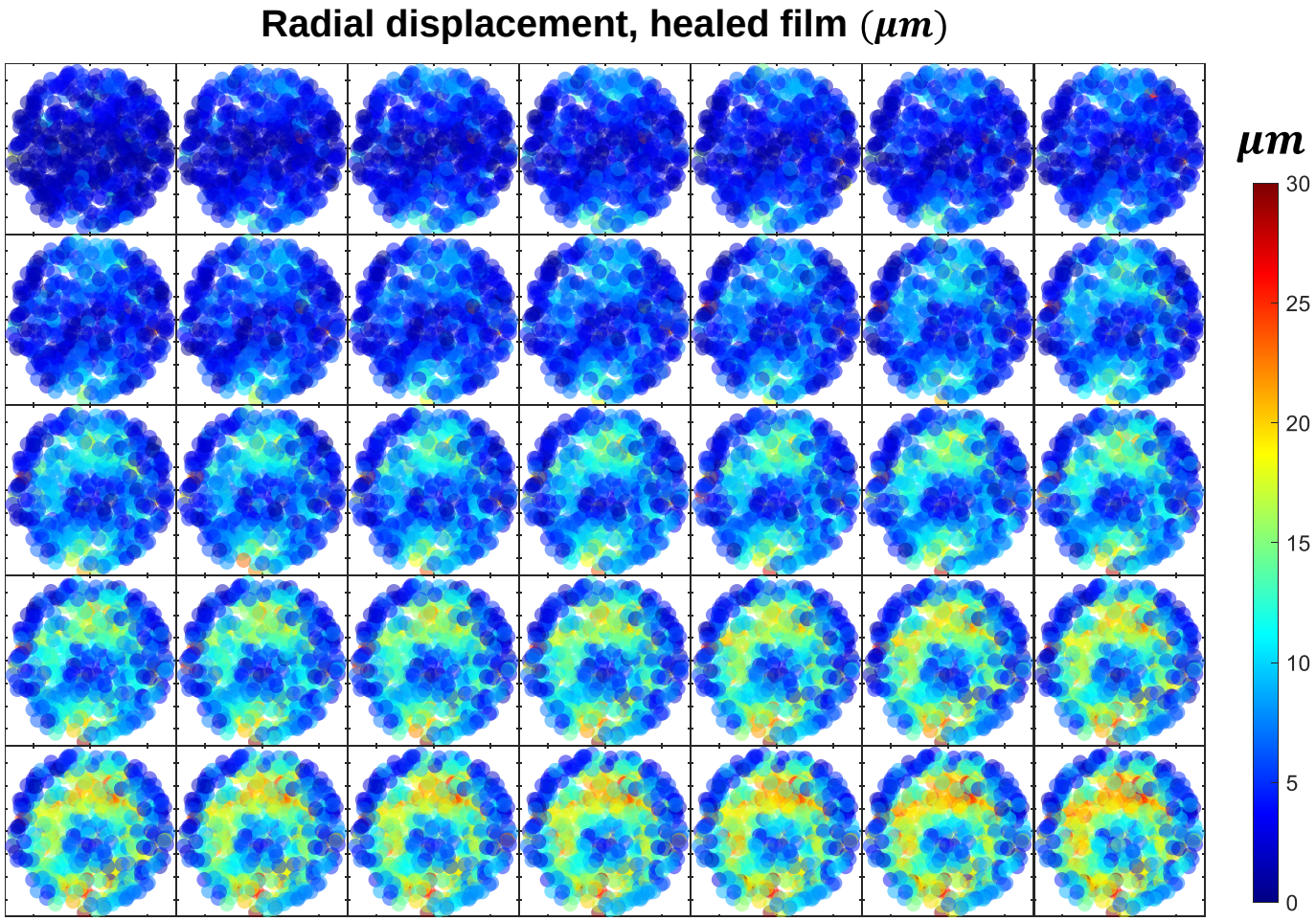


Figure 4.26. Plots of radial displacement plotted across frames of the bulge test (ordered left to right, top to bottom) for healed CE6 biofilm do not reveal the clear presence of heterogeneity.

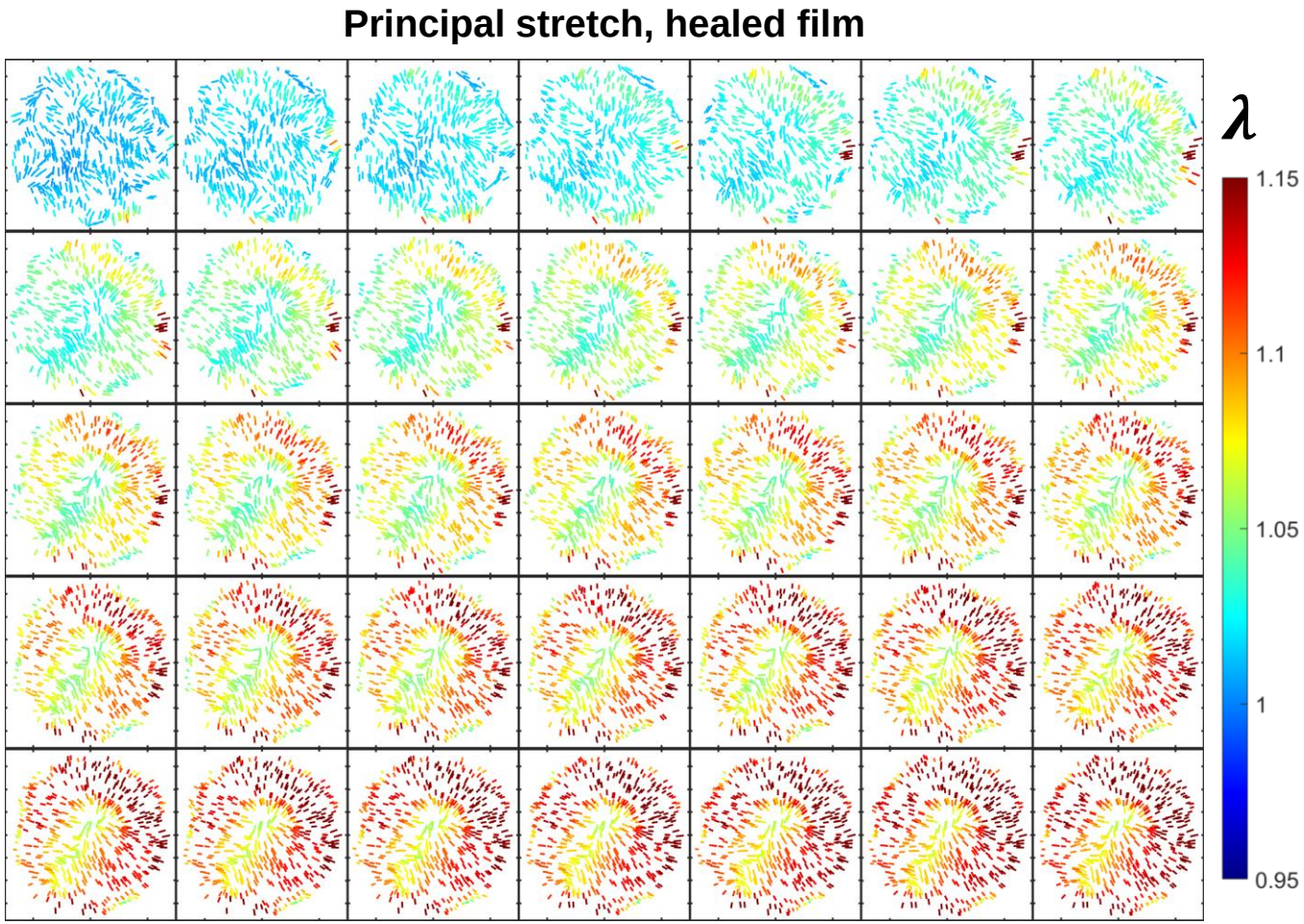


Figure 4.27. Principal stretches ordered from maximum to minimum in Figures 4.27-4.29 respectively, for frames of the bulge test (ordered left to right, top to bottom) for healed CE6 biofilm show a clear region of film with a distinct response (bottom left region).

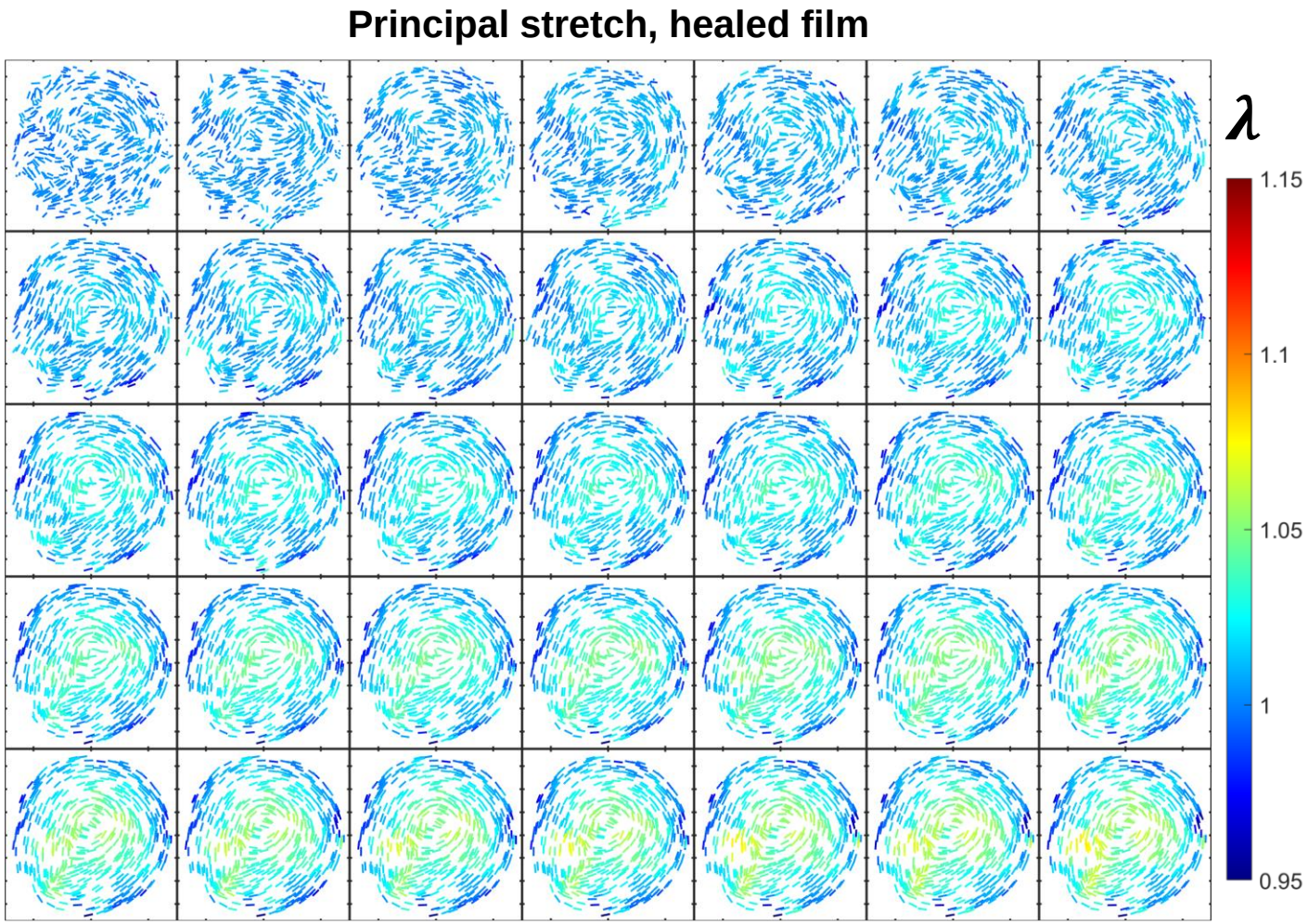


Figure 4.28. Principal stretches ordered from maximum to minimum in Figures 4.27-4.29 respectively, for frames of the bulge test (left to right, top to bottom) for healed CE6 biofilm: with continuing heterogeneous region in the bottom left of the film.

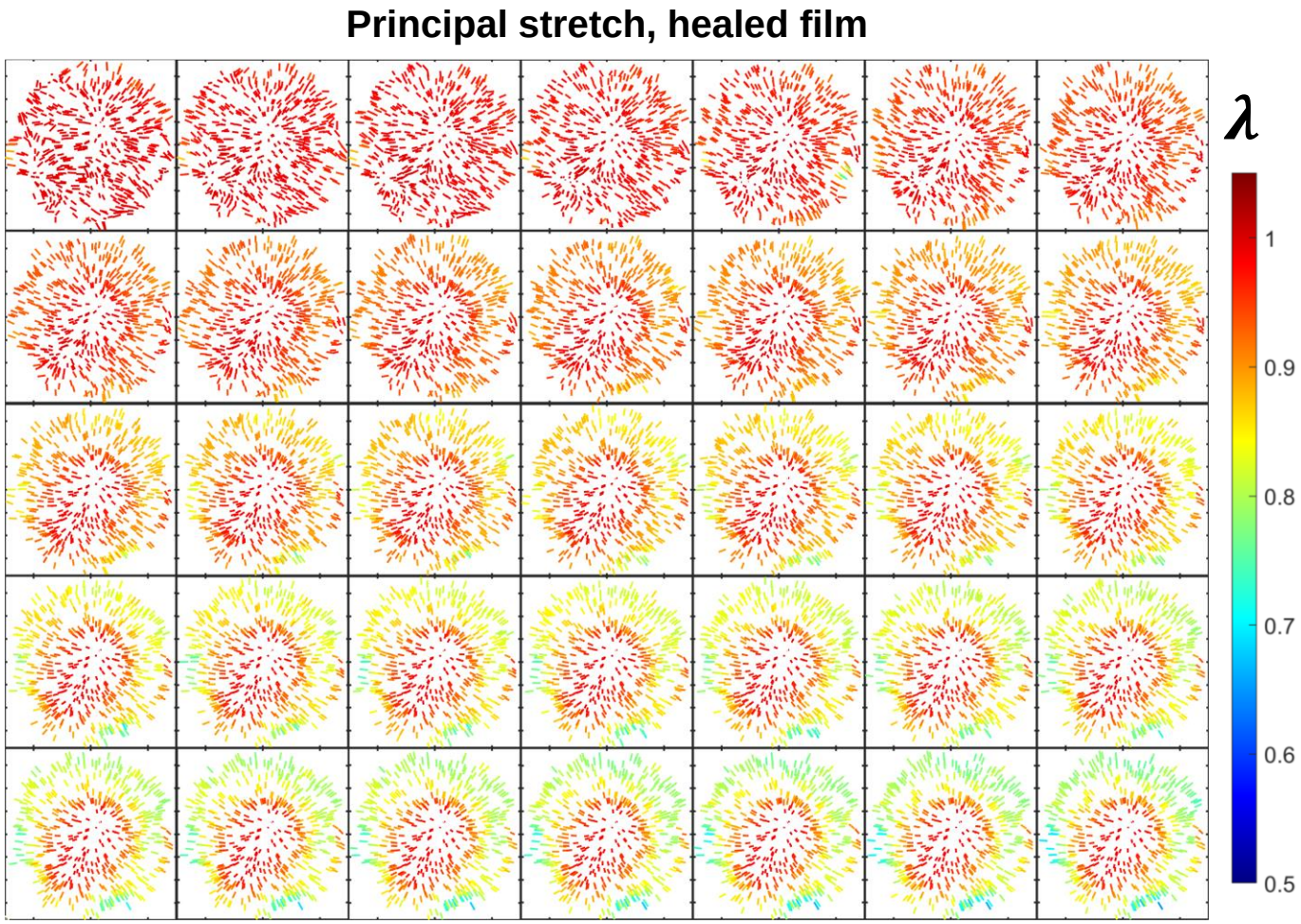


Figure 4.29. Principal stretches ordered from maximum to minimum in Figures 4.27-4.29 respectively, for frames of the bulge test (left to right, top to bottom) for healed CE6 biofilm: film thickness decreases.

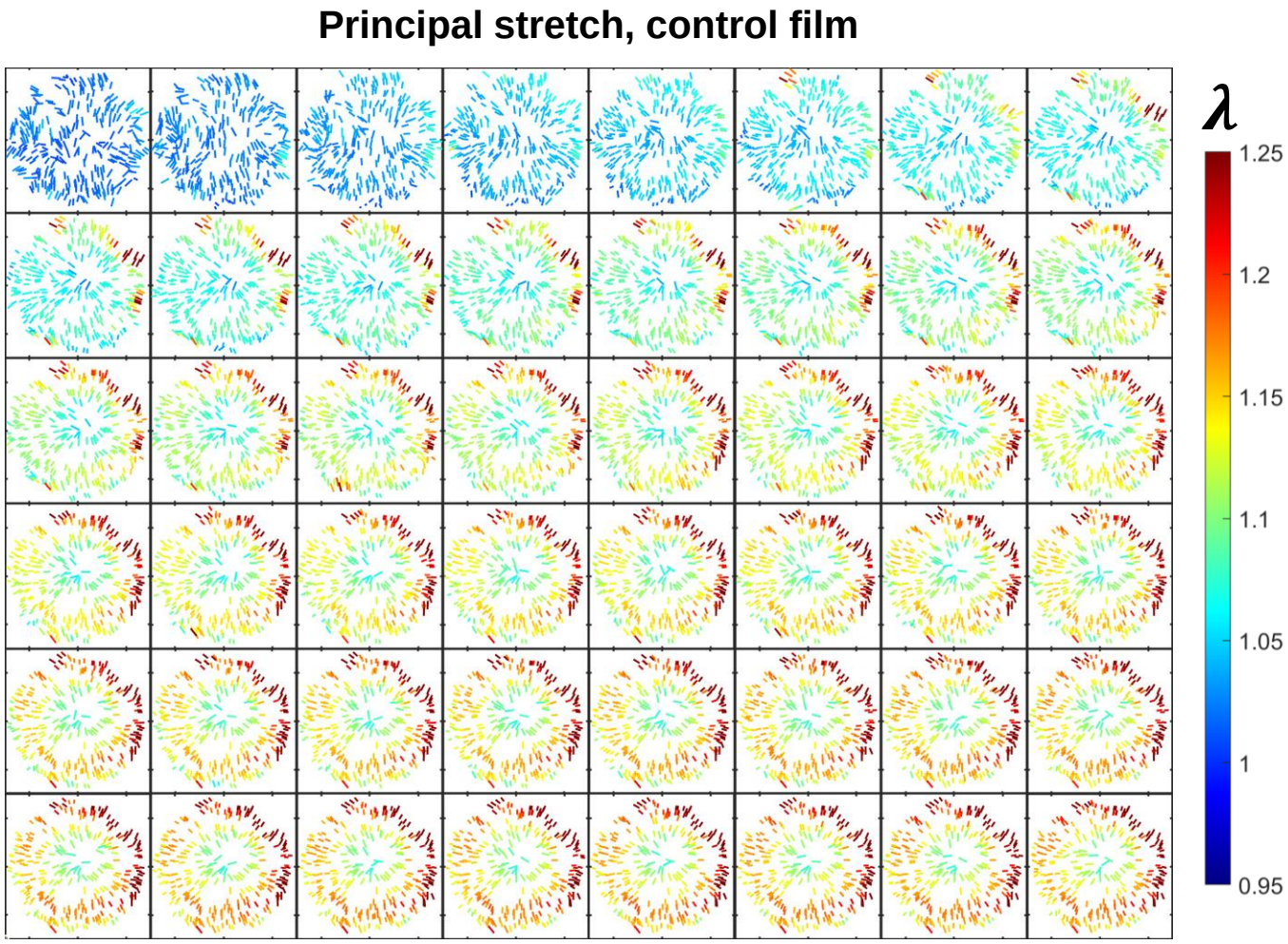


Figure 4.30. Principal stretches ordered from maximum to minimum (Figures 4.30-4.32) for control film show axisymmetric response.

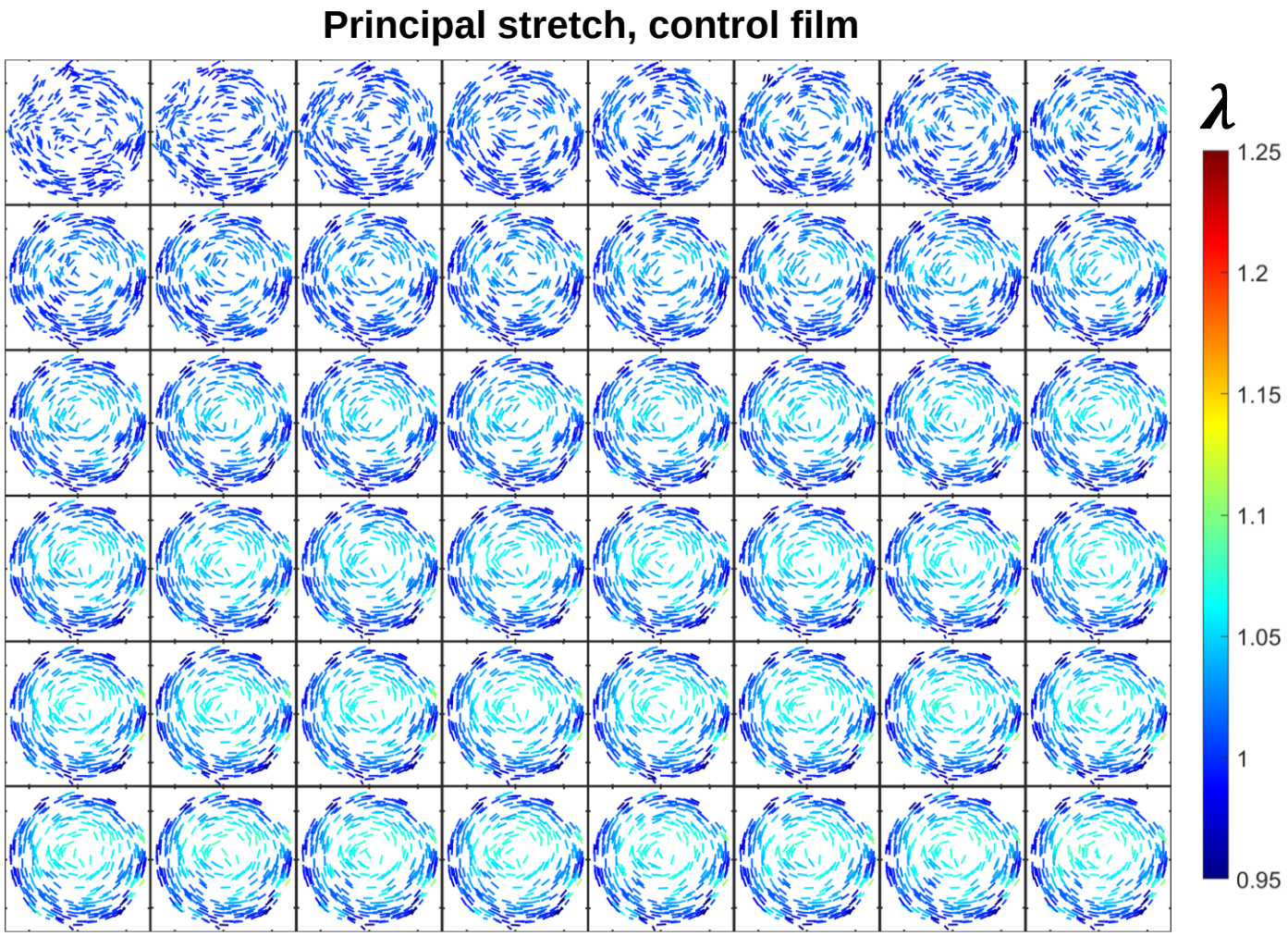


Figure 4.31. Principal stretches ordered from maximum to minimum (Figures 4.30-4.32) for control film show axisymmetric response.

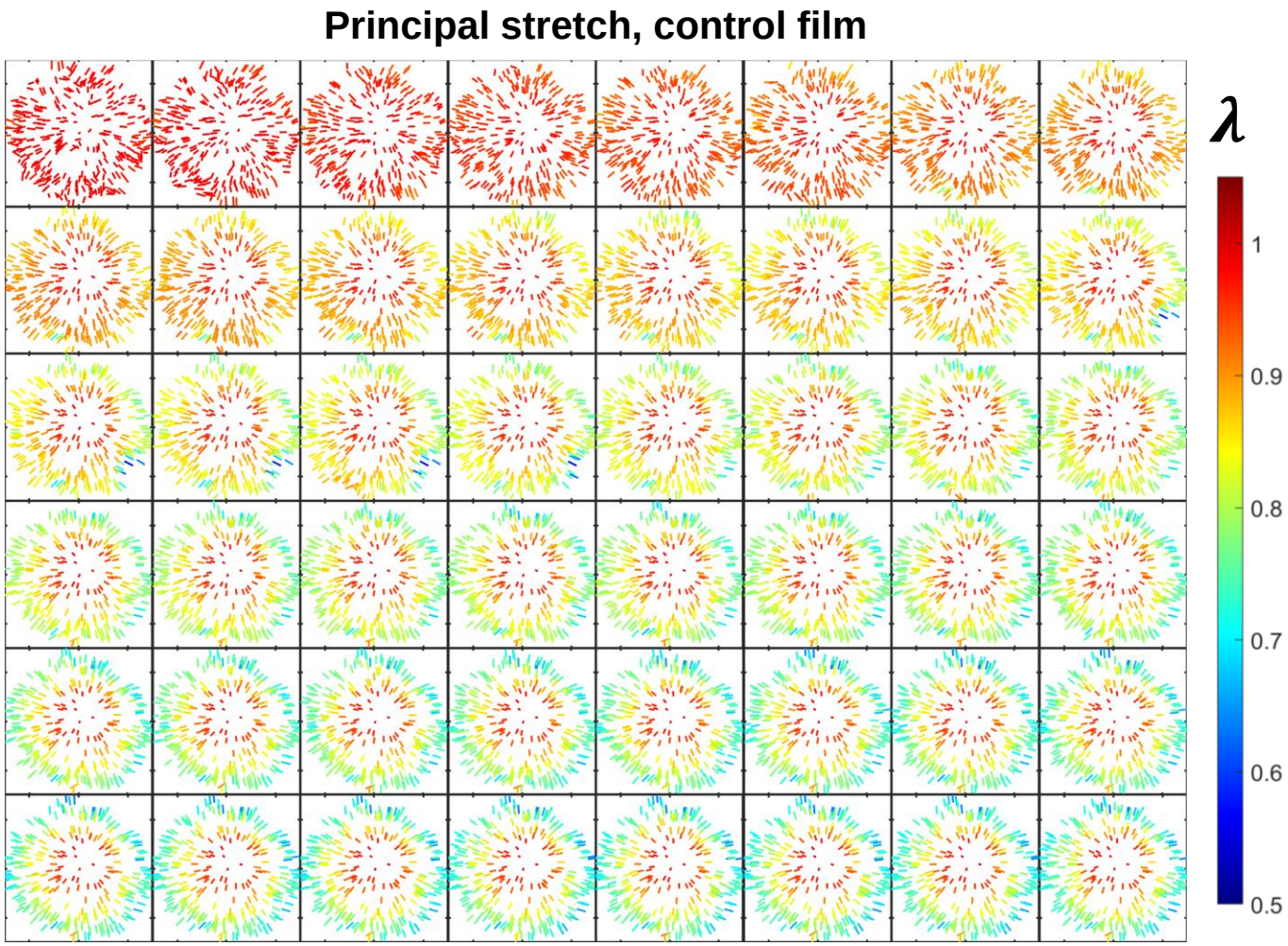


Figure 4.32. Principal stretches ordered from maximum to minimum (Figures 4.30-4.32) for control film show axisymmetric response.

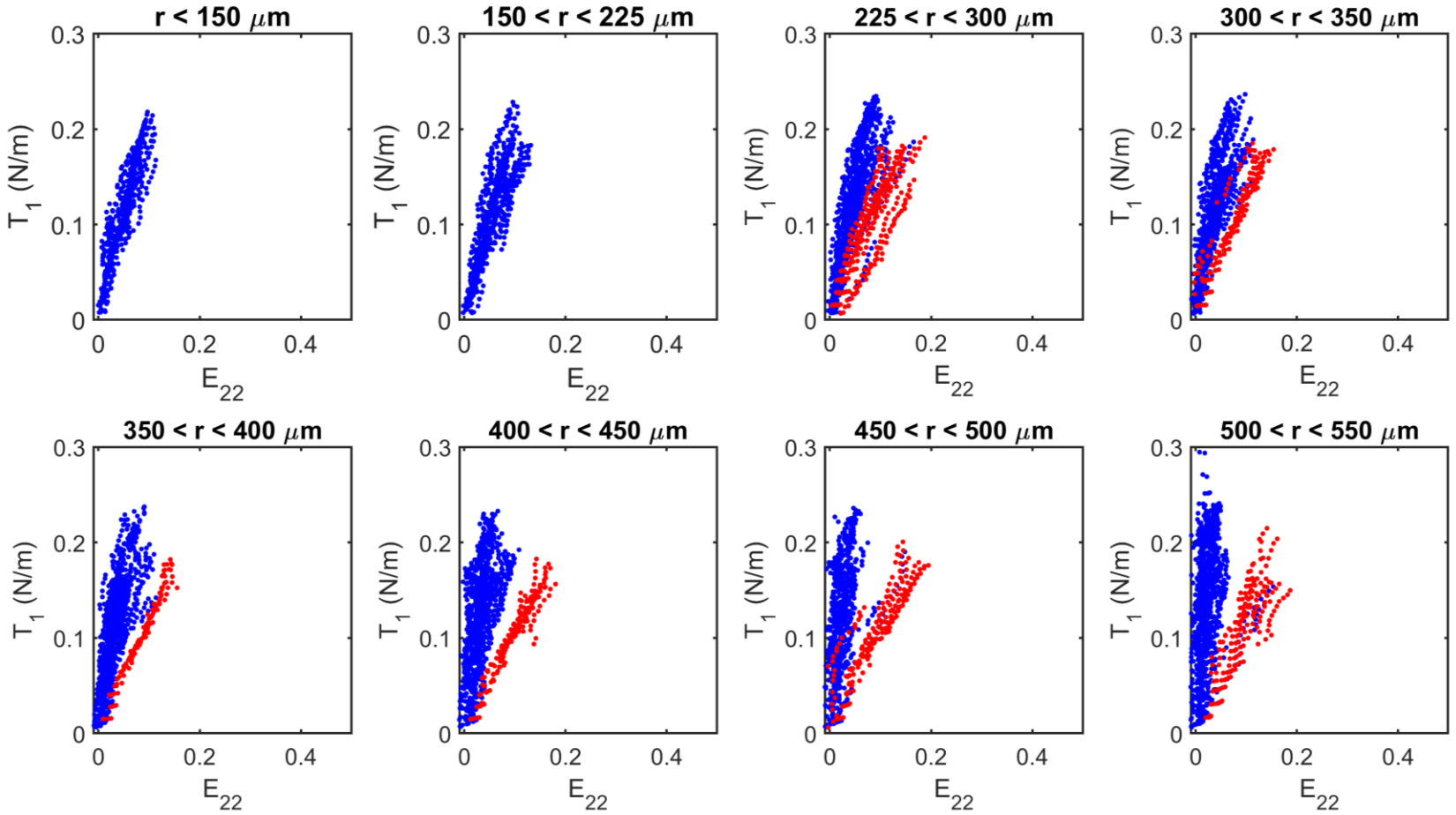


Figure 4.33. $E_{22}$ vs. $T_1$ for healed film, with traces showing clear separation in red and remainder in blue.

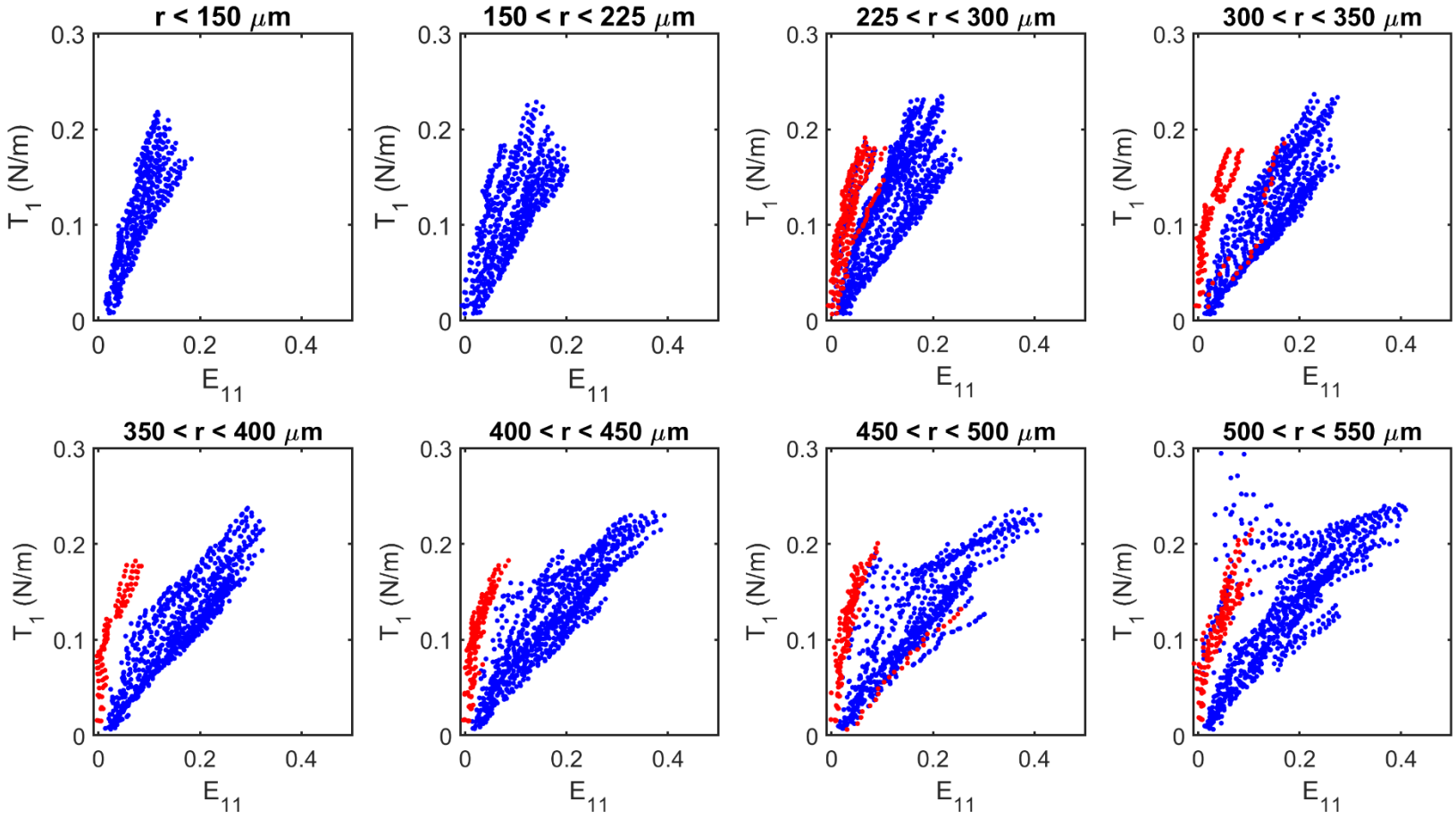


Figure 4.34. $E_{11}$ vs. $T_1$ for healed film; identified traces from $E_{22}$ plots used to find corresponding traces in above plots (red).

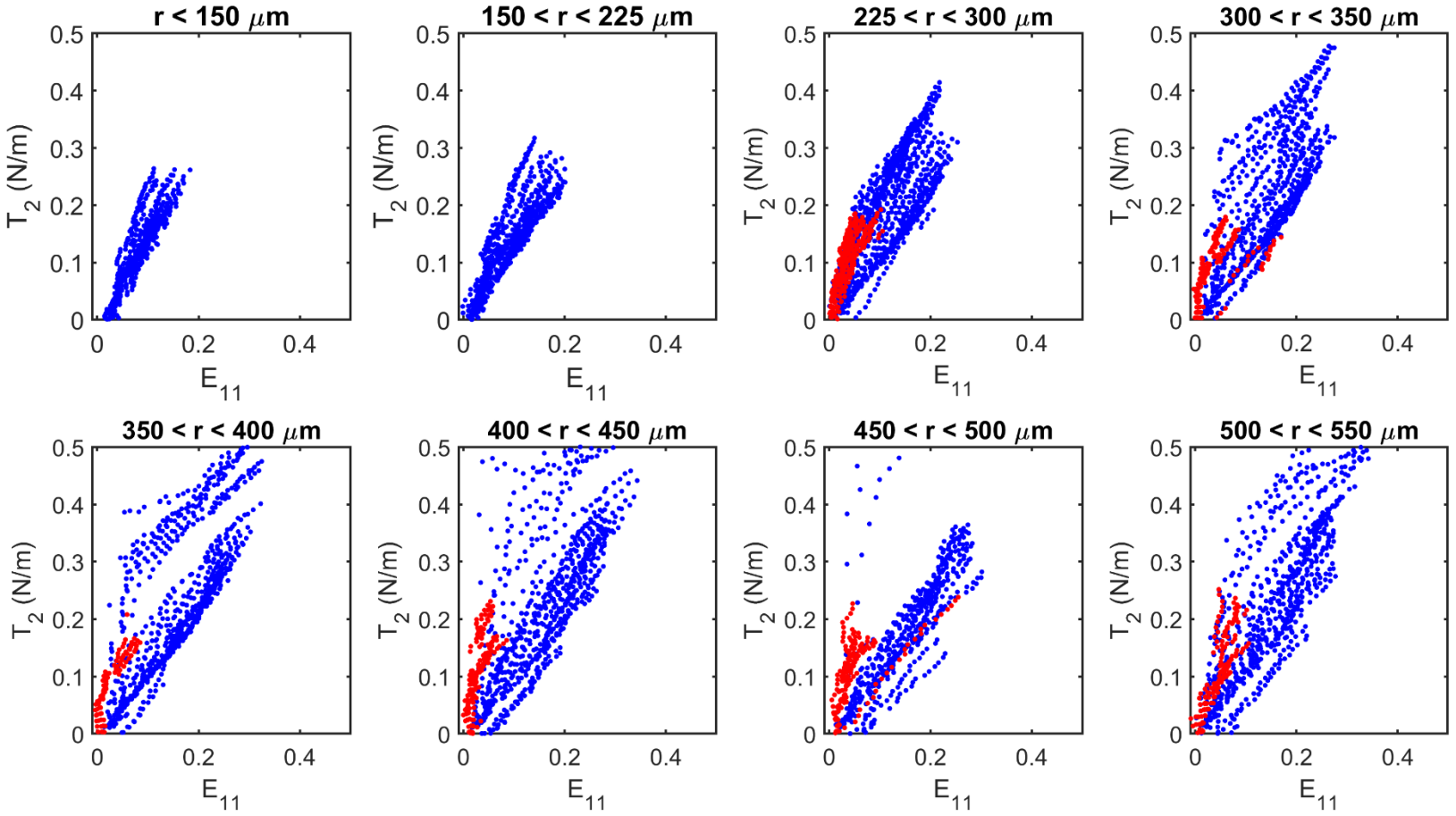


Figure 4.35. $E_{11}$ vs. $T_2$ for healed film; identified traces from $E_{22}$ plots used to find corresponding traces in above plots (red).

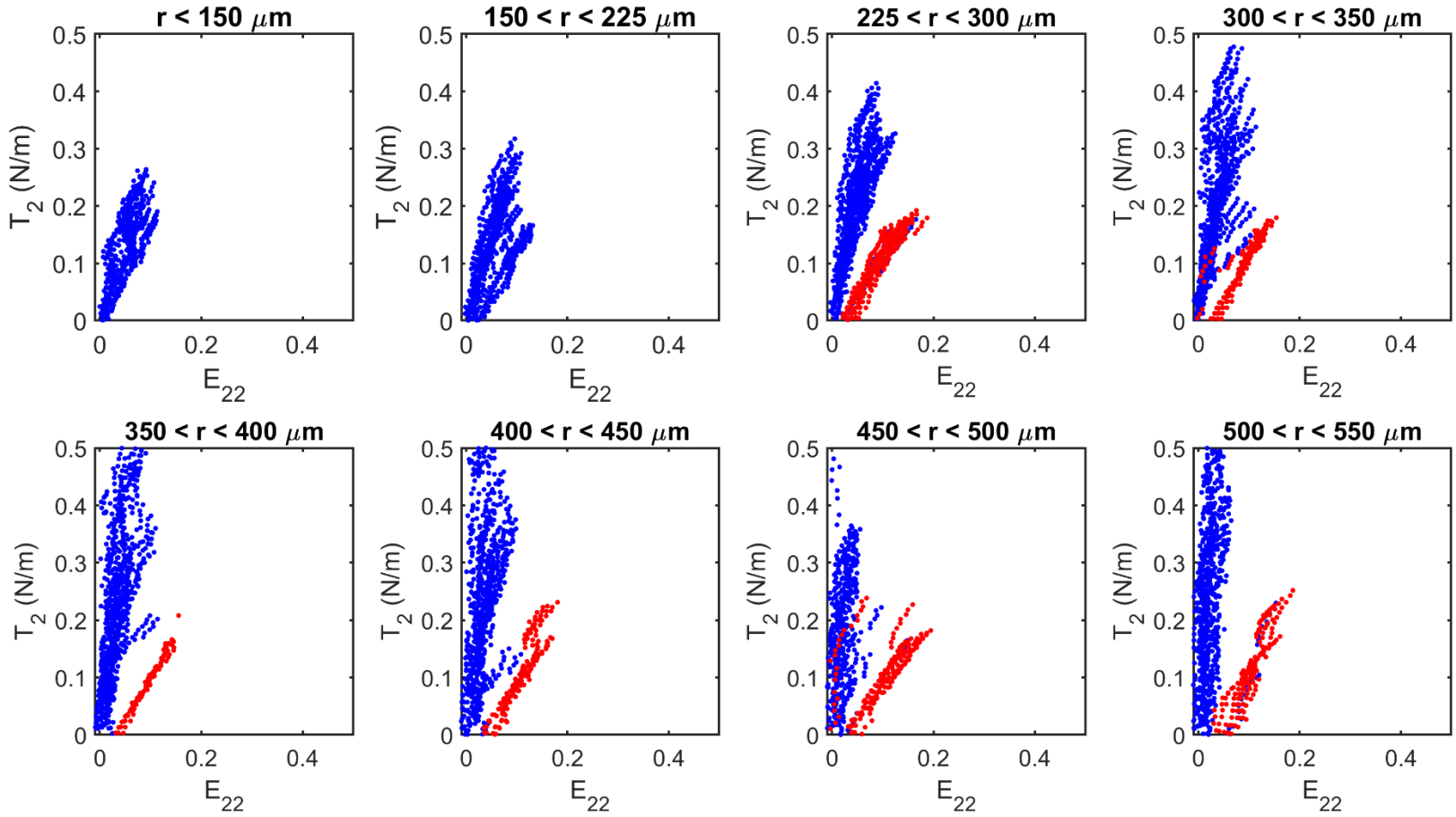


Figure 4.36. $E_{22}$ vs. $T_2$ for healed film, with traces showing clear separation in red and remainder in blue.

The principal stretches mapped across the healed film allowed for the visual detection of regions of heterogeneity. Following similar methods as described previously, we can also plot $E_{11}$, $E_{22}$, $T_1$, and $T_2$ for these films (Figures 4.33-4.36). Here, in agreement with the results observed from the principal stretches, we observed traces corresponding to unusual properties relative to those at a similar radial coordinate (highlighted in red, identified most clearly from $E_{22}$ plots and used to mark corresponding traces on $E_{11}$plots as well; compared to other traces plotted in blue). The microsphere coordinates corresponding to these anomalous traces are highlighted in red in Figure 4.37A, and were found to correspond to the areas highlighted from the plots of principal stretches. Further work could separately fit a strain energy density function to these regions to quantify the effects of the local heterogeneity.

The second aspect of interest is: what are the properties of the region of the film immediately adjacent to the original tear? We highlighted the microspheres closest to (on either side of) the tear (red, Figure 4.37B) and plotted the *E* vs. *T* traces once more. Surprisingly, these traces were indistinguishable from the neighboring regions of the film (Figure 4.38 as a representative example; additional figures in Figure S7).

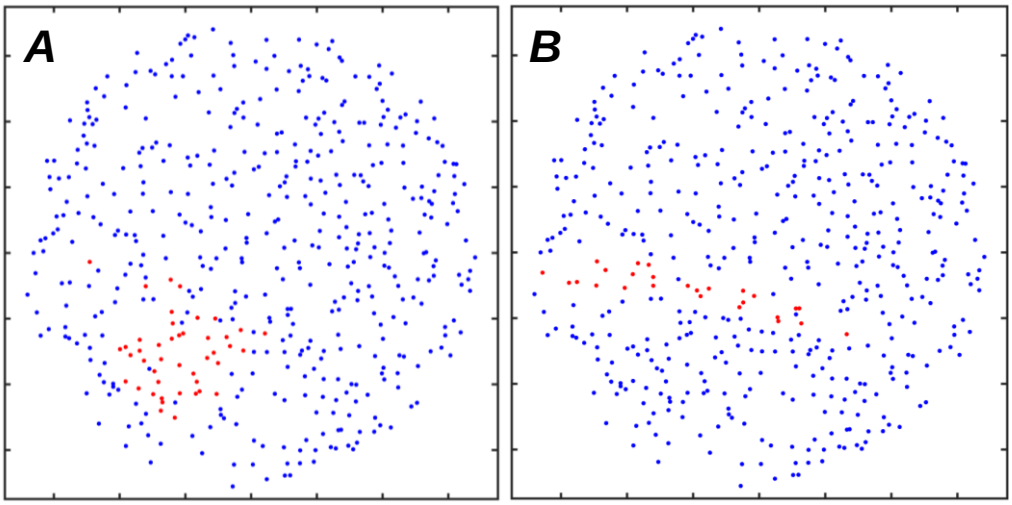


Figure 4.37. (A) Region of heterogeneity (red) formed in healed CE6 biofilm, identified independently of known tear location; identified from anomalous regions of *E* vs. *T*. plots and agrees well with observed heterogeneity in principal stretches. (B) Region of interest (red) corresponding to a known physical feature: original defect location that tore a second time, with corresponding *E* vs. *T* plot in Figure 4.38.

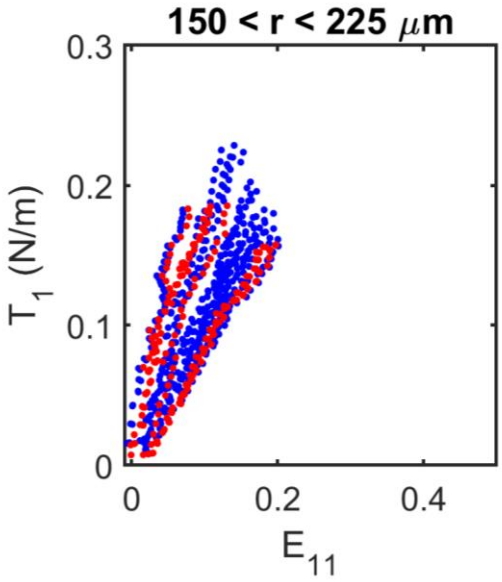


Figure 4.38. Representative *E* vs. *T* plot for region highlighted in Figure 4.34B corresponding to initial and secondary tear formation. Unexpectedly, the traces are undistinguishable from others in a similar radial coordinate.

Overall, the above results suggest that the original defect creation and healing process create a region of heterogeneity in the healed biofilm that is distinct from the location of

the original tear. It is still unclear as to the factors leading to heterogeneity in this location, and how it relates to the location of the original defect (where the film failed a second time as well). This anomalous region shows an increase in circumferential stretch compared to meridional stretch, and the correlation between this and the failure/healing is not yet understood or explored in detail. Although the region of heterogeneity did overlap with portions of the eventual tear, unlike earlier cases studied in this section, there was not a clear correlation between "weak" regions and failure – at the same time, the healed biofilm was also unique in the way it deformed relative to other types of heterogeneity observed (Figures S7, S8).

Further studies could probe these observed features in more detail: for example considering shear, categorizing heterogeneities based on their impact on material response, or fitting models of hyperelasticity to quantify effects of heterogeneity. Future work could also better identify the detection limits of heterogeneity, either using patternable or 3D printable living materials for targeted feature sizes as a reference or other model systems (e.g. gels with patternable local properties of different sizes, perhaps using photolithography). Additional areas of interest would include the effect of "neighborhood" radius on the sensitivity to heterogeneity, and, from a practical standpoint, methods to improve particle dispersion beyond our current capabilities could lead to studies that consider deformation through the thickness of a material as well (thus accommodating thicker biofilms and other types of deformations).

## 4.4 Conclusion

In this chapter, we built upon the analysis presented in Chapter 3 and extended it to a full picture of “local”, rather than “global” biofilm properties by dispersing tracer microspheres in engineered biofilms and acquiring volumetric rather than cross sectional OCT images. Our analysis effectively maps properties across the film, from the center where we verified the presence of equibiaxial deformation, to the edge where we observed a constant width elongation.

We also explored the presence and implications of heterogeneity: E6 exhibits naturally occurring heterogeneity that is eliminated by the addition of a cysteine residue to form CE6, and observed heterogeneity leads to observable physical features. In healed biofilm, heterogeneity develops in a region distinct from the original tear and displays a unique mechanical response, but the presence of tracers allowed us to confirm that secondary failure occurs at the same site as the original defect.

While our analysis is still limited by certain assumptions, for example membrane behavior, we were able to obtain new insights into the properties of engineered living materials using our method, and conclusions from our analysis can inform the design of new experiments to study living material healing, heterogeneity, and the mechanical implications of cell-cell chemistry.

### 4.4 Additional figures and supplementary information

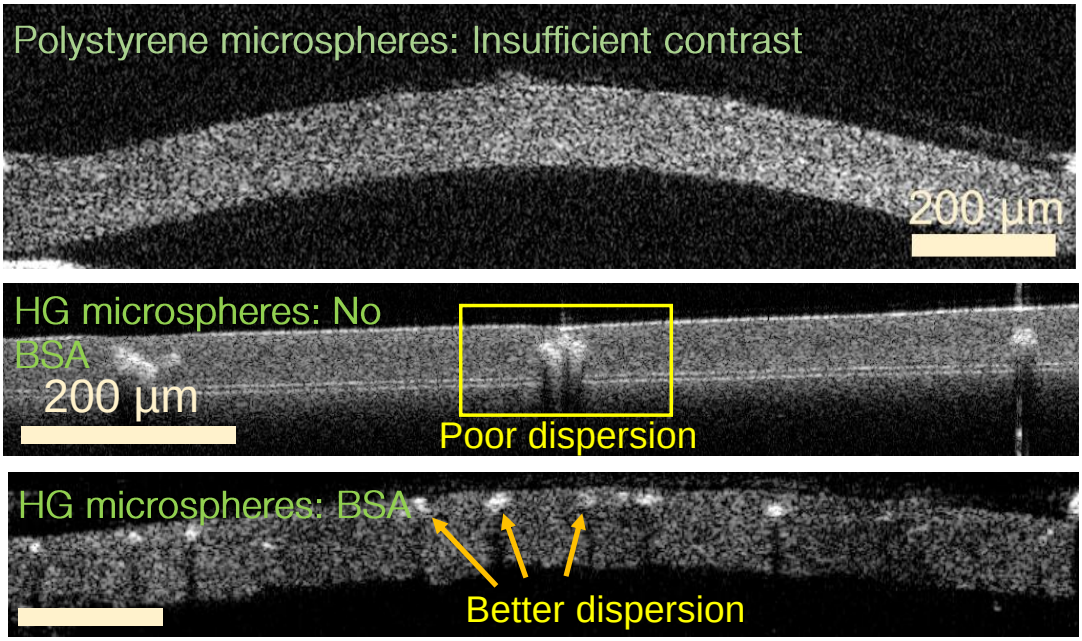


Figure S4.1. Top: Polystyrene microspheres (embedded in CE3 biofilm at $10^4$ microspheres/µl of biofilm) generate insufficient contrast for tracking under OCT. Middle, bottom: Silver coated hollow glass microspheres provided sufficient contrast under OCT (at comparable concentration; see main text for details), but resulted in poor dispersion. Bottom: The addition of BSA enabled better dispersion of the microspheres through the plane of the biofilm. Dispersion through the thickness was limited to the top half of the film. 7 day sample growth.

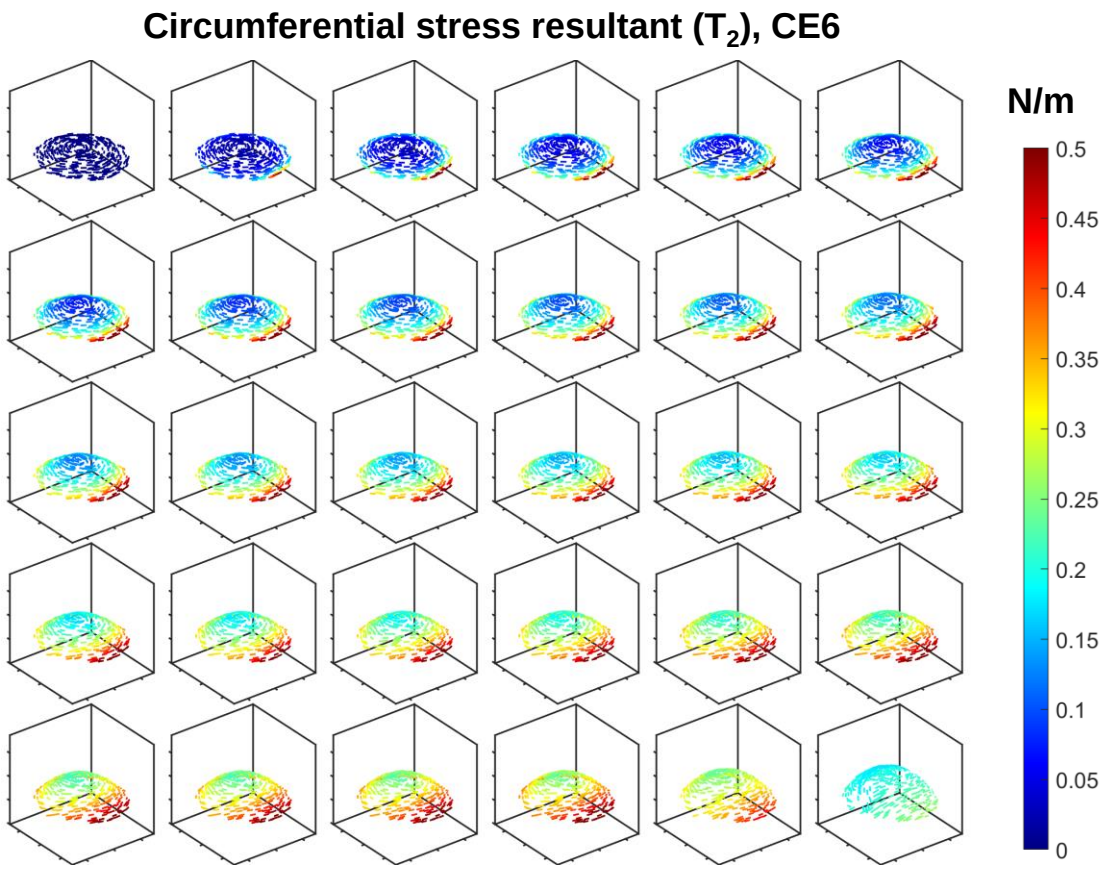


Figure S4.2. Circumferential stress resultant ($T_2$) for CE6, frames ordered left to right, top to bottom (last two frames are at a pressure 300 Pa and 450 Pa greater than the frame immediately prior). Note that orientation is plotted according to calculated maximum or minimum curvature (see text for details). Near the center, curvatures are comparable and vectors depicting orientation may be switched.

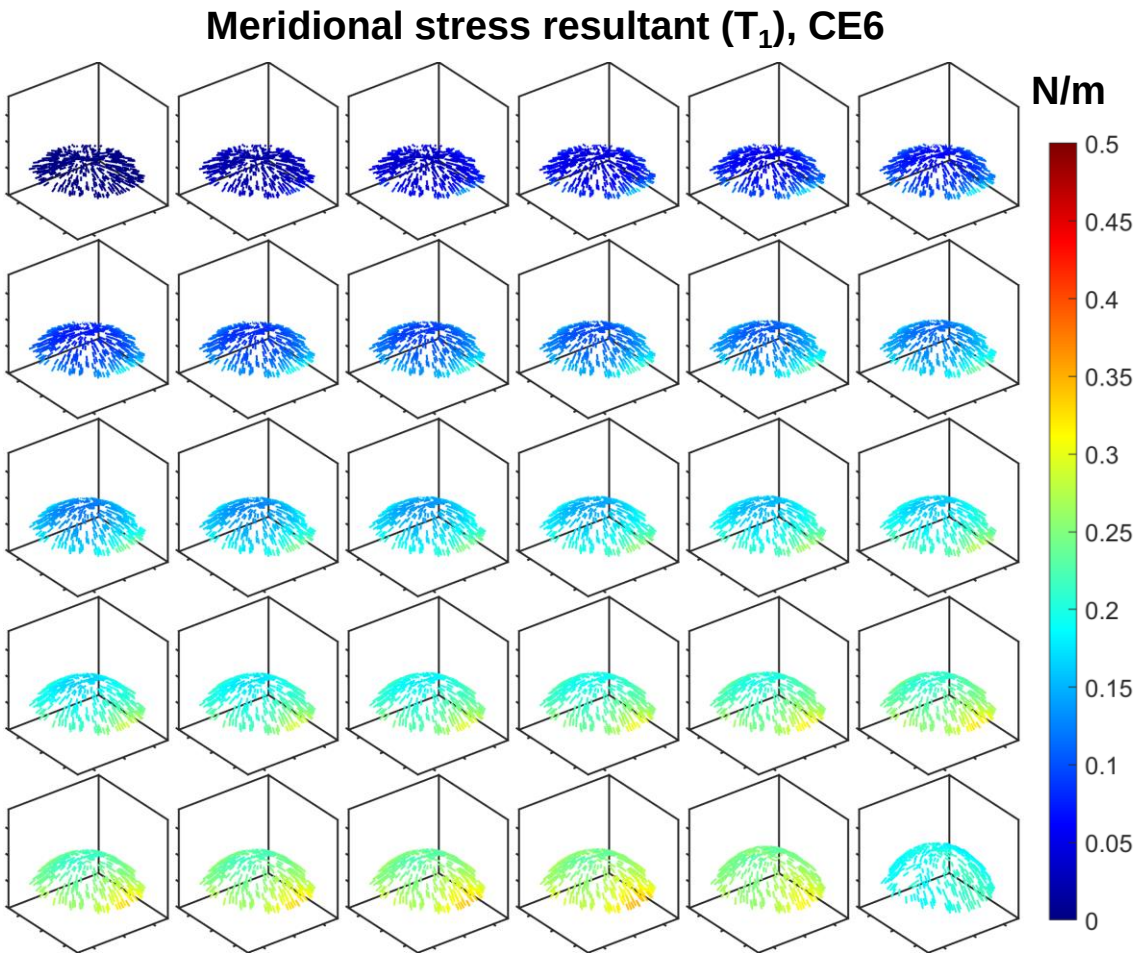


Figure S4.3. Meridional stress resultant ($T_1$) for CE6, frames ordered left to right, top to bottom (last two frames are at a pressure 300 Pa and 450 Pa greater than the frame immediately prior). Note that orientation is plotted according to calculated maximum or minimum curvature (see text for details). Near the center, curvatures are comparable and vectors depicting orientation may be switched.

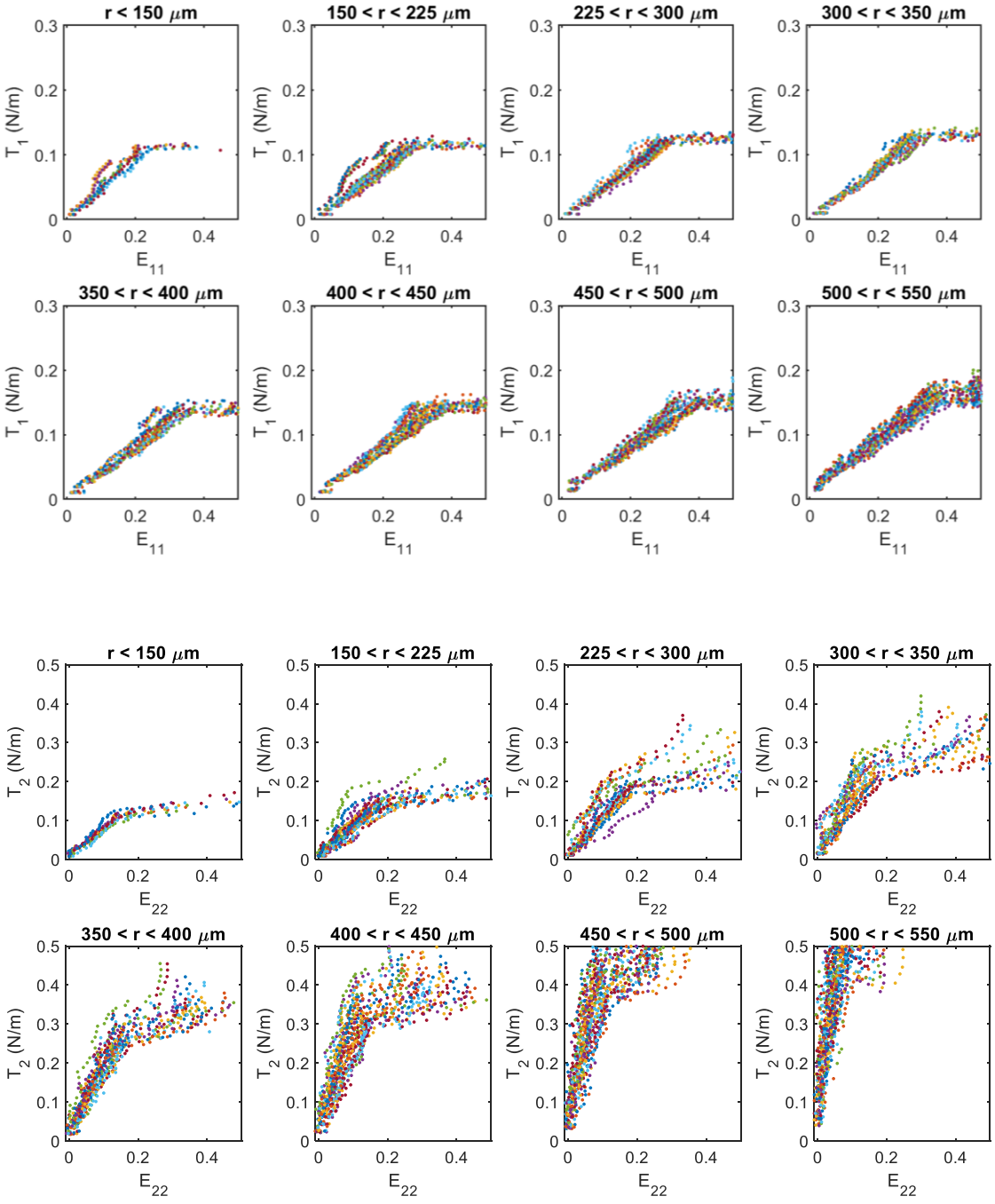
r < 150 μm
150 < r < 225 μm
225 < r < 300 μm
300 < r < 350 μm
350 < r < 400 μm
400 < r < 450 μm
450 < r < 500 μm
500 < r < 550 μm
T1 (N/m)
E11
T2 (N/m)
E22

(continued)

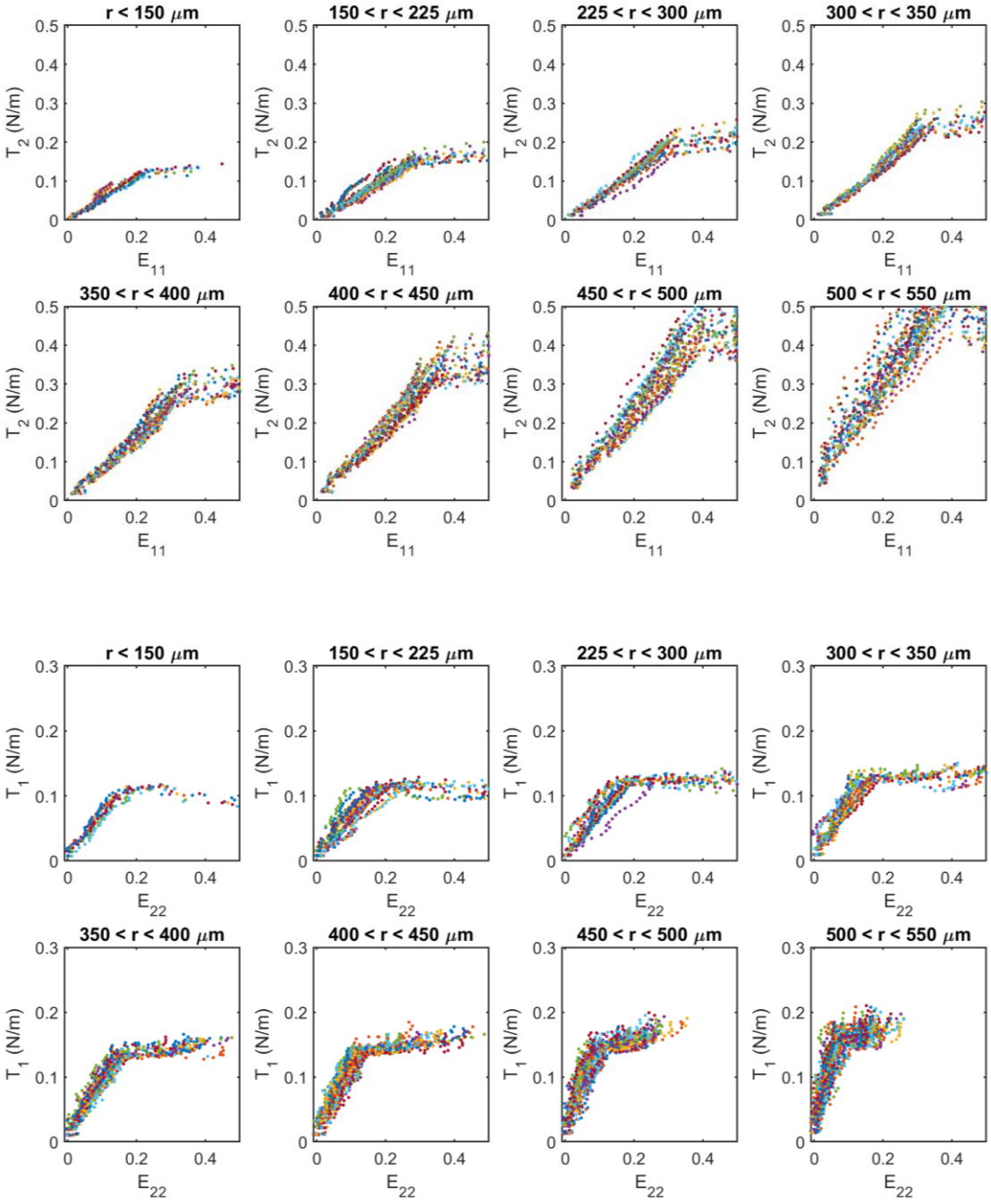


Figure S4.4. Properties for E6 biofilm mapped from center to edge in radial sections. Properties correspond to biofilm shown in Figure 4.19D in main text.

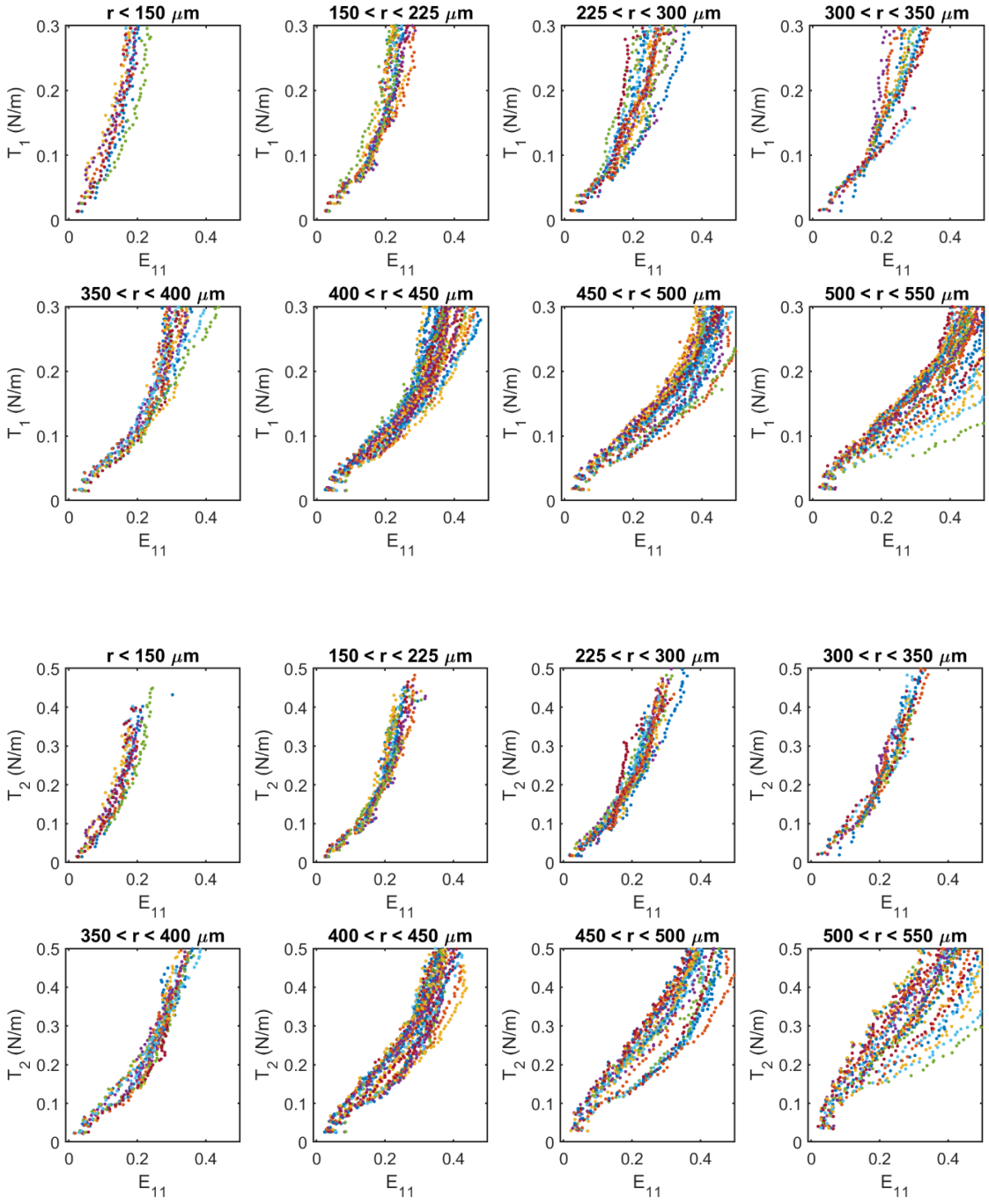
r < 150 μm
150 < r < 225 μm
225 < r < 300 μm
300 < r < 350 μm
350 < r < 400 μm
400 < r < 450 μm
450 < r < 500 μm
500 < r < 550 μm
T1 (N/m)
T2 (N/m)
E11
0
0.1
0.2
0.3
0.4
0.5

(continued)

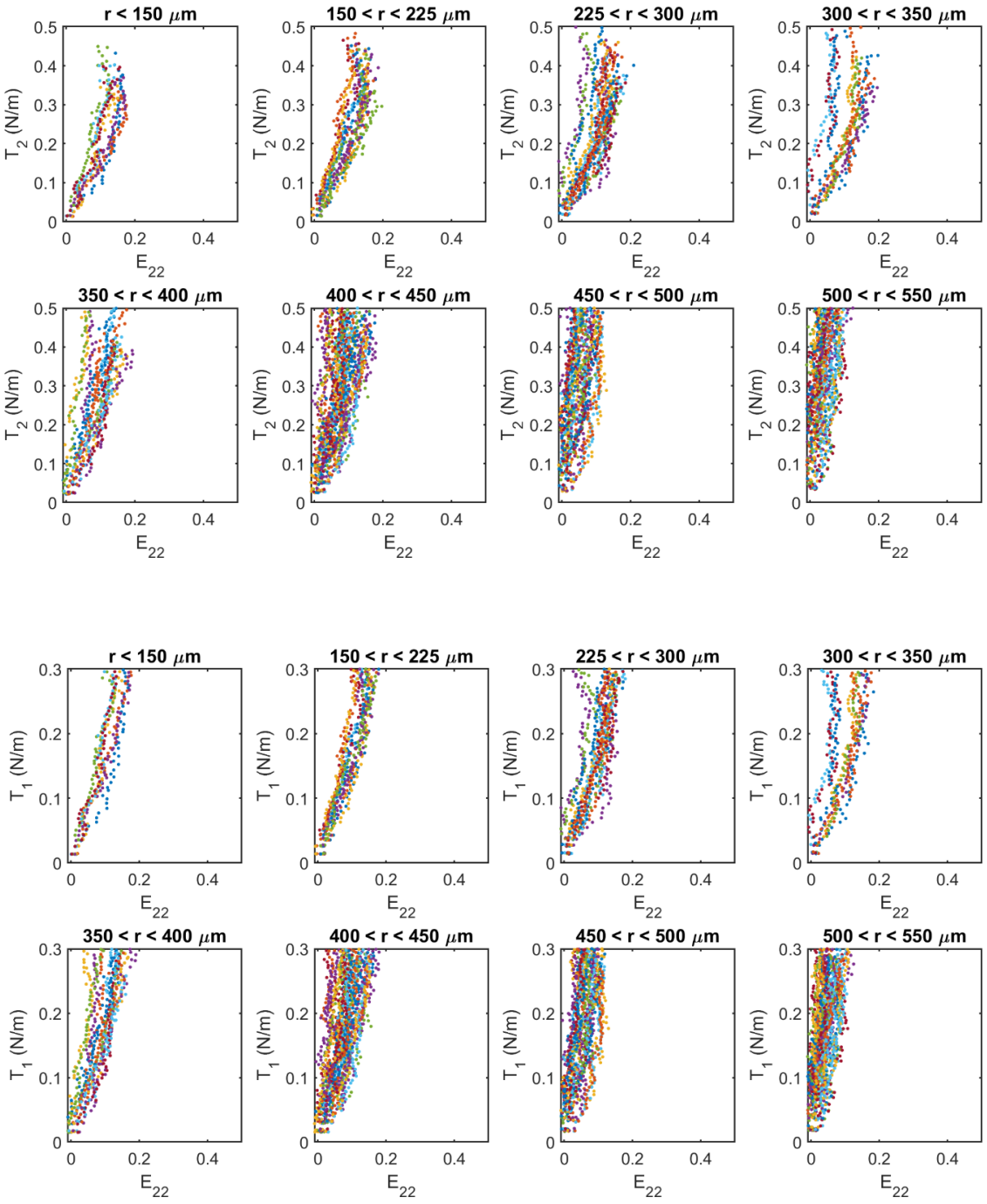


Figure S4.5. Properties for CE6 control biofilm mapped from center to edge in radial sections. See main text for details of healing experiment.

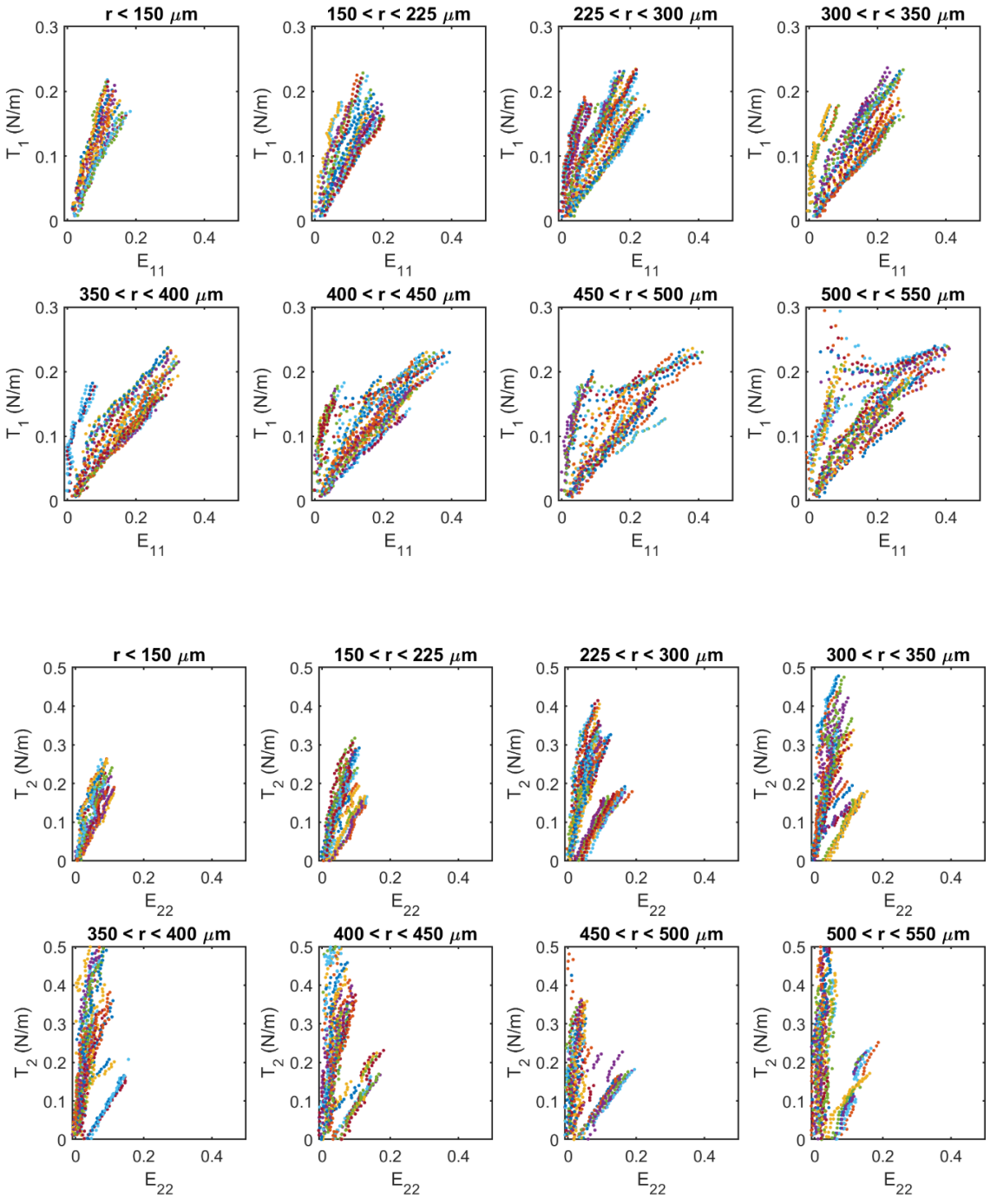
r < 150 μm
150 < r < 225 μm
225 < r < 300 μm
300 < r < 350 μm
350 < r < 400 μm
400 < r < 450 μm
450 < r < 500 μm
500 < r < 550 μm
T1 (N/m)
E11
T2 (N/m)
E22

(continued)

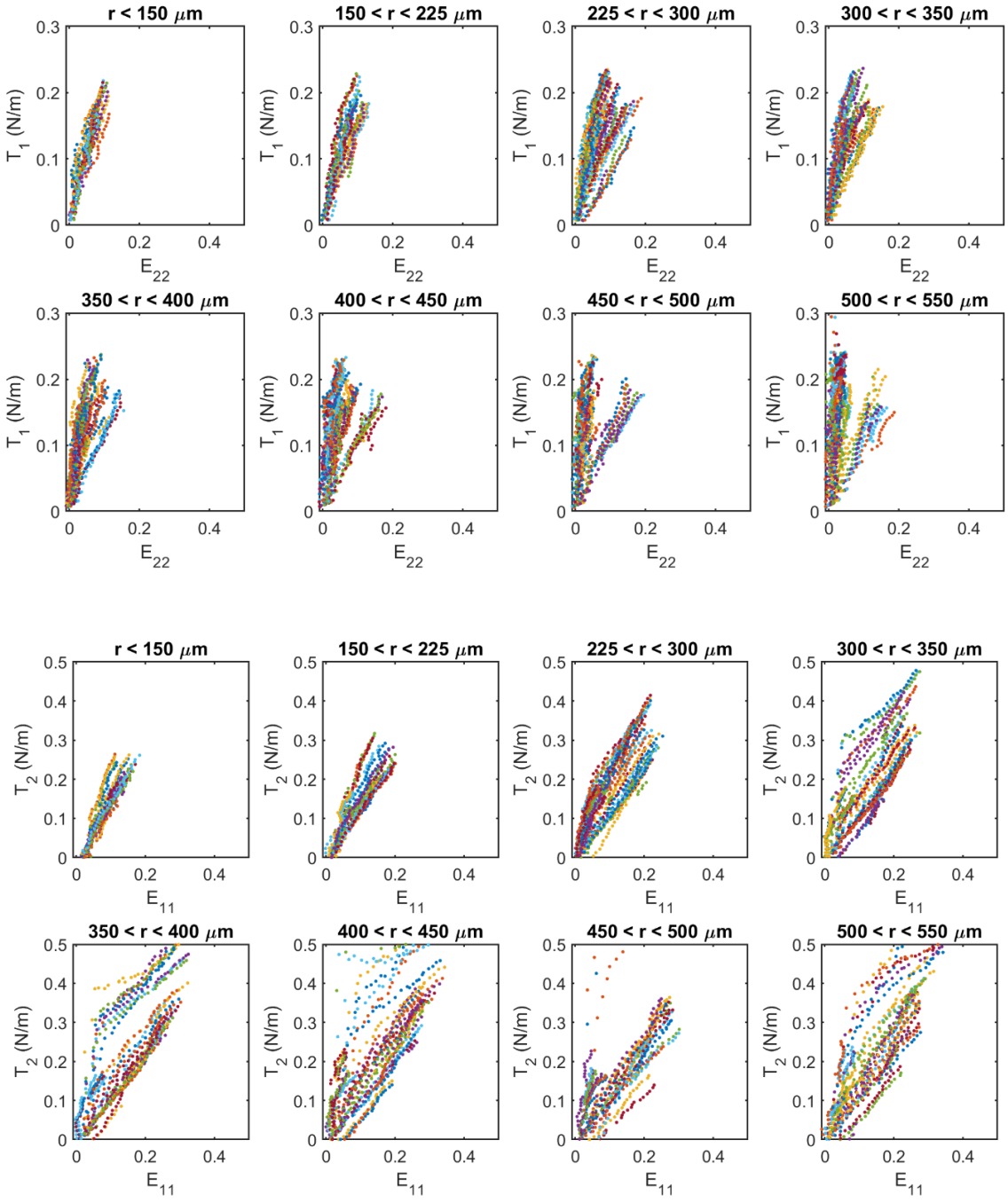


Figure S4.6. Properties for CE6 healed biofilm mapped from center to edge in radial sections. See main text for details of healing experiment. Note that fitting quality not only decreases near the edge in general, but poor quality of plots near the edge in the healed biofilm can be attributed to axes of principal stretches not coinciding with either the meridional or circumferential directions. Orientation was assigned according to the closest match; however in certain cases the orientation was close to 45° to both.

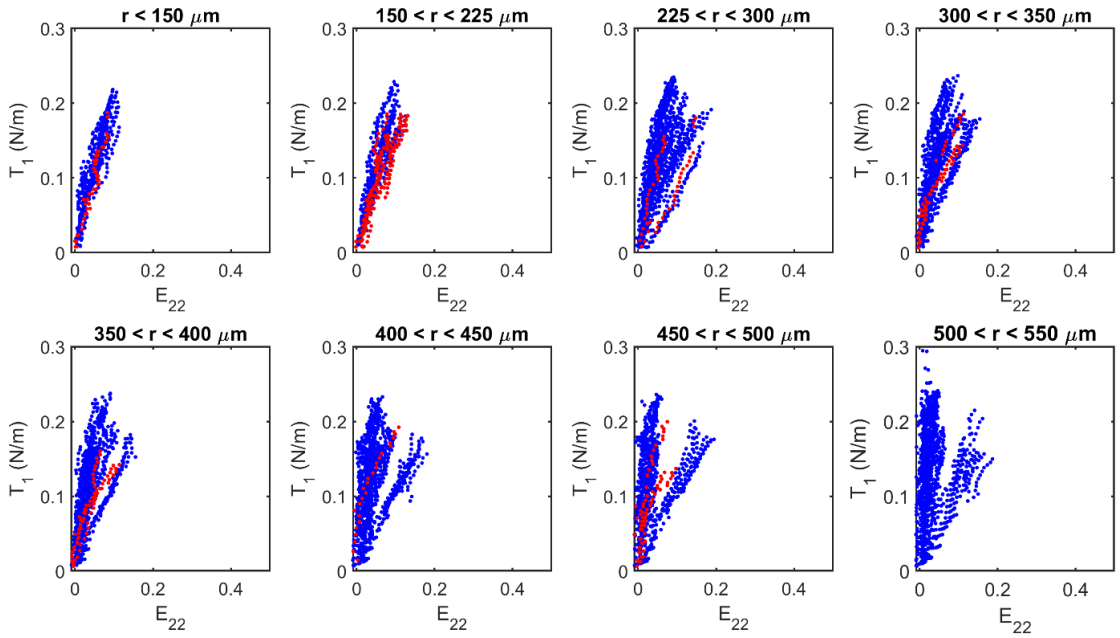


Figure S4.7. Properties of the biofilm adjacent to original (and secondary) defect are indistinguishable from surrounding material.

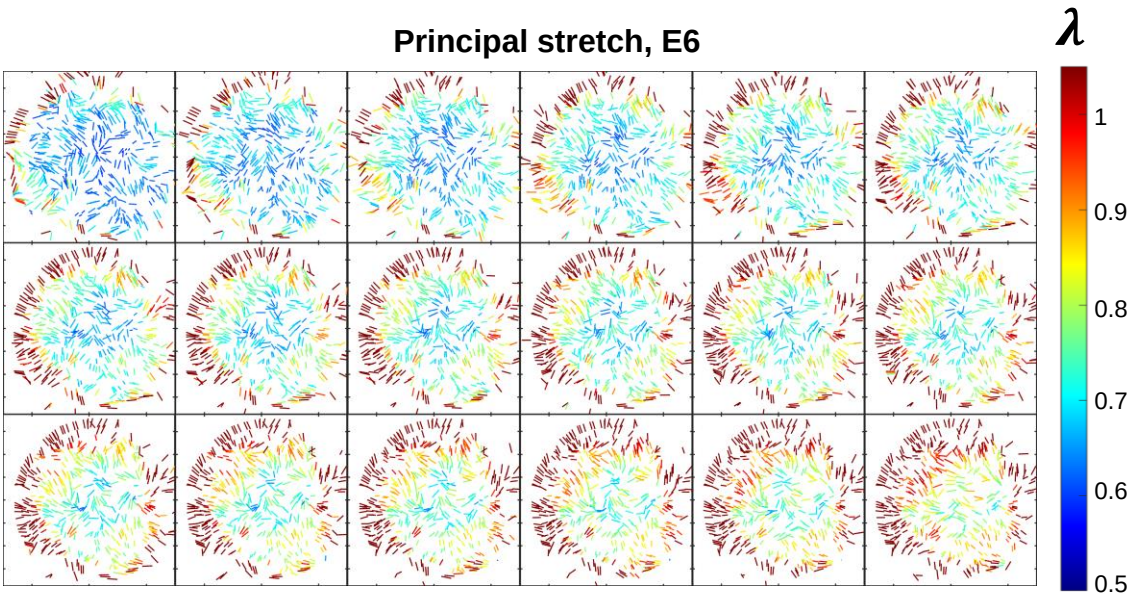


Figure S4.8. Heterogeneity as observed by plot of maximum principal stretches in E6. Data corresponds to Figure 14.19C in main text. Frames ordered left to right, top to bottom.

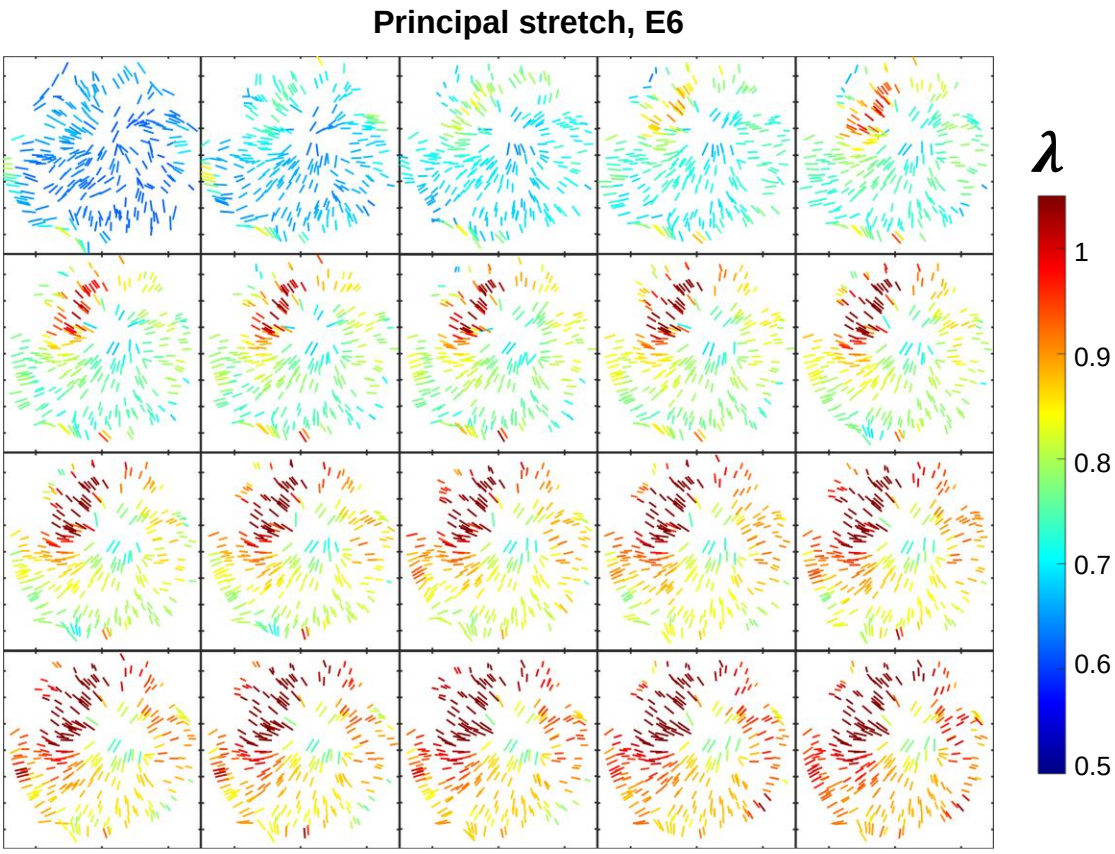


Figure S4.9. Heterogeneity as visible in plots of maximum principal stretch. Data corresponds to Figure 4.19B in the main text.

## References


1. Hall, M. S., Long, R., Hui, C. Y. & Wu, M. Mapping three-dimensional stress and strain fields within a soft hydrogel using a fluorescence microscope. *Biophys. J.* **102**, 2241–2250 (2012).

2. Neggers, J., Hoefnagels, J. P. M., Hild, F., Roux, S. & Geers, M. G. D. Direct Stress-Strain Measurements from Bulged Membranes Using Topography Image Correlation. *Exp. Mech.* **54**, 717–727 (2014).

3. Belytschko, T., Krongauz, Y., Fleming, M., Organ, D. & Liu, W. K. S. Smoothing and accelerated computations in the element free Galerkin method. *J. Comput. Appl. Math.* **74**, 111–126 (1996).

4. Humphrey, J. D., Strumpf, R. K. & Yin, F. C. P. A Constitutive Theory for Biomembranes: Application to Epicardial Mechanics. *J. Biomech. Eng.* **114**, 461–466 (1992).

5. Humphrey, J. D. Computer Methods in Membrane Biomechanics. *Comput. Methods Biomech. Biomed. Engin.* **1**, 171–210 (1998).

6. Hsu, F. P. K., Schwab, C., Rigamonti, D. & Humphrey, J. D. Identification of response functions from axisymmetric membrane inflation tests: Implications for biomechanics. *Int. J. Solids Struct.* **31**, 3375–3386 (1994).

7. Hsu, F. P. K., Liu, A. M. C., Downs, J., Rigamonti, D. & Humphrey, J. D. A Triplane Video-Based Experimental System for Studying Axisymmetrically Inflated Biomembranes. *IEEE Trans. Biomed. Eng.* **42**, 442–450 (1995).

*Chapter 5*

# Optical and mechanical insights into iridescent biofilms

## 5.1 Motivation

In Chapters 1-4, we described an apparatus and analysis protocols to characterize bulk and local mechanical properties of engineered biofilms. In Chapter 4, we showed tha that these films exhibit an isotropic response to equibiaxial stretch, and this isotropic nature is further confirmed by the microstructure (discussed below). In Chapter 5 we further consider this feature: what if a biofilm was not isotropic? How would its properties differ? Our journey to grow and characterize oriented biofilms is described in this chapter: we initially began with the same engineered biofilms described in Chapters 1-4, but soon realized that nature may have already created an ideal system that we could improve upon and characterize as a model highly oriented biofilm.

The engineered biofilms used in Chapters 1-4 had a somewhat isotropic microstructure in the regions used for the bulge test (Figure 5.1) which was in accordance with our mechanical measurements. Initially we attempted to induce local cellular order by various methods – for example, suction coating films at an angle under flow, but found that a persistent ordered microstructure was difficult to induce.

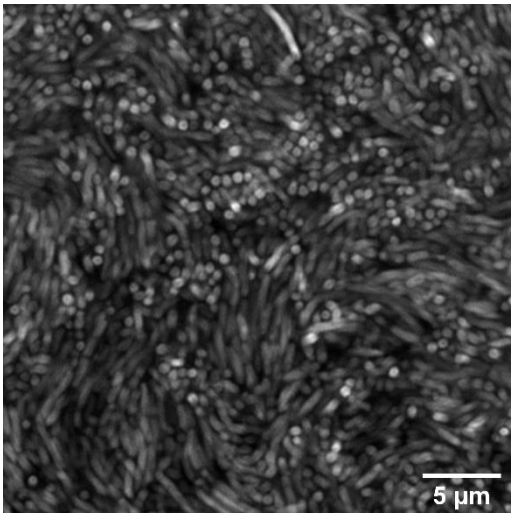


Figure 5.1. Confocal micrograph of engineered *E.coli* biofilms (here CE3) with isotropic microstructure. Imaging of biofilm with LSM 880 (Zeiss) with Airyscan.

We then turned to literature on naturally occurring biofilms that have spontaneous orientation and discovered a wealth of information on such species which, in addition to striking spontaneous orientation, also possess unique optical properties that result from the cell periodicity!

*5.1.1 Biofilms with ordered microstructure*

Iridescence, angular and wavelength dependent structural color, occurs via the interaction of light with periodically arranged structures of micron to submicron scale.

Prokaryotic iridescence is a striking feature exhibited by some strains of bacteria, mostly reported in Cytophaga-Flavobacterium-Bacteroidetes phyla[1–10]. In the appropriate environment, some strains form colonies that exhibit brilliant colors that depend on illumination angle and wavelength (Figure 5.2).

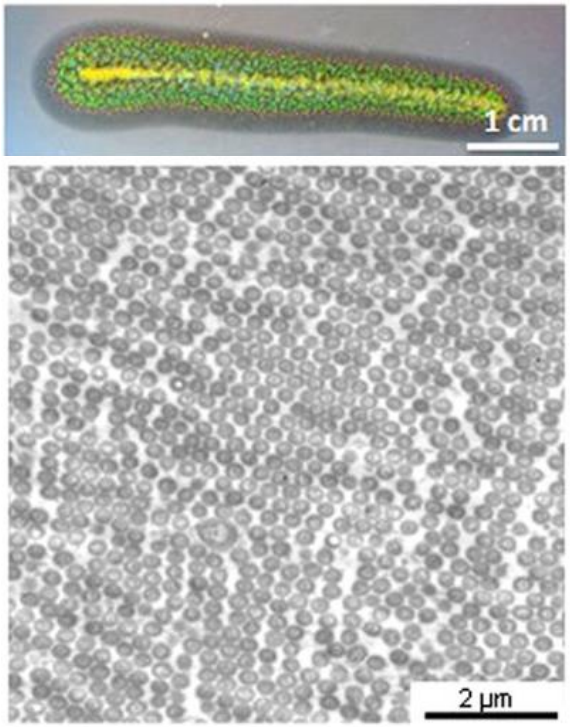


Figure 5.2. *Cellulophaga lytica* is one example of a naturally occurring biofilm that forms iridescent colonies (top) owing to hexagonal packing of the cells (bottom). Image adapted from [10] with permission (open access).

Transmission and Scanning Electron Microscopy (TEM and SEM) and genetic studies in the last decade,[3–10] including work by the Microbial Diversity Initiative, have shown that iridescent biofilms of *Cellulophaga lytica* (Kientz and coworkers[3,5,6,10]), *Flavobacterium sp. IR1* (Schertel and coworkers[4]), and certain *Tenacibaculum* species (Kientz and coworkers[3] and Kee and coworkers[11]) are some examples of bacterial subcommunities with orientational and positional order–equally spaced, uniformly aligned and hexagonally packed cells—extending over domains tens of microns in size[4,6,9,10]. Non-iridescent biofilms of these strains and others lack long-range order. Iridescent colonies strongly reflect wavelengths in the near UV, visible, and NIR regions, with green iridescence dominating at grazing incidence angles or near the center of the colonies and red and purple appearance near the advancing edges of colonies.[6,10] Iridescence color and intensity has

been tuned by adjusting genetic and environmental factors, including hypersaline growth conditions, growth temperature, colony thickness, cell shape distribution[5], genes involved in interactions with plant hormones[9] or transcription regulation, and interaction with algal polymers and indole derivatives.[7] Also among these factors, gliding motility stands out as a critical common feature enabling cells to recover their ordered structure and iridescence after disruption; without gliding motility they can only rely on growth and cell division to form sparse local order.[3,7–9]

We hypothesized that not only would these oriented biofilms serve as ideal materials for the study of cell anisotropy-dependent mechanical properties, they would also be interesting from the standpoint of optomechanical studies. The optical properties are directly dependent on cell shape and packing; we anticipated that bulk deformations of the material would be expected to change one or both aspects.

**5.2 Sample collection, isolation, and characterization**

Based on the fact that many iridescent microbes are polysaccharide degrading organisms, we anticipated that similarly iridescent species might be isolated from Pacific Coast environments due to the abundance of kelp and other marine algae.

We chose multiple sampling sites along the coast (full details with GPS coordinates in Table 5.1 below): the first two sampling sites were at Malibu Lagoon (Malibu, CA) both near the inner part of the lagoon and closer to the freshwater region of the Malibu Creek. The next set of samples was collected from Malibu Point Beach and comprised kelp leaves and seawater. The final sampling site was further along the coast in Solstice Canyon

(Malibu, CA). In particular, samples 5 and 7 from Table 5.1 were fresh kelp leaves from kelp that washed ashore shortly prior to sample collection.

Table 5.1. Sample collection (pH ~ 7 for all samples)

| # | GPS coordinates | Description | Temperature (°C) | Salinity(ppt) | Specific gravity |
|---|---|---|---|---|---|
| 1 | 34.033876, -118.684289 | Malibu Lagoon (ML): inner region of lagoon | 12.5 | 11 | 1.008 |
| 2 | 34.033895, -118.683187 | ML: closer to freshwater. | 9.4 | 11 | 1.008 |
| 3-7 | 34.031154, -118.682158 | Malibu Point Beach (MB): kelp samples | N/A | N/A | N/A |
| 8 | 34.031143, -118.682162 | MB: Seawater | 12.5 | 36 | 1.027 |
| 9 | 34.032859, -118.741627 | Corral Beach (CB): kelp sample | N/A | N/A | N/A |
| 10 | See previous | CB: Seawater | 17.4 | 35 | 1.027 |

All marine samples were collected between 11:08 and 12:15 PM at or after the onset of high tide conditions. Temperature was recorded on site; salinity was recorded after samples were transported back to the lab. Kelp samples were placed in Ziploc bags with sterile 1X Seawater Base (SWB) added while seawater samples were collected in 50 ml falcon tubes. All samples were stored in a cooler with gel packs for transport back to the lab.

Dilution and plating were performed within 5 hours of sample collection. Nutrient plates (1X Seawater Complete, SWC) were prepared the previous night to minimize moisture on the surface of the plate.

SWC and SWB were prepared based on protocols from Professor Jared Leadbetter. 1X SWB (per 20 L): NaCl (400 g), $MgCl_2.6H_2O$ (60 g), $CaCl_2.2H_2O$ (3 g), KCl (10 g). All

ingredients were purchased from Sigma Aldrich unless otherwise specified. The recipe was scaled to 2 L each time and autoclaved. 1X SWC: 1X SWB (1 L), Bacto tryptone (5 g, Thermo Fisher Scientific), yeast extract (1 g, Thermo Fisher Scientific), agar (15 g for 1.5% plates, adjusted accordingly for other percentages) and 1 M MOPS adjusted to pH 7.2 (5 mL) were autoclaved; pre-autoclaved glycerol (3 mL) was then added, mixed, and poured into Petri dishes. Dye (Acid Black 2 at  100 mg/L); first batch of plates used India Ink diluted 500X from original stock) was added and mixed prior to pouring. The initial set of plates was left on the bench overnight prior to using but later protocols were modified (as specified in the relevant sections below) to adjust and control for variables such as temperature of the solution prior to pouring, Petri dish lid being on or off while cooling, cooling/solidification time, cooled temperature of agar prior to inoculation, etc.

Cultures transported from collection sites were serially diluted 0-3 times and 100 µL of final volume was spread on 1X SWC plates and grown at 15°C, with one set of the final dilution grown at 25°C for comparison. Colonies were counted for each dilution (Table 5.2), starting day 2 (no colonies were observed on day 1). Colony counts at 25°C not shown below since none of the final isolated colonies were selected from these plates.

| Table 5.2. Colony growth | | | |
|---|---|---|---|
| # | Day 2 (0/1/2/3D) | Day 3 (0/1/2/3D) | Day 4 (0/1/2/3D) |
| 1 | >100/26/2/0 | >100/44/1/0 | >100/54/7/1 |
| 2 | >100/21 | >100/28/4/1 | >100/33/5/1 |
| 3 | 15/0/0/0 | 17/1/0/0 | 17/0/0/0 |
| 4 | 12/0/0/0 | 22/2/1/0 | 28/2/1/0 |
| 5 | >200/>100/78/15 | >100/>100/74/16 | >100/>100/69/15 |
| 6 | >200/>100/25/8 | 20/8/0/0 | >100/>100/18/8 |
| 7 | 103/24/0/0 | >100/49/0/0 | >100/64/2/2 |
| 8 | 18/2/0/0 | 26/2/1/0 | 41/3/1/1 |
| 9 | 14/1/0/0 | 96/10/0/0 | 118/16/0/0 |
| 10 | 9/1/0/0 | 12/0/1/0 | 12/0/1/0 |

In the initial set of plates, multiple colonies were observed to be iridescent in transmitted but not reflected light. Although these were isolated and sequenced as well (Figure S5.1-2), further studies are not reported here. Four weeks after the original inoculation, microbes iridescent in reflection had still not been observed and so we attempted to make replica plates of all of the original plates onto new nutrient media containing India Ink.

Here, iridescence in reflection was observed on from two plates: the "0" dilution plates from Samples 5 and 7 (kelp leaves from the Malibu Point Beach, Figure 5.3) and restreaked three times for purity on SWC agar; single colonies appeared after 24-36 hours of incubation at 15°C. The colonies were submitted for 16s rDNA sequencing with universal bacterial primers (Laragen) and identified using the RDP database. All of the iridescent colonies were found to be from various strains of *Cellulophaga lytica:* e.g. *Cellulophaga lytica* str. DSM 7489 (NR_074464.1, 100% sequence identity), referred to as "R1" in

further text, *Cellulophaga lytica* str. IFO16021 (AB032512.1, 98.1% sequence identity), referred to as “R2”, and *Cellulophaga lytica* str. IMCC34136 (MG456766.1, sequence identity 100%), “R3” in further text.

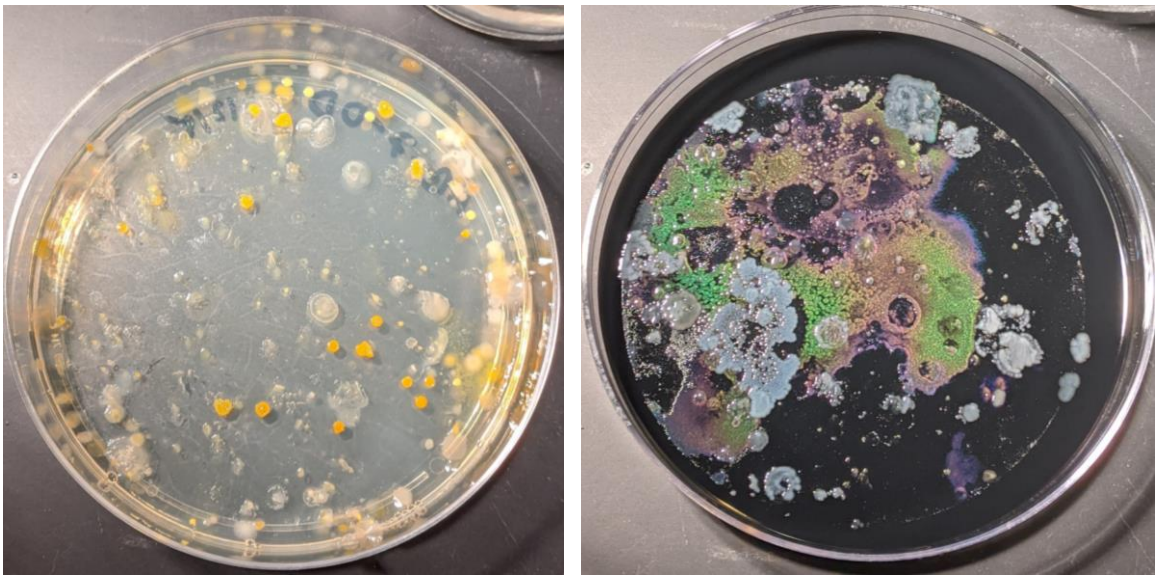

Figure 5.3. Left: Sample 5, original plate. Right: Sample 5, replica plate with black ink shows colonies iridescent in reflection.

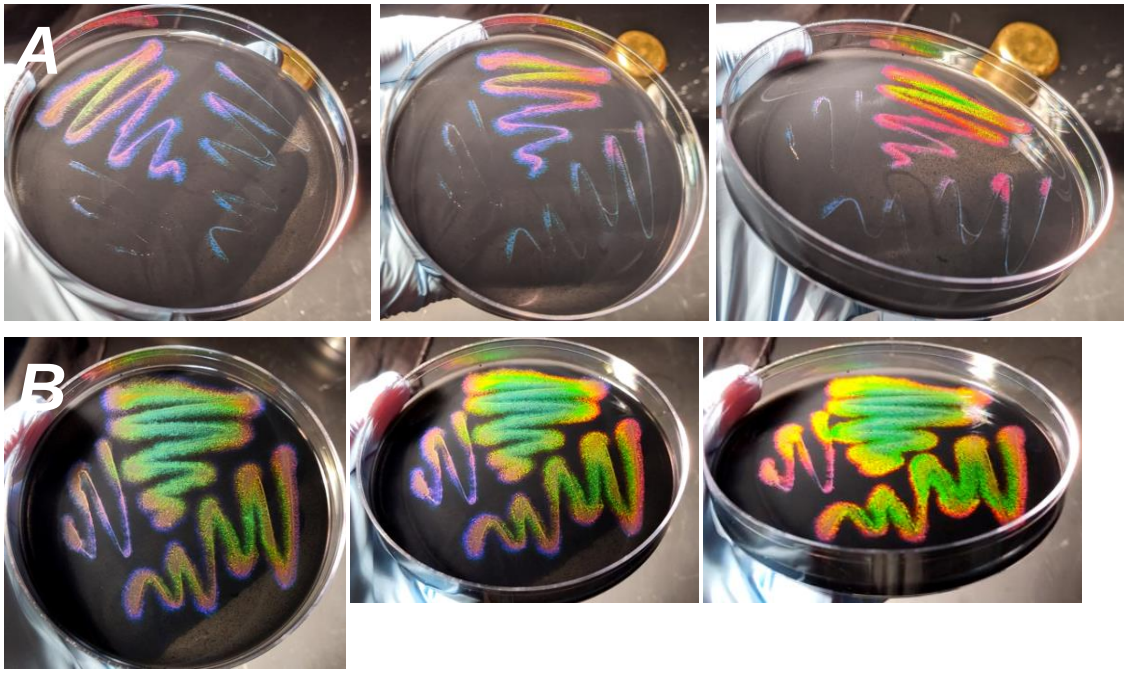


Figure 5.4. “R3” iridescent *C. lytica* A) purple to pink iridescence in early growth transitions to B) bright green iridescence as colonies grow thicker

R3 displayed blue-purple-pink iridescence during early growth (48 hours) while mature colonies (120 hours) displayed a striking green iridescence at the center transitioning to purple at the edges (Figure 5.4). In contrast, R2 was primarily green (Figure 5.5A) with reddish edges throughout growth. All colonies showed what we hypothesized to be spontaneous mutations as well – for example sudden transitions from one morphotype to another (Figure 5.5B, C) that persisted through successive rounds of restreaking.

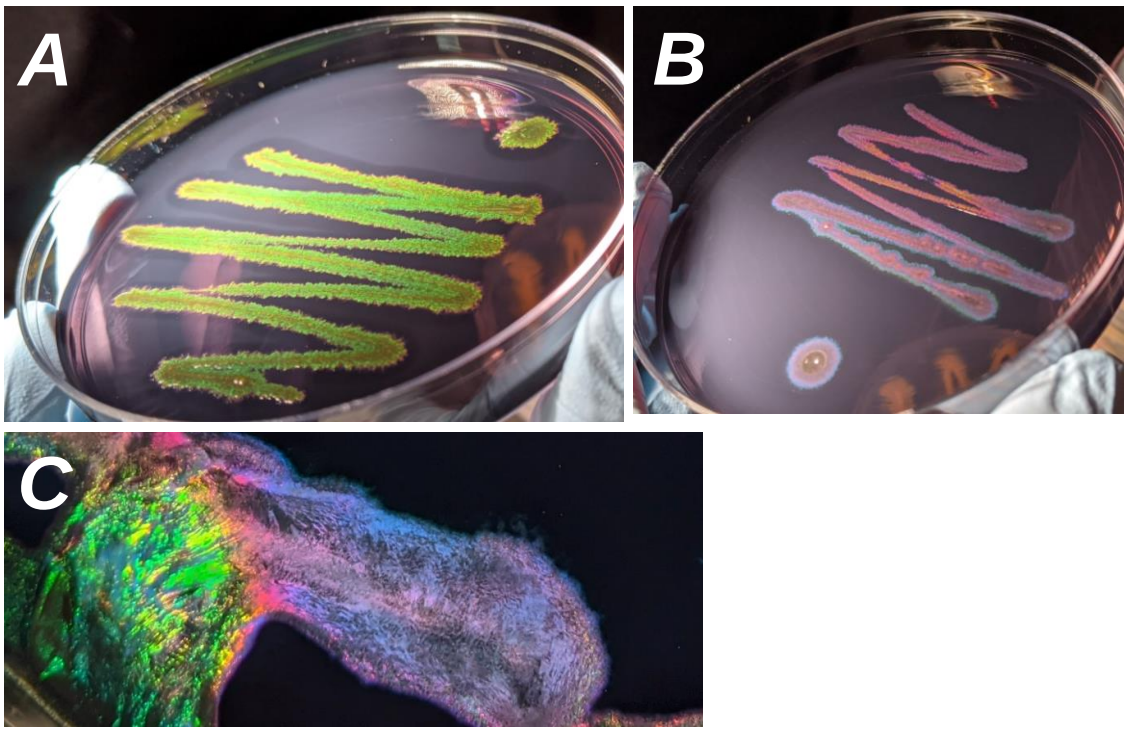


Figure 5.5. R2 primarily shows green and red iridescence (A). Colonies can display spontaneous mutations. B) Purple-blue morphotype isolated from a spontaneous mutation of R2. C) Example of regions of mutation during growth.

Phase contrast micrographs were used to compare cell morphologies and confirm the presence of orientation within the colonies. A 200 µm pipette tip was used to scrape the center of 5-day old colonies of R2 and R3 and the scraped biofilm was suspended in 2 µL of 1X SWB. The suspension was dropped onto a 25 x 50 mm No. 1.5 coverslip and covered with a 1 mm agarose pad. Phase contrast imaging was performed on a Zeiss LSM 800

inverted microscope with a 100×/1.4 NA Ph3 objective. Depending on field of view and level of zoom needed, images were captured either using the T-PMT or using the attached color CCD camera (Zeiss Axiocam 506). Despite the agarose pad, cells, especially near the edge, showed rapid movement. Phase contrast micrographs revealed that R3 and other mutations with blue-purple coloration (Figures 5.6-5.7) had longer, curved (and possibly thinner) cells while R2 and other green-red strains had shorter, rod-like cells with little to no discernable curvature.

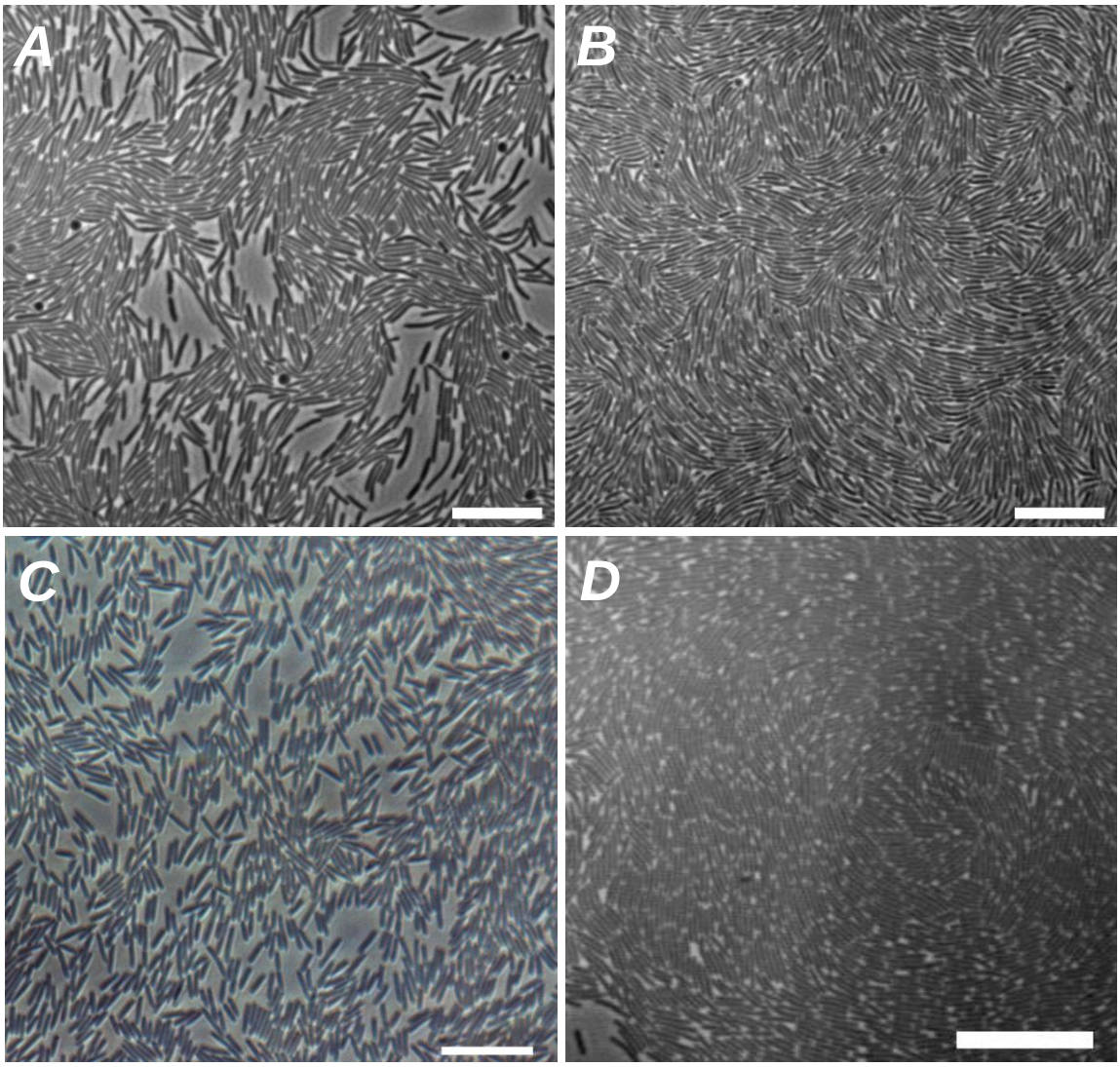


Figure 5.6. Phase contrast micrographs of R3 (top, A-B) vs R2 (bottom, C-D). R3 cells are longer and curved both near the edge (A) and center (B). R2 cells are shorter and less curved both near the edge (C) and center (D). Scale bar 10 μm.

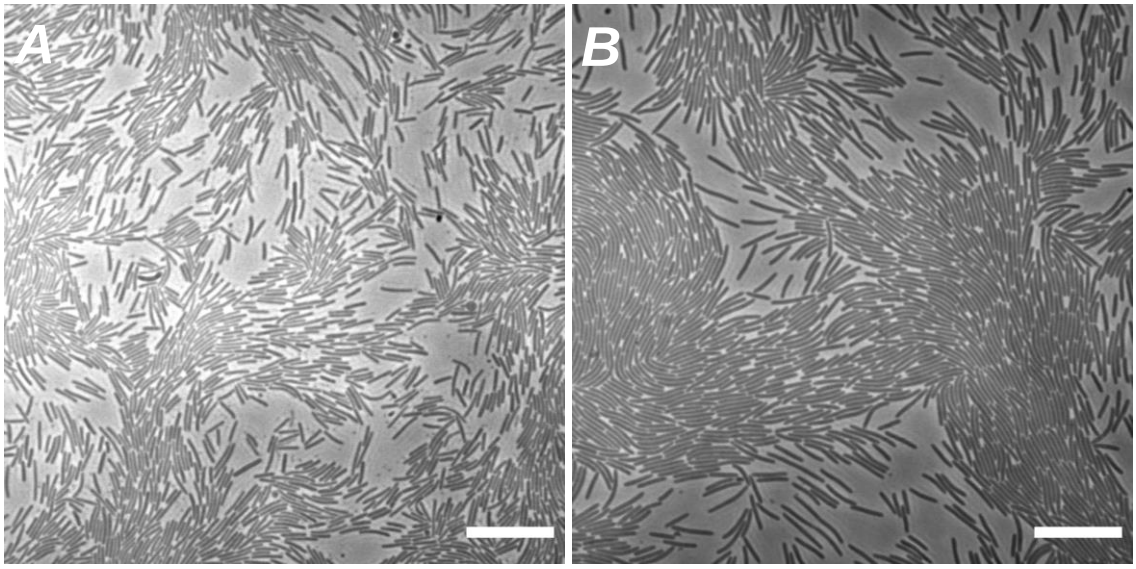


Figure 5.7. Cells from R2 biofilm with spontaneous mutation in Figure 5.5C. A) Scraped from green outgrowth of B) main purple streak. Cells in (A) are noticeably shorter and less curved than those in (B). Scale 10 μm.

While not detailed here, this curvature may make R3 and other similarly packed and oriented microbes interesting from the perspective of colloidal liquid crystals for their structure and optical properties.

### 5.3 Wildtype C. lytica films show oriented domains of 10-20 μm length scale

Further experiments below are detailed for R2 since the iridescence was consistent across a range of agar stiffnesses and inoculation conditions (biofilm grown from streaking a solid colony vs. a suspension in SWB).

Wildtype *C. lytica* exhibited oriented domains in the 10-20 μm length scale (Figure 5.8), but without any macroscopic orientation in-plane or through the thickness of the film. This feature has been reported in other films as well[9] and is the reason iridescence is visible independent of in-plane rotation angle "ϕ". Phase contrast and polarized light microscopy were performed on intact colonies or regions of the original streak grown on ~1-2 mm thick SWC plates with the section to be imaged directly cut with a scalpel, inverted onto a cover

slip, and imaged in order to preserve the internal structure. Polarized light microscopy was performed at 10× magnification with a Zeiss Universal microscope equipped with a Lumenera INFINITY5-3 camera; images were taken at 20° rotation increments through crossed linear polarizers. Both measurements confirmed the presence of local domains but lack of bulk orientation.

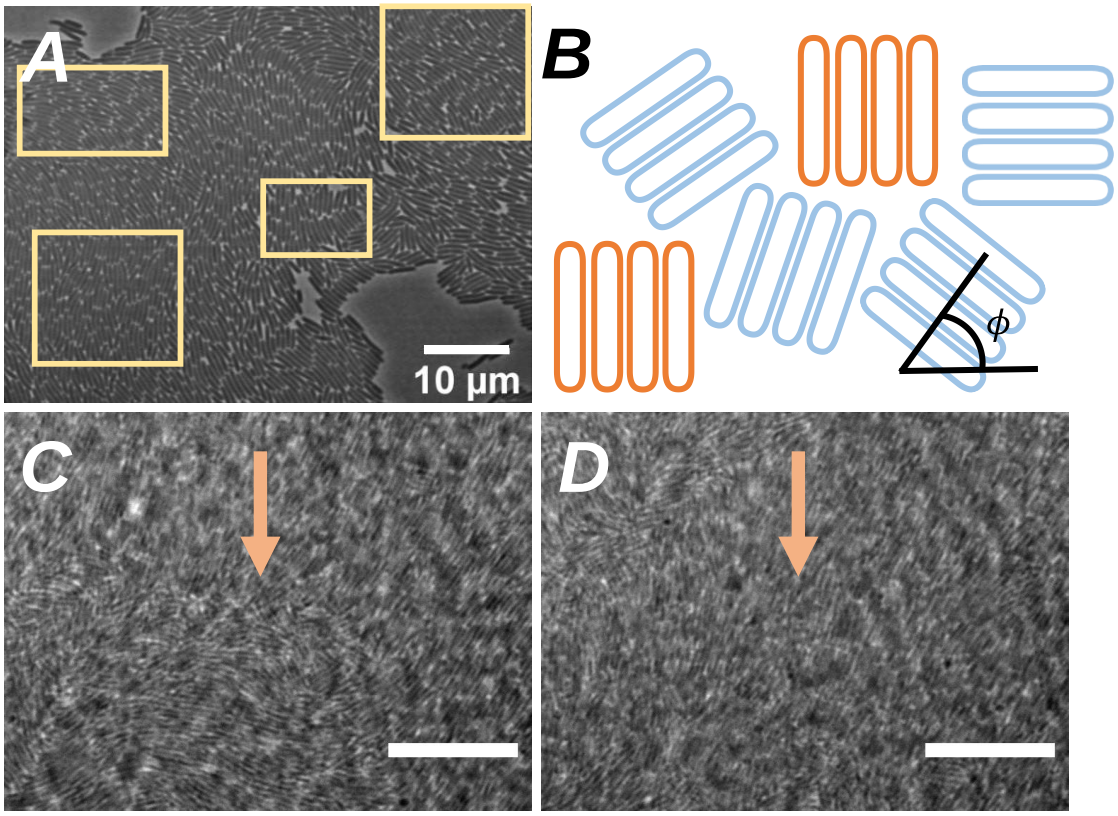


Figure 5.8. *C. lytica* biofilms show domains of orientation but no macroscopic orientation preference either (A) in plane or (C, D) out of plane. A) Rectangular highlights indicate short regions of orientation. B) Schematic depicting domains of orientation with varying in-plane rotation angle ϕ. Only domains highlighted in orange will contribute to iridescence visible in the plane perpendicular to their orientation. Schematic based on illustration from [9]. C, D) z-scans at varying depths in the film. Arrows highlight an example region with orientation varying through the thickness. Scale 10 µm.

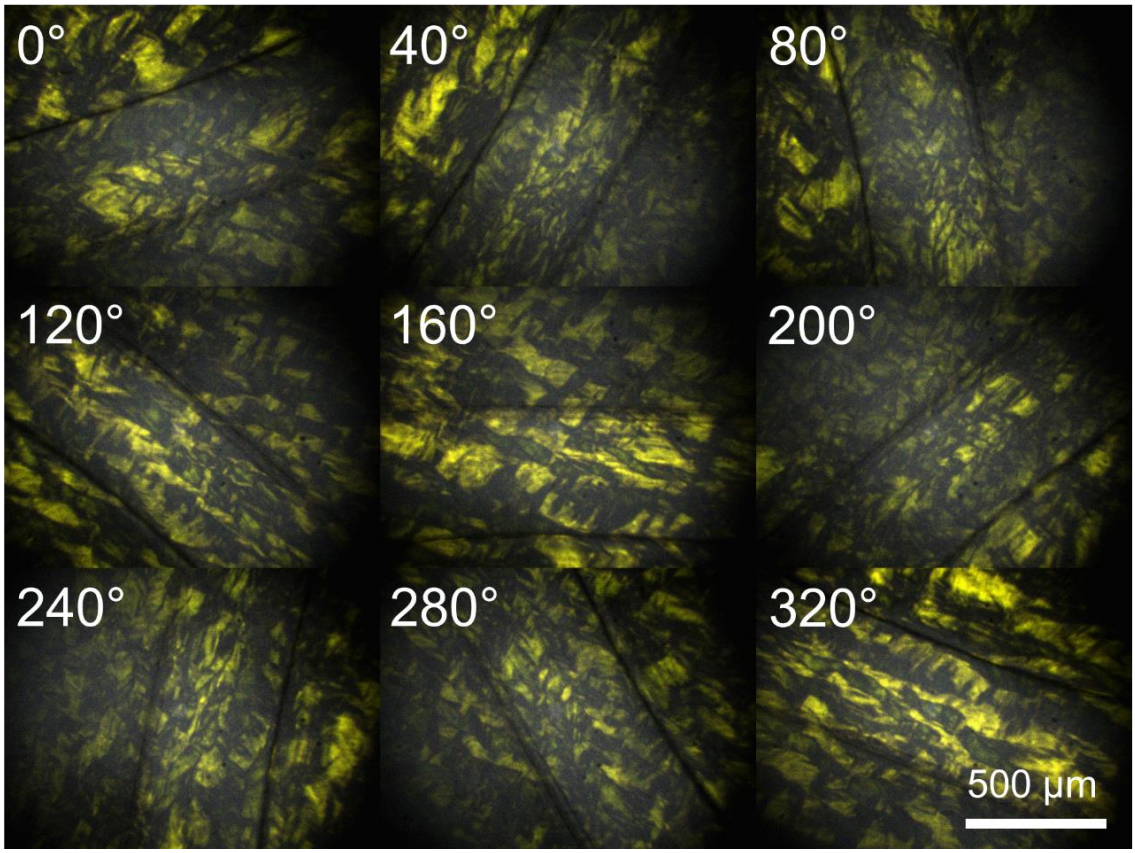


Figure 5.9. Polarized light microscopy images of R2 shown in 40° increments of rotation. Original streak visible as dark horizontal lines in images. Individual oriented domains display maximum birefringence when aligned at 45° to the polarizers and complete extinction when parallel to either polarizer. Some color distortion was observed due to the camera.

For purposes of bulk characterization, we required orientation over larger length scales, ideally hundreds of microns to millimeters. Thus, we sought ways to accomplish this.

### 5.4 Inducing long range orientation in C. lytica biofilms

Initially, we hypothesized that, since agar was both a source of nutrients and a source of stiffness for the cells, changes in agar concentration in the nutrient medium might result in interesting biofilm properties. We attempted to prepare gradients of agar by tilting the empty Petri dish roughly 4-5° prior to pouring the first nutrient solution (e.g. with 0.3% agar), then setting the plate flat and pouring the other percentage (1.5%). However, preparing gradients this way proved to be challenging and resulted in plates with inadequate mixing and only partial overlap of the two agar percentages. Surprisingly however, these imperfect nutrient plates yielded biofilms with "striped" or "banded" regions (Figure 5.10, representative camera image from repeated experiment with black dye to highlight banded morphology) that proved to correlate to long range orientation in the hundreds of microns to millimeter length scale! We confirmed this long range orientation with phase contrast microscopy (Figure 5.11).

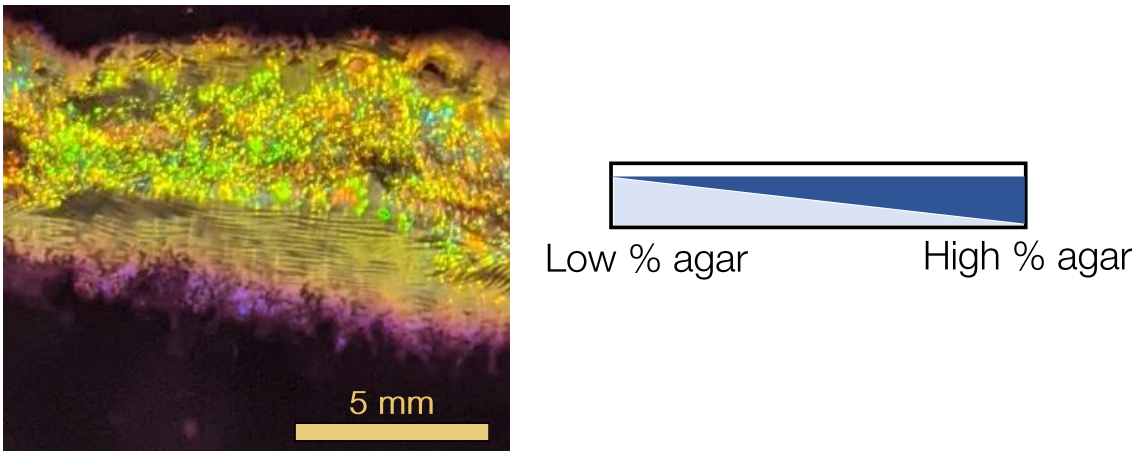


Figure 5.10. Nutrient plate with imperfect agar gradient (here, 0.3% and 1.5%) resulted in banded morphology in regions of the film.

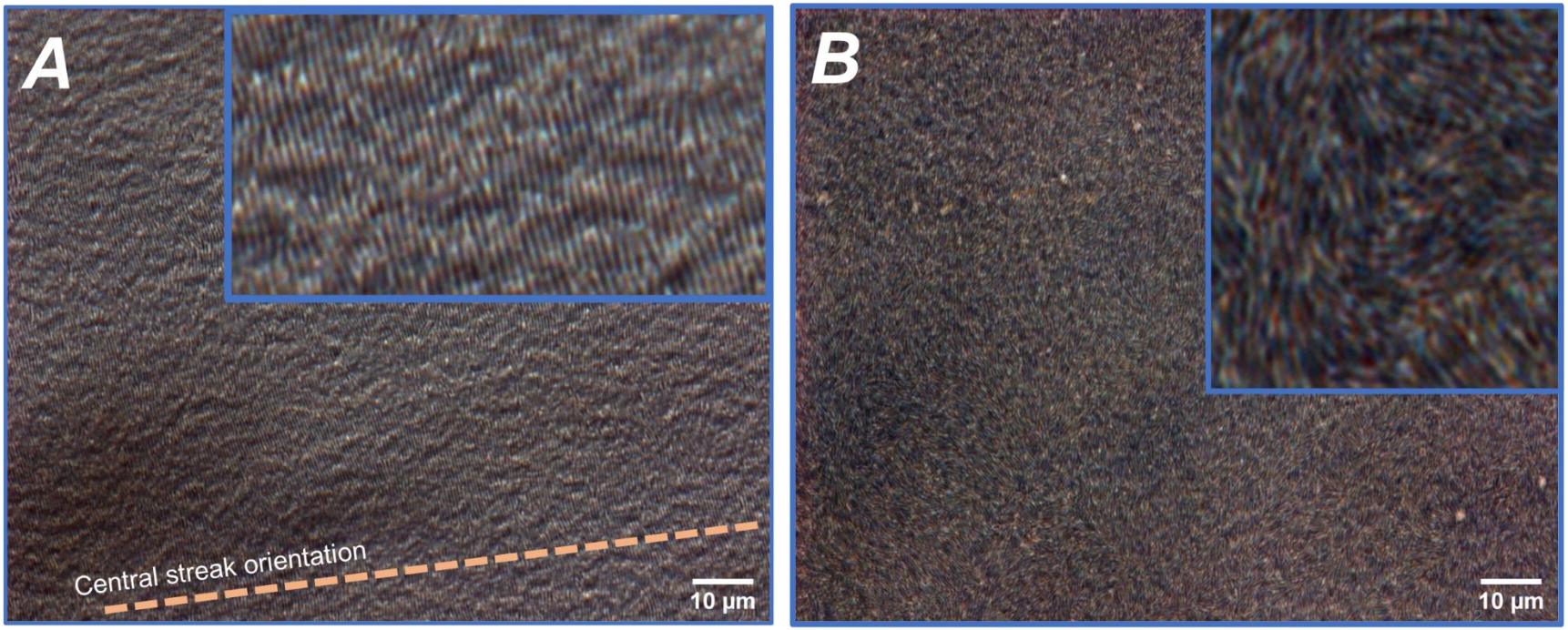


Figure 5.11. Long range orientation extends for millimeters in banded region of the film (see Figure 5.10). A) Cell orientation is perpendicular to central streak direction. B) Central region of the film (without banded morphology) lacks long range orientation, similar to wildtype film.

With this unexpected result, we then sought to find an explanation and screened a variety of conditions detailed briefly below.

*5.4.1 Screening conditions*

The various conditions screened are described briefly below; results were initially confounded by the presence of an external source of variability. This variability was identified later and thus experiments after that point are described in greater detail. All experiments were performed for plates with and without dye. Different dyes were initially screened (Waterman, India Ink, Acid Black 2) for their impact on colony growth for 4 iridescent mutants; Acid Black 2 and India Ink were found to not affect colony growth. Acid Black 2 was used for further experiments.

Initially the long range orientation phenomenon was observed on plates with 0.3%-1.5% agar and not on 1.5% agar. 0.3% agar was difficult to work with as a control due to its release of large amounts of fluid (as agar was degraded by the microbes) that would wash away the colony. We found that 0.7% agar could act as an alternative low stiffness agar and repeated the experiments above with sets of plates: 0.7% only, 1.5% only, or 0.7%-1.5% with colonies streaked along only the 0.7% side, only the 1.5% side, perpendicular to both, or two streaks at a time in various combinations of orientations and solid vs. liquid cultures. The purpose of these experiments was to determine whether this long range orientation was dependent in any way on the relative orientations of the two agar stiffnesses and/or the presence of volatile/other compounds that could travel between multiple colonies on the same plate. Surprisingly, we observed a contrasting result in this experiment: any plate that had either 0.7% agar only or 0.7%-1.5% agar *and* a few of the

plates with 1.5% agar showed patches of long range orientation. The long range orientation was more visible in any plate that had 0.7% agar and only formed in small local regions of the 1.5% plate. On the other hand, a sufficiently thin substrate (< 1 mm) would not result in long range orientation even with 0.7% agar.

Simultaneously, we screened other conditions that we hoped could induce bulk orientation more consistently, without success: bulk orientation with growth on a rocker (here we tested both solid inoculum and liquid suspensions and the effect of droplet flow prior to allowing the colonies to grow as well, for 0.3%, 0.7%, and 1.5% agar), growth on a substrate that had 10% compression based on reports of polymertropism of rod shaped bacteria[1], manual shearing of solid inoculum (glass slide) and of a viscous suspension of the inoculum (doctor blade)). We also attempted to grow the inoculum under continuous flow of SWB but found that the biofilms formed were < 10 μm in thickness after 7 days of growth and tended to preferentially grow in the regions around the flow.

At this time, we noted a key feature present in all of the plates that developed long range orientation. All of these plates developed droplets of fluid that would inflate in size between 24 and 48 hours after the initial inoculation (Figure 5.12). The droplets would then slowly disappear, being reabsorbed into the media. Any areas with droplets would result in clear long range orientation (Figure 5.14).

Figure 5.12. Fluid droplets developing on nutrient plate. Some droplets (such as those above) were localized to one edge of the colony and developed into regions of the biofilm oriented outward from the center (Figure 5.13).

Long range orientation was confirmed using camera images taken at different in-plane rotation angles ϕ, with a bright light source fixed at 70° with respect to the plate (Figure 5.13) and a cellphone mounted as the camera at 40°. The idea was that only the region of the film with the correct orientation would appear visible.

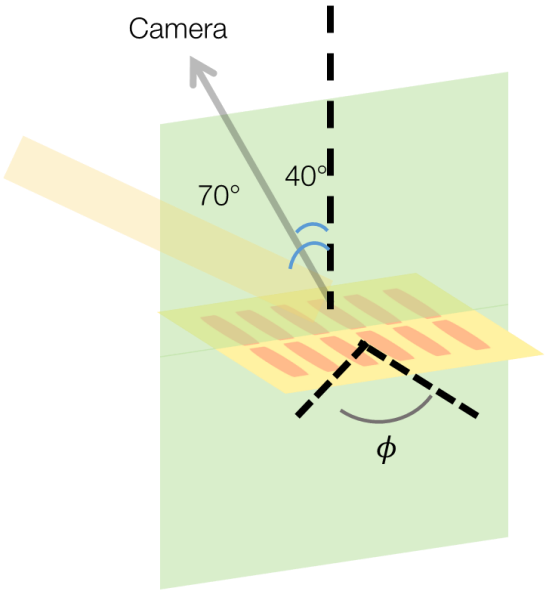


Figure 5.13. Setup for imaging of long range orientation.

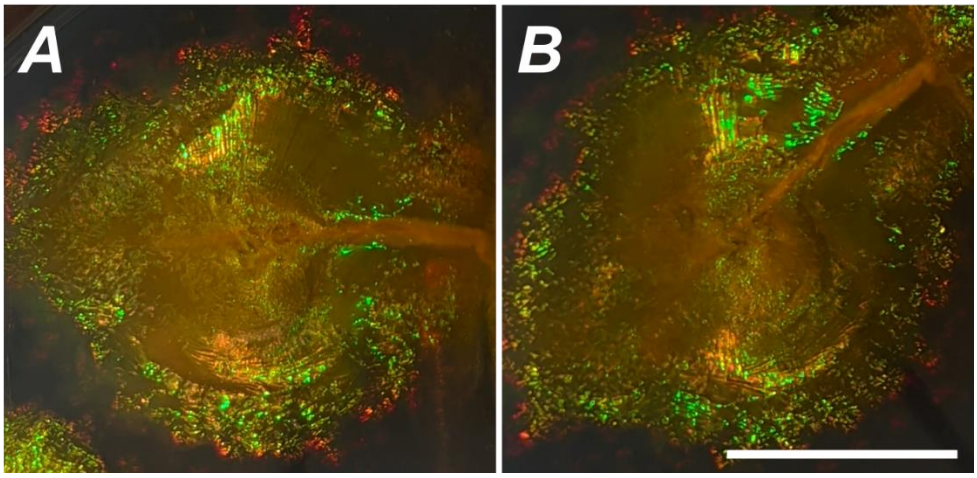


Figure 5.14. Long range orientation (~5 mm) in a circular pattern as "spokes" oriented outward.

Droplets that formed at the edge of a colony (Figure 5.13) resulted in patterns of orientation similar to a wheel with spokes pointed outward (Figure 5.14), showing only the regions perpendicular to the direction of imaging as the rotation angle was changed ($\phi$).

We hypothesized that the fluid might somehow be connected to the long range orientation, and/or might promote cell mobility across the agar surface. Thus, we screened possible conditions that might promote the drawing out of moisture from the agar and/or improve motility across the surface of the (0.7%) agar (various synthetic polymers, surfactants in culture vs. in the medium, and surfactant gradients). Here, we observed a surprising result: *all* of the plates formed large droplets after 1-2 days that persisted for more than 5 days. After this, some degree of long range orientation was present in every colony that grew including the control, with all streaks having grown to double or triple their usual width. One plate (with 0.002 wt% DEAE dextran added to the cell suspension) developed bulk orientation over a 6 $cm^2$ patch, the largest we had observed (Figure 5.15).

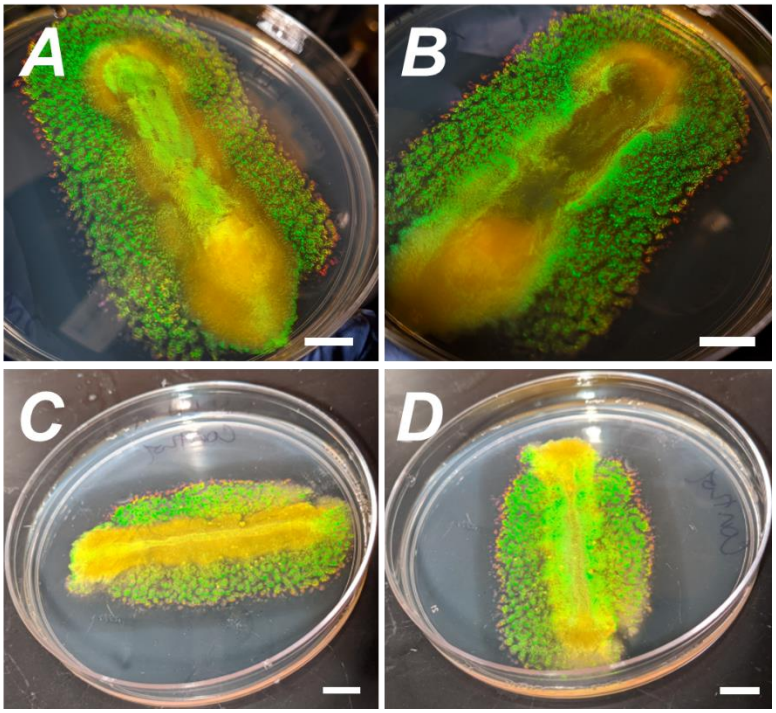


Figure 5.15. Long range orientation present in multiple conditions A,B) Long orientation formed from cell suspensions with DEAE dextran added. (B) depicts disappearing region when plate is rotated. C,D) Control plate also showed 5-6 mm halo of long range orientation. Camera images for A and B not captured using the setup described previously.

The presence of orientation in the control sample along with the fact that these results could not initially be replicated suggested an external source of variability. We then tested the effects of the following factors: humidity, the amount of time the agar was allowed to dry with the lid partially placed on top, and cell density.

16 plates with two replicates per condition (8 conditions total) were prepared. 1X SWC with 0.7% agar was prepared and autoclaved and immediately poured (25 mL) into each of the plates. Half the plates were left open for 10 minutes and then cooled for the remainder of the time with the lid on, while the remaining plates were left open to cool for one hour prior to placing the lid back on. The final temperature of the cooled agar (as measured by an IR temperature meter) was 13.5°C. The temperature of incubation varied between 13.5

and 15°C but was consistent for all the plates. Half of the plates were inoculated with an R2 suspension in SWB of OD 0.5 and the other half with OD 0.05. Half the plates were placed for incubation in a chamber with a full dish of water (relative humidity measured with a calibrated hygrometer to be 72%) while the other half were placed in room conditions (relative humidity measured to be 41.6%). The presence or absence of the fluid droplet was tracked as a proxy for long range orientation, since they were observed to be connected. Humidity was also measured again after 48 hours and found to be 71% in the chamber with the water dish and 40% in the room.

Results below are reported as "+" for droplet formation and "-" in the absence of a droplet, with reported results in the order 24/48/72 hours for top row corresponding to 24 hours and bottom row corresponding to 72 hours.

Table 5.3. Effect of humidity, dry time, and cell density on long range orientation

| High humidity | | | | Low humidity | | | |
|---|---|---|---|---|---|---|---|
| 10 minutes | | 1 hour | | 10 minutes | | 1 hour | |
| OD 0.5 | OD 0.05 | OD 0.5 | OD 0.05 | OD 0.5 | OD 0.05 | OD 0.5 | OD 0.05 |
| + | + | - | - | + | + | - | - |
| + | + | - | - | + | + | - | - |
| + | + | - | - | - | - | - | - |

In conclusion, we determined that the humidity and drying time were key factors, suggesting that the original hypothesis was correct in that the droplet was related to fluid being drawn out of the nutrient agar. This also supported the evidence that lower percentages of agar more often led to colonies with long range orientation. The role of humidity also explained the external variability we observed in previous experiments since,

depending on the outside environment, the humidity in the room could at times drop to as low as 7% or approach 70%.

Next, we set up experiments to vary cell density and bulk tilt together to assess whether there was an optical condition for the formation of long range orientation. 3D printed supports at various slopes from 0 to 10° were used to impose bulk tilt conditions. Frozen stock of R2 was grown in liquid (1X SWC) culture for 72 hours after which the suspension was centrifuged to pellet the cells and the pellet was resuspended in 1 ml of 1X SWB. The suspension was diluted either 0, 2, 5, 10, or 100 times and each dilution was denoted #1-5 respectively (with $OD_{600}$ measured to be 0.97, 0.658, 0.277, 0.147, and 0.021 respectively). 1X SWC plates were prepared as described previously and poured and allowed to dry with the lid completely on until the plates reached 15°C. 2 µl of each suspension was placed on each plate for a total of 5 droplets (Figure 5.16). Two extra sacrificial plates were used to collect the fluid after 48 hours and measure the mass. Due to difficulties in humidity control with the original setup shown in Figure 5.16A, we placed the plates and 3D printed slopes as is into a sealed chamber. The chamber was covered with Velmex window tint cut to size to avoid changes in light conditions and accommodate fluorescently labeled samples, and we placed a humidifier (Levoit) with tunable humidity control inside (Figure 5.17), with a laptop fan to circulate air. We observed that there was roughly an 10% discrepancy between the values measured by the hygrometer and those achieved by the humidifier with a higher value observed than set. For example our experiments targeted a humidity of 75% (the maximum set by the app) but we frequently measured values of 80-82%.

A second set of plates were placed in ambient conditions at RH = 28% and compared after three days of growth.

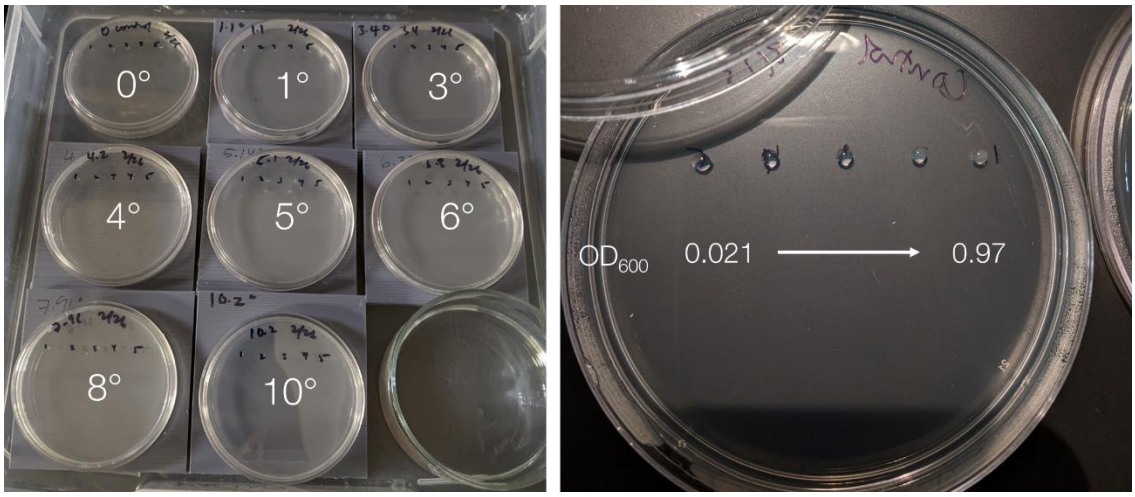


Figure 5.16. Cell density and bulk tilt experiment


Figure 5.17. Humidity chamber for growth

*5.4.2 Results: Humid conditions promote long range orientation*

We observed three main results. First, as expected, increased tilt did lead to increased long range orientation (Figure 5.18). Second, increased OD also led to increased long range orientation (Figure 5.18B, C). Third, the volume of fluid in the inflated droplets collected from the sacrificial plates suggested that the droplet volume grew by over ten times within

48 hours. Re-streaking the cell suspension in these droplets onto new plates did not result in long range orientation.

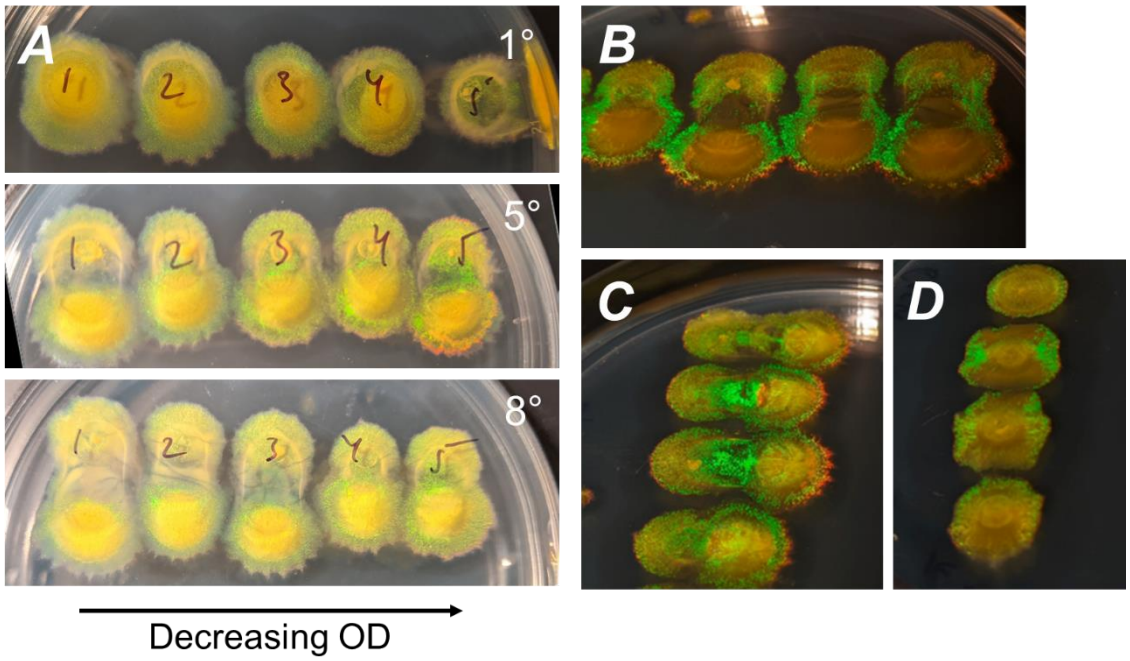


Figure 5.18. Effect of OD and bulk tilt on orientation in humid growth conditions. A) Bulk tilt results in increasing long range orientation. B, C) Long range orientation is visible as patches of the biofilm that appear only at a specific angle ϕ and disappear at other angles. D) Biofilm with no (deliberate) bulk tilt also showed orientation outwards from the central point of inoculation.

Surprisingly, bulk tilt was useful but not necessary for long range orientation at all, with even the control plate showing spoke-like orientation outward from the central point of inoculation (Figure 5.18D). On the other hand, all biofilms grown in low humidity conditions did not show long range orientation despite both increasing cell density and bulk tilt angle (Figure 5.19).

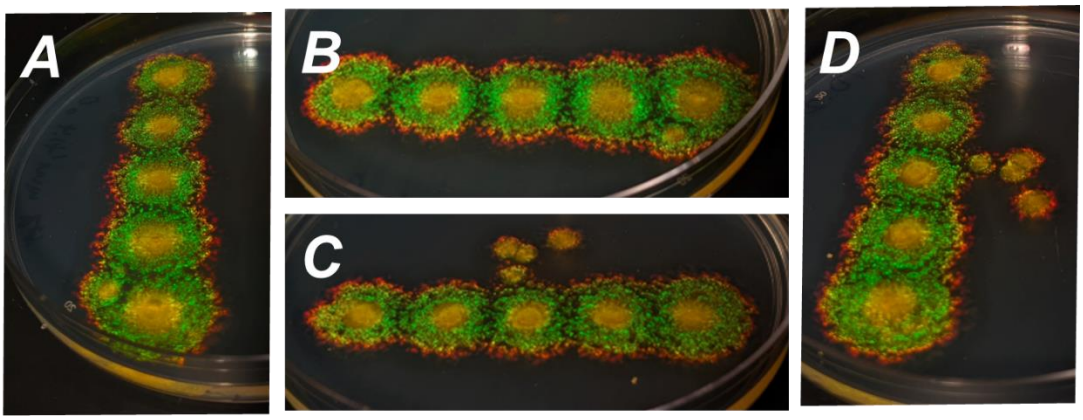


Figure 5.19. Biofilms grown in low humidity conditions do not show long range orientation despite bulk angle. A, B) Control sample (no deliberate tilt): the biofilms at different ϕ do not show discernable patches appearing and disappearing, characteristic of long range orientation. C, D) A 10° tilt also does not induce long range orientation.

Biofilms already grown under low humidity conditions also did not develop long range orientation once they were placed in high humidity conditions (Figure 5.20).

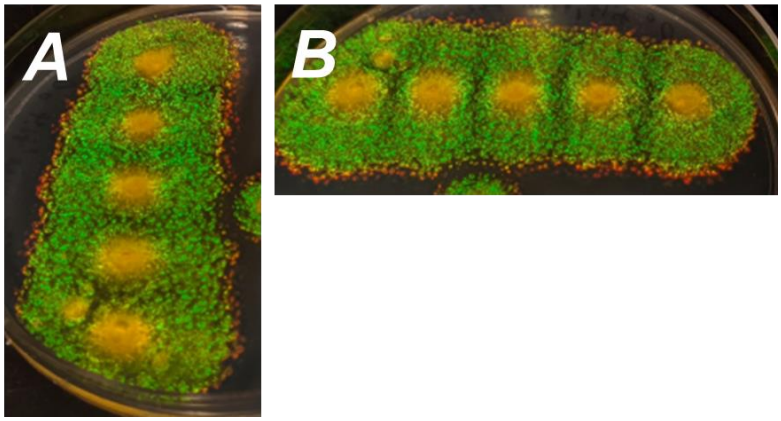


Figure 5.20. Control biofilm (Figure 5.19 A,B) placed in humidity chamber for 3 days does not develop long range orientation.

To confirm long range orientation, we built a goniometer spectrometer (Figure 15.21) based on work by Schertel and coworkers[2] and Kientz and coworkers[3], adapted to a rotating breadboard (RBB12A, Thorlabs) using an available Ocean Optics light source (HL-2000-HP-FHSA) and spectrometer (Thorlabs CCS200). The sample was mounted at the center

on a one-axis 100 mm translation mount (Thorlabs, XF100) for future studies on combined mechanical-optical measurements. Spectra were acquired between 360 and 900 nm. UV wavelengths could not be collected due to the limitations of the light source.

We observed characteristic scattering along the plane perpendicular to cell orientation, but not when the sample was rotated 90° in-plane (ϕ). Incident angle was fixed at 60° (Figure 5.22).

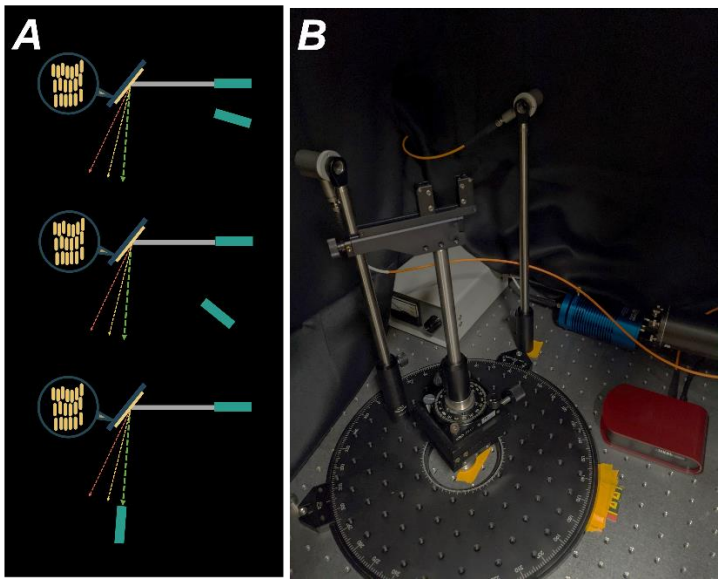


Figure 5.21. A) Schematic of goniometer spectrometer setup: detector rotates around sample detecting scattered light. B) Photo of setup.

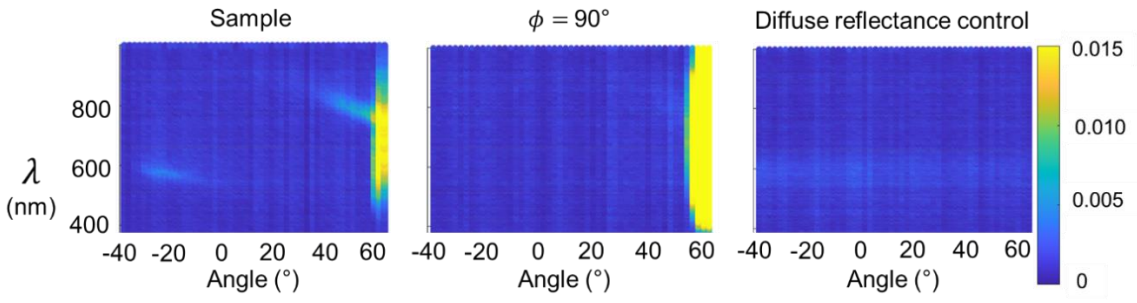


Figure 5.22. Scattering is dependent on in-plane rotation for samples with long range orientation.

The next step was to determine the connection between humidity and orientation: why would moisture be drawn out of the agar, and why would that result in long range orientation?

Based on our experiments, it appeared to be a physical phenomenon. Aspirating the droplet and placing it on a new plate did not result in long range orientation in the new plate, and placing a colony that had already been grown under low humidity conditions back into high humidity conditions did not result in a change in the colony morphology, and did not induce long range orientation in the newly grown region. This suggested that the first few hours to days were essential in the process. The process was also unrelated to nutrition or stiffness gradients, polymer orientation, or volatile compounds.

A similar phenomenon of sensitivity to humidity (without mention of orientation) is reported in work by Hennes and coworkers[4] on *B. subtilis* suspensions on nutrient plates with low percentage agar (< 0.7%) and high humidity (RH = 70%). They report a phenomenon by which the cells are able to draw moisture out of the plate in order to effectively increase droplet volume and "surf" on even shallow slopes. Much like the way rainwater droplets are pinned to windows by capillary forces, droplets of bacteria are also pinned by capillary forces to surfaces such as the agar plate. They can only flow once the ratio of gravitational forces to capillary forces (the Bond number) exceeds a critical threshold, 0.25 for water. For a *B. subtilis* suspension, the authors found the critical initial Bond number was 0.003, two orders of magnitude lower.

The mechanism proposed is as follows: *B. subtilis* secretes surfactin, a surfactant which creates a concentration gradient generating inward osmotic flows of water from the plate and also reduces the surface tension. As moisture is drawn out of the agar, the initial suspension of cells inflates to even 20 times the initial volume, effectively increasing the gravitational pull and allowing the droplet to flow even on slopes as shallow as 0.1°, commonly encountered on any surface. The first few hours are critical for this process, since evaporation, agar drying, and surfactant diffusion limit the process, and increased cell density promotes the process.

This phenomenon would explain our observations, and for *C. lytica* which tends to form local domains of orientation, induce long range orientation due to the local flows.

But where are the slopes?

Our experiments showed that the presence of a bulk slope (while effective) was not necessary. We hypothesize that the growth of the biofilm generates its own slopes as it grows due to the differences in thickness between the central region and the expanding edge, which we found varied between 1 and 54° depending on time of growth, more than sufficient to result in local orientation. As a local “pile” of cells forms (e.g. in the original site of inoculation), a slope is generated pointing outward from the center, causing local flows in those directions. This theory supports the “spokes” of orientation observed in Figure 5.14 and (wherever I end up putting the figures from humidity) as well as orientation such as in Figure 5.19 which resulted from colonies grown in the humidity chamber.

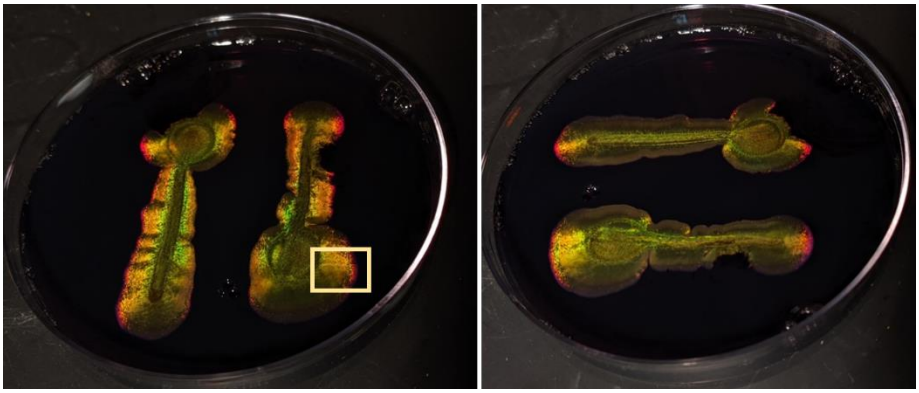

Figure 5.23. Inoculated streak of *C. lytica* grown at high humidity results in orientation outward from central point (line) of inoculation. Rectangular highlight indicates sloped region hypothesized to cause local flow.

Future work could investigate other interesting patterns that have been observed such as in Figure 5.14 and 5.15 A and B, where the region of long range orientation transitions to an orientation in the perpendicular direction, suggesting the presence of some sort of secondary flow that could form and result in changes in local orientation. Further work could also investigate the compounds responsible for the initial concentration gradient.

## 5.4 Preliminary microsphere indentation of C. lytica biofilms with long range orientation

Finally, we returned to the purpose of this experiment: investigating whether cell orientation could result in anisotropic mechanical properties.

*C. lytica* films were not cohesive and presented challenges to crosslink, and so could not be tested with the bulge test. Alternative options for testing were nanoindentation or microindentation. Here we lay the foundation for further work with preliminary experiments using microsphere indentation.

The idea was based on indentation experiments on other anisotropic media by Moghaddam and coworkers[5] and Efremov and coworkers[6]. For an isotropic material, the indentation profile would be identical along all cross sections. For an anisotropic material, the profiles would be different (Figure 5.24).

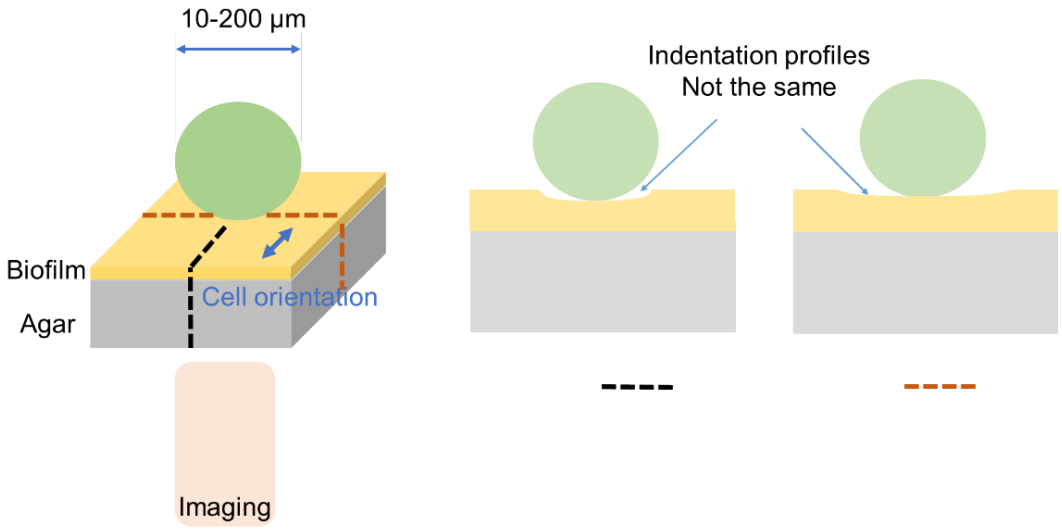


Figure 5.24. Indentation profiles vary according to cross section in anisotropic materials

We envisioned that 2D scans through a fluorescently labeled *C. lytica* biofilm with long range orientation would capture the deformation profiles (Figure 5.25) as ellipses in individual sections of the deformed material, with aspect ratios that could be correlated to the extent of anisotropy.

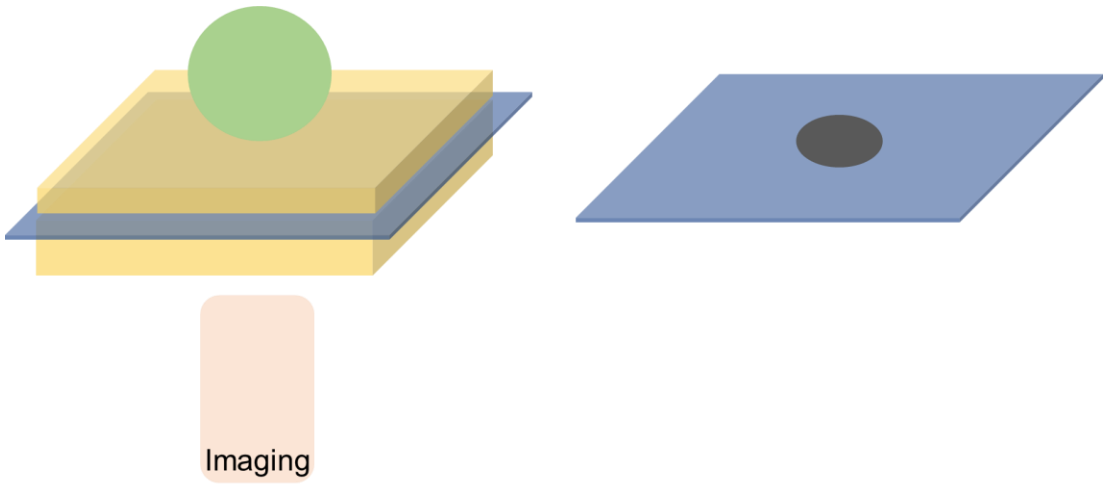


Figure 5.25. 2D scans (right) through biofilm indented with microsphere (left) depicting deformed material as a dark ellipse contrasting with the fluorescently labeled background material.

We screened a variety of available microspheres (barium titanate, polystyrene, silver coated hollow glass, soda lime glass, polyethylene) and chose polyethylene polydisperse microspheres since they were nonfluorescent, did not penetrate through the film in the size ranges tested, and did not cause optical effects with microscopy.

Next, we wanted to fluorescently label the *C. lytica* films without impacting their long range orientation or growth. 10 µL of 100 µg/mL stock of FM-143 was added to 5 mL of cooled nutrient agar and poured into a 60 mm diameter Petri dish with a No. 1.5 coverslip placed at the bottom. The agar formed a layer of thickness between 800 and 840 µm (compared to ~4 mm in typical growth experiments). Films were compared to their counterparts without dye.

Preliminary experiments in low humidity (42%) conditions revealed that after 3 days of growth, films with FM-143 had a thickness of 71 ± 8 µm at the center, and those grown on agar without dye had a thickness of 65 ± 9 µm at the center (N = 6). Although the dye did

not appear to have an effect on film thickness, neither film grew beyond a thickness of 70 μm even after 7 days.

In high humidity conditions (75%), this limitation was not present and in addition to the formation of consistent long range orientation which was previously not observed, the films were observed to be thicker without the 70 μm limitation. At the center, after 7 days of growth, regions without bulk orientation (yet grown on thinner agar) grew to 119 ± 7 μm in thickness while regions of bulk orientation were 105 ± 8 μm in thickness transitioning to 73 ± 6 μm closer to the propagating edge.

The addition of FM-143 was also found to not impact the formation of long range orientation (Figure 5.26), which was still present under humid conditions. SYTO9 was also tested in this manner but found to photobleach.

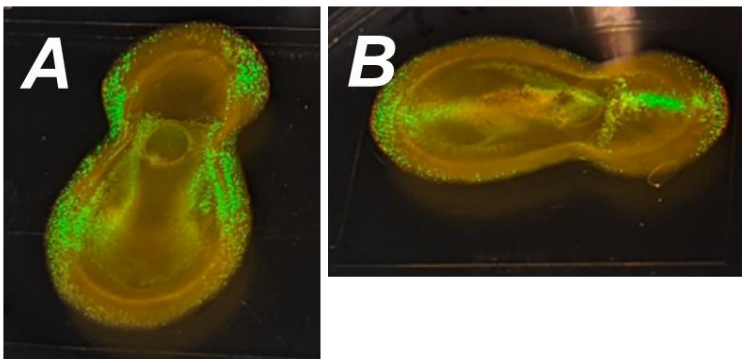


Figure 5.26. Films with FM-143 grown in humid conditions show long range orientation. Long range orientation shown as regions of film appearing and disappearing as film is rotated (ϕ) from A to B.

The fluorescently labeled colonies were lifted out of the petri dish by gently cutting the agar with a scalpel and lifting out the coverslip, and the backside of the coverslip was cleaned. The coverslip was then placed on an inverted microscope for imaging through the agar. Initial images were acquired and then clear polyethylene microspheres (Cospheric,

0.96g/cc, 10-106um diameter) were dispersed on top of the film. Regions of the film with isolated microspheres were imaged and z-stacks were acquired (Zeiss LSM 980 with Airyscan, objective: Zeiss 40×, NA = 0.6, WD = 3.3 mm).

Representative results are shown below; three biofilms were tested. Biofilm central thickness was measured to be approximately 97 μm from confocal microscopy. Indentation by a microsphere of diameter 33 μm (Figure 5.27, top left, approximate force as weight-buoyancy ~ 100 pN) resulted in dark elliptical regions in the 2D scans. Precise determination of indentation depth was challenging due to poor signal (lower NA/magnification objectives provided better signal but could not resolve the shape of the ellipse as clearly), but was estimated to be around 15 μm or 16% of the biofilm thickness. Slices in Figure 5.27 shown are spaced 3.1 μm apart in z.

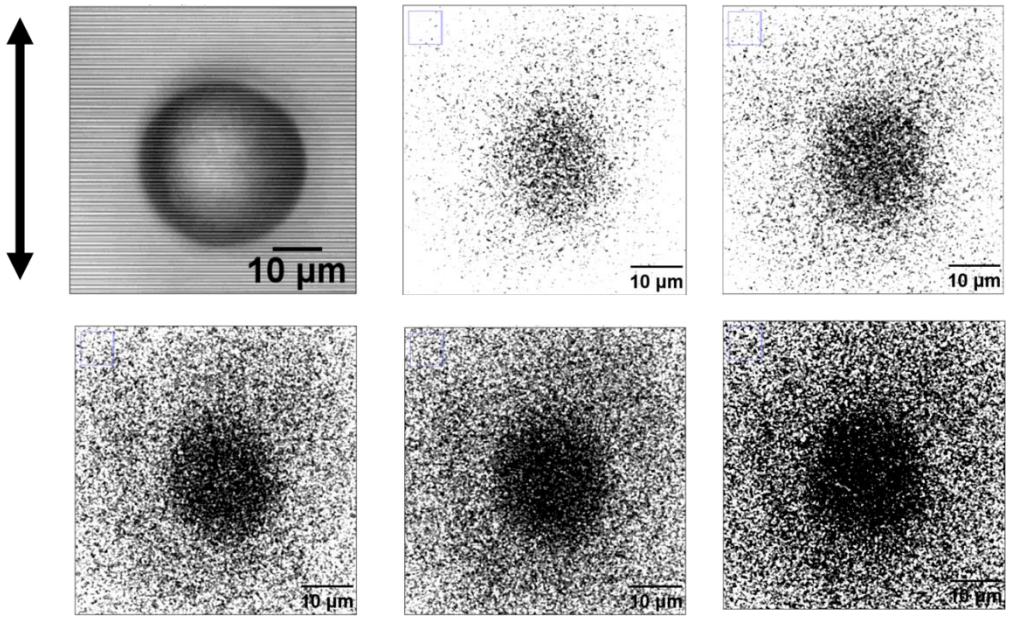


Figure 5.27. Z-scans through fluorescently labeled *C. lytica* with long range orientation with known cell orientation indicated by black vertical arrow. Indentation pattern transitions from elliptical to circular.

Images of slices were processed (Figure 5.28) to detect ellipses and output the ratio of major to minor axis length. For a biofilm with long range orientation, this ratio was found to vary between 1.2 and 1.25 depending on the 2D slice and processing. These values are not representative of slices close to either the top of the film or bottom of the indentation since these were highly noisy and could not be processed effectively; however the features near the top of the biofilm were less elliptical and more circular in shape. Control indentation patterns were acquired from the same sample in a region without long range orientation to avoid variability due to different growth conditions. Major to minor axis aspect ratios were found to be between 1.03 and 1.05 (Figure 5.29; microsphere diameter 26 μm).

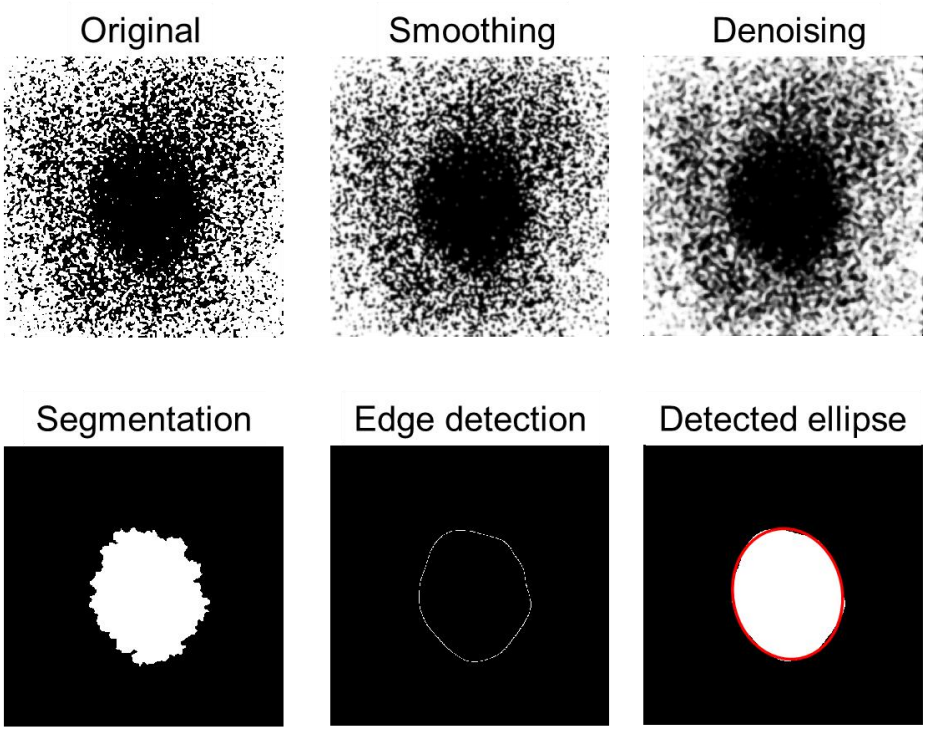


Figure 5.28. Image processing of 2D scans for ellipse major and minor axis detection.

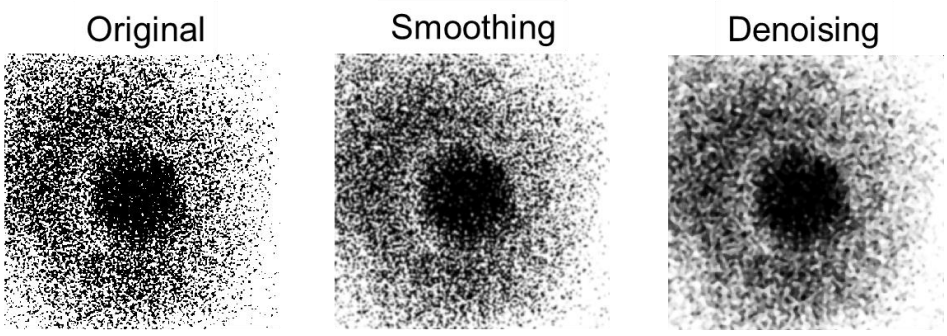


Figure 5.29. Control sample with major to minor axis aspect ratio of 1.03-1.05.

Our preliminary results suggest that *C. lytica* biofilms with long range orientation can have mechanical anisotropy with the material more easily deforming along the axis of cell orientation. These are preliminary studies however, and more data is needed to draw a conclusion about both the mechanism of anisotropy as well as quantify the mechanical properties.

**5.6 Conclusions and future work**

In this chapter, we extended our study of physical properties to marine organisms that exhibit interesting optical properties. We collected, isolated, and sequenced iridescent microbes from Pacific coast environments and chose *C. lytica* as a model organism for further optical and mechanical studies. We then developed methods to increase the orientation length scales of *C. lytica* biofilms from 10-20 μm to millimeters, more relevant for bulk studies, and confirmed the long range orientation with microscopy, imaging, and goniometry-spectrometry. Finally, we presented preliminary mechanical studies with microsphere indentation that suggested that *C. lytica* biofilms exhibit anisotropic mechanical properties as a result of their long range orientation.

In future work, we hope to expand upon many of the aspects presented here. First, in addition to the iridescence in reflection observed in *C. lytica*, we also observed many biofilms with iridescence in transmission but not reflection (see Section 5.7). Further characterization of these microbes could yield interesting insights into optical phenomena that could be useful for engineered living materials. Secondly, some strains (such as R3) had cells with curved morphology that could be interesting from the perspective of liquid crystal colloids to study different types of packing and optical effects at longer (non-visible) wavelengths.

Moving to mechanical studies, although we were not able to characterize *C. lytica* with the bulge test due to its lack of cohesiveness and difficulty with crosslinking, other families of iridescent biofilms that have been reported to be more cohesive[7] may be more amenable to bulge testing. Alternatively, full force-indentation profiles would be possible for *C. lytica* using either the above method with multiple microsphere sizes or nanoindentation/ microindentation. In the case of microsphere indentation described above, we found that microspheres below 20 μm in diameter tended to aggregate and could not be imaged individually; better dispersion methods would be required. A better protocol (e.g. with a micromanipulator and controlled suction) would also be required to unload the microspheres and determine whether or not the indentation is elastic. Microspheres also present challenges in that indentation at smaller diameters is difficult to resolve and adds to the challenges already present from the low signal and high noise. Micro or nanoindentation would be preferable: we briefly explored microindentation but film adhesion to the indenter was a significant challenge even after coating the indenter with silicone oil. Further, although not discussed in this chapter in detail, we discovered that the

long range oriented films can accommodate 0.87 µm diameter fluorescent microspheres mixed into the culture prior to growth. Long range orientation is still possible using this method, and these films (where microspheres localize near the top) may be a better system for imaging the full deformation profile instead of fluorescent labeling of the cells, which can also impact their properties. Another aspect that would need to be addressed is film drying during imaging: ideally the film would be imaged in a humid chamber to prevent the thickness and properties from changing.

Other features have also been observed but not explored: for example *C. lytica* shows patterns during OCT imaging that are not yet explained and are not correlated to the direction of long range orientation (Figure 5.30).

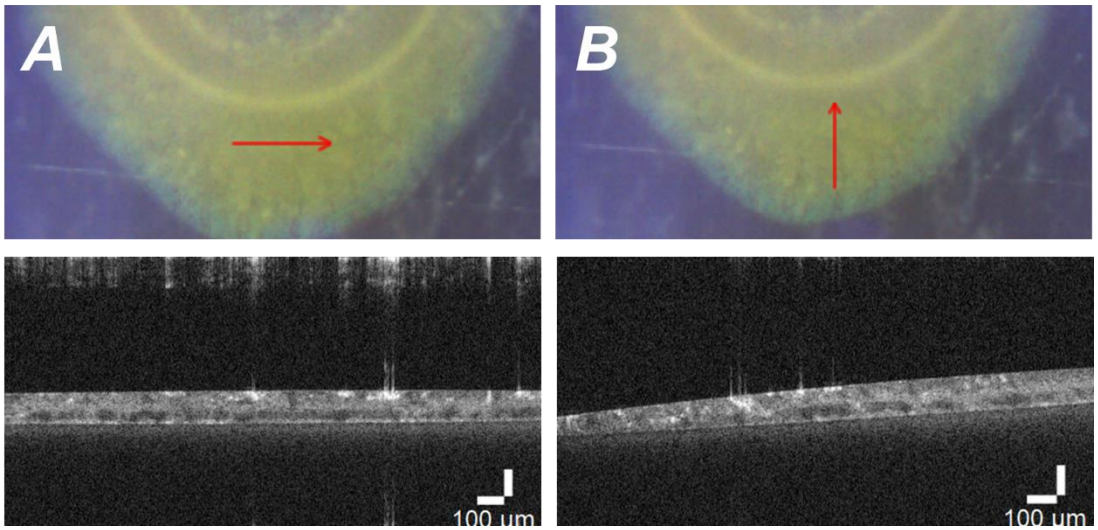


Figure 5.30. Features in OCT images of *C. lytica* biofilms, independent of orientation (A vs. B). A) Scan perpendicular to direction of orientation. Top: camera image with red arrow indicating scan. Bottom: OCT scan. B) Scan parallel to direction of orientation.

Finally, although we did observe a connection between optical and mechanical behavior (Figure 5.31), it could not be explored in detail.

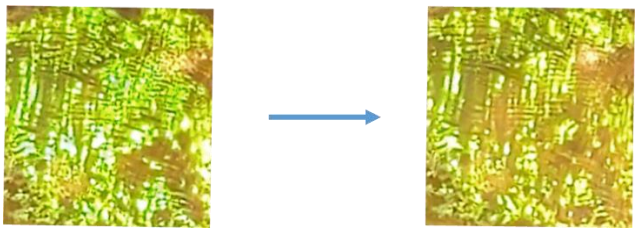

Figure 5.31. *C. lytica* film with long range orientation (vertical), when compressed horizontally, results in a redshift in iridescence.

Further experiments using the goniometer-spectrometer setup described above in conjunction with simple mechanical studies could yield insights into the design of optomechanical properties of engineered living materials for sensing and response. These studies would also help answer the question of how these materials respond to mechanical stress: do the cells elongate? Do layers of cells simply slide over one another? For now, these remain open questions.

## 5.7 Additional figures and supplemental information

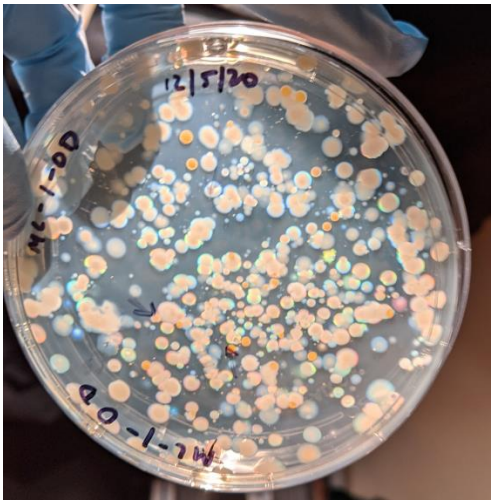

Figure S5.1. Colonies (sampling site #1) iridescent in transmission

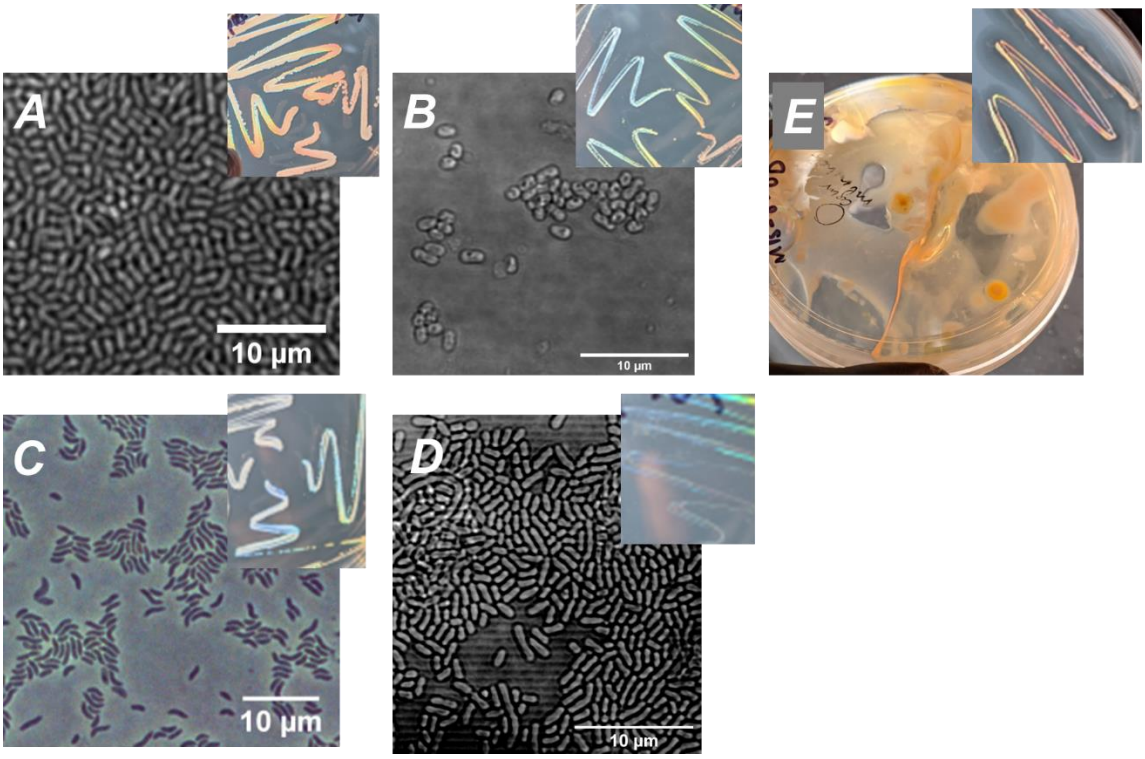


Figure S5.2. Colonies iridescent in transmission from various sampling sites sequenced (16s rDNA) for closest matches. Insets: camera images of iridescence in transmitted light. A) *Pseudoalteromonas sp.* B) *Oceanisphaera sp.* C) *Marinomonas sp.* D) *Polaribacter dokdonensis* E) *Agarivorans albus* (main image: colony degraded agar in the main plate within two weeks. Inset: dark halo visible around colony indicating agar degradation)

**References**


1. Hahnke, R. L. & Harder, J. Phylogenetic diversity of Flavobacteria isolated from the North Sea on solid media. *Syst. Appl. Microbiol.* **36**, 497–504 (2013).

2. McBride, M. J. Bacterial gliding motility: Multiple mechanisms for cell movement over surfaces. *Annual Review of Microbiology* vol. 55 49–75 (2001).

3. Kientz, B. *et al.* Isolation and distribution of iridescent Cellulophaga and further iridescent marine bacteria in the Charente Maritime coast , French Atlantic coast To cite this version : HAL Id : hal-01090460 Isolation and distribution of iridescent Cellulophaga and furt. *Syst. Appl. Microbiol.* **36**, 244–251 (2014).

4. Schertel, L. *et al.* Complex photonic response reveals three-dimensional self-organization of structural coloured bacterial colonies. *J. R. Soc. Interface* **17**, (2020).

5. Kientz, B., Marié, P. & Rosenfeld, E. Effect of abiotic factors on the unique glitter-like iridescence of Cellulophaga lytica. *FEMS Microbiol. Lett.* **333**, 101–108 (2012).

6. Kientz, B., Vukusic, P., Luke, S. & Rosenfeld, E. Iridescence of a marine bacterium and classification of prokaryotic structural colors. *Appl. Environ. Microbiol.* **78**, 2092–2099 (2012).

7. Chapelais-Baron, M. *et al.* Colony analysis and deep learning uncover 5-hydroxyindole as an inhibitor of gliding motility and iridescence in cellulophaga lytica. *Microbiol. (United Kingdom)* **164**, 308–321 (2018).

8. Kientz, B. *et al.* Glitter-Like Iridescence within the Bacteroidetes Especially Cellulophaga spp.: Optical Properties and Correlation with Gliding Motility. *PLoS One* **7**, (2012).

9. Johansen, V. E. *et al.* Genetic manipulation of structural color in bacterial colonies. *Proc. Natl. Acad. Sci. U. S. A.* **115**, 2652–2657 (2018).

10. Kientz, B. *et al.* A unique self-organization of bacterial sub-communities creates iridescence in Cellulophaga lytica colony biofilms. *Sci. Rep.* **6**, 19906 (2015).

11. Kee, H. L. *et al.* Draft Genome Sequence of the Iridescent Marine Bacterium Tenacibaculum discolor Strain IMLK18. *Microbiol. Resour. Announc.* **8**, (2019).